Study on the Plasma Waves in the Geomagnetic Tail Region via Spacecraft Observations

by
Hirotsugu Kojima

September 1998

Study on the Plasma Waves in the Geomagnetic Tail Region

via

Spacecraft Observations

by
Hirotsugu Kojima

A thesis submitted for the degree of Doctor of Philosophy
in Faculty of Engineering of Kyoto University

September 1998

Thesis Supervisor: Prof. Hiroshi Matsumoto

Acknowledgments

I am deeply indebted to my research supervisor Professor Hiroshi Matsumoto for his continued guidance, helpful suggestions, fruitful discussions, and his support throughout the present work as well as for the use of the plasma wave data of the Geotail plasma wave instrument (PWI). I also thank him for his leadership and coordination of the Geotail PWI team which kept it in good shape before and after the launch of the spacecraft so that we could proceed with our data analyses and collaborations smoothly.

I wish to thank Professor Kozo Hashimoto for his continuous and successful efforts to design the Geotail PWI electronic circuits from the very initial phase of the Geotail mission. I also thank him for many suggestions and discussions in our laboratory meetings and his careful reading the manuscript of this thesis.

I sincerely thank Prof. Tokuhiro Obiki for his careful reading and evaluating the manuscript for the accomplishment of this thesis. I also thank him for his many helpful comments and suggestions on this thesis.

I am deeply grateful to Dr. Yoshiharu Omura for his collaboration on computer experiments. The achievements on understanding the Electrostatic Solitary Waves were possible only because of the good collaborations between spacecraft observations and computer experiments. I also thank him for his careful reading the manuscript of this thesis and many helpful comments to me.

I wish to express my appreciation to Professor Iwane Kimura of Osaka Technical College for his encouragements to complete my thesis. He was the supervisor of my Bachelor Thesis. I appreciate that he provided me a first chance to proceed doing research in this field.

I wish to express my deep appreciation to Professor Isamu Nagano of Kanazawa University for his efforts to design the Geotail PWI receivers and search coil sensors and to establish the Wave-Form Capture calibration programs. I also thank him for his tremendous efforts to reduce artificial noises emitted from the spacecraft. The procedures for the EMC tests on Japanese scientific spacecraft were well established by his efforts.

I wish to thank Professor Minoru Tsutsui of Kyoto Sangyo University for his large efforts in the EMC tests and for his very helpful suggestions during the ground tests of the Geotail PWI. The EMC strategy developed for scientific spacecraft was possible because of his eager and continuous endeavors in the EMC tests. I also thank him for his calculations of the precise antenna impedance.

I sincerely thank Dr. Roger R. Anderson of The University of Iowa for his developing the Multi-Channel Analyzer. His experiences from his participating in many space missions were always very helpful to me in the establishment of the Geotail PWI subsystem. Furthermore, his frank personality always made us calm down during the Geotail ground tests.

I thank Professor Toshimi Okada of Toyama Prefectural University for his efforts to develop preamplifiers for the Geotail PWI. He repeated his experiments many times in order to realize the excellent low noise and stable preamplifiers for electric fields.

I am sincerely indebted to the late Dr. F. L. Scarf for his many helpful suggestions and unique ideas on the design of the plasma wave receivers as well as the strategy for the noise reduction from the spacecraft.

I am grateful to Dr. Hideyuki Usui for many fruitful discussions on his view points of computer experiments for the more than 10 years I have worked with him. He has also always been a good advisor for me in my life as well as in my research. I always appreciate his suggestions and opinions on my problems. I am also grateful to Dr. Naoki Shinohara for many suggestive opinions in our laboratory meetings.

Many thanks are due to all of the staff members of Radio Atmospheric Science Center (RASC) in Kyoto university.

I wish to express my appreciation to all of the members supporting the Geotail missions. Especially, I deeply thank Professor Atsuhiro Nishida of Institute of Space and Astronautical Science (ISAS), program manager of the Geotail mission, for his directing and coordinating the Geotail mission. Furthermore, I also thank him for the support of my overseas trips for the collaborations with other Geotail groups.

I am deeply grateful to Professor Toshifumi Mukai of ISAS, project scientist of the Geotail mission, for his continuous efforts to make the Geotail mission successful before and after the launch of Geotail. I learned many things about the spacecraft and his attitude for building up the spacecraft mission. The success of the EMC tests was possible only because of his coordination. I also thank him for the use of the Low Energy Particle (LEP) measurement data of Geotail.

I thank Prof. Susumu Kokubun of Solar Terrestrial Environment Laboratory in Nagoya university and Prof. Koichiro Tsuruda of ISAS for the use of the Magnetic field (MGF) and Electric field (EFD) data of Geotail.

I sincerely wish to thank the late Professor Tatsundo Yamamoto for his contributions to the EMC tests as well as for providing us the magnetic field data. Furthermore, his comments and suggestions were always very helpful for me. I will never forget that we repeated the EMC tests more than 100 times with him in order to achieve a clean spacecraft with regard to the electromagnetic environment.

I sincerely wish to thank Professor L. A. Frank and Dr. W. R. Paterson of The University of Iowa for the use of their CPI plasma measurement data. I was very pleased with their efforts to proceed with the study of wave-particle interaction very actively.

I wish to thank Professor Maha Ashour-Abdalla of University of California Los Angeles for her helpful comments and fruitful discussions since her visit to our research center and for her continuous encouragement to my thesis writing.

I am grateful to Professor Nobuyuki Kaya of Kobe University for his continuous encouragements to complete the present thesis. His advice based on his experiences with many rockets and satellites have always been helpful for me.

I appreciate to Dr. Kazuhiro Akimoto of Teikyo University for his encouragements to write up this thesis and providing many knowledges about the nonlinear evolution of the Langmuir waves.

I am sincerely grateful to Dr. Greg K. Crawford of the Stanford Research Institute for many discussions about the plasma wave properties associated with the interplanetary shocks during his stay in RASC. I also thank to Dr. Y. Zhang of Saskatoon university in Canada for collaborations about whistler waves observed by Geotail during his stay in RASC.

I thank Dr. Masaki Okada of the National Institute of Polar Research for many discussions about the electrostatic solitary waves. I examined many plausible potential structures

for explaining the ESW waveforms with him. I also appreciate for his contribution to develop the Geotail PWI data analysis softwares.

I thank Mr. Yoshihiro Sato and Mr. Wataru Taguchi, engineers in Meisei electric company, for their big efforts to design and assemble the Geotail PWI subsystem. I also thank Mr. Dan Odem and Mr. Michael Mitchell, engineers at The University of Iowa, for their efforts to complete the MCA receiver. I learned many things from their vast experience with plasma wave receivers onboard spacecraft.

For their support and cooperation in the Geotail PWI data analyses, I am grateful to the graduate students in Kyoto University, Messrs. Hiroaki Sato, Tomohiro Takeda, Yoshitoshi Takeshita, Atsushi Fujita, Osami Nishimura, Takeshi Miyatake, Hiroyuki Yokoyama, Satoshi Chikuba, Hiroaki Hamada, Taketoshi Miyake, Hiroki Furuya, Kouhei Otsuka, Sen Kudo, Nobuhiko Miki, Daisuke Morikawa, Masashi Arakawa, and Kenichi Miyaguti, Mses. Satoko Horiyama, and Jyunko Koizumi.

I wish to thank Ms. Keiko Miwa, secretary to Professor Matsumoto, for her continuous hearty encouragements and kindness to me.

I thank Ms. Mitsuko Abe, secretary in the library, for searching for many papers referred in the present thesis and making photocopies of them.

My work was also always supported by secretaries in Matsumoto Laboratory and Hashimoto Laboratory. I am grateful to Mses. Kaori Shiomi, Noriko Takemura, Makiko Abe, Nanako Izumi, Tomomi Kawamata, and Satomi Nishisaka.

All of the Geotail raw telemetry data have been processed in Kyoto University by Mses. Reiko Kita, Tomoe Sugimoto, Tomoko Taniguchi, Reiko Yamada, and Ayako Shozu. I am sincerely grateful to them. Without their efforts, I could not have proceeded with my work on the Geotail data analyses.

I wish to thank my parents for their encouragements and support in my life. Their implicit and explicit care for me are always my pleasure.

Finally, special thanks are due to my wife Chiho, and my son Hiroaki for their continuous encouragements and hearty words for my completing the present thesis. They have really always been there with me and they have always made me feel relieved.

Abstract

Geotail spacecraft was designed for investigating the geomagnetic tail region under the Japan-US collaboration program. Spacecraft and five instruments were developed in Japan and two instruments and a launch vehicle were provided by US. Since the successful launch of Geotail on July 24, 1992, we have been receiving a tremendous amount of data from the spacecraft.

The geomagnetic tail region is the energy reservoir of the terrestrial magnetosphere. The injected energies from the solar wind are reserved once in the magnetotail region and reserved energies are suddenly released through emissions of plasmas triggered by magnetic reconnections.

In the present thesis, we investigate plasma waves excited in the magnetotail region. One of the main objectives in the present thesis is to study the microscopic processes of wave-particle interactions by make clear the generation mechanism of electrostatic waves observed in the geomagnetic tail region. Another objective is to study the macroscopic structure of the magnetotail region by processing the plasma wave data statistically. This new attempt to apply plasma wave data to the study of the macroscopic structure is a first step to combine the microscopic phenomena with the macroscopic phenomena.

In order to meet objectives of the plasma wave observations in the geomagnetic tail region, we designed plasma wave receivers and sensors with very high sensitivities and very low noise levels. We describe the detailed specifications of the Plasma Wave Instrument (PWI) onboard Geotail spacecraft. The PWI has a newly designed Wave-Form Capture (WFC) receiver as well as conventional spectrum receivers, so-called Sweep Frequency Analyzer (SFA) and Multi-Channel Analyzer (MCA). The WFC has a capability to collect waveforms directly. We mainly use the WFC data in the present thesis.

Since the magnetotail is inhomogeneous in space and nonstationary in time, we observe different types of plasma waves in each distinct region of the magnetotail and in each encounter of the transient phenomena. We summarize plasma waves observed in each distinct region of the magnetosphere, or in each encounter with transient phenomena before discussing the detailed plasma wave observation results which we focus on in the present thesis. These knowledges of the plasma wave signatures are very helpful for identifying the region where the spacecraft is located.

Using the WFC receiver, we succeeded in constructing waveforms of the Broadband Electrostatic Noise (BEN), Narrowband Electrostatic Noise (NEN), and electron plasma waves observed in the magnetotail region. The observed waveforms of the BEN in the plasma sheet boundary layer consist of a series of isolated bipolar pulses. We show the broadband and bursty natures of the BEN spectra are caused by such isolated pulses. We term these pulses "Electrostatic Solitary Waves (ESW)." We also find that such solitary waves are observed in the magnetosheath region. On the other hand, we find the quasi-sinusoidal waveforms of the NEN. We term the waveforms of the NEN "Electrostatic Quasi-Monochromatic Waves (EQMW)." The EQMW are also frequently observed in the magnetosheath region.

In order to study generation mechanisms of these ESW and EQMW, we consult computer experiments using the full particle electromagnetic computer simulation code. Our computer experiments succeed in reproducing the waveforms of the ESW and EQMW. Based on the results of computer experiments, we conclude that the ESW are equivalent to

isolated electrostatic potential structure which is formed as the result of the nonlinear evolution of the electron bump-on-tail instability. Further, we also conclude that the EQMW can be generated by the electron velocity space hole mode.

The waveform observations of electron plasma waves show that their amplitudes are strongly modulated. Further, our detailed polarization analyses show that the modulated electron plasma waves include Langmuir waves and Electron Cyclotron Harmonics (ECH) waves propagating in the parallel and perpendicular directions relative to the ambient magnetic field, respectively. Since upper hybrid resonance frequencies are almost equal to electron plasma frequencies in the tail lobe, it is very difficult to distinguish Langmuir waves from ECH waves without examination of their polarizations. We extensively apply our results to other spacecraft observations in various regions, and discuss a possibility that their proposed nonlinear Langmuir waves include the ECH waves.

In the final part of the present thesis, we show results of new attempts to study the magnetotail structures using the plasma wave signatures. In general, plasma wave data are mainly dedicated to the study of microscopic physics. However, since plasma waves are results of wave-particle interactions in each distinct region, they well reflect features in each region. Therefore, by processing plasma wave data statistically, we can study macroscopic structures. We discuss structures of the magnetopause and plasma sheet by statistical analyses on observed plasma waves and local plasma densities obtained from plasma wave data.

Contents

1 General introduction 1

1.1 Geomagnetic tail . . . 1
1.2 International solar terrestrial physics (ISTP) . . . 6
1.3 Plasma wave observations in space . . . 8
1.3.1 Objectives and advantages of plasma wave observations . . . 8
1.3.2 Geotail plasma wave observations . . . 9
1.4 Contribution of the present work . . . 16

2 Plasma wave instrument onboard Geotail spacecraft 21

2.1 Introduction . . . 21
2.2 General descriptions of the Geotail spacecraft . . . 23
2.3 Electric/magnetic sensors and their peripheral circuits . . . 26
2.3.1 Electric field sensors . . . 27
2.3.2 Magnetic field sensors . . . 33
2.4 Sweep frequency analyzer (SFA) . . . 35
2.5 Multi-channel analyzer (MCA) . . . 39
2.6 Wave-form capture (WFC) . . . 41
2.7 Calibrations . . . 44
2.7.1 Onboard calibration system . . . 44
2.7.2 Measurements of antenna impedance . . . 46
2.7.3 Calibrations including the antenna impedance . . . 49
2.8 Electromagnetic compatibility (EMC) . . . 52
2.8.1 Geotail EMC specifications . . . 52
2.8.2 Strategies for suppressing artificial noises in spacecraft . . . 57

3 Plasma wave signatures in the magnetosphere 63

3.1 Solar wind and electron/ion foreshock regions . . . 63
3.2 Bow shock . . . 66
3.3 Dayside outer magnetosphere . . . 68
3.4 Magnetosheath . . . 69
3.5 Magnetopause boundary . . . 71
3.6 Tail lobe, central plasma sheet and its boundary layer . . . 75
3.7 CME and CIR . . . 75
3.8 Plasmoid . . . 79
3.9 Summary . . . 81

4 Waveform observations of the broadband electrostatic noise in the plasma sheet 85
4.1 Introduction · · ·

9.4.2 IMF dependence of the plasma sheet structure 202
9.5 Summary and discussion 203

10 Summary and concluding remarks 211
10.1 Summary 211
10.2 Energy flows from the solar wind 215
10.3 Remained problems to be resolved in the future 218
10.3.1 Source of electron beams 218
10.3.2 Low frequency component of the BEN 220
10.4 Missions to other planets 221

A Definitions of coordinate systems 227
A.1 Spacecraft coordinate system 227
A.2 Geocentric solar ecliptic coordinate system (GSE) 227
A.3 Geocentric solar magnetospheric coordinate system (GSM) 228
A.4 Solar magnetic coordinate system (SM) 228
A.5 HVD coordinate system 228
A.6 Modified GSM coordinate system 230

B Acronyms 231

References 235

List of Figures

1.1 Illustration on the magnetic field configuration of the magnetosphere [*Copyright NASA/ISTP*]. 2
1.2 Three-dimensional drawing of the geomagnetic tail region [*after Lui*, 1987]. 2
1.3 A cross-section of the Earth's magnetotail at about x = -20 R_E. Distinct regions including polar mantle (plasma mantle), lobe, plasma sheet boundary layers, central plasma sheet and low-latitude boundary layers are shown by shading patterns [*after Mcpherron*, 1991]. 3
1.4 Magnetic reconnection between the IMF and the Earth's magnetic field [*after Russell*, 1972] 4
1.5 An approximate scale drawing showing the formation of three types of neutral lines [*after Mcpherron*, 1991]. 5
1.6 Sequence of changes of magnetic and plasma configuration of the plasma sheet for generating a plasmoid [*after Hones*, 1977]. 7
1.7 ISTP fleet and related spacecraft [*Copyright NASA/ISTP*]. 8
1.8 Whistler wave observed by the Vanguard 3 satellite [*after Cain et al.*, 1961]. 9
1.9 An example of the nonthermal continuum radiation observed by Geotail. . 10
1.10 An example of the Auroral Kilometric Radiation observed by Geotail spacecraft. 11
1.11 An example of the Auroral Myriametric Radiation observed by Geotail spacecraft [*after Hashimoto et al.*, 1998]. 12
1.12 Frequency-time spectrograms of five representative ECH waves observed by Geotail in the dayside outer magnetosphere, and magnetotail regions [*after Matsumoto et al.*, 1998]. 13
1.13 Frequency-time spectrogram of B_z component (upper) and corresponding wavenormal angles [*after Nagano et al.*, 1998]. 15
1.14 Contribution of the present work in the Geotail plasma wave mission. . . 17

2.1 Block diagram of the PWI onboard Geotail spacecraft. 22
2.2 Chassis of the PWI-M. PWI-M contains all of the circuits of the PWI except the PWI-MA. 22
2.3 Chassis of the PWI-MA. PWI-MA was developed by the University of Iowa, USA. 23
2.4 External view of the Geotail spacecraft and configuration of the PWI and related sensors. 24
2.5 Geotail distant tail orbits plotted on the modified GSM coordinates. . . . 25
2.6 Near tail orbits plotted on the modified GSM coordinates. 25

2.7 Two boxes of the WANT (WANT-A and WANT-B). 26
2.8 Two boxes of the PANT (PANT-A and PANT-B). 26
2.9 Configuration and relative angles between each sensor. 27
2.10 Tri-axial search coils (PWI-SC) mounted on the top of the MST-S. 28
2.11 Drawings of (a) WANT and (b) PANT elements [*after Matsumoto et al.*, 1994a]. 29
2.12 Electric circuits for the antenna and preamplifiers of (a) WANT and (b) PANT. 30
2.13 Minimum noise levels of the WANT and PANT preamplifiers measured during the preflight calibration test [*after Matsumoto et al.*, 1994a]. 32
2.14 Frequency responses of the gain in a low frequency range of (a) the WANT and (b) the PANT preamplifiers [*after Matsumoto et al.*, 1994a]. 32
2.15 Frequency responses of the phase rotation in a low frequency range of (a) the WANT and (b) the PANT preamplifiers [*after Matsumoto et al.*, 1994a]. 33
2.16 Illustration of the electric circuit of the PWI-SC and its preamplifier [*after Matsumoto et al.*, 1994a]. 34
2.17 (a) Frequency response of the gain for a representative search coil (γ component) and its preamplifier circuit. The measurement was conducted in a parallel magnetic field of 100pT, but the characteristic curve illustrated in this figure represents the response which has been scaled down to the noise level ($\sim$ 1 pT). (b) Phase rotation as a function of frequency for the same search coil and preamplifier circuit [*after Matsumoto et al.*, 1994a]. 36
2.18 Sensitivity for search coils onboard several spacecraft in their flights [*after Matsumoto et al.*, 1994a]. 37
2.19 Block diagram of the SFA main electronics for a representative frequency band [after Matsumoto et al., 1994a]. 38
2.20 A representative example of Input/Output amplitude characteristics of an SFA receiver (Band 4 for electric field) [after Matsumoto et al., 1994a]. . . 38
2.21 SFA amplitude ranges of (a) five band receivers for the electric field, and of (b) three for the magnetic field. In each band of the electric field receivers, high (H) and low (L) gain amplifications with a 30 dB difference are selectable in keeping an inherent dynamic range (90 dB) of the circuit, while the sensitivity for magnetic field is constant. In each figure, a representative sensor sensitivity is drawn by a broken line [*after Matsumoto et al.*, 1994a]. 39
2.22 Block diagram of the MCA system [*after Matsumoto et al.*, 1994a]. 40
2.23 Block diagram of the WFC system [*after Matsumoto et al.*, 1994a]. 41
2.24 Frequency responses of (a) gain and of (b) phase rotation for a representative receiver (E_U) in the Low gain Memory mode of the WFC [*after Matsumoto et al.*, 1994a]. 43
2.25 Example of the frequency spectrum of the onboard calibration signal. . . . 44
2.26 Waveforms of the onboard calibration signal received by the WFC. (a) Uncalibrated waveforms, and (b) Calibrated waveforms [*after Matsumoto et al.*, 1994a]. 45
2.27 Basic block diagram for the principle of measuring the antenna impedance by the Geotail PWI. 47

2.28 Simplified block diagram for the principle of measuring the antenna impedance by the Geotail PWI. 48
2.29 Further simplified block diagram. 49
2.30 A quantitative relation between the resistance and capacitance values derived from WANT impedance measured by the 65 experiments conducted in the Earth's magnetosphere. The height and width between the facing sides of each rectangle indicate fluctuation ranges of the resistance and capacitance values, respectively. C_0, which is shown by the vertical dashed line, is the theoretical value for a linear dipole antenna with one element length of 50 m in a vacuum [*after Tsutsui et al.*, 1997]. 50
2.31 Block diagram for the principle of calibrations including the effect of the antenna impedance. 51
2.32 Military standard specifications (MIL-STD-461A) [*after White*, 1981]. . . 53
2.33 Geotail EMC specifications for (a) Conducted emissions, (b) Radiated emissions (electric field) and (c) Radiated emissions (magnetic field). 54
2.34 Magnetic shield chamber at ISAS. 54
2.35 Connections of each sensor and spectrum analyzers. 55
2.36 EMC measurement system. 55
2.37 Configurations of the Geotail EMC tests in the magnetic shield chamber. 56
2.38 Example of the individual EMC test: Despan motor with the Despan antenna. 57
2.39 (a) Electric field noise emitted from the MGF fluxgate magnetometer. (b) The noise is suppressed by shielding the connectors of the fluxgate magnetometer. 58
2.40 (a) RE-04 noise radiated from the DC-DC converter of the SAS. (b) Noise reduction by shielding the instrument with μ-metal. Note that the intense peaks at 9 kHz in both panels are the calibration signals radiated from the standard loop antenna. 60
2.41 Intense magnetic field noise radiated from the PIM lines. 61
2.42 Connection and signal current route among a subsystem, DHU and PCD. 61

3.1 Subregions of the foreshock region, which are proposed based on the plasma wave and plasma measurements [*after Matsumoto et al.*, 1997b]. 64
3.2 Frequency-time spectrogram observed in the electron foreshock. Equivalent subregions are shown in the top panel. The representative wave signature of the electron foreshock is the intense electron plasma waves [*after Matsumoto et al.*, 1997b]. 65
3.3 Frequency-time spectrogram observed in the ion foreshock. Equivalent subregions are shown in the top panel. The representative wave signature of the ion foreshock is the ion acoustic-like wave [*after Matsumoto et al.*, 1997b]. 65
3.4 Plasma wave signatures in the bow shock crossing. The transition timings of the bow shock are indicated by arrows in the top panel [*after Matsumoto et al.*, 1998]. 67

3.5 Plasma waves observed around the dayside magnetopause. (a) Overview of the frequency-time spectrogram for a whole interval of the magnetopause skimming [*after Matsumoto et al.*, 1998]. (b) Detailed spectra of the Totem Pole emissions (Bursty ECH emissions) [*after Matsumoto and Usui*, 1997a]. (c) Spectral structure of the chorus emissions [*after Nagano et al.*, 1996]. · 68
3.6 Typical plasma wave signatures observed in the magnetosheath region [*after Matsumoto et al.*, 1998]. · · ·

4.7 Spin dependence of the PSBL ESW. This shown result suggests that the polarization of the PSBL ESW is parallel to the ambient magnetic field [*after Kojima et al.*, 1994]. · · ·

4.27 Frequency-time spectrogram]generated from the WFC data (top), snapshots of waveforms and corresponding Fourier spectra observed at two different times. We can clearly see that the PSBL ESW mainly contribute to the high frequency component of the BEN. · 119
4.28 Waveforms and electric field orientation of the PSBL ESW. · · · · · · · · · 120
4.29 Same as Fig. 4.28 but for low frequency component. · · · · · · · · · · · · · 121
4.30 Magnetic field spectra observed by the MCA. There exist no differences in the observed spectra in the cases of PSBL ESW, without PSBL ESW, and without BEN. · 122

5.1 Schematic illustration on the method of propagation analyses. · · · · · · · · 126
5.2 An example of PSBL ESW propagation analysis. Upper two panels show observe waveforms of E_U and E_V component. The lower panel is schematic drawing for configuration of antenna polarity and potential flow direction at this time. · 128
5.3 Same as Fig. 5.2 but for different spin phase. · · · · · · · · · · · · · · · · · 129
5.4 Statistical analyses on the ESW propagation directions. · · · · · · · · · · · · 130
5.5 Frequency-time spectrogram generated from SFA (a), and MCA(b) and representative waveforms (c) [*after Kojima et al.*, 1997a] · · · · · · · · · · · · · · · 132
5.6 Snapshots of the ESW observed at three different time periods. The tailward ESW are observed in the initial phase of one WFC sequence. However, after that as shown in the middle panel, both earthward and tailward ESW are observed simultaneously, and finally only the earthward ESW can be observed. · 133
5.7 Time chart of the observations of tailward or earthward ESW as well as the observations of Langmuir waves. · 134
5.8 Computer experiment on counterstream BGK potentials excited by counterstream electron beams [*after Omura et al.*, 1996]. · · · · · · · · · · · · · · · 135
5.9 Electron velocity distribution observed by LEP. (a) Color coded electron velocity distribution on $v_{\parallel}$ -- $v_{\perp}$, (b) reduced velocity distribution, and (c) beam components extracted from the reduced velocity distribution shown in panel (b). · 136
5.10 Schematic drawing for observations of the couterstream PSBL ESW. · · · 137

6.1 Typical wave spectra around the slow mode shocks as well as the variation of the ambient magnetic field [*after Scarf et al.*, 1984b]. · · · · · · · · · · · 140
6.2 Variation with radial distance of electric field spectra in the magnetopause boundary layer (top), and those in the plasma sheet (bottom) [*Scarf et al.*, 1984a]. · 141
6.3 Polarizations of electrostatic waves observed in the magnetopause boundary layer [*Scarf et al.*, 1984a]. · 141
6.4 Frequency-time spectrograms from (a) SFA and (b) MCA and (c) waveforms from WFC of the narrowband electrostatic noise (NEN) observed in the tail lobe on May 29, 1993. [*after Kojima et al.*, 1997a]. · · · · · · · · · · · · · · 143

6.5 (left) Time series of the lobe electrostatic quasi-monochromatic waves (EQMW) waveforms observed by the WFC. (right) Corresponding spectra calculated with the fast Fourier transform (FFT) method. [*after Kojima et al.*, 1997a]. 145
6.6 Spin dependence of the lobe EQMW waveforms during the interval from 1200 to 3100 ms for (a) E_U and (b) E_V: (c) Variation of the product of E_U and E_V components. When E_U (E_V) is parallel (perpendicular) to the ambient magnetic field at 2050 ms, we can see the minimum amplitude of E_V component in panel (b) and the change of signs of $E_U \times E_V$ in panel (c). [*after Kojima et al.*, 1997a]. 146
6.7 Schematic drawing of the lobe EQMW potential. The spin dependence of the lobe EQMW shows that the lobe EQMW are the plane waves which propagate along the ambient magnetic field B_o [*after Kojima et al.*, 1997a]. 147
6.8 Relation between the frequencies of the lobe NEN and the local plasma frequencies. Their clear correlation can be seen during the interval from 02:50 to 03:00 (UT) [*after Kojima et al.*, 1997a]. 149
6.9 Electrostatic potentials versus position at time when the amplitude of excited most unstable mode reaches its maximum value [*after Ashour-Abdalla et al.*, 1989]. 150
6.10 Time variation of the NEN intensities observed in five different frequency channels of the MCA. 151
6.11 Time series of the Electron velocity distributions observed by the CPI. The color coding denotes the phase space density of electrons on $v_{\parallel} - v_{\perp}$ plane. 152
6.12 Same as Fig. 6.10 but for the different time interval. 153
6.13 Same as Fig. 6.13 but for the different time interval. 154
6.14 Relation of NEN frequencies and local electron plasma frequencies. It is evident that the NEN frequencies focus on the frequency range below $0.1 f_{pe}$. 155
6.15 Time evolution of the electron velocity space hole instability in the same display format of Fig. 4.15 and Fig. 4.17 [*after Omura et al.*, 1996]. 156

7.1 Three representative electric field waveforms of the beat-type modulation observed by the Voyager 1 spaceprobe in the upstream region of the Jovian bowshock [*after Gurnett et al.*, 1981]. 160
7.2 Electric field waveforms of the isolated wave packet type [*after Gurnett et al.*, 1981]. 160
7.3 Frequency time spectrogram of the observed type III solar radio bursts with the Langmuir waves (a), high resolution waveform data of the Langmuir waves observed with the type III solar radio bursts (b), and Fourier spectra (c) corresponding to the waveforms of the third snapshot of (b) [*after Gurnett et al.*, 1993]. 161
7.4 Geotail observations of the type III solar radio bursts and associated Langmuir waves [*Matsumoto et al.*, 1998]. 162
7.5 Electron plasma waves observed in the lobe close to the plasma sheet. (a) Frequency-time spectrogram generated from the SFA, (b) time variation of the magnetic field magnitude and its azimuthal direction, and (c) modulated waveforms of the electron plasma waves shown in panel (a). 164

7.6 Example of waveforms ((a) and (b)) and polarization ((c)) of the modulated electron plasma waves [*after Kojima et al.*, 1997b]. · · · · · · · · · · · · · · · 165

7.7 Another example of the waveforms and polarizations of the modulated electron plasma waves [*after Kojima et al.*, 1997b]. · · · · · · · · · · · · · · · 166

7.8 Classification of the modulated electron plasma waves. Left and right panels illustrate the waveform and corresponding Fourier spectra in each type of the modulated electron plasma waves, respectively [*after Kojima et al.*, 1997b]. 167

7.9 Relation between frequency gaps of each spectrum in the type(II)-2 to type(II)-5 and local electron cyclotron frequency. · · · · · · · · · · · · · · · · · · · 168

7.10 Relation of low frequency emissions as ion acoustic waves and the modulated Langmuir waves. (a) Frequency-time spectrogram generated from the WFC data for the modulated Langmuir waves and their waveforms, (b) Frequency-time spectrogram focused on the low frequency portion of the above spectrogram. · 170

7.11 Quick change of amplitude modulations in the Langmuir waves. · · · · · · · 171

7.12 Comparison of the modulated Langmuir waves and electron velocity distributions. (a) waveforms of modulated Langmuir waves, (b) frequency-time spectrogram generated from the MCA, and (c) electron velocity distributions detected by the LEP. · 173

7.13 Same with Fig. 7.12 but for the ECH waves. · · · · · · · · · · · · · · · · · 174

7.14 Quick change of the polarizations. The polarization changes from the perpendicular direction to the parallel one relative to the ambient magnetic field in a short time scale less than 1 sec [*after Kojima et al.*, 1997b]. · · · · · · · 175

8.1 Sample of magnetosheath spectrum observed by IMP 6 satellite. The three components of spectra are schematically display in the right-bottom panel [*after Rodriguez*, 1979]. · 178

8.2 ISEE-3 measurements on 00:00 to 12:00 (UT) on September 12, 1983. The upper four panels present the one-minute average components and magnitude of the ambient magnetic field. The center panel is a color-coded display of the electric field frequency-time spectrogram. The bottom panel show the cone angle and the longitude and latitude of the ambient magnetic field in the GSM coordinates [*after Coroniti et al.*, 1994]. · · · · · · · · · · · · · · · 179

8.3 A scatter plot of the plasma wave electric field amplitude versus cone angle [*after Coroniti et al.*, 1994]. · 180

8.4 The frequency-time spectrograms for (a) SFA and (b) MCA and (c) waveform of the magnetosheath ESW observed on June 23, 1993. Panel a (bottom) shows the magnetic component spectra observed with the search coil magnetometer. The low-frequency electromagnetic waves below 100 Hz are called the MNB, which is the typical wave signature of the magnetosheath [*after Kojima et al.*, 1997a]. · 181

8.5 Same as Fig. 8.4, but for magnetosheath EQMW [*after Kojima et al.*, 1997a]. 182

8.6 Time series of the waveforms and corresponding spectra observed in the magnetosheath. We can see the rapid switching between the MS EQMW and MS ESW in panel (a) and panel (b). As shown by arrows, the six clear pulses of the MS ESW appear in panels (a) and (b), and in other intervals, the MS EQMW are dominant [*after Kojima et al.*, 1997a]. · · · · · · · · · 184
8.7 Spin dependence of the MS EQMW. In order to avoid the effect of the MNB superposing on the MS EQMW, we eliminate the waves below 700 Hz, making use of the FFT. We can see the same tendencies on the relation of the wave amplitudes and the change of signs of $E_U \times E_V$ with those of the PSBL ESW and lobe EQMW [*after Kojima et al.*, 1997a]. · · · · · · · · · 186
8.8 Waveforms and corresponding polarization of the MS ESW, with waveforms of the MS ESW detected by two sets of an orthogonal electric dipole antenna (top) E_U and (middle) E_V. (bottom) Polarization of the MS ESW shown by arrows above, with each dot representing sampled waveform level in the spacecraft coordinates. The solid line is the ambient magnetic field line on this plane [*after Kojima et al.*, 1997a]. · 187
8.9 The relation of NS NEN intensities and orientations of the ambient magnetic field. (a) frequency-time spectrogram observed on February 7, 1994 in the distant magetosheath. (b) elevation angle of the ambient magnetic field. (c) power of the MS NEN observed in the frequency range of the SFA-E2. · · 190
8.10 Cone angle dependence of the EQMW intensities observed by the Geotail. 191
8.11 Schematical drawing on the relation of velocity distributions and cone angles. 191

9.1 Plasma density profiles at four different distance ranges from the earth. The horizontal axis in each panel means radial distance of observation points from the modified $X_{GSM'}$ axis. · 194
9.2 Schematical drawing on the tail flapping effect. · · · · · · · · · · · · 195
9.3 Spatial distributions of the MNB on the tail cross-section at four different distance ranges from the earth. · 197
9.4 Distance dependence of the MNB intensities (upper) and data counts of the MNB observations (lower). · 198
9.5 Observation points of the electron plasma waves along the Geotail orbits. 199
9.6 Distribution of the electron plasma wave observation points on $Y_{GSM'} - Z_{GSM'}$ plane at four different distances from Earth. · · · · · · · · · · · · · · · · 200
9.7 Observation probabilities of the electron plasma waves. · · · · · · · · · · · 201
9.8 B_z dependence of the current sheet tilt angle during positive B_y of the IMF in the view from the tail toward the earth. For a negative B_y, a mirror image about the z axis applies. [*after Maezawa et al.*, 1997]. · · · · · · · · · · · 202
9.9 IMF dependence of the plasma sheet structure. · · · · · · · · · · · · · · 203
9.10 Multiple crossings of the magnetopause and neutral sheets. · · · · · · · · 205
9.11 An example of a solar-flare-related high-speed interplanetary stream and its geomagnetic effects [*after Tsurutani and Gonzalez*, 1993]. · · · · · · · · · 206
9.12 Multiple magnetopause crossings just after the encounter with the interplanetary shocks. · 208

10.1 Energy flow chart from the solar wind through plasma waves to background plasmas 216
10.2 Spatial distribution of plasma wave excitations as consumption of solar wind energies. 218
10.3 Schematical drawing for the formation of electron beams due to the velocity filter effect 220
10.4 A series of frequency-time spectrograms observed by Voyager spaceprobes in each planet's magnetosphere [*after Kurth and Gurnett*, 1991]. 223
10.5 Comparison of the BEN spectra observed in the Earth and Venus magnetospheres [*after Intrigator and Scarf*, 1984]. 224
10.6 Whistler observed in Neptune [*after Gurnett et al.*, 1992]. 225

A.1 Coordinate systems which we make use of in the present thesis. (a) Spacecraft coordinates, (b) GSE coordinates, and (c) GSM coordinates 229
A.2 Modification of the neutral sheet. We assume that the hinging distance is 10 R_E. 230

List of Tables

1.1 ISTP and related spacecraft 6

2.1 Power and weight budgets 22
2.2 Specification of SFA 35
2.3 Frequency table of SFA 37
2.4 Parameter descriptions in the front-end circuit of the preamplifiers 47
2.5 Parameter table of the WANT/PANT front-end circuits 48

3.1 Typical parameter related to plasma waves 83

4.1 Characteristics of the solitary waves observed in the various regions. . . . 115
4.2 Characteristic time scales of solitary waves observed by different spacecraft. 117

8.1 Summary of wave natures 188

10.1 List of planetary missions with plasma wave observations 221
10.2 Representative waves observed by the previous planetary missions 225

Chapter 1

General introduction

1.1 Geomagnetic tail

The intrinsic magnetic field of the Earth is continuously subjected by the plasma flow called "solar wind" [*Parker*, 1958]. The direct interaction between the intrinsic Earth magnetic field and the solar wind plasmas result in the distortion of the intrinsic magnetic field structure. While the distortion in the dayside region appears to be the compression of the dipole magnetic field lines, in the nightside region, a tail-like magnetic field configuration is formed in which the intrinsic magnetic field lines are configured to be parallel or anti-parallel direction along the solar wind direction (see Fig. 1.1). The shape is very similar to a comet with a coma and tail. However, the difference between a comet and Earth is whether they have their intrinsic magnetic field or not. While the terrestrial magnetosphere and tail are formed due to the direct interaction between the Earth intrinsic magnetic field and solar wind plasma, a comet coma and tail are due to the interaction between its ionized atmosphere and solar wind plasma. In the sense of this, Earth belongs to a group of Jupiter, Saturn, Uranus, and Neptune as magnetized planets, while a comet belongs to a group of the Mars and Venus as unmagnetized planets.

The magnetopause is the boundary where the solar wind dynamic pressure is equivalent to the static magnetic pressure of the Earth. The cavity enclosed by the magnetopause is called "magnetosphere" and the nightside tail-like region is especially called "geomagnetic tail" or "magnetotail." Such a static structure of the magnetosphere is theoretically expected by *Chapman and Ferraro* [1931] and the geomagnetic tail was discovered by *Ness* [1965] using the IMP 1 satellite.

Since the high speed solar wind (typically $\sim$ 500 km/s at 1 AU from the Sun) exceeds the local sound or Alfvén speed, a shock structure called "bow shock" is formed ahead of the magnetosphere. A part of the solar wind plasmas is reflected or takes a detour along the bow shock, other solar wind plasmas are decelerated and thermalized in the bow shock and flow into the downstream region. The region behind the bow shock is called "magnetosheath." The magnetosheath is the region between the bow shock and the magnetopause (see Fig. 1.1). The magnetosheath is filled with turbulent plasmas decelerated and thermalized in the bow shock.

Figures 1.2 and 1.3 show a three-dimensional drawing and a cross-section of the magnetotail, respectively. As shown in these figures, the inside magnetotail consists of very

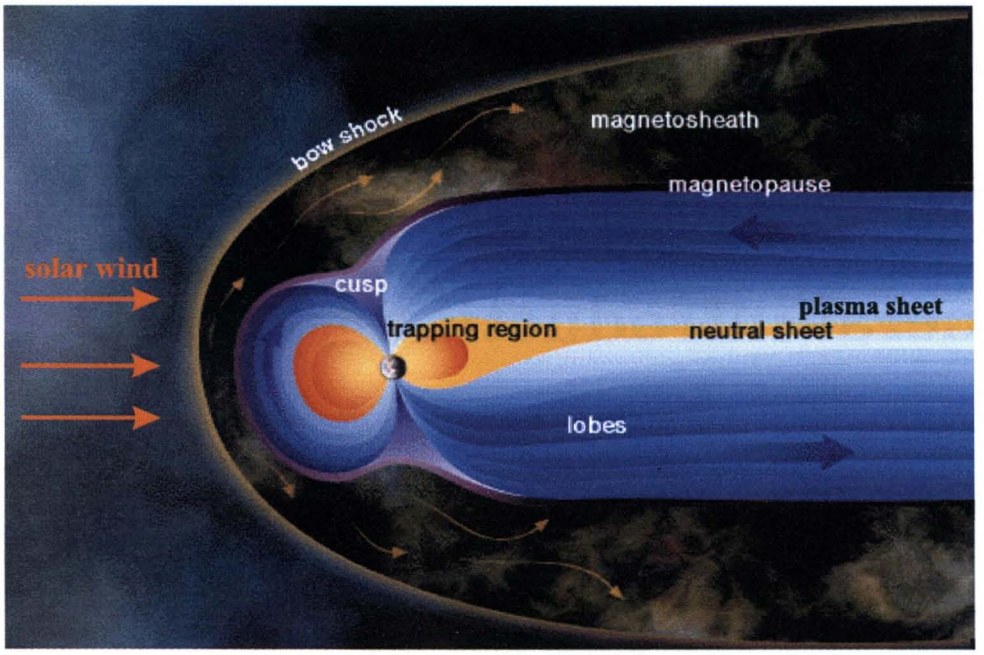

Figure 1.1: Illustration on the magnetic field configuration of the magnetosphere [*Copyright NASA/ISTP*].

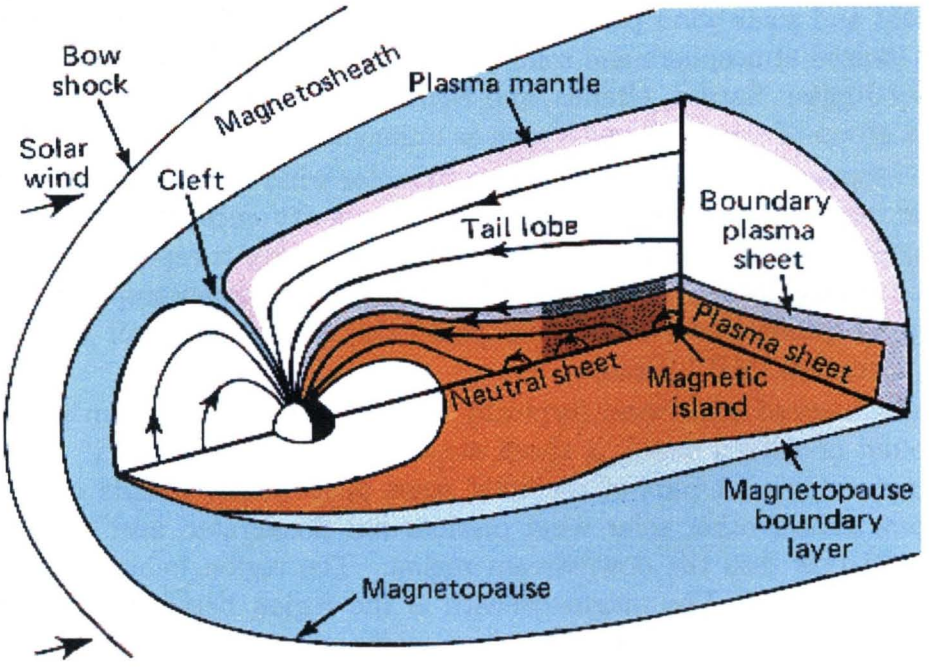

Figure 1.2: Three-dimensional drawing of the geomagnetic tail region [*after Lui*, 1987].

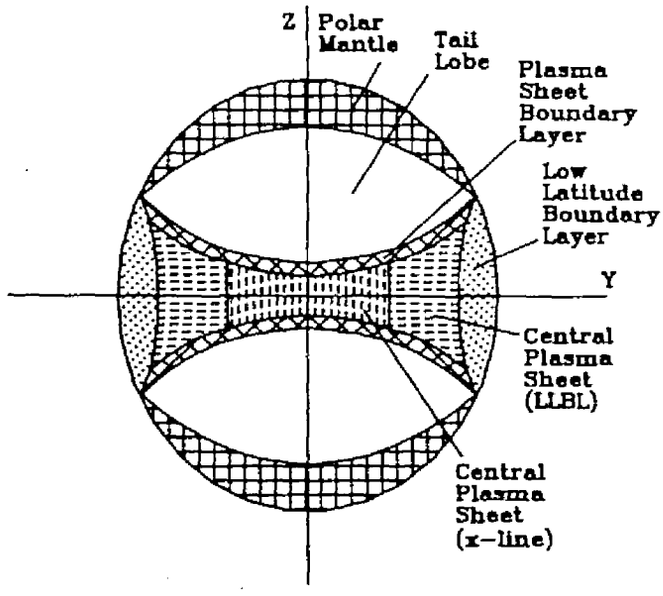

Figure 1.3: A cross-section of the Earth's magnetotail at about x = -20 R_E. Distinct regions including polar mantle (plasma mantle), lobe, plasma sheet boundary layers, central plasma sheet and low-latitude boundary layers are shown by shading patterns [*after Mcpherron*, 1991].

non-uniform plasmas. They are divided by several characteristic regions and boundary layers.

The magnetopause does not completely shield the invasion of the magnetosheath plasmas originated from the solar wind. The plasma invasion from the magnetosheath forms a boundary layer called "magnetopause boundary layer." The magnetopause boundary layer is divided into two different layers. They are: plasma mantle (polar mantle) and low-latitude boundary layer (LLBL). The magnetic field lines in the plasma mantle are connected to the cusp region (see Fig. 1.2). The cusp is the window to the magnetosheath in the high latitude region. The magnetosheath plasmas penetrate into the cusp region and stream anti-sunward in the plasma mantle region. The magnetic field lines are finally linked with the Interplanetary Magnetic Field (IMF) (open field lines) in the downstream region. The LLBL is also filled with invading magnetosheath plasmas, however, magnetic field lines in this region are closed and they eventually return to Earth in the other half of magnetotail (closed field lines). In both regions, we see decelerated cold magnetosheath plasmas steaming in the tailward direction.

The lobe is the lowest density region in the magnetotail. While the interface in the high latitude region is the plasma mantle, in the low latitude region, the lobe is divided into a north lobe and a south lobe by the plasma sheet which was discovered by *Bame et al.* [1967] (see Fig. 1.3). The plasma sheet consists of the plasma sheet boundary layer (PSBL) and the central plasma sheet (CPS). The plasma sheet contains hot plasmas with typical electron and ion temperatures of 4.4 keV (protons) and 1.0 keV at 20 R_E [*Speiser*, 1991].

The PSBL region is characterized by high speed and hot ion streams as well as hot

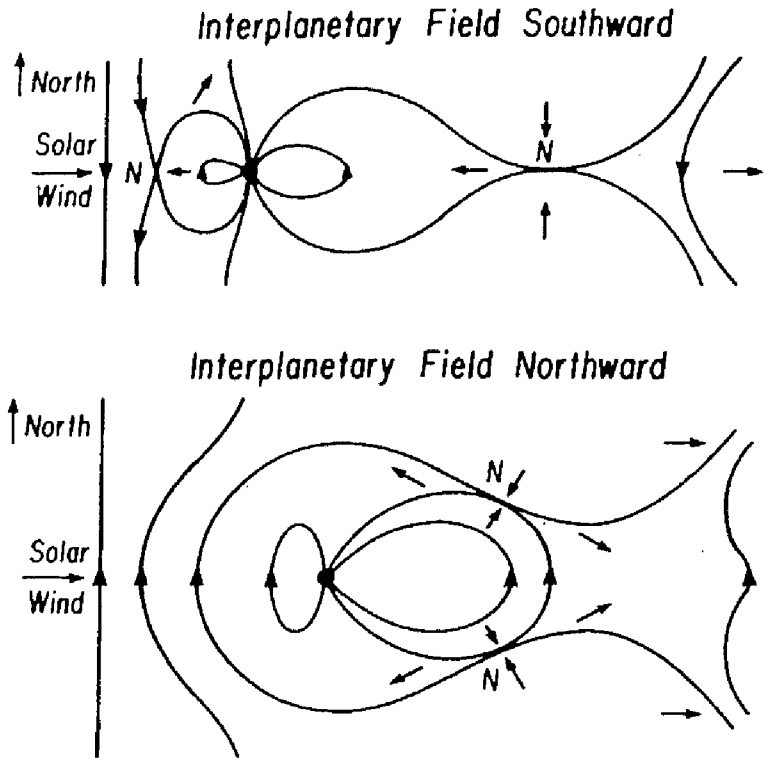

Figure 1.4: Magnetic reconnection between the IMF and the Earth's magnetic field [*after Russell*, 1972]

electrons. Magnetic field-aligned currents, flowing toward or away from the Earth, are often observed. Plasma wave activities in the PSBL are highest in the magnetotail. These activities gradually diminish as one approaches the central plasma sheet. As shown in Fig. 1.3, the plasma sheet is reported to be thinnest in the midnight region.

The above introduced magnetotail structure is based on "stationary model." By previous spacecraft observations, this stationary model agrees with the structure of the magnetotail on the average. However, since the magnetosphere is formed due to the direct interaction between the solar wind and the Earth magnetic field, it should be strongly affected by conditions of the solar wind. *Dungey* [1961] proposed the quasi-stationary magnetosphere model. His model depends on the orientation of the IMF. As shown in the upper panel of Fig. 1.4, when the IMF is southward (anti-parallel to the Earth's dipole field) at the front of the magnetopause, the neutral lines (x type neutral line) can form in the superposed magnetic fields. At the x type neutral line, so-called magnetic reconnection takes place. This reconnection means that the closed magnetic field line of the Earth's dipole field is connected to the IMF as open field line. The recent Geotail observations succeeded in detecting the evidence of this "dayside reconnection" [*Nakamura et al.*, 1997]. The reconnected open field lines are transported by the solar wind over the poles and in the magnetotail region, where they reconnect at a second x type neutral line. This second neutral line is very important, because without this neutral line, the total number of open field lines in the magnetotail continuously increase, while closed field lines in the dayside

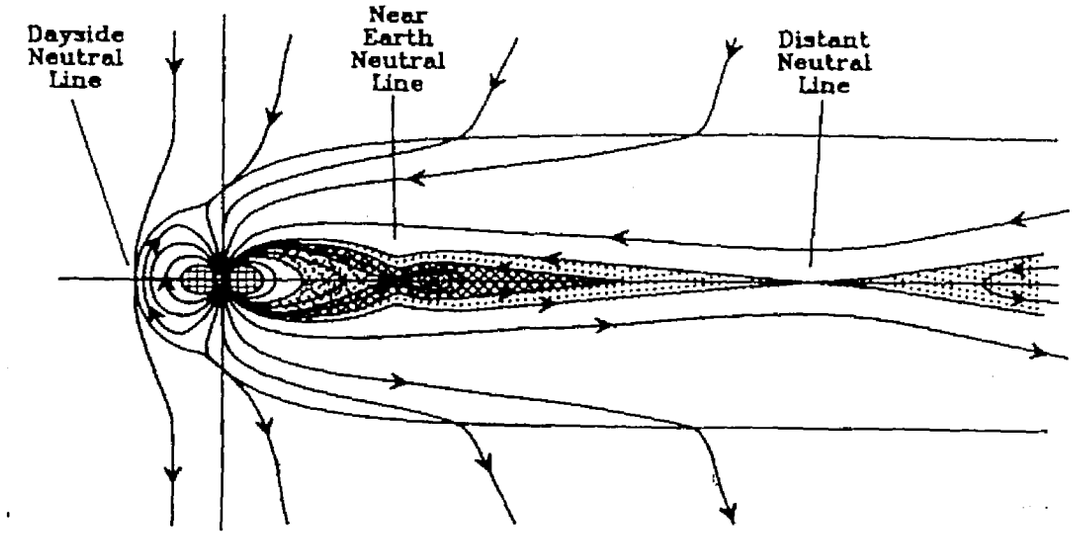

Figure 1.5: An approximate scale drawing showing the formation of three types of neutral lines [*after Mcpherron*, 1991].

magnetosphere decrease. This means that when the IMF is southward, magnetic field energies are injected to the magnetotail region by the solar wind and injected energies are released by the second reconnection in the magnetotail region. We call the second neutral line "Near Earth Neutral Line (NENL)." The Geotail observation results show that the reconnection in the near earth region starts in the premidnight sector between -20 R_E and -30 R_E [*Nishida et al.*, 1997; *Nagai et al.*, 1997; *Nagai et al.*, 1998].

The third neutral line is the distant neutral line. ISEE-3 observations suggested the existence of a permanent neutral line from magnetic field and plasma measurements [*e.g.*, *Cowley et al.*, 1984; *Baker et al.*, 1984; *Slavin and Kamide*, 1986]. At about 100 R_E the tail lobe field becomes constant, B_z in the plasma sheet becomes nearly zero, and the plasma sheet flow becomes continuously tailward. These signatures strongly suggest that the reconnection point is located in the earthward direction relative to the spacecraft. The distant neutral line has been also confirmed to exist in the distance from -100 R_E to -140 R_E down the tail by Geotail data [*Nishida et al.*, 1996; *Nagai et al.*, 1997]. Three types of neutral lines are schematically shown in Fig. 1.5. Such x type neutral lines are important for plasma wave physics in the following two points:

1. In order to cause x type reconnection, we need an anomalous resistivity in order to decrease currents flowing from the dawn to dusk at the reconnection point. The most possible candidate for this anomalous resistivity is a kind of wave-particle interaction. This means that plasma waves are excited at the neutral line. The plasma waves are an important proof of x type reconnection.

2. At x type reconnection line, the magnetic field energies convected with the inflowing plasmas is converted to kinetic and thermal energies of particles, which is forced to flow out along the interface. Such energetic particles are important free energy source of plasma waves around the plasma sheet.

Table 1.1: ISTP and related spacecraft

Spacecraft	Agency	Mission	Region
Geotail	ISAS(JAPAN), NASA(US)	July 26, 1992 –	Magnetotail
Wind	NASA(US)/ ESA(Europe)	Nov. 1, 1994 –	Solar wind
SOHO	ESA (Europe)	Dec. 2, 1995 –	Sun
Polar	NASA(US)	Feb. 24, 1996–	Polar region
IMP-8	NASA(US)	Oct. 26, 1973–	Magnetotail/Solar wind
Ulysses	ESA(Europe)/NASA(US)	Oct. 6, 1990 –	High latitude solar wind
Interball (Tail)	IKI (Russia)	Aug. 3, 1995 –	Magnetotail
Interball (Auroral)	IKI (Russia)	Aug. 29, 1996 –	Polar region
Equator-S	ESA(Europe)	Dec. 2, 1997 –	Near Earth Equator

Hones [1977] demonstrated that the continuous reconnection at the NENL results in the formation of magnetic field islands consisting of closed magnetic field lines, so-called "Plasmoid." Figure 1.6 schematically shows a sequence of the generation of a plasmoid. In the figure, closed field lines (No. 1 to 4) and open field lines (No. 5 and 6) are displayed. We see that the continuous reconnection at the NENL results in the formation of the magnetic islands with plasma sheet plasmas between the NENL and the distant neutral line. When a spacecraft, which is displayed as a black dot in Fig. 1.6, observes such a plasmoid, we see a bipolar signature in observed magnetic field B_z component.

1.2 International solar terrestrial physics (ISTP)

As we introduced in the previous section, the structure of the magnetotail is closely linked to the solar wind. In order to study the link between the magnetosphere and solar wind by spacecraft, a single point observation is not enough because the magnetosphere and its surround system broaden over the huge space.

In order to understand the environments including the magnetosphere and solar wind, the International Solar-Terrestrial Physics (ISTP) program has been planned under the international collaboration. The ISTP is a comprehensive effort to observe and understand the Earth and its effects on our environment. The ISTP includes space- and ground-based observations and computer experiments. Especially, multi-spacecraft observations of the Earth's space are unique in the progress of the space science. The spacecraft of ISTP, ISTP fleet, are placed in orbits that allow physicists to observe the key regions of the Earth's space. Those regions include the Sun's surface and atmosphere, the solar wind, Earth's magnetosphere from the bow shock to the auroral regions and to the magnetotail. The ISTP fleet and related spacecraft are schematically shown with their orbits in Fig. 1.7.

ISTP was planed in the 1980s, and it has started by the successful launch of the first spacecraft, Geotail, in 1992. The ISTP fleet and a part of related spacecraft shown in Fig. 1.7 are listed in Table 1.1. The detailed information of the spacecraft which collaborate with the ISTP fleet is summarized by *King* [1997].

Among the spacecraft listed in Table 1.1, the Geotail is the important spacecraft for investigating the magnetotail region. It has a role to measure magnetic/electric fields, plasmas, and plasma waves and to provide information: what controls the magnetotail,

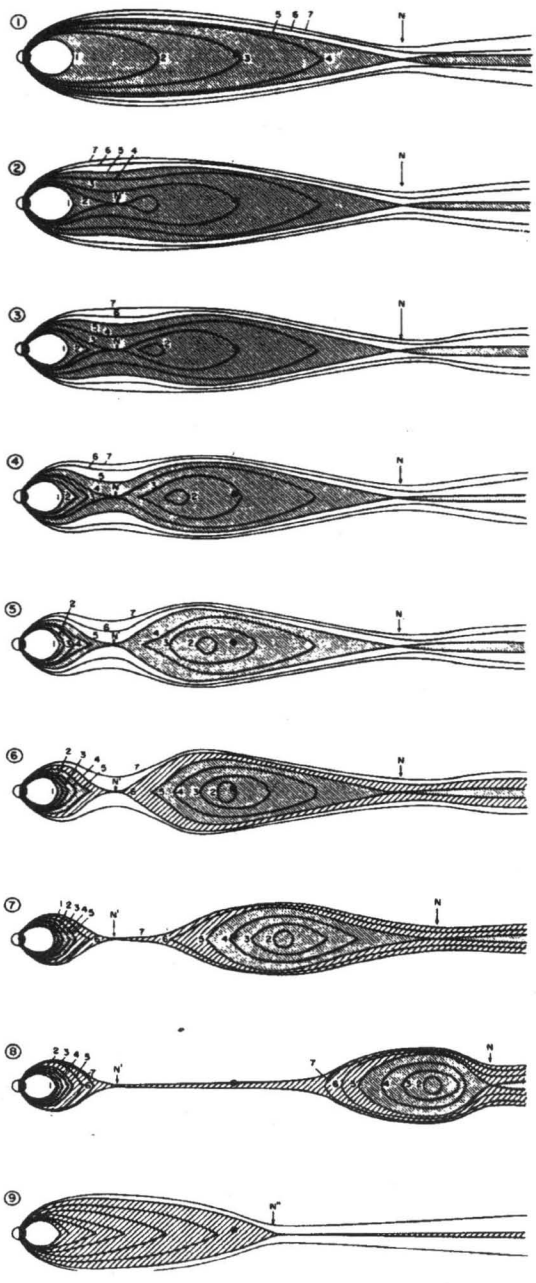

Figure 1.6: Sequence of changes of magnetic and plasma configuration of the plasma sheet for generating a plasmoid [*after Hones*, 1977].

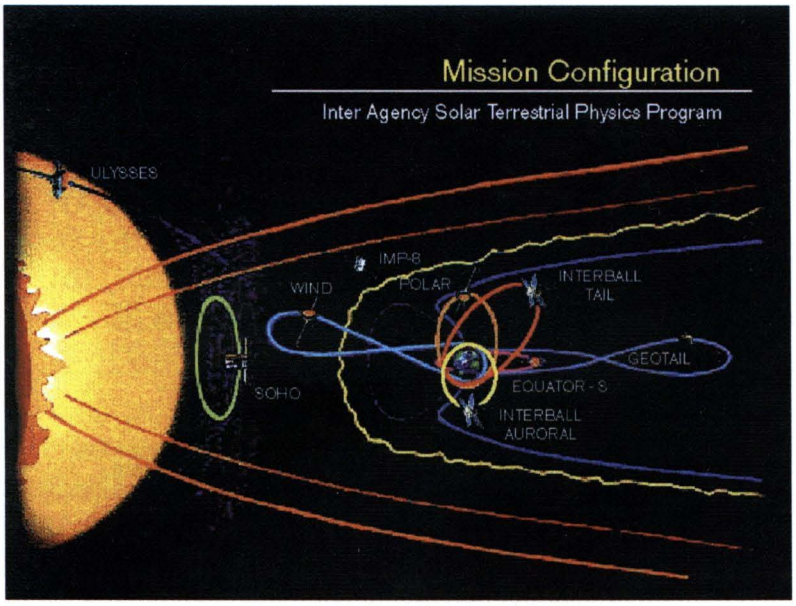

Figure 1.7: ISTP fleet and related spacecraft [*Copyright NASA/ISTP*].

how coupling occurs between the solar wind input and the Earth's fields, and how input energies are released by macroscopic and microscopic processes.

Before Geotail, the distant tail was surveyed only by ISEE-3 spacecraft in 1982 and 1983, but the ISEE-3 was not designed to investigate the distant tail, because its distant tail orbits are on its way to the comet Giacobini-Zinner. Therefore, Geotail is the first spacecraft to be designed for the observations of the distant/near magnetotail regions. Detailed orbits and spacecraft design of Geotail will be introduced in Section 2.2.

1.3 Plasma wave observations in space

1.3.1 Objectives and advantages of plasma wave observations

Study on the naturally occurring electromagnetic waves has been started from ground observations of the "whistlers" since the pioneering work of *Storey* [1953]. The whistlers are known to be a lightning discharge.

Historically, the first plasma wave observations using satellites were conducted by Vanguard 3 [*Cain et al.*, 1961], Lofti 1 [*Leiphart*, 1962], and Alouette 1 [*Barrington and Belrose*, 1963]. Figure 1.8 shows the first satellite observation of the whistlers by Vanguard 3 [*Cain et al.*, 1961]. These first satellites focused on the observations of the whistlers. Therefore, the coils or loop antennas were used for their observations. Since the first successful launch of Sputnik 1 was in 1958, we find that plasma wave observations in space quickly started after the success of the Sputnik. This suggests that the importance of plasma waves was generally understood from the dawn of space physics.

Gurnett and O'Brien [1964] pointed out several advantages of satellite plasma wave observations compared with ground-based observations mainly by focusing on the attenu-

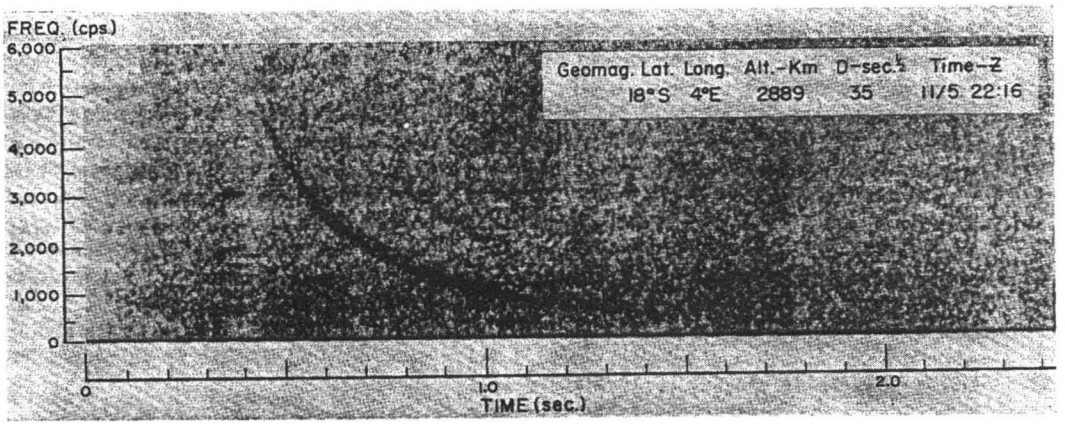

Figure 1.8: Whistler wave observed by the Vanguard 3 satellite [*after Cain et al.*, 1961].

ation of whistler waves in the ionosphere. In addition to their points, we stress following objectives and advantages of the plasma wave observations by satellites.

1. *in-situ* observations reveal the local wave-particle interactions at observation points. Particularly, since electrostatic waves are not likely to propagate, *in-situ* observations are very important.

2. Plasma waves are very sensitive to changes of plasma environments. Since a specific wave-particle interaction corresponds to excitation of a specific plasma wave mode, we can identify a physical process taking place by using plasma wave signatures.

3. In general, plasma wave receivers have a capability to perform observations with very high time resolution relative to other instruments such as plasma measurement instruments. Only plasma wave receivers with high time resolutions can detect transition phenomena with very short time durations.

In the present thesis, we focus on quick plasma wave phenomena in the magnetotail region mainly using the Geotail high time resolution waveform data.

1.3.2 Geotail plasma wave observations

In this section, we introduce several kinds of waves observed by Geotail, which are not discussed in the latter chapters but are indirectly related to the present thesis. A part of following introduced plasma waves have been already reported by previous spacecraft. However, the Geotail plasma wave observations provided further knowledge about them due to the success of sophisticated onboard receivers.

Nonthermal continuum radiation

The nonthermal continuum radiation (CR) is a very useful wave for the region identification, because we can obtain a local electron plasma density from this radiation. The CR was initially reported by *Brown* [1973] and *Gurnett and Shaw* [1973]. *Gurnett* [1975]

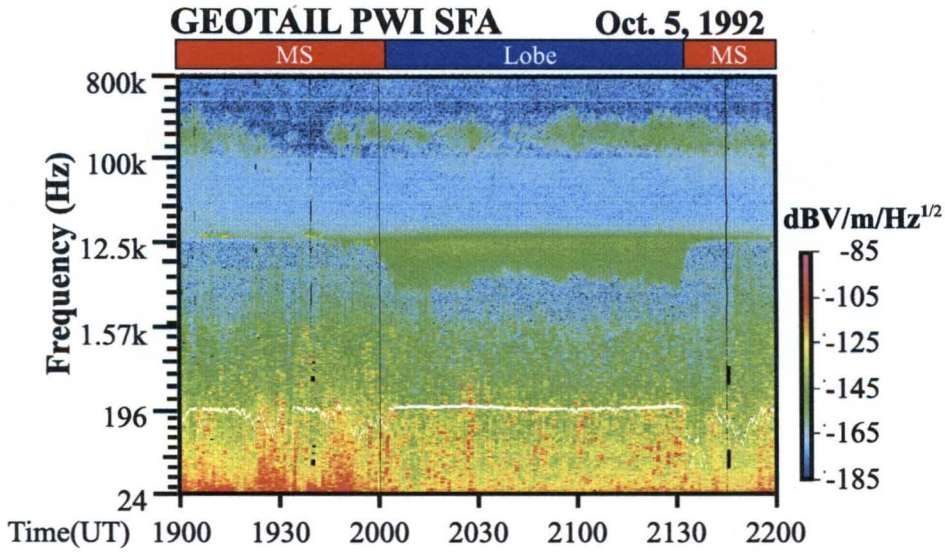

Figure 1.9: An example of the nonthermal continuum radiation observed by Geotail.

first introduced the term of "nonthermal continuum radiation," while *Jones* [1981a, b; 1982; 1990] used a different term of "terrestrial myriametric radiation." Recently, *Nagano et al.* [1994] classified the CR into three types. They are "magnetosheath trapped CR," "lobe trapped CR," and "escaping CR." The magnetosheath trapped CR is a classical CR. It is believed to be radiated by the linear wave conversion mechanism (upper hybrid waves to electromagnetic L-O waves) at the low latitude plasmapause, where the density gradient perpendicular to the ambient magnetic field is maximized [*Jones*, 1981a, b; 1982: 1990]. The excited CR waves with lower frequencies than the magnetosheath electron plasma frequencies are trapped in the magnetosphere, while the CR with frequencies beyond the magnetosheath electron plasma frequencies can escape without the reflection at the magnetopause. These two CRs are called as magnetosheath trapped CR and escaping CR, respectively. The lobe trapped CR is a very low frequency portion of the magnetosheath trapped CR. *Nagano et al.* [1994] found that the low frequency portion of the magnetosheath trapped CR frequently consists of harmonics of local electron cyclotron frequencies. They have peak intensities at the local upper hybrid frequencies. This means that this low frequency portion of the magnetosheath trapped CR is not radiated at the plasmapause. They concluded that this low frequency portion is excited in the plasma sheet boundary based on the observation points and observed intensities. They address this CR "lobe trapped CR."

Figure 1.9 shows an example frequency-time spectrogram of trapped CR observed by the Geotail spacecraft. The weak continuous emissions can be seen during the interval from 20:00 to 21:35 (UT). They have the clear lower and upper frequency cutoffs. The time variation of the CR lower cutoff frequencies shown in Fig. 1.9 mean that the local plasma densities decrease from 20:00 to 20:05 (UT), become stable with small fluctuations between 20:05 and 21:30 (UT) and increase from 21:30 to 21:35 (UT). On the other hand, the upper cutoff frequencies are very stable. This upper cutoff frequencies correspond to the limit frequency for the reflecting effect at the magnetopause. Therefore, we can expect

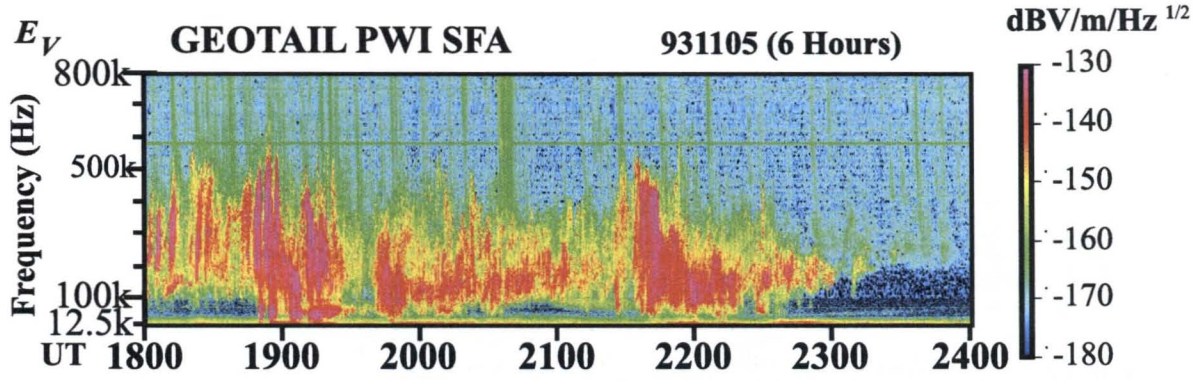

Figure 1.10: An example of the Auroral Kilometric Radiation observed by Geotail spacecraft.

that the upper cutoff frequency of the CR is equal to the magnetosheath electron plasma frequencies.

In Chapter 9, we will discuss the magnetotail structures using distributions of plasma densities obtained from lower cutoff frequencies of the CR.

Auroral Kilometric Radiation/Auroral Myriametric Radiation

The Auroral Kilometric Radiation (AKR) is the most common and the most extensively studied plasma waves. The AKR was initially referred to as "Terrestrial Kilometric Radiation (TKR)" by *Gurnett* [1974], because the wavelength of this radiation is usually in the kilometric range. The TKR was discovered by *Dunckel et al.* [1970] from the very low frequency radio receiver onboard Ogo 1 satellite. They reported bursts lasting tens of minutes with frequencies above 20 kHz. They referred these waves as "highpass noise," because of lower cut off frequencies about 20 kHz. *Gurnett* [1974] provided the first comprehensive study of the AKR using the IMP 6 and 8 satellites and discussed their relation of discrete auroral arcs.

The AKR has a frequency spectrum extending from several tens of kHz up to several hundreds of kHz. The average radiation power of the AKR is $10^7 - 10^8$ watts [*Gallagher and Gurnett*, 1979]. Figure 1.10 shows an example of the AKR spectra observed by Geotail. The intense emissions below 500 kHz are the AKR.

The AKR is believed to be generated through the cyclotron maser instability [*Wu and Lee*, 1979] in the plasma cavity [*Calvert*, 1981] on the field lines of discrete auroras in the nightside (22:00 to 00:00 MLT) auroral region [*Green et al.*, 1977]. Therefore, the AKR excitation is related to the geomagnetic activities. Its intensities and observation possibility have a good correlation with geomagnetic activity indices such as K_p, AE, and Dst [*e.g., Murata*, 1995; *Matsumoto et al.*, 1998]. *Murata* [1995a, b] and *Murata et al.* [1997] showed that the appearance of the AKR is closely related to the substorm onsets and proposed a new index for geomagnetic activities called "AKR Index," which is calculated from the AKR power. The advantage of the AKR index compared with other indices is that the AKR index easily and quickly can be produced using a single spacecraft.

The Auroral Myriametric Radiation (AMR) was the new emission observed by Geotail

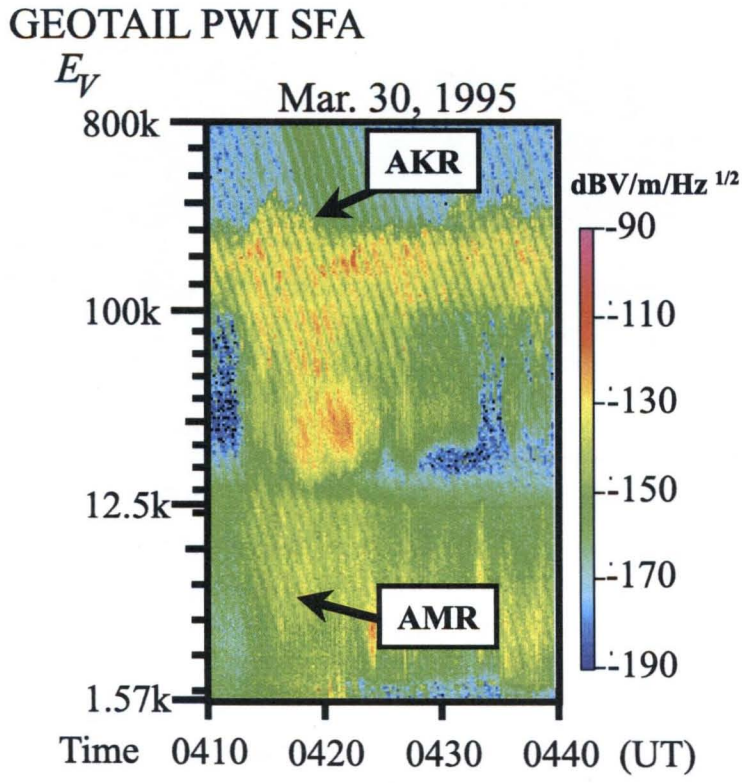

Figure 1.11: An example of the Auroral Myriametric Radiation observed by Geotail spacecraft [*after Hashimoto et al.*, 1998].

[*Hashimoto et al.*, 1994]. The emissions in the myriametric frequency range from 1 kHz to 100 kHz were originally reported by *Jones* [1982], which we introduced in the previous section of "Nonthermal continuum radiation." *Hashimoto et al.* [1994] discovered new emissions in this frequency range. Since the intensities of these emissions are very correlated with the AKR emissions, they termed these emissions "Auroral Myriametric Radiation (AMR)."

Figure 1.11 shows an example of the AMR observed by Geotail. The AMR emissions are observed in the frequency range between 1.57 kHz to 20 kHz, while the AKR emissions can be seen up to 500 kHz above 20 kHz. The good correlation between two emissions is evident in this figure.

Hashimoto et al. [1998] conducted the ray tracing studies and compared the results with Geotail observations. They concluded that the most plausible generation source is the auroral cavity and that expected wave mode is the L–O mode. They claimed that energetic particles which generate AKR at the local cyclotron frequency in the auroral cavity can indirectly generate AMR at the local plasma frequency.

Electron Cyclotron Harmonics

Electron Cyclotron Harmonics (ECH) waves in the magnetosphere were initially observed

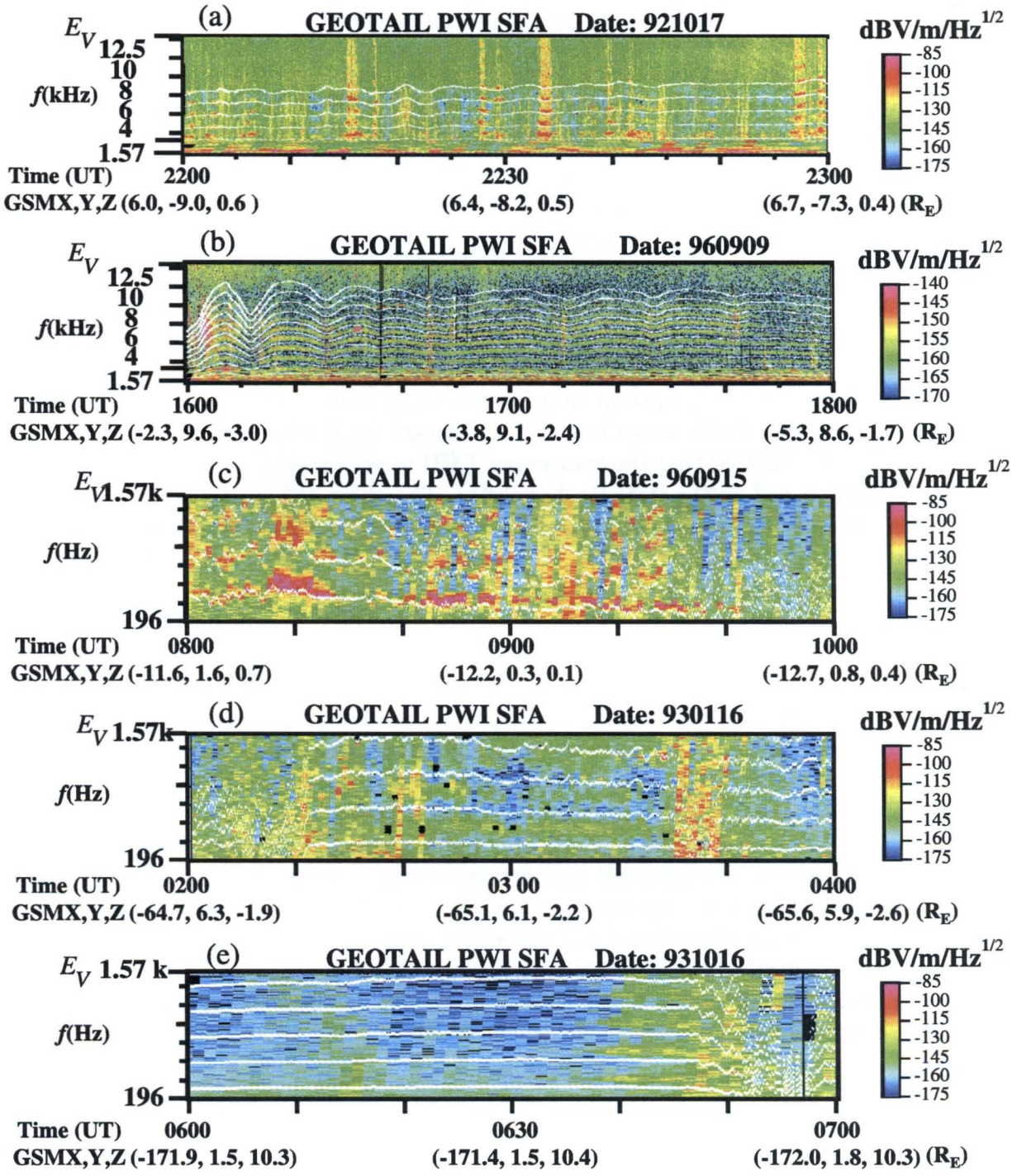

Figure 1.12: Frequency-time spectrograms of five representative ECH waves observed by Geotail in the dayside outer magnetosphere, and magnetotail regions [*after Matsumoto et al.*, 1998].

by the OGO-5 satellite in the near earth region of $4 < L < 10$ [*Kennel et al.*, 1970; *Fredricks and Scarf*, 1973]. The ECH emissions are observed at $f \sim (n + 1/2)f_{ce}$, where f_{ce} and n denote the electron cyclotron frequency and a positive integer value, respectively. The observed ECH waves were almost electrostatic with the frequency spectrum with a structure of multiple harmonics. Many theoretical attempts on the generation of the ECH waves have been made. They concluded that the most possible candidate for the generation mechanism is an instability caused by the temperature anisotropy of electrons [see a review by *Ashour-Abdalla et al.*, 1979].

ECH waves are observed by GEOTAIL not only in the tail lobe but also in the dayside outer magnetosphere and even in the deep tail regions. Figure 1.12 shows five examples of the ECH waves observed by GEOTAIL in the dayside magnetosphere and in the tail region. The superposed white lines display the electron cyclotron frequency and its harmonics. Figure 1.12(a) shows the ECH waves observed on the dayside of the outer magnetosphere. In the figure, two types of the ECH waves can be identified. They are: continuous and weak ECH waves and intermittent and intense ECH waves. The continuous ECH waves belong to the diffuse ECH waves in the classification by *Hubberd and Birmingham* [1978]. *Usui et al.* [1997] showed that the continuous ECH waves broadly appear along the dayside magnetopause, based on the statistical analyses. They have the multiple harmonic spectral structure with a weak amplitude of the order of $\sim 0.3\mu V/m/\sqrt{Hz}$. The latter type of ECH emission is seen at 22:16, 22:27, 22:34, 22:57, and 22:59 (UT). This type of ECH emission is observed intermittently and sporadically in time. *Usui et al.* [1997] showed that such intense and bursty ECH waves are mainly observed at the dawnside region near the magnetopause. Further, *Matsumoto and Usui* [1997] studied these bursty ECH waves using the WFC data as well as the spectrum data by the SFA and MCA. They called these ECH waves 'Totem Pole emissions (TP emissions)' after their spectral forms in the dynamic spectra. Though the TP emissions seem to be simply the intensified versions of the diffuse type ECH waves, *Matsumoto and Usui* [1997] using more detailed spectral structure based on the high time WFC data, revealed the existence of two spectral peaks in the first electron cyclotron harmonic band from f_{ce} to $2f_{ce}$. Their maximum amplitude is about $-100dBV/m/\sqrt{Hz}$. The similar fine structure between f_{ce} harmonics was observed by the SCATHA satellite [*Koons and Fennell*, 1984]. *Matsumoto and Usui* [1997] stressed that two spectral peaks are not special but are often found associated with the intense ECH waves near the dayside magnetopause. Since we cannot expect such two spectral peaks in the first harmonic band from the linear dispersion for the Maxwellian plasma, we need to consider other effects including nonlinear phenomena.

Figure 1.12 (b) to (e) illustrate the frequency-time spectrograms of ECH emissions observed by GEOTAIL in the tail region. ECH waves in panels (b) and (c) are observed in the near earth region ($|X| < 30R_E$), those in panels (d) in the middle tail region ($|X| \sim 60R_E$), and those in panel (e) in the distant tail region ($|X| > 100R_E$). The ECH waves in the near and distant tail regions have already been reported by *Roeder and Koons* [1989] and *Gurnett et al.* [1976], respectively.

The ECH waves in the near earth region had been discussed in relation to the diffuse auroral electron precipitation [e.g., *Kennel and Ashour-Abdalla*, 1982]. However, *Belmont et al.* [1983] reported their intensities observed by the geostationary spacecraft GEOS 2 are too small for the precipitation. Further, using the data from AMPTE IRM and SCATHA

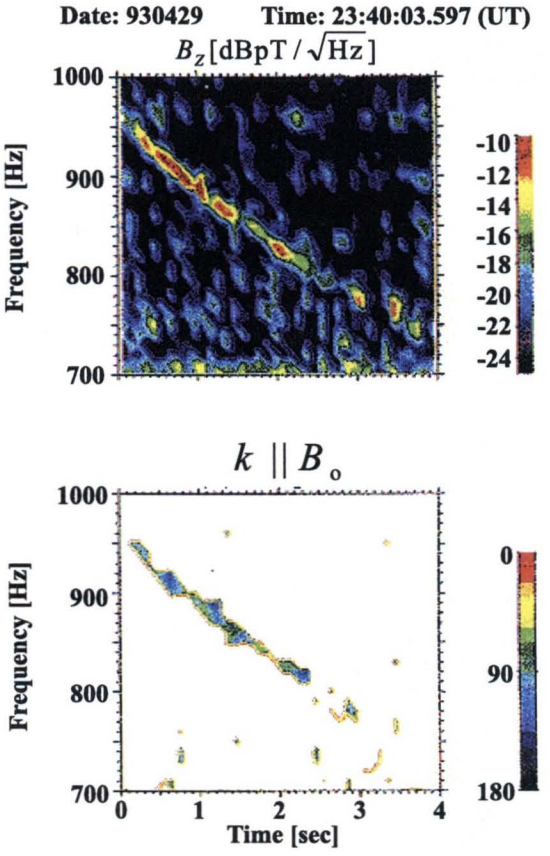

Figure 1.13: Frequency-time spectrogram of B_z component (upper) and corresponding wavenormal angles [*after Nagano et al.*, 1998].

satellites, *Roeder and Koons* [1989] also showed that the occurrence and intensity of ECH waves observed below $L < 20$ is too small to account for the continuous precipitation of magnetospheric electrons in the diffuse aurora. The GEOTAIL observations shown in Figure 1.12 (b) and (c) are consistent with the above results. As far as we examined our data, the observed ECH wave intensities are in most of cases less than 1 mV/m/$\sqrt{\text{Hz}}$. Their amplitudes are not large enough to cause the diffuse electron precipitation due to pitch angle diffusion [*Lyons*, 1974].

The ECH emissions observed in the middle tail region at radial distances ranging from about 23.1 to 46.3 R_E are briefly reported by *Gurnett et al.* [1976]. They showed that the ECH waves can be observed very close to the neutral sheet. They reported that the ECH waves have a correlation with high temperature electrons in the central plasma sheet but their occurrence rate is very low. However, GEOTAIL data displayed in Figure 1.12 (d) and (e) show that the ECH emissions are observed in the lobe region close to the plasma sheet but not observed near the neutral sheet. In Chapter 7, we will show waveform observations of the ECH waves which can be observed in the edge of the lobe region close to the plasma sheet.

Whistler mode waves

Whistler mode waves are the plasma waves which have been studied very extensively through the ground and satellite observations, because "whistlers" are known to be lightning discharges. We showed an example of the whistler spectra in Fig. 1.8. Note that the "whistler mode wave" is the name of one normal wave mode in plasmas, while "whistler waves" or "whistlers" mean "whistler mode waves generated by lightning discharges."

Since the perigee of the Geotail orbits is more than 10 R_E, it is difficult to observe the whistlers excited by lightning discharges. However, *Nagano et al.* [1998] reported a very important event on "whislters" observed by Geotail. Figure 1.13 shows the whistler mode wave spectra observed by the Geotail WFC just inside the dayside magnetopause. As we will introduce in Chapter 3, the chorus emissions, which are also "whistler mode waves," can be observed inside the dayside magnetopause, but the spectra shown in Fig. 1.13 are different from the chorus emissions. The observed spectra are highly dispersed and they are very similar to those of whistler waves as shown in Fig. 1.8. *Nagano et al.* [1998] show that polarizations are right-handed and their frequencies are below a half of local electron cyclotron frequencies. These natures indicate that the waves shown in Fig. 1.13 are whistler mode waves. *Nagano et al.* [1998] concluded that these whistler mode waves are radiated due to lightning discharges at high latitudes based on the results of Geotail observations and ray-tracing.

Another type of "whistler mode waves" can be observed in the various regions of the magnetotail. Most of these whistler mode waves have broadband spectra and we call them "Magnetic Noise Burst (MNB)." The terminology of the MNB was initially used for the low frequency electromagnetic waves observed in the plasma sheet by *Gurnett et al.* [1976]. We use this terminology for the low frequency broadband electromagnetic waves in the present thesis. The MNB is observed by Geotail in the Magnetosheath [*Kojima et al.*, 1997a; *Matsumoto et al.*, 1998], the bow shocks [*Zhang et al.*, 1998b], the central plasma sheet [*Matsumoto et al.*, 1998], the interplanetary shocks [*Zhang et al.*, 1998c], the plasmoid [*Murata et al.*, 1995a], and the Low Latitude Boundary Layer (LLBL) [*Matsumoto et al.*, 1998]. We confirmed that these waves have the right-handed polarizations on the plane perpendicular to the ambient magnetic field and that their frequencies are well below local electron cyclotron frequencies. Therefore, these observations are consistent with whistler mode waves. *Zhang et al.* [1998a] also introduced the monochromatic low frequency whistler mode waves so called "Lion roars" in the magnetosheath. The waveform observations of these whistler mode waves revealed the common nature that they include very short lived wavepackets with time durations of a few hundreds of milliseconds [*Zhang et al.*, 1998a; *Zhang et al.*, 1998b]. The short-lived wavepackets suggest that the generation and damping of these whistler mode waves take place very intermittently. The whistler mode waves destabilize due to anisotropic electron velocity distributions and/or energetic electron beams. We can infer that these conditions quickly change in the above regions, but unfortunately the time resolution of plasma measurements is not enough to study such quick wave-pariticle interactions.

1.4 Contribution of the present work

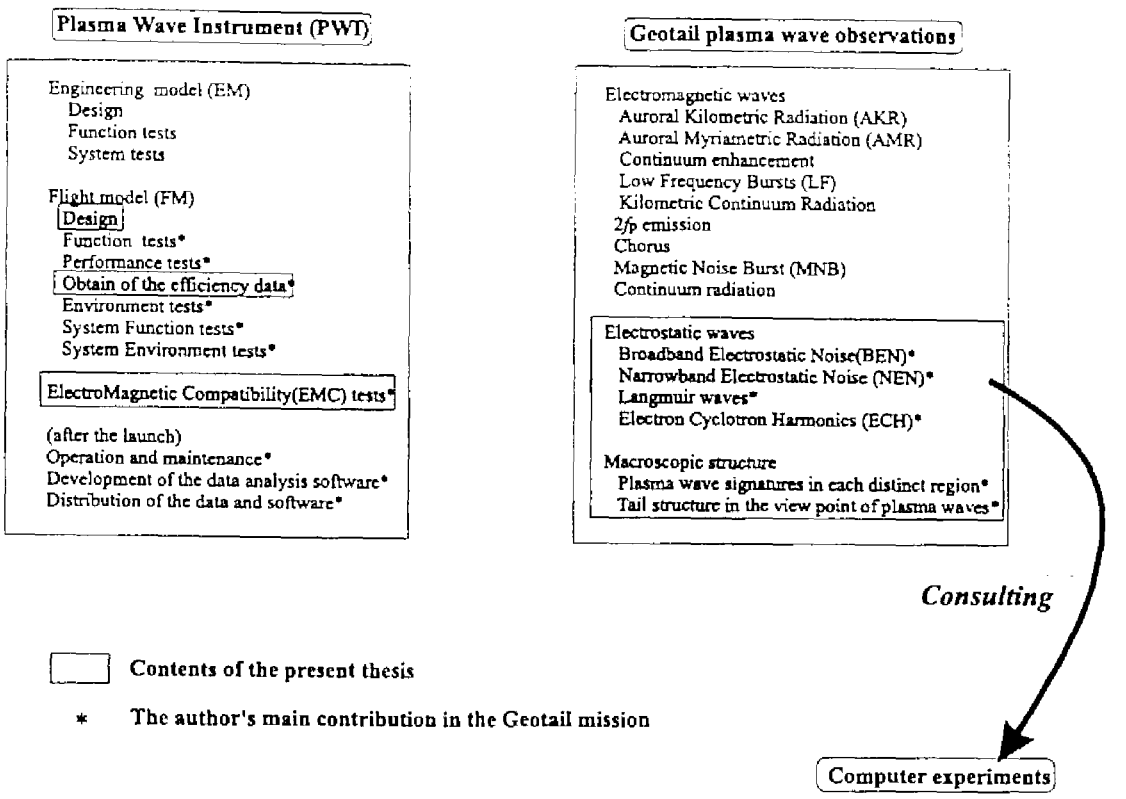

Figure 1.14: Contribution of the present work in the Geotail plasma wave mission.

The present paper describes the design and features of the Plasma Wave Instrument (PWI) onboard Geotail spacecraft, and discuss the results of plasma wave observations using the Geotail PWI in the magnetotail. In order to show the contribution of the present thesis and author, Figure 1.14 summarizes the items on the procedure for developing and maintaing the plasma wave receivers (left panel) and on representative plasma waves observed by Geotail and related research items (right panel). The items marked with "*" are the author's main contributions in the plasma wave observations in the Geotail missions. The hatched items are the main topics which we show and discuss in the present thesis.

The Geotail PWI has a newly designed Wave-Form Capture (WFC) receiver, which has a capability to collect waveforms in the duration of 8.7 sec. Geotail waveform observations with the WFC receiver provided a breakthrough in plasma wave observations by spacecraft. In most of the parts in the present thesis, we make use of the waveform observations by the Geotail WFC receiver. Before the analyses of observations results and discussions about them, we describe the design and features the Geotail PWI in Chapter 2. Since the PWI was designed to observe plasma waves in the distant magnetotail, it consists of receivers and sensors with quite high sensitivities and quite low noise levels. We will describe the features of each component of the PWI and after that we summarize the calibration method including the antenna impedance immersed in space plasmas. The discussion of the antenna impedance immersed in space plasmas is very important, because errors in the estimation of antenna impedance cause some distortions of the waveforms generated by the WFC in the calibration process. Further, we introduce the ElectroMagnetic Compatibility (EMC) in the Geotail spacecraft. Geotail is the first Japanese spacecraft, which the EMC tests

were systematically conducted. We introduce the EMC specifications we proposed in the Geotail missions and show representative results from the Geotail EMC tests. Finally, as the strategy for the EMC in spacecraft, we propose several new specifications based on the experience in the Geotail EMC tests.

Chapter 3 is dedicated to summarizing the plasma wave signatures in each characteristic region of the magnetosphere. Geotail orbits are designed to traverse different regions slowly in the magnetotail. Therefore, it is very convenient to survey plasma wave signatures in the magnetotail. Understanding of plasma wave signatures in each region is very helpful to identify the spacecraft locations. The plasma wave signatures introduced in Chapter 3 are used in the other chapters.

In Chapters 4 and 5, we demonstrate the waveform observations of the Broadband Electrostatic Noise (BEN) in the plasma sheet boundary. The generation mechanisms of the BEN have been studied for many years since its discovery. However, the broadband frequency of its spectra has always bothered us. Geotail waveform observations of the BEN provided an answer at least for the high frequency portion of the BEN. We show that the observed BEN spectra consist of a series of bipolar isolated waveforms, which contribute to the high frequency portion of the BEN. In Chapter 4, we analyze the waveforms of the BEN and show the detailed natures of isolated pulses which we address "Plasma Sheet Boundary Layer Electrostatic Solitary Waves (PSBL ESW)." Further, we consult computer experiments on the nonlinear evolution of electron beam instabilities using the full-particle code and show that we succeeded in reproducing the ESW waveforms by the nonlinear evolution of electron beam instabilities resulting in the formation of BGK potentials. Based on the results in Chapter 4, we perform the propagation analyses of the PSBL ESW. In general, it is very difficult to identify propagation directions of purely electrostatic waves, but in the ESW case, we can identify the propagation direction using the electric field antenna polarities and the phase of the ESW waveforms. The propagation analysis provides us with important information on the source location. We estimate the source location using the results of the propagation analyses.

Another common electrostatic wave in the magnetotail is analyzed in Chpater 6. The narrowband electrostatic noise (NEN) is discussed in the relation to the slow mode shocks around the plasma sheet. Our waveform observations reveal that the NEN waveforms are quasi-monochromatic and they are not noise. In Chapter 6, we analyze the NEN waveforms and show their detailed natures. Further, we compare electron velocity distributions with the NEN spectra and show that the structures of the velocity distributions are closely related to the intensities of the NEN. We discuss the generation mechanism of the NEN based on the above results consulting computer experiments.

In Chapter 7, we focus on the electron plasma waves observed in the lobe close to the plasma sheet. Our waveform observations show that the amplitudes of electron plasma waves are strongly modulated. Such waveforms with amplitude modulations have been observed by several spacecraft in the Jovian bow shock, solar wind, and polar regions. All of the papers discussing the generation mechanism claim that the amplitude modulation is caused by the nonlinear parametric instability of the Langmuir waves. However, the main difficulty on this theory is the poor correlation between observed Langmuir waves and ion acoustic waves, which should be excited as the result of the nonlinear parametric instability. In our Geotail case, we also confirm the poor correlation between the Langmuir

waves and ion acoustic waves. However, our detailed polarization analyses show that the modulated electron plasma waves consist of the Langmuir waves and Electron Cyclotron Harmonic (ECH) waves. Modulated waveforms of the ECH waves can be realized without any nonlinear instabilities. We extend and apply this result to the observations by other spacecraft.

Chapter 8 describes the electrostatic waves observed in the magnetosheath region. Several types of electrostatic waves have been observed by previous spacecraft. We perform detailed analyses of such electrostatic waves using waveform data and find that their observed waveforms and their natures are quite similar to those of the PSBL BEN and lobe NEN waveforms. We compare the electrostatic waves in the magnetosheath with the PSBL BEN and lobe NEN waveforms, and discuss their generation mechanism. Further, we report a good correlation of the cone angle of the ambient magnetic field and intensities of magnetosheath electrostatic waves. This correlation provides us with important information to identify the generation mechanism.

We show a new attempt to study the macroscopic structures by using the plasma wave measurements in Chapter 9. As will be shown in Chapter 3, plasma waves have specific signatures for each characteristic region in the magnetotail. Further, as introduced in Section 1.3.2, we can obtain local electron plasma densities using lower cutoff frequencies of the continuum radiation. By analyzing these wave data statistically, we obtain the macroscopic structure of the magnetotail. Since plasma waves reflect the results of wave-particle interactions, they are usually used for the study on microscopic phenomena. However, we show that the plasma waves can also be useful for the macroscopic study in the magnetotail region.

In Chapter 10, we summarize the present study and show a comprehensive chart of energy flows from the solar wind related to the plasma waves.

Chapter 2

Plasma wave instrument onboard Geotail spacecraft

2.1 Introduction

Scarf et al. [1980] proposed to provide instrumentation to study the wave-particle interactions found in the geomagnetic distant tail in the original US OPEN program. A fundamental objective of the so-called OPEN program was to analyze the flow of mass, momentum and energy through the solar wind/magnetosphere system. Many physical processes controlling the entry, transport, storage, acceleration and loss of plasma in the Earth's magnetosphere are related directly to the underlying wave-particle interactions.

To meet the requirement for studying wave-particle interactions, design and manufacturing specifications for a Plasma Wave Instrument (PWI) onboard the Geotail spacecraft were solicited [*Matsumoto et al.*, 1994a]. In the design of the subsystem, an attempt in simultaneously capturing waveforms of electric and magnetic components was proposed, in addition to the highly sensitive measurement of electric and magnetic field spectra with fine frequency and time resolution.

The PWI consists of following three different sets of receivers:

1. Sweep Frequency Analyzer (SFA),
2. Multi-Channel Analyzer (MCA) and
3. Wave-Form Capture receiver (WFC).

The first two sets of receivers are devoted to measuring wave spectra, while the last one is designed to capture waveforms from two electric and three magnetic field components of the measured wave emissions, simultaneously. PWI circuits are divided and contained in two different chassis, called PWI-M and PWI-MA. The PWI-M (see Fig. 2.2) contains all of the PWI circuits except the MCA, while the PWI-MA was developed and assembled in the University of Iowa, USA and it contains the MCA circuits (see Fig. 2.3). Table 2.1 summarizes the power and weight budgets of the PWI.

Geotail has 14 types of telemetry formats, which are selected depending on the spacecraft operation modes. PWI observation data are available in three types of telemetry formats called Format 1, 2, and 3. Format 1 includes the SFA and MCA data. These data are

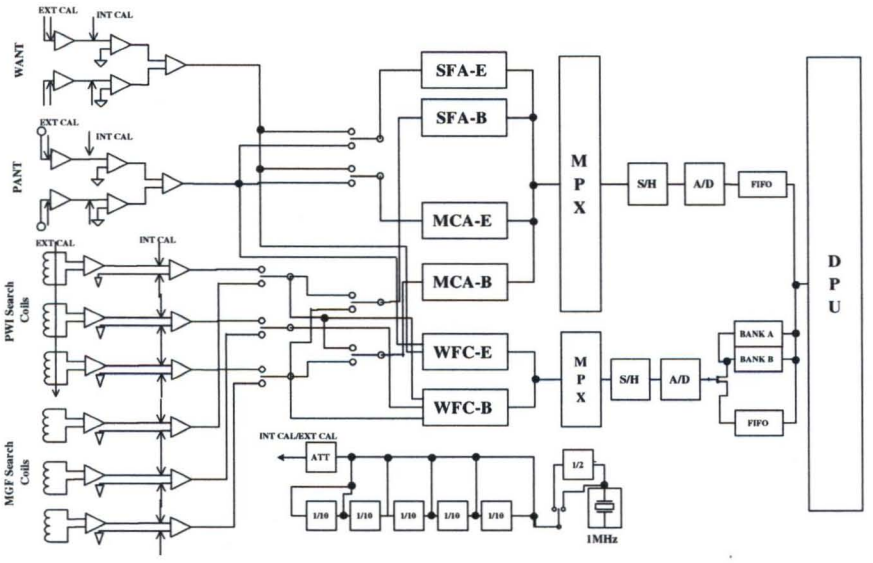

Figure 2.1: Block diagram of the PWI onboard Geotail spacecraft.

Table 2.1: Power and weight budgets

Instruments	Max. power (W)	Weight (kg)
SFA, WFC, DPU (PWI-M)	9.4	10.07
MCA (PWI-MA)	3.8	3.8

Figure 2.2: Chassis of the PWI-M. PWI-M contains all of the circuits of the PWI except the PWI-MA.

Figure 2.3: Chassis of the PWI-MA. PWI-MA was developed by the University of Iowa, USA.

recorded onboard magnetic data recorder and played back mainly to NASA Deep Space Network (DSN).

Format 2 is a real time observation mode supported by Usuda Deep Space Center (UDSC) in Japan. It includes all of PWI observation data with the highest resolution.

Format 3 is an unusual observation mode. We mainly use this format, when we need to monitor US instruments' data in real time, because Format 2 does not include them. Format 3 includes all of PWI observation data, however, WFC data qualities are coarse relative to those in Format 2.

In the following sections, we describe the detailed capabilities of each PWI receiver and electric/magnetic sensors which are used for the plasma wave measurements as well as the brief introduction of the Geotail spacecraft.

2.2 General descriptions of the Geotail spacecraft

The Geotail mission was originally proposed as the OPEN-J mission which targets to investigate the near-earth geomagnetic tail region in 1980. On the other hand, the GTL (Geomagnetic Tail Laboratory) mission in the US OPEN program was independently proposed by NASA for investigating the distant magnetotail region. In 1983, these two missions were combined to be the Geotail mission and the OPEN program was rearranged to be the ISTP program under international collaborations in 1984.

Geotail spacecraft was launched on July 24, 1992 in the Kennedy Space Center by the Delta-II launch vehicle. Geotail is the first spacecraft which is designed for the investigation of the distant geomagnetic tail. The cylindrical spacecraft body with 2.2 m of diameter and 1.6 m of height has two sets of 100 m tip-to-tip dipole antennas and six meter long masts (see Fig. 2.4). Two sets of dipole antennas are dedicated to measuring the DC and AC electric fields. One of the masts called MST-F mount two sets of fluxgate magnetometers (FXI and FXO) used for the measurement of the DC magnetic field. The FXI magnetometer

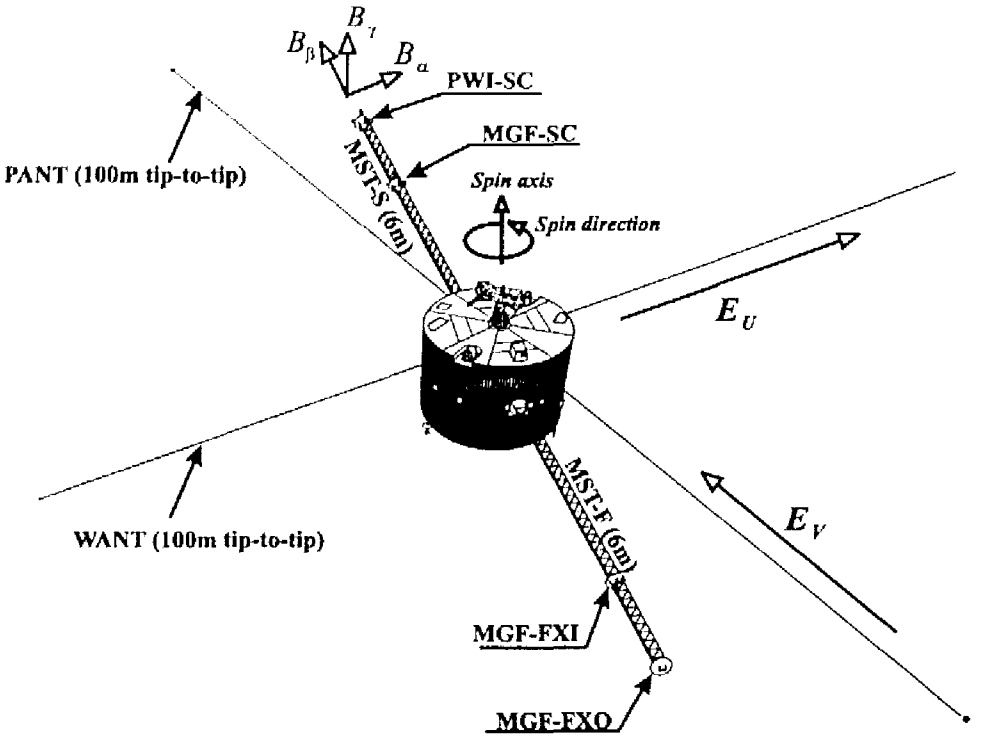

Figure 2.4: External view of the Geotail spacecraft and configuration of the PWI and related sensors.

is designed and supplied by the NASA/Goddard Space Flight Center and the FXO was developed by the Japanese MGF team [*Kokubun et al.*, 1994].

Two sets of tri-axial search coils (MGF-SC and PWI-SC) are mounted on another mast called MST-S. The MGF-SC is developed by the Japanese MGF team and is designed for the measurement of magnetic field components of low frequency waves up to 50 Hz, while the PWI-SC was developed by the PWI team and is used for the high frequency waves up to 12.5 kHz [*Matsumoto et al.*, 1994a].

Since the main objective of the Geotail spacecraft is to investigate the structure and dynamics of the geomagnetic tail, its orbit is designed to cover various regions of the geomagnetic tail. The Geotail mission has two different orbit phases: Distant tail orbit phase and Near tail orbit phase. Figure 2.5 shows all of the Geotail distant tail orbits plotted in the modified Geocentric Solar Magnetospheric (GSM) coordinate system (see Appendix A). Geotail spacecraft was injected onto the distant tail orbit which makes use of the Sun-synchronus double lunar swingby. The orbital plane is almost the same as that of the moon and its apogee is always located in the night side of the earth in order to survey the tail region. The farthest apogee is about 220 R_E down the tail, while the perigee in the dayside magnetosphere is 5 to 10 R_E. After the two-year distant tail phase, the Geotail was injected onto the near tail orbit through the Trans-near-tail phase in November 1994. As shown in Fig. 2.6, the orbits are almost circular and the apogee ($\sim$ 30 R_E) and perigee ($\sim$ 10 R_E) rotates in a period of almost one year.

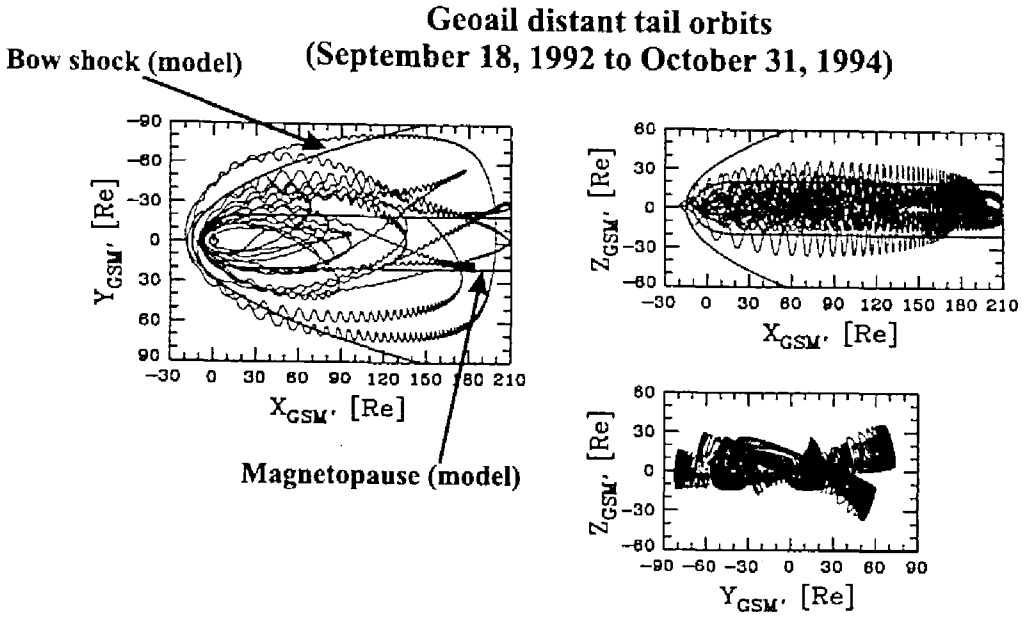

Figure 2.5: Geotail distant tail orbits plotted on the modified GSM coordinates.

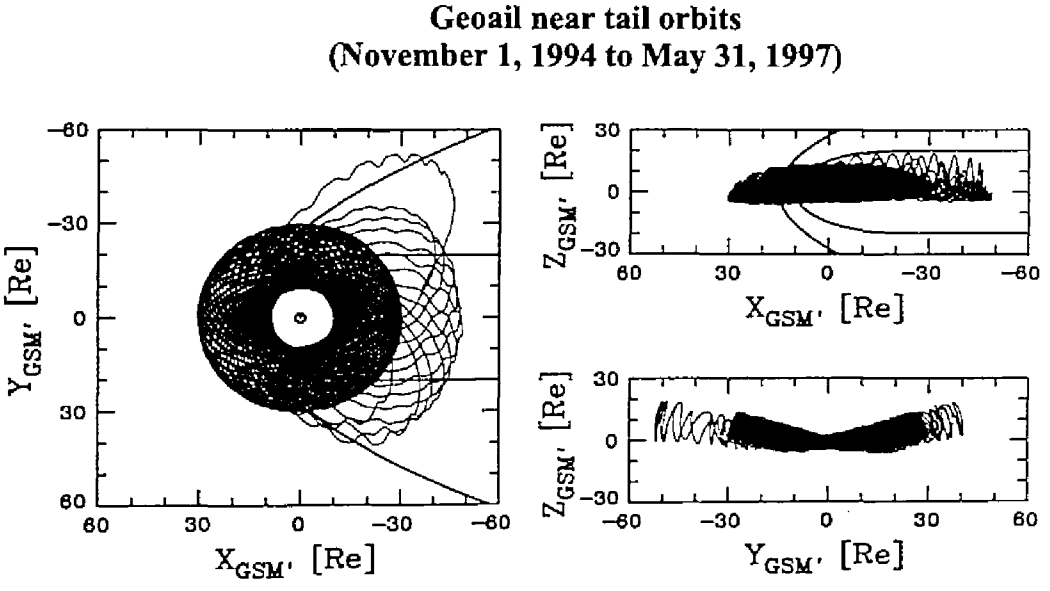

Figure 2.6: Near tail orbits plotted on the modified GSM coordinates.

Figure 2.7: Two boxes of the WANT (WANT-A and WANT-B).

Figure 2.8: Two boxes of the PANT (PANT-A and PANT-B).

2.3 Electric/magnetic sensors and their peripheral circuits

In order to measure the weak electric and magnetic fields of plasma waves in the geomagnetic tail region, we have designed two kinds of electric sensors and tri-axial search coils, having taken into account both the most suitable condition for field detection and reduction of spacecraft noise. Figure 2.4 shows the configuration of the GEOTAIL spacecraft along with the definition of coordinates on each sensor. Two sets of long dipole antennas with a length of 100 m tip-to-tip are wire and probe antennas termed "WANT" and "PANT," respectively. These each antennas are stored in two chassis (see Fig. 2.7 and Fig. 2.8) and they were successfully deployed on August 27, 1992. Two masts of six meters in length are used for mounting the magnetic field sensors well away from the spacecraft in an attempt to reduce the spacecraft noise. The MST-F and MST-S were successfully deployed on September 4 and September 16, 1992, respectively.

The antenna elements of the WANT and PANT are radially deployed from the spacecraft

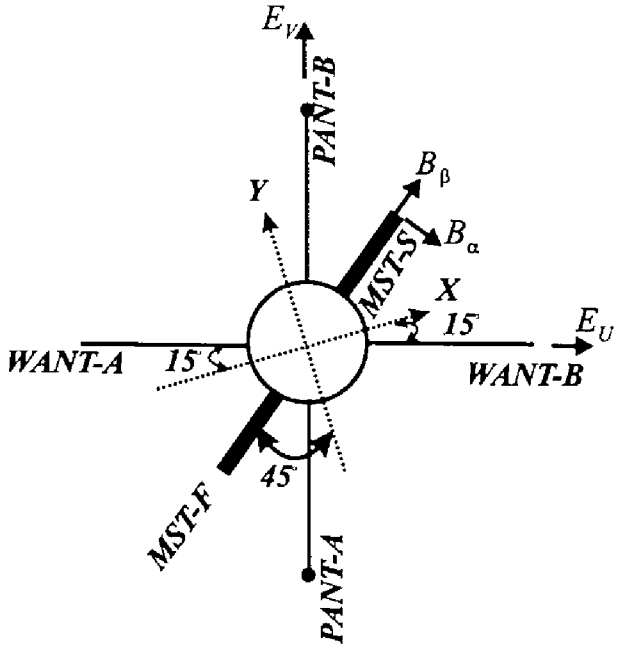

Figure 2.9: Configuration and relative angles between each sensor.

and orthogonal to each other. Their axes, U and V, deviate by 15° clockwise from the X and Y mechanical coordinate directions fixed on the spacecraft, respectively (see Fig. 2.9). The assembly of PWI tri-axial search coils (which is hereafter called PWI-SC) and their preamplifiers is mounted on the top of the MST–S. The tri-axial search coils associated with the MGF (MGF-SC) are mounted on the same mast but two meters inside the PWI-SC (see Fig. 2.10). The PWI-SC is normally connected to the PWI measurement system. However, we can select the MGF-SC by a telemetry command if necessary. The direction of the MST-S (and MST-F) deviates by 45° clockwise from the spacecraft Y (and $-Y$) axis as shown in Fig. 2.9. The three axes of the PWI search coils are defined in a cylindrical coordinate system as follows: α is in the tangential direction, β measures in the radial direction, and γ is parallel to the spin Z axis of the spacecraft.

2.3.1 Electric field sensors

The GEOTAIL spacecraft is equipped with two types of electric field measurement capabilities in the form of the PWI and EFD. The main purpose of the PWI is the detection of wave electric fields whereas the EFD measures DC electric fields in the magnetospheric plasma. Electric potentials picked up by the antennas are fed to both the PWI and EFD main electronics having already passed through their own individual preamplifiers. Both antennas, WANT and PANT, are basically electric dipoles. Preamplifiers for each antenna element are placed behind the antenna deploying mechanism which is mounted on top of the upper equipment shelf in the spacecraft.

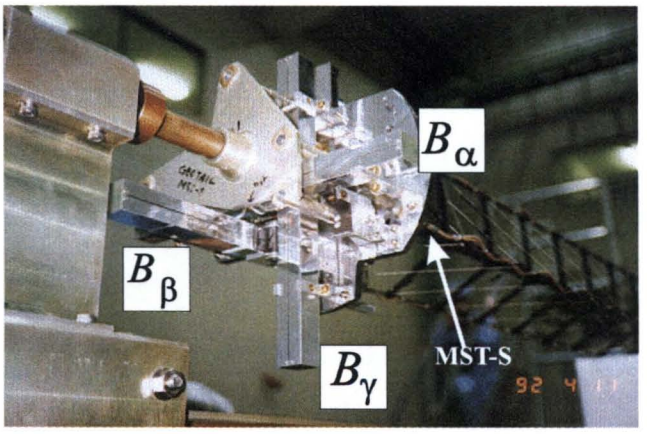

Figure 2.10: Tri-axial search coils (PWI-SC) mounted on the top of the MST-S.

WANT

The WANT is a wire dipole antenna. Figure 2.11(a) shows the outline drawing of the WANT antenna element. The element is a stainless steel wire of 50 m in length and 1.05 mm in diameter. The surface of the wire, except a portion of 10 m from the tip, is coated with a thin (0.12 mm) Polyamide film whose resistance coefficient is 10^{18} /cm to insulate it electrically from the ambient plasma. The base of the wire from the antenna deploying mechanism out to 3 m is shielded by a copper-mesh sleeve in order to suppress the electrical interference radiated from the spacecraft. The copper-mesh sleeve is connected to the spacecraft chassis through a breeding resistance of 1 kΩ. The PWI makes use of the WANT in two different modes: one is a dipole mode and the other is a monopole mode. The instrument is nominally operated in the dipole mode. The purpose of the monopole mode is to detect spatial inhomogeneity in the plasma potentials around the spacecraft which might be formed by a plasma wake. The selection of the operation mode (dipole and monopole) is carried out by a telemetry command.

Figure 2.12(a) shows the electric circuit for the WANT and its preamplifier. The electric potential induced on the WANT element is fed to the preamplifier input terminal through a decoupling capacitance of 220 pF. Since an input resistance of 200 MΩ is connected between the preamplifier and the chassis, the lower limit of the passing frequency becomes 3.6 Hz (see Fig. 2.14(a)). In order to calibrate the amplitude and phase of the observed signal, a calibration signal from the PWI main circuit is imposed (CAL Mode) onto the WANT element through a resistance of 2 kΩ (the lower side of switch K2). Further, we can measure the antenna impedance (IMP Mode) using the same calibration signal by switching the resistance to the higher value 5.1 MΩ (the upper side of K2). In this mode, the preamplifier picks up a different potential from that in the CAL mode because the potential is modified by the sheath impedance formed around the antenna elements.

PANT

The PANT is a pair of top-hat antennas composed of a sphere attached at each end of a stainless wire 50 m in length and 1.05 mm in diameter (same as WANT). Figure 2.11(b)

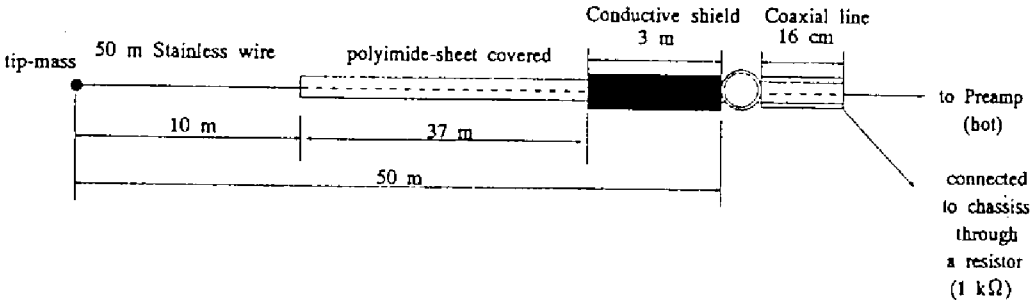

(a)

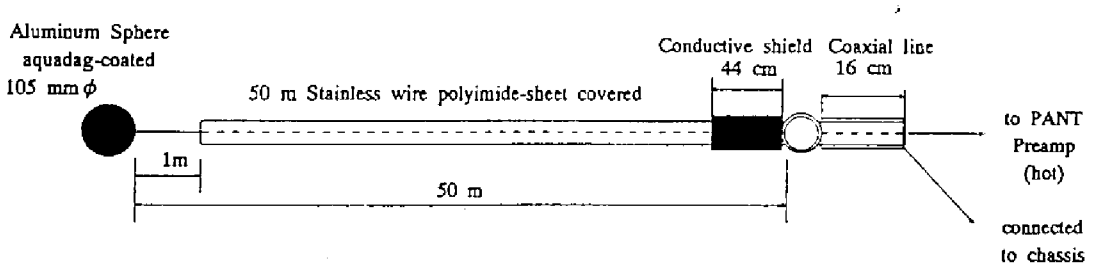

(b)

Figure 2.11: Drawings of (a) WANT and (b) PANT elements [*after Matsumoto et al.*, 1994a].

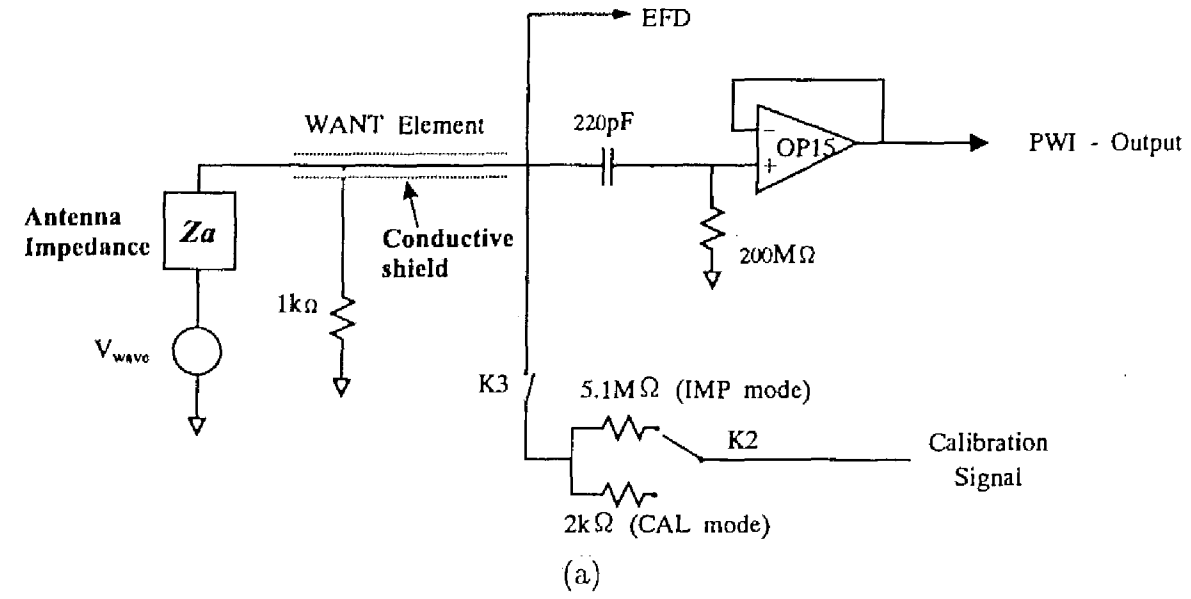

(a)

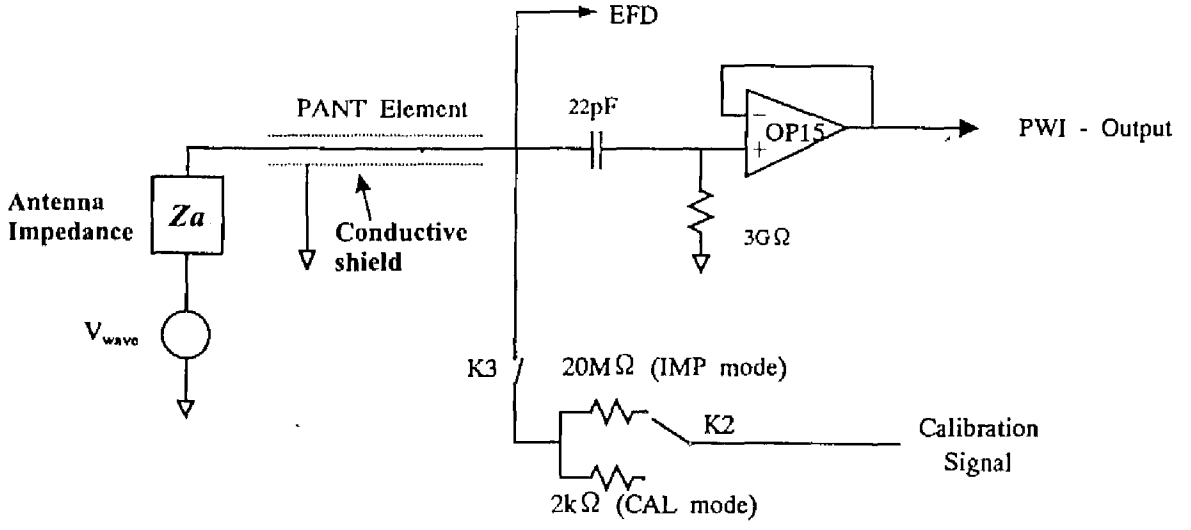

(b)

Figure 2.12: Electric circuits for the antenna and preamplifiers of (a) WANT and (b) PANT.

shows an outline drawing of the PANT element. A hollow aluminum sphere of 105 mm in diameter is attached to the tip of the wire. The sphere surface is coated with Aquadag to ensure uniform emission of photo-electrons. The entire wire surface except the outer portion 1 m from the sphere, is coated with Polyamide film. The inner portion extending 44 cm from the base of the wire is shielded with a copper-mesh sleeve connected directly to the chassis to suppress spacecraft noise.

Figure 2.12(b) shows the electric circuit for the PANT preamplifier. Because of the necessity for sensitive DC electric field measurements, the EFD team requires the input impedance of the preamplifier circuit to be larger than 5 GΩ at a frequency of 0.3 Hz. Therefore, the decoupling capacitance and the input resistance connected to the PWI preamplifier were chosen to be 22 pF and 3 GΩ, respectively. This means that the lower limit of the passing frequency for this circuit is 2.4 Hz (see Fig. 2.14 (b)). The measured stray and input capacitances at the input terminal of the preamplifier are 20 pF. By these two capacitances (22 pF and 20 pF), the signal amplitude picked up by the PANT antenna is reduced to about half level at the input terminal of the preamplifier. The total gain of the PANT circuit then becomes −5.6 dB even though the gain of the preamplifier itself is unity.

The methods for calibrations and the measurement of the antenna impedance are the same as those of the WANT, though the resistance used for the IMP mode is 20 MΩ as shown in Fig. 2.12(b).

Figure 2.13 shows the minimum noise levels of the WANT and the PANT preamplifiers measured during the preflight calibration tests. The levels shown in the figure were obtained from the output of front-end circuits, when both input terminals of preamplifiers are connected to the ground. The frequency characteristics of the WANT noise level coincide with the theoretical value, whereas that for PANT includes an additional operational amplifier connected in cascade after the circuit shown in Fig. 2.12(b). Thus, noise level of PANT is higher than that of WANT.

Frequency characteristics of preamplifiers

As shown in Fig. 2.12, each dipole antenna (WANT and PANT) is connected to both EFD and PWI preamplifiers. These preamplifiers are designed to operate independently without disturbing their counterparts. Frequency responses of the gain for the WANT and PANT preamplifiers used in the PWI (hereafter termed WANT-Pre and PANT-Pre, respectively) are shown in Fig. 2.14(a) and (b). These figures show the lower limits of the passing frequencies to be 3.6 Hz and 2.4 Hz (WANT-Pre and PANT-Pre respectively) as described in Sections 2.3.1. The important difference point between (a) and (b) is the gain in the mid-frequency range of flat response. The PANT-Pre exhibits a −5.6 dB gain, while the WANT-Pre provides a −0.6 dB gain. This difference is caused by differences in the signal attenuation for the input circuits of the WANT and PANT preamplifiers. Here the ratio of the decoupling capacitance to the stray capacitance formed in the input terminal for the two preamplifiers is different. Figure 2.15(a) and (b) show the phase rotations as a function of frequency for both these preamplifiers. The phase rotation effect in the high pass filter circuits having cutoff frequencies of 3.6 and 2.4 Hz is seen in each figure and last up to 500 Hz. In order to precisely estimate the field polarizations from the captured waveforms, these phase rotation effects must always be included. Calibration data for frequencies up

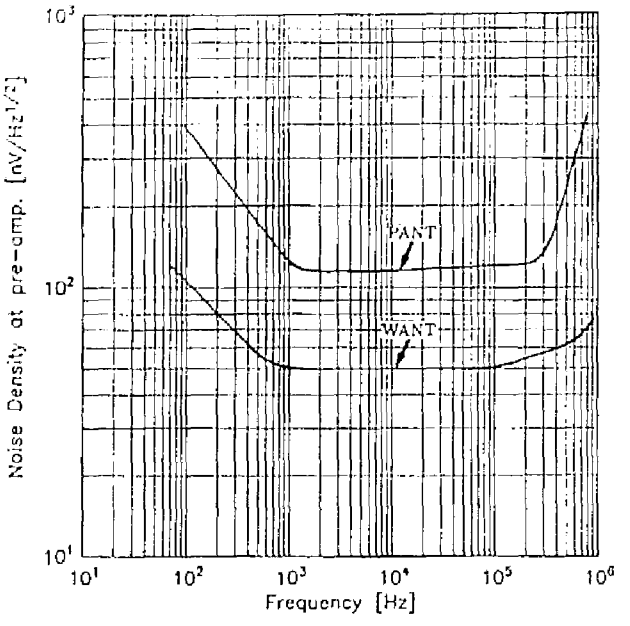

Figure 2.13: Minimum noise levels of the WANT and PANT preamplifiers measured during the preflight calibration test [*after Matsumoto et al.*, 1994a].

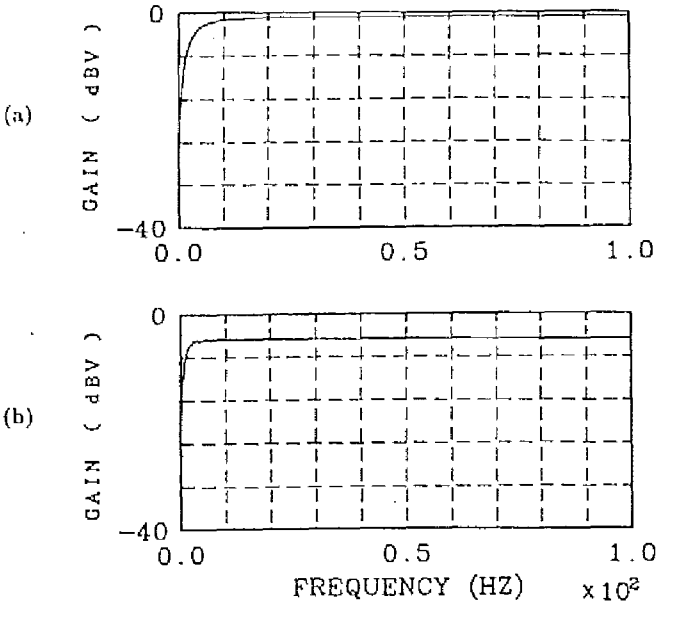

Figure 2.14: Frequency responses of the gain in a low frequency range of (a) the WANT and (b) the PANT preamplifiers [*after Matsumoto et al.*, 1994a].

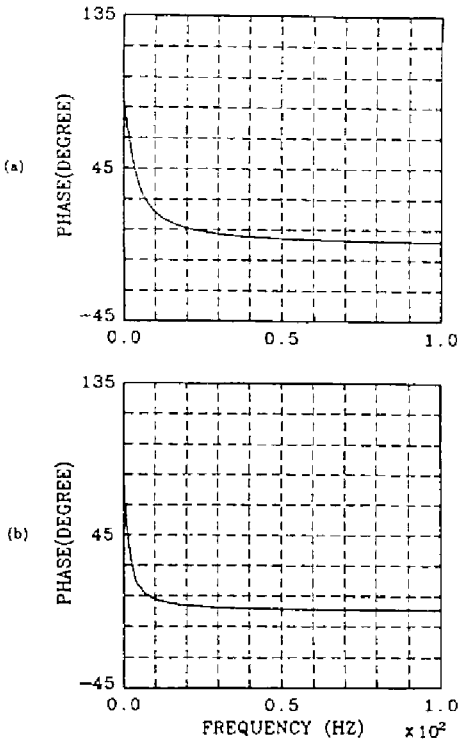

Figure 2.15: Frequency responses of the phase rotation in a low frequency range of (a) the WANT and (b) the PANT preamplifiers [*after Matsumoto et al.*, 1994a].

to 1 MHz have been acquired for every decade in frequency.

2.3.2 Magnetic field sensors

Tri-axial Search Coils

Two sets of tri-axial search coils, the PWI–SC and MGF–SC, are mounted on the MST–S mast. The PWI–SC measures wave magnetic fields over a frequency range up to 12.5 kHz, while the MGF–SC covers a frequency range up to 50 Hz. Each axial search coil of the PWI–SC is constructed from 20,000 turns of a copper wire 0.1 mm in diameter wound on a lightweight bobbin 30 cm in length. The coils are divided into 10 sectors over the central 20 cm portion of the bobbin to reduce the stray capacitance among the wound wire. At the center of the each main (search) coil, additional two sets of 2-turn coils are provided to form negative flux feedback and for supplying the calibration signal. The core of these coils, which is situated inside the bobbin, consists of laminated layers (0.05 mm thick) of parmalloy which has a high permeability. The layers are electrically insulated from each other in order to suppress the formation of eddy currents. The core is 30 cm long and has a cross-section of 5 mm square. The total specific permeability of the core is effectively 940. Each main coil, together with the additional two sets of 2-turn coils, is covered with aluminum (0.5 mm thick) housing having a dimension of 25 mm × 25 mm × 304 mm. The housing having a slit along the coil axis serves as electrostatic shielding. The PWI–SC is assembled on an aluminum plate mounted on the top of the MST–S. The

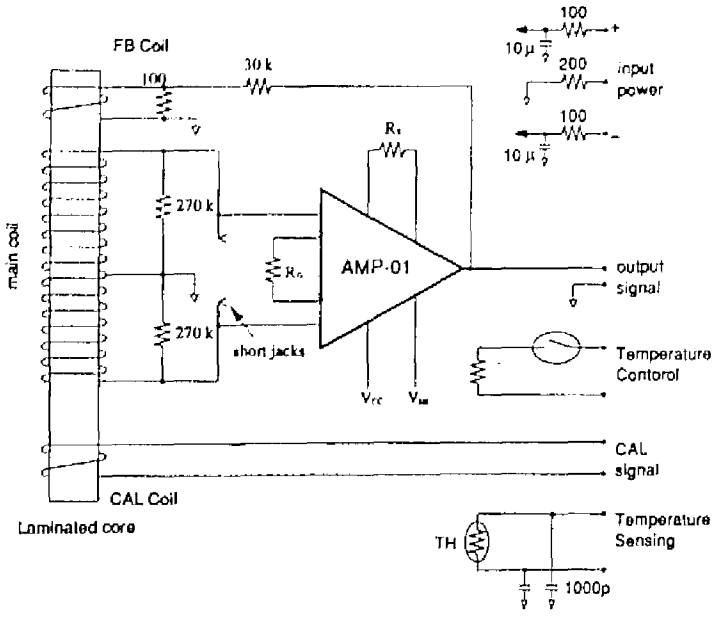

Figure 2.16: Illustration of the electric circuit of the PWI-SC and its preamplifier [*after Matsumoto et al.*, 1994a].

three search coils are deployed orthogonally to each other within a directional accuracy of $\pm 0.5°$ after full extension of the MST–S. The aluminum plate induces some phase errors in our measurement of the null field direction with respect to the nearest search coil, which is about 3° in the frequency range concerned. However, this error does not affect the main direction of the field pattern which is used for determination of the wave properties such as the polarization phase.

Figure 2.16 shows a simplified illustration of a representative circuit diagram for the search coil preamplifiers. A negative flux feedback loop is introduced in order to suppress resonant characteristics of the search coil itself and to obtain a flat response in gain over the range of observation frequencies. The voltage induced in the main coil by the wave magnetic field is fed to the preamplifier with an open loop gain of 60 dB. The output signal from the preamplifier drives the secondary coil through a divider with two resistances of 30kΩ and 100Ω, thereby magnetically coupling to the main coil and achieving the negative flux feedback.

Figures 2.17 (a) and (b) show frequency response curves for the gain and phase rotation of a representative search coil (γ component) and its preamplifier circuit when a magnetic field of 1 pT was applied to the coil axis. In Fig. 2.17 (a) the characteristic curve shown corresponds to an applied magnetic field 1 pT. This field strength was chosen to match the average order of the magnitude field strength of waves expected in the geomagnetic tail, thereby showing the probable instrument performance in this region. However, these results were deduced from the actual calibration measurements which were made using 100 pT field strengths. The curve shows a linear increase in gain up to 400 Hz, then constant for all frequencies above 400 Hz. The responses for the two other axial search coils are nearly equal to the one depicted to within ± 1 dB for the gain and ±3° for

Table 2.2: Specification of SFA

Band	Frequency Range	Freq. Step	Bandwidth	Source	Sweep
1	24 Hz $\sim$ 200 Hz	1.3 Hz	2.6 Hz	B and E	64 sec
2	200 Hz $\sim$ 1600 Hz	10.7 Hz	10 Hz	B and E	64 sec
3	1.6 kHz $\sim$ 12.5 kHz	85.4 Hz	85 Hz	B and E	8 sec
4	12.5 kHz $\sim$ 100 kHz	683 Hz	680 Hz	E only	8 sec
5	100 kHz $\sim$ 800 kHz	5.47 kHz	5.4 kHz	E only	8 sec

the phase rotation. Since the calibration coils for the three search coils are connected in series, a calibration signal with the same magnetic intensity is applied to each search coil. Therefore, the differences in the phases as well as the amplitudes among the three search coil circuits can be obtained precisely from the captured waveforms.

The measured in-flight sensitivities of the search coils as a function of frequency are plotted in Fig. 2.18. The dot-dash curve shows the expected theoretical sensitivity of the GEOTAIL PWI search coils. The + symbols indicate noise levels actually measured when the GEOTAIL spacecraft was in the geomagnetic tail region, and these clearly coincide well with the theoretical curve. The other curves in the figure represent the noise levels from the search coils on board ISEE-1 and -3 and OGO-5 [*Scarf et al.*, 1978; *Gurnett et al.*, 1978; *Frandsen et al.*, 1969]. This comparison shows clearly that the GEOTAIL PWI search coils have the highest sensitivity among these types of magnetic sensors for the frequency range from 30 Hz to 1 kHz. A distance dependence in the noise intensity of $r^{-2.5}$ for the magnetic field was confirmed during the ground ElectroMagnetic Compatibility (EMC) tests of the GEOTAIL spacecraft, where r is the distance from the center of the spacecraft. In-flight observations have demonstrated that mounting of the PWI-SC at six meters in distance from the spacecraft surface has made a favorable reduction in the noise level measured by this instrument.

2.4 Sweep frequency analyzer (SFA)

The SFA provides spectral information on plasma wave amplitudes over the frequency range from 24 Hz to 800 kHz for the electric field and 24 Hz to 12.5 kHz for the magnetic field. The SFA consists of eight independent receivers covering 5 frequency bands for the electric fields and three frequency bands for the magnetic fields. The receiver specifications are listed in Table 2.2. Figure 2.19 shows a block diagram of the main electronics of one of the eight receivers in the SFA which measures a single frequency band. The lowest frequency band (Band 1) is a single conversion super heterodyne receiver while the other frequency bands correspond to double conversion super heterodyne ones. Each receiver has a very good frequency resolution of 1/128 of the receiver frequency band although their time resolution (64 sec for Bands 1 and 2, and 8 sec for Bands 3 $\sim$ 5) is somewhat coarse. The "H/L" in Fig. 2.19 represents a gain control with a 30 dB difference and can be varied by a telemetry command. Frequencies of the LPF, the 1st and 2nd Local OSCs and the 1st and 2nd IFs in each band are listed in Table 2.3. The signal from the 2nd IF amplifier passes through quasi-logarithmic amplifiers labeled "Log" where its

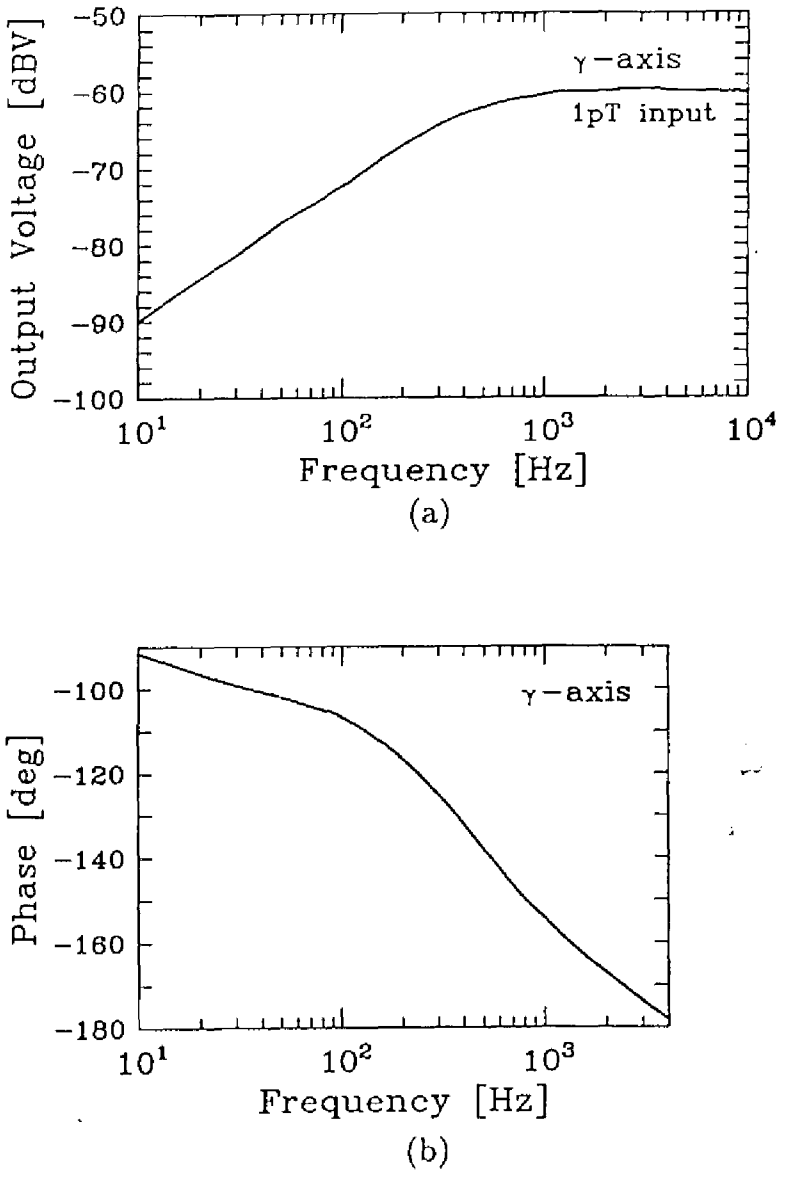

Figure 2.17: (a) Frequency response of the gain for a representative search coil (γ component) and its preamplifier circuit. The measurement was conducted in a parallel magnetic field of 100pT, but the characteristic curve illustrated in this figure represents the response which has been scaled down to the noise level ($\sim$ 1 pT). (b) Phase rotation as a function of frequency for the same search coil and preamplifier circuit [*after Matsumoto et al.*, 1994a].

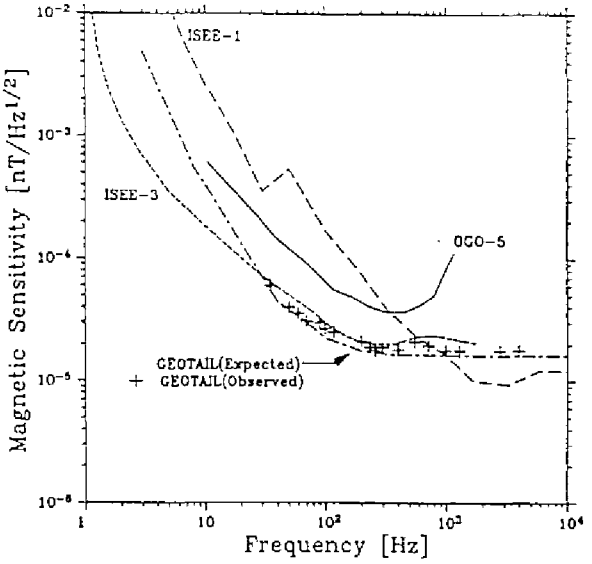

Figure 2.18: Sensitivity for search coils onboard several spacecraft in their flights [*after Matsumoto et al.*, 1994a].

signal amplitude is detected linearly then converted to digital data. Figure 2.20 shows the input/output amplitude characteristics obtained at a frequency of 55.67 kHz in Band 4 for electric field. Four ripples seen in the characteristic are caused by a cascade connection of four quasi-logarithmic amplifiers. This connection realizes the wide dynamic rage of 90 dB. The SFA measures one wave electric field component of either the E_U or E_V component and one wave magnetic field component of either the B_α or B_γ component. The selection of which field component is measured is carried out by a telemetry command. The dynamic range of the observed field intensities in each frequency band are shown in Fig. 2.21(a) for the electric field and (b) for the magnetic field. Each receiver has an effective dynamic range of $\sim$ 90 dB. The electric field receivers are placed in the High gain mode by stepping up the level in the Low gain mode by 30 dB. These two dynamic ranges are depicted in Fig. 2.21(a). The SFA has another mode of operation which can be used. Despite its operation as the SFA, we can also fix the measured frequency to one preset value in each frequency band. This mode provides very high time resolution for the observed signals at an arbitrarily selected frequency. The time resolutions in this mode are 0.5 sec for Bands 1 and 2, and 62.5 msec for Bands 3, 4, and 5, respectively. This observation mode was used

Table 2.3: Frequency table of SFA

Band	LPF	1st local	1st IF	2nd local	2nd IF
1	250 Hz	415.2 $\sim$ 584.8 Hz	390.6 Hz	–	–
2	1.875 kHz	3.322 $\sim$ 4.678 kHz	3.125 kHz	2.84 kHz	289 Hz
3	12.8 kHz	26.57 $\sim$ 37.43 kHz	25 kHz	20 kHz	5 kHz
4	110 kHz	212.6 kHz $\sim$ 299.4 kHz	200 kHz	210 kHz	10 kHz
5	880 kHz	1.701 MHz $\sim$ 2.395 MHz	1.6 MHz	1.61 MHz	10 kHz

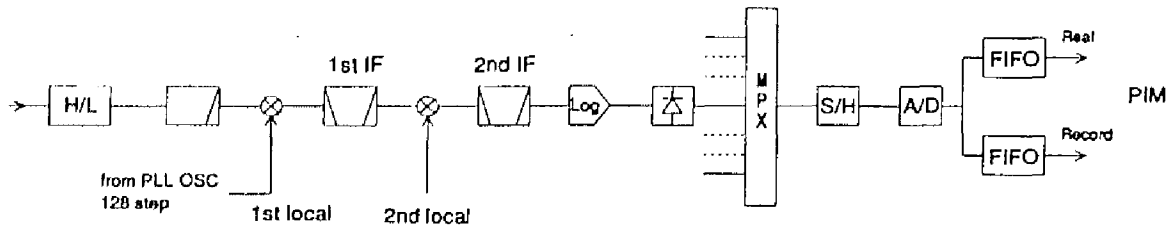

Figure 2.19: Block diagram of the SFA main electronics for a representative frequency band [after Matsumoto et al., 1994a].

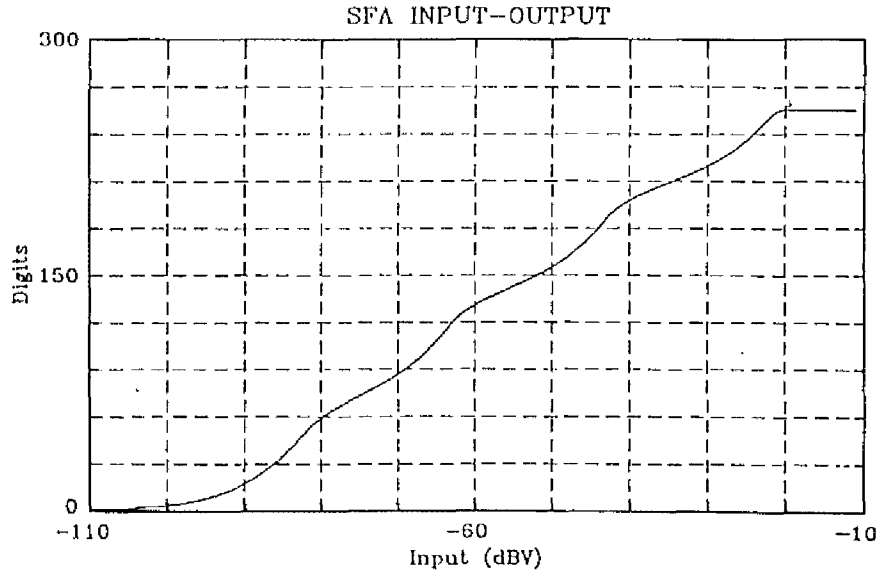

Figure 2.20: A representative example of Input/Output amplitude characteristics of an SFA receiver (Band 4 for electric field) [after Matsumoto et al., 1994a].

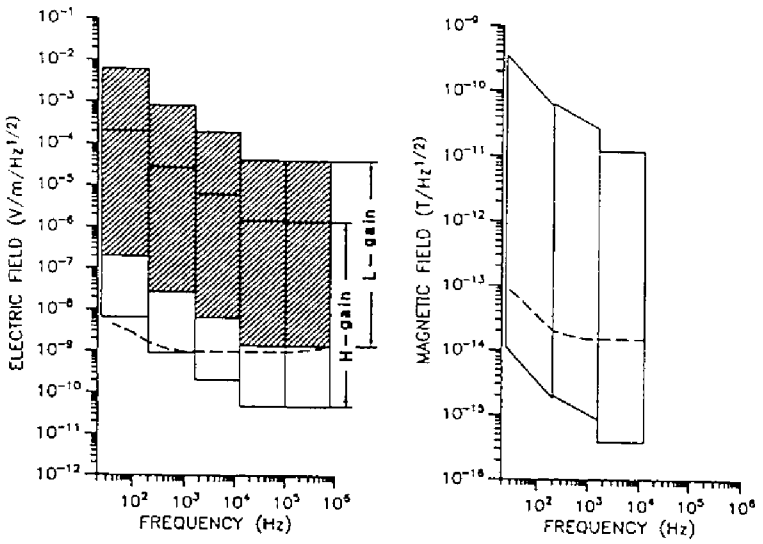

Figure 2.21: SFA amplitude ranges of (a) five band receivers for the electric field, and of (b) three for the magnetic field. In each band of the electric field receivers, high (H) and low (L) gain amplifications with a 30 dB difference are selectable in keeping an inherent dynamic range (90 dB) of the circuit, while the sensitivity for magnetic field is constant. In each figure, a representative sensor sensitivity is drawn by a broken line [*after Matsumoto et al.*, 1994a].

for the attempts to monitor the Jovian radiation triggered by the collision of the comet Shoemaker-Levy in 1994 [*Kasaba et al.*, 1996].

2.5 Multi-channel analyzer (MCA)

This subsystem is provided by the University of Iowa. The MCA contains two spectrum analyzers with fixed frequency channel filters as shown in Fig. 2.22. It provides high time resolution data to complement the coarser time resolution data of the SFA. However, their frequency resolution is coarse because they have only four frequency channels per decade in frequency. The input signal to the MCA is provided from the output of the common front-end circuit of the PWI system as well as to SFA and WFC receivers. One multi-channel spectrum analyzer is used to measure the electric field and is composed of 20 channels covering the frequency range from 5.62 Hz to 311 kHz. The other spectrum analyzer is used for magnetic field measurements and has 14 channels covering the frequency range from 5.62 Hz to 10 kHz. The bandwidths of the filters are ±15% of the channel center frequency in the frequency range below 10 kHz and ±7.5% of the center frequency for frequency above 10 kHz. The MCA instrument measures the wave electric field of either the E_U or E_V component (depending on which antenna is used) with a dynamic range of $\sim$ 110 dB and the wave magnetic field of either the B_α or B_γ component with a dynamic range of $\sim$ 100 dB.

Signals from all channels are sampled simultaneously so that the ratio of the electric to magnetic field strength may be calculated accurately. The signals are sampled once

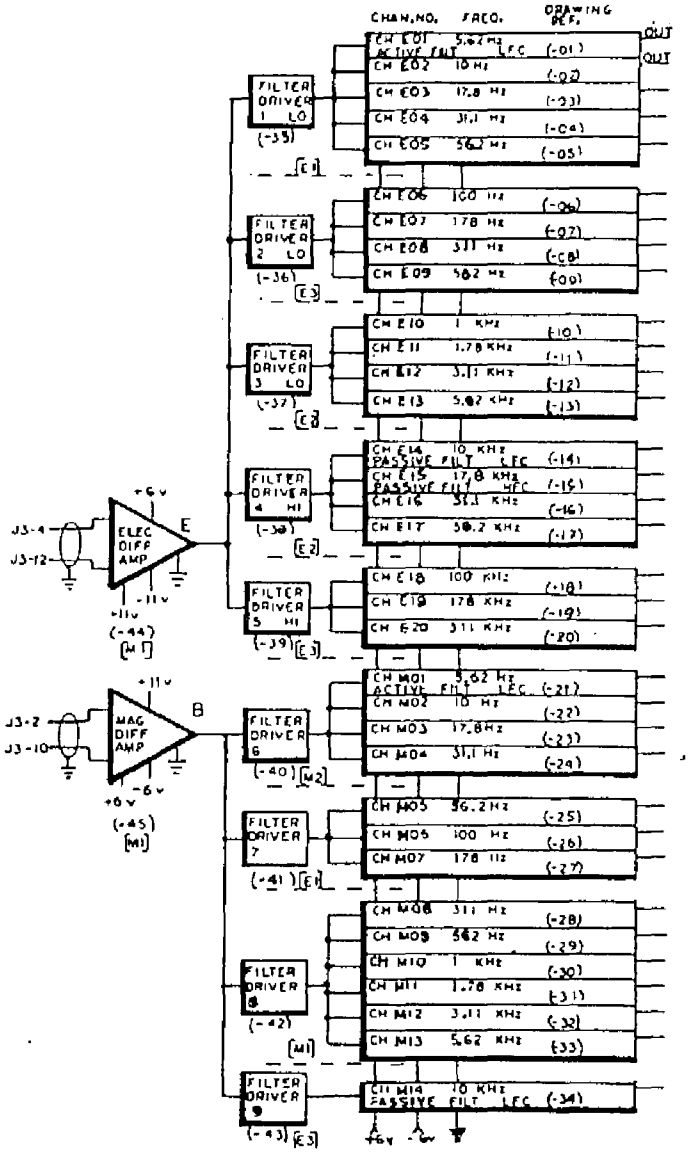

Figure 2.22: Block diagram of the MCA system [*after Matsumoto et al.*, 1994a].

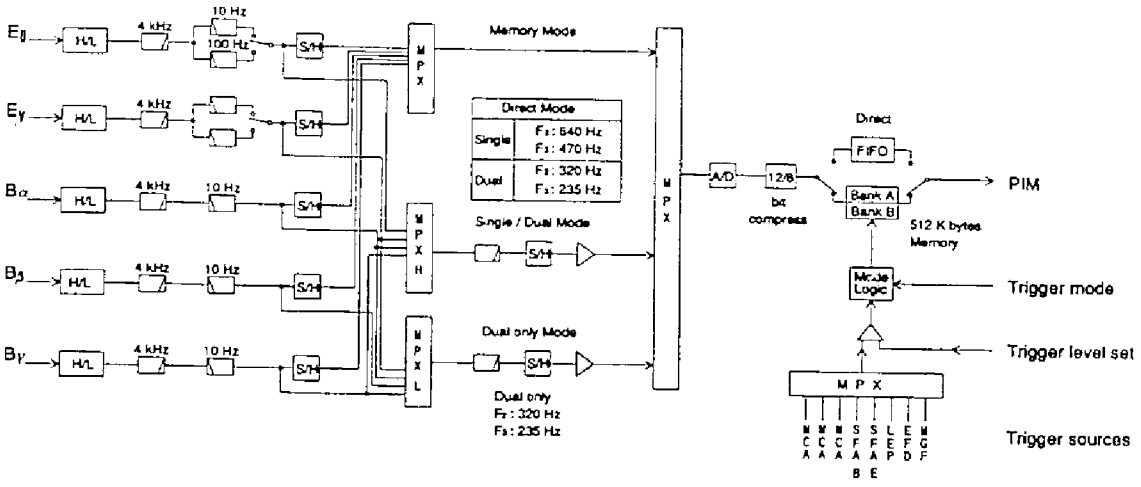

Figure 2.23: Block diagram of the WFC system [*after Matsumoto et al.*, 1994a].

(data acquisition time is 1.037 msec) every 250 msec in Format 2 (and every 500 msec in Format 1). Each channel of the spectrum analyzer has a suitable integration time in the linear detection of signal ranging from 500 msec in the lower frequency channels and decreasing to a few milliseconds for those channels above 3 kHz.

2.6 Wave-form capture (WFC)

The WFC data are used for the detailed analysis of the wave characteristics, such as determination of the wave vector, polarization, Poynting flux, and antenna impedance. Figure 2.23 shows a block diagram of the WFC system. The system has five (two electric and three magnetic) receivers each connected to a sensor through each front end circuit. The WFC has two different operation modes: Memory mode and Direct mode. In the Memory mode, wave signals are measured simultaneously as E_U E_V, B_α, B_β, and B_γ. These are fed to a gain-controller followed by an anti-aliasing filter (LPF) with an upper frequency cutoff of 4 kHz, then through high pass filters (HPF) which have a low frequency cutoff of 10 Hz. In Bands 1 and 2, an alternate HPF with a low frequency cutoff of 100 Hz can be used with the electric field measurements. Waveforms of the analog signal are sampled then converted into 12 bit data by an A/D converter with a frequency of 12 kHz. The 12 bit digital data are compressed into 8 bit by a quasi-logarithmic compression method. The compressed 8 bit data are then stored into onboard memory with a storage of 512 kBytes for a period of 8.7sec. The stored waveform data are read out of memory and telemetered to the ground using the PCM telemetry during an uninterrupted period of 275 seconds in telemetry Format 2 and 375 seconds in telemetry Format 3. The start timing for initiating waveform capture is controlled by either free running timing pulse (INTER. mode) or triggering signals from one of eight different sources. The instrument is triggered when one of the following measurements exceeds a preset level:

1. The intensity of Z axis component of the DC magnetic field as measured by the outboard fluxgate magnetometer of the MGF.
2. The amplitude of the plasma turbulence detected by a single probe of the EFD.
3. The magnitude of ion and/or electron moments as measured by the electrostatic analyzers of the LEP-EA.
4. The amplitude of the electric field measured on the 100 kHz channel of the MCA.
5. The amplitude of the electric field measured on the 316 Hz channel of the MCA.
6. The amplitude of the magnetic field measured on the 10 Hz channel of the MCA.
7. The integral amplitude of the electric field over the entire frequency range of Band 1 (frequencies less than 250 Hz) of the SFA.
8. The integral amplitude of the magnetic field over the entire frequency range of both Bands 1 and 2 (frequency less than 1.875 kHz) of the SFA.

The selection among the possible eight triggering sources and its preset level or amplitude is made via telemetry commands.

When the WFC instrument is operated in the Memory mode the following three modes of operation are available for storing and reading the data:

1. AFT: Storage of 512 kBytes of data after instrument triggering.
2. MID: Storage of two successive 256 kByte sequences of data, one before and the other after instrument triggering.
3. BEF: Storage of 512 kBytes of data before instrument triggering.

In the last two modes, a continuous sequence of signal sampling and storage into the memory is repeated until a triggering signal is detected by the instrument.

A common problem of noise interference in the plasma wave instruments on spinning occurs as each group of solar cell circuits cycles on/off when the solar cell surface of the group faces to the sunlit side then to the shadow side of the spacecraft [*Scarf, private communications*]. This repetition of the circuit from on to off to on again causes radiation of electromagnetic noises. To mitigate this problem, a high pass filter (HPF) with a cutoff frequency of 10 Hz is inserted in the receivers in order to suppress the detection of low frequency noise from the solar cell circuits. For the electric field receivers, we prepared an option for changing the HPF cutoff frequency from 10 Hz to 100 Hz in case the noise extended to higher frequencies then expected. The selection of the lower frequency cutoff is based upon the observed *in-situ* noise level. These noise suppression measures limit frequency range of the observed waveforms to a band from 10 Hz (or 100 Hz) to 4 kHz.

Besides the Memory Mode, the WFC can be operated in a Direct mode, with two possible variations: one is the Single channel mode in which only one field component is measured continuously and telemetered to ground on a real-time basis. In this operation mode the instrument can measure continuous waveforms of one electric or one magnetic component

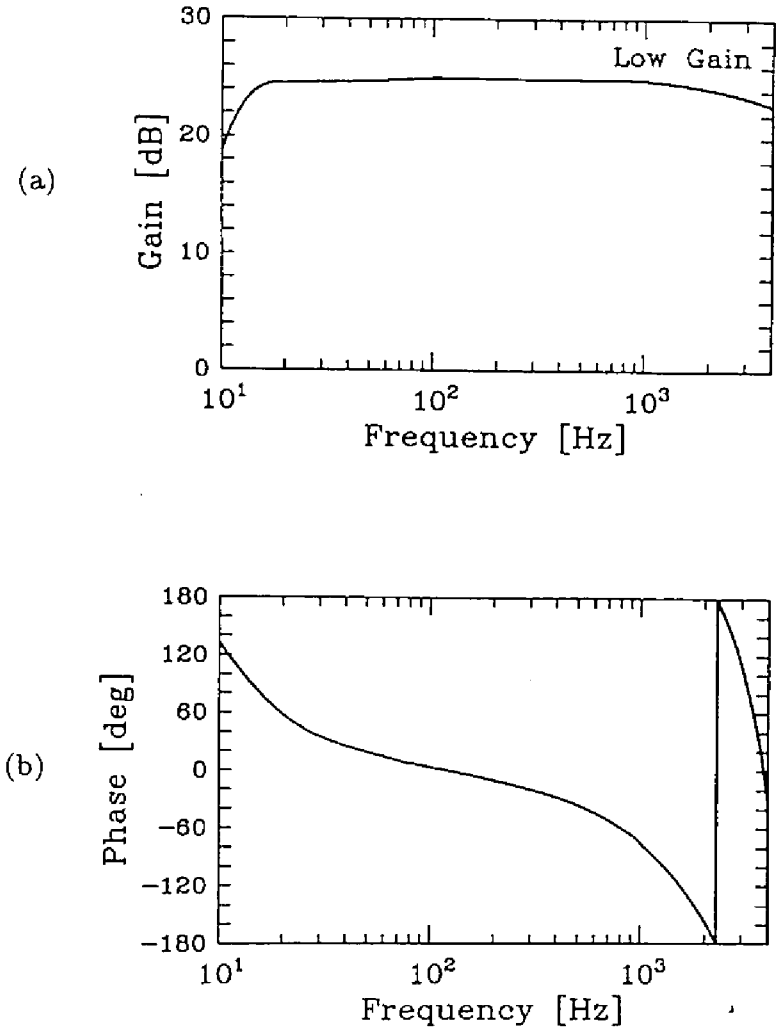

Figure 2.24: Frequency responses of (a) gain and of (b) phase rotation for a representative receiver (E_U) in the Low gain Memory mode of the WFC [*after Matsumoto et al.*, 1994a].

with an upper limit in frequency of 640 Hz in telemetry Format 2 (or 470 Hz in telemetry Format 3). The other method of instrument operation is in the Dual channel mode where two field components are measured and telemetered alternately. In this mode the upper limit in frequency is 320 Hz in telemetry Format 2 (or 235 Hz in telemetry Format 3) for each component. For both of these modes, the data sampling frequency is three times the upper limit in frequency.

The WFC system can measure the wave amplitude with a dynamic range of 66 dB. The receiver gain keeping its dynamic range can be stepped up in the gain controller "H/L" by 40 dB and 20 dB in electric and magnetic channels to amplify the weak signal, respectively.

Figure 2.24 shows the frequency response of the gain and phase rotation for the WFC circuit in the Low gain and memory mode of the E_U channel. Since the WFC observes waveforms directly, we need to calibrate the phase rotation in the circuit in order to obtain wave polarizations, wave normal vectors, and Poynting flux, precisely.

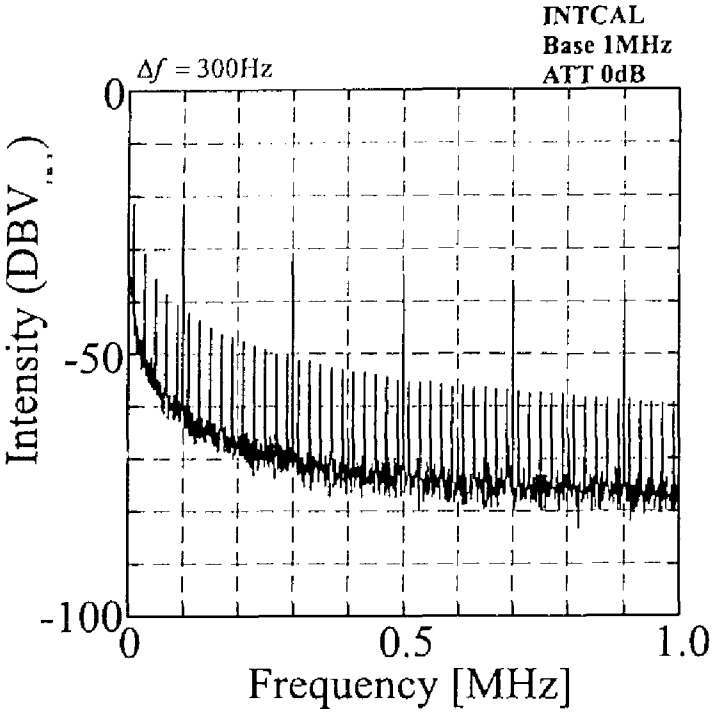

Figure 2.25: Example of the frequency spectrum of the onboard calibration signal.

2.7 Calibrations

2.7.1 Onboard calibration system

In order to obtain absolute values of the observed wave amplitude and the phase differences between the different field components, a signal calibration system is included in the PWI system. We use two types of calibration signals; one is a sinusoidal waveform of 100 Hz and the other is a composite signal of six rectangular waveforms. Since the SFA has a wide frequency range extending up to 800 kHz, the frequency components of the composite signal are designed to encompass this entire frequency range (all five bands of the SFA receivers). The fundamental frequencies of the six rectangular waveforms are 10 Hz, 100 Hz, 1 kHz, 10 kHz, 100 kHz, and 1 MHz. For more precise calibrations in the same frequency domain, they can be switched to their half frequency values by a telemetry command.

The calibration signal is supplied to all five sensors (both sets of dipole antennas and the tri-axial search coils) simultaneously. The calibration operation is initiated via a telemetry command. The start time of the calibration is synchronized with the timing of the frequency sweep in the SFA measurements and the time duration of the calibration signal is the same as one sweep period. The amplitude attenuation of the calibration signal can be changed from 0 to 60 dB in 20 dB step by telemetry commands. An example of the frequency spectra for the calibration signal is shown in Fig. 2.25.

For the analysis of SFA and MCA data, only the amplitude calibration is needed. However, for the WFC data, extremely precise measurements of both amplitudes and phase differences among the different field components are required. This is because the main objective in the analysis of the WFC data is to determine the wave vector, wave polariza-

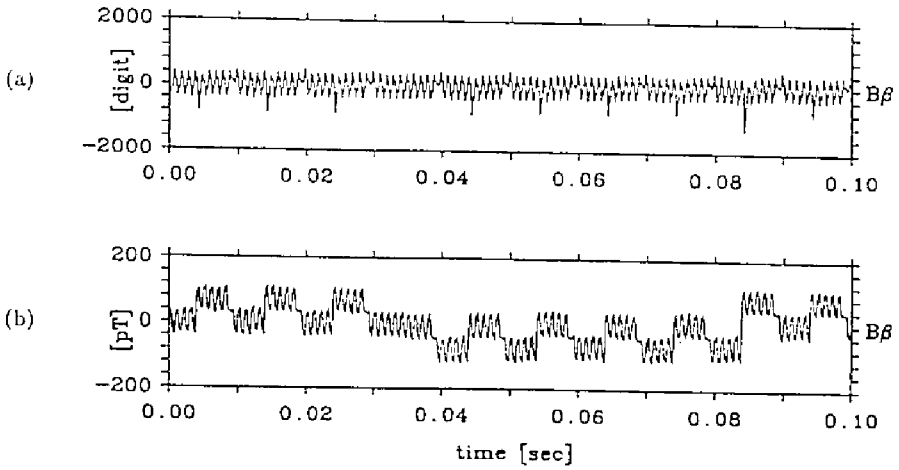

Figure 2.26: Waveforms of the onboard calibration signal received by the WFC. (a) Uncalibrated waveforms, and (b) Calibrated waveforms [*after Matsumoto et al.*, 1994a].

tion and Poynting flux of the observed waves as well as to estimate the sheath impedance formed around the WANT and PANT antennas. The waveform data stored in the memory must be restored to that of each component (E_U, E_V, B_α, B_β and B_γ) as measured at the respective sensor points using the appropriate transfer function. Although the transfer function obtained from preflight calibration data for each receiver circuit can be utilized for this purpose, there is a possibility that the instrument properties and hence the transfer function can change over times. Any temporal change in the transfer function will cause an erroneous estimation in the wave properties. Thus, in case of possible changes in the preflight transfer functions, in-situ calibrations are indispensable for the reliability of the data analysis.

An example of waveforms before and after the restoration using the preflight transfer function of the receiver circuit is shown in Fig. 2.26. The procedure used in restoring the waveforms is as follows: The telemetered waveform data is first transformed to frequency spectrum data using an FFT. The phase and amplitude in each frequency component are restored to those at the sensor point using the transfer function of the receiver circuit. The restored frequency spectrum is then transformed to the waveforms using an inverse FFT. The example in Fig. 2:26 shows the waveforms of a calibration signal imposed on a search coil (B_β axis) on October 13, 1992. Figure 2.26 (a) shows a waveform generated from the WFC telemetry data prior to applying the transfer function. The waveform data contain less low frequency components because of the transfer function of the search coil circuit shown in Fig. 2.17. Figure 2.26 (b) shows the waveform after the transfer function for the entire circuit (from the preamplifier to the WFC receiver) was taken into account in the restoration process. The processed waveform restores the data to the original known input waveform of the calibration signal.

Since the calibration signal is applied to the electric dipole antennas via a small resistance, the potential drop in the plasma medium can be neglected. On the other hand, by applying the calibration signal to the antenna elements via a large resistance, the potential drop in the plasma medium cannot be neglected. This is because the antenna impedance can

become comparable to the large value of the resistance used. Using this effect, the sheath impedance formed around the electric antenna elements can be estimated from differences in the amplitude and phase for two different values of the resistance. The equivalent circuits shown in Fig. 2.12 for the electric antenna when it is immersed in plasma are used to the estimate the antenna sheath impedances (Z_a in the figure) and the absolute value of the wave electric field.

2.7.2 Measurements of antenna impedance

In order to realize precise calibrations of electric field waves observed in space plasmas, we need to know the antenna impedance immersed in space plasmas. As well-known, in plasmas there exists various wave modes with various wave lengths. This means that the antenna impedance strongly depends on wave modes and their wave lengths. Therefore, we need to take account into the plasma dispersion relation $D(\omega, k)$ for theoretical calculations of antenna impedance.

The theoretical attempt to calculate the impedance of short dipole antennas immersed in ionospheric cold plasmas was initially conducted by *Balmain* [1964]. He showed that the antenna impedance drastically changes around the local electron plasma frequency f_{pe} and upper hybrid resonance frequency f_{UHR}. *Aso* [1974] extended the above theory by including effects of the ion sheath.

Based on the above theories, many rocket experiments were conducted to compare the theories with measurements in the ionosphere [*e.g., Oya and Obayashi*, 1966; *Ejiri et al.*, 1968; *Aso*, 1974] and they applied their results to the measurements of electron densities.

The above theories and results from rocket experiments are not simply applied to our results by Geotail plasma wave observations in the geomagnetic tail region, because the plasmas in the geomagnetic tail are much hotter than those in the ionosphere. Further, since plasma densities are much smaller than those in the ionosphere and electron Debye length is much larger, antenna impedance is strongly affected by the sheath surrounding antennas and photoelectrons. The progress of computer experiments these years allow us to calculate antenna impedance immersed in hot plasmas with arbitrary plasma parameters [*Yamashita*, 1998]. However, the calculation precision is not enough to apply the results to the practical observations in space from the restrictions in CPU power and capacities in computer memories.

It is very important to know the antenna impedance of Geotail in each observation region. Especially, in waveform observations conducted by the WFC, errors of the antenna impedance in the calibration process lead to artificial distortions of calibrated waveforms. However, as stated above, it is very difficult to obtain the theoretical antenna impedance of the Geotail. The Geotail PWI has the capability to obtain the antenna impedance of the WANT/PANT antennas using the onboard calibration system and the WFC receiver [*Matsumoto et al.*, 1994a; *Tsutsui et al.*, 1997]. *Tsutsui et al.* [1997] introduced the detailed procedure for obtaining the antenna impedance by using the PWI functions and detailed discussions about the results obtained from the observations.

Figure 2.27 shows the peripheral circuits of preamplifiers connected to the WANT/PANT antennas and circuits for the onboard calibration as well as the impedance Z_{a-a} between poles of each dipole antenna (i.e., WANT-A and WANT-B or PANT-A and PANT-B), and the impedance Z_{a-s} between each pole of a dipole antenna and spacecraft chassis.

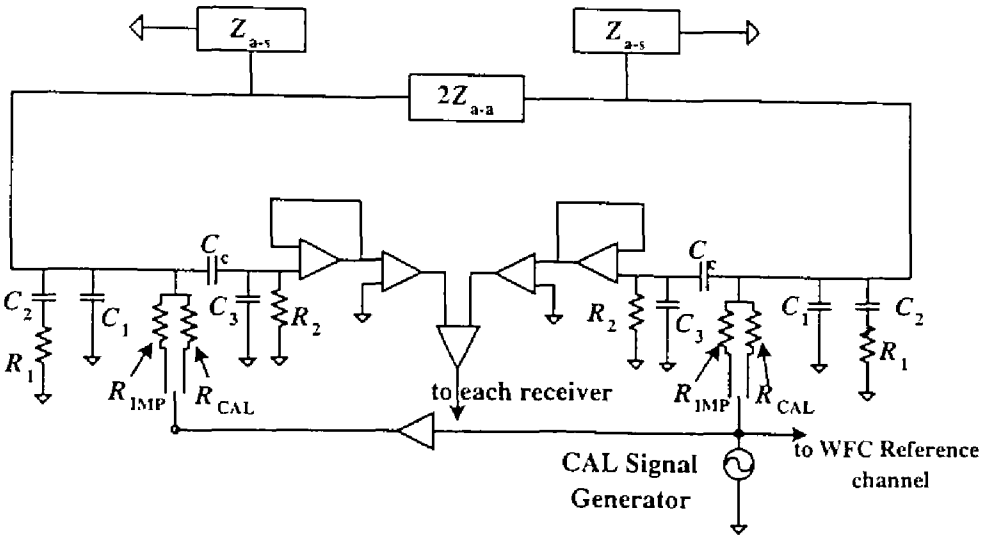

Figure 2.27: Basic block diagram for the principle of measuring the antenna impedance by the Geotail PWI.

The parameter descriptions and corresponding values are summarized in Table 2.4 and Table 2.5, respectively. The calibration signal as shown in Figure 2.25 is supplied to the preamplifiers through two different resistances R_{CAL} and R_{IMP} switched by telemetry commands. Further, simultaneously, the calibration signal is also directly supplied into one magnetic field channel of the WFC for the reference. We address the measurement mode, when R_{CAL} or R_{IMP} is selected, "CAL mode" and "Impedance mode," respectively. We calculated the antenna impedance Z_{a} (combination of $Z_{\mathrm{a-a}}$ and $Z_{\mathrm{a-s}}$) by comparing the WFC data obtained in CAL mode and IMP mode.

Figure 2.28 shows the circuit simplified by picking up one component of the symmetric circuit shown in Fig. 2.27. Additionally, the transfer functions of $G_{\mathrm{WFC}}(f)$ and $G_{\mathrm{REF}}(f)$ are inserted at the output of the preamplifiers, where $G_{\mathrm{WFC}}(f)$ and $G_{\mathrm{REF}}(f)$ mean that the

Table 2.4: Parameter descriptions in the front-end circuit of the preamplifiers

$Z_{\mathrm{a-a}}$	Impedance between each component of the dipole antennas
$Z_{\mathrm{a-s}}$	Impedance between one component of the dipole antennas and the chassis of the spacecraft
R_1	Resistance inserted between the PANT conductive shield and the chassis of the spacecraft
R_2	Input impedance of the preamps
C_1	Capacitance of a coaxial line
C_2	Capacitance of the conductive shield
C_3	Stray capacitance at the input of the preamps
C_{c}	Decoupling capacitance

Table 2.5: Parameter table of the WANT/PANT front-end circuits

Component	C_1	C_2	C_3	C_c	R_1	R_2	$R_{\rm CAL}$	$R_{\rm IMP}$
WANT	20 pF	645 pF	21 pF	220 pF	1 kΩ	200 MΩ	2 kΩ	5.1 MΩ
PANT	0	136 pF	16 pF	22 pF	0	3 GΩ	2 kΩ	20 MΩ

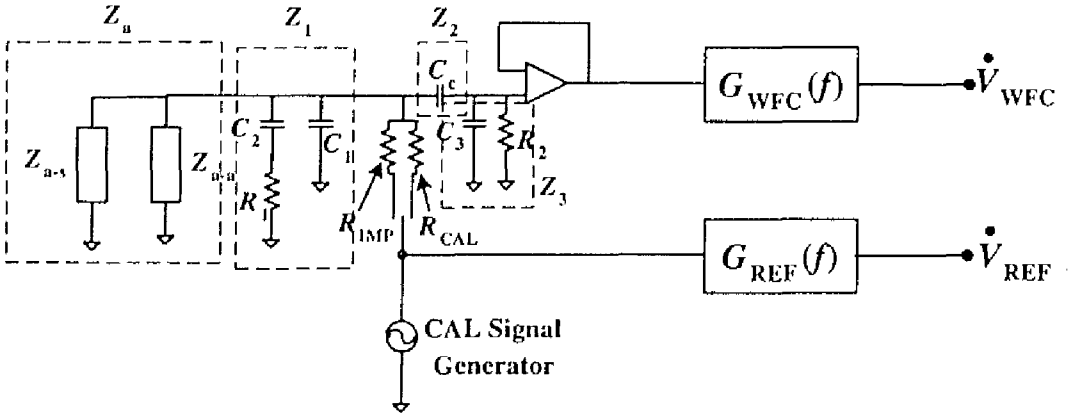

Figure 2.28: Simplified block diagram for the principle of measuring the antenna impedance by the Geotail PWI.

complex transfer functions of the WFC circuits including differential amplifiers shown in Fig. 2.27 and of the WFC reference circuit which the calibration signal is directly supplied into, respectively. $\dot{V}_{\rm WFC}$ and $\dot{V}_{\rm REF}$ denote the complex outputs of the calibration signals from the WFC and WFC reference circuits, respectively. Since the antenna impedance and response of the WFC circuits strongly depend on frequencies, we convert temporal waveforms obtained by the WFC into spectra and phase information in frequency space using the complex Fourier transformation in order to calculate the frequency dependence of the antenna impedance.

Further simplified circuit is shown in Fig. 2.29. $Z_{\rm a}$ is the antenna impedance which we need to know in our calibration process. In the CAL mode, the output of the WFC $\dot{V}_{\rm WFC-CAL}$ is calculated by

$$\dot{V}_{\rm WFC-CAL} = \frac{\dot{V}_{\rm s-CAL}}{(Z_{\rm a} \parallel Z_{\rm f}) + R_{\rm CAL}} \cdot G_{\rm WFC}(f), \tag{2.1}$$

where $Z_{\rm f}$ is defined by

$$Z_{\rm f} = (Z_2 + Z_3) \parallel Z_1. \tag{2.2}$$

$\dot{V}_{\rm REF-CAL}$ is simultaneously obtained as

$$\dot{V}_{\rm REF-CAL} = \dot{V}_{\rm s-CAL} \cdot G_{\rm REF}(f) \tag{2.3}$$

From Eq. (2.1) and Eq. (2.3), we remove $\dot{V}_{\rm s-CAL}$ and obtain

$$\dot{V}_{\rm WFC-CAL} = \dot{V}_{\rm REF-CAL} \cdot \frac{Z_{\rm a} \parallel Z_{\rm f}}{(Z_{\rm a} \parallel Z_{\rm f}) + R_{\rm CAL}} \cdot \frac{G_{\rm WFC}(f)}{G_{\rm REF}(f)}. \tag{2.4}$$

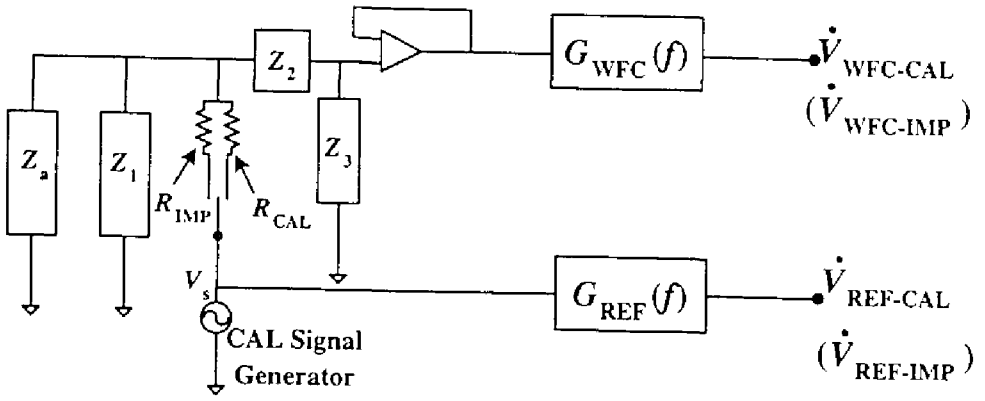

Figure 2.29: Further simplified block diagram.

Using the similar way, $\dot{V}_{\mathrm{WFC-IMP}}$ can be obtained as follow:

$$\dot{V}_{\mathrm{WFC-IMP}} = \dot{V}_{\mathrm{REF-IMP}} \cdot \frac{Z_{\mathrm{a}} \parallel Z_{\mathrm{f}}}{(Z_{\mathrm{a}} \parallel Z_{\mathrm{f}}) + R_{\mathrm{IMP}}} \cdot \frac{G_{\mathrm{WFC}}(f)}{G_{\mathrm{REF}}(f)}. \tag{2.5}$$

Using Eq. (2.4) and Eq. (2.5), we obtain

$$\frac{\dot{V}_{\mathrm{WFC-CAL}}}{\dot{V}_{\mathrm{WFC-IMP}}} = \frac{\dot{V}_{\mathrm{REF-CAL}}}{\dot{V}_{\mathrm{REF-IMP}}} \cdot \frac{(Z_{\mathrm{a}} \parallel Z_{\mathrm{f}}) + R_{\mathrm{IMP}}}{(Z_{\mathrm{a}} \parallel Z_{\mathrm{f}}) + R_{\mathrm{CAL}}}, \tag{2.6}$$

and we can calculate the antenna impedance Z_{a} as follow:

$$Z_{\mathrm{a}} = \frac{R_{\mathrm{IMP}} Z_{\mathrm{f}} - R_{\mathrm{CAL}} Z_{\mathrm{f}} \dot{V}_{\mathrm{R}}}{(Z_{\mathrm{f}} + R_{\mathrm{CAL}})\dot{V}_{\mathrm{R}} - Z_{\mathrm{f}} - R_{\mathrm{IMP}}}, \tag{2.7}$$

where

$$\dot{V}_{\mathrm{R}} = \frac{\dot{V}_{\mathrm{WFC-CAL}} \dot{V}_{\mathrm{REF-IMP}}}{\dot{V}_{\mathrm{WFC-IMP}} \dot{V}_{\mathrm{REF-IMP}}}. \tag{2.8}$$

Tsutsui et al., [1997] applied this method to calculate the antenna impedance in various regions of the magnetosphere. They found that the antenna impedance of the Geotail antenna forms an equivalent electric circuit consisting of a resistance and a capacitance connected in parallel. They also showed that the resistance value is easily changed by the ambient plasma density (see Fig. 2.30). In the present thesis, the calibration of the observed waveforms by the WFC is conducted by using representative values of the antenna impedance for each region of the geomagnetotail region.

2.7.3 Calibrations including the antenna impedance

In this section, we introduce the method of the calibration including the effect of the antenna impedance which is calculated by Eq. (2.7).

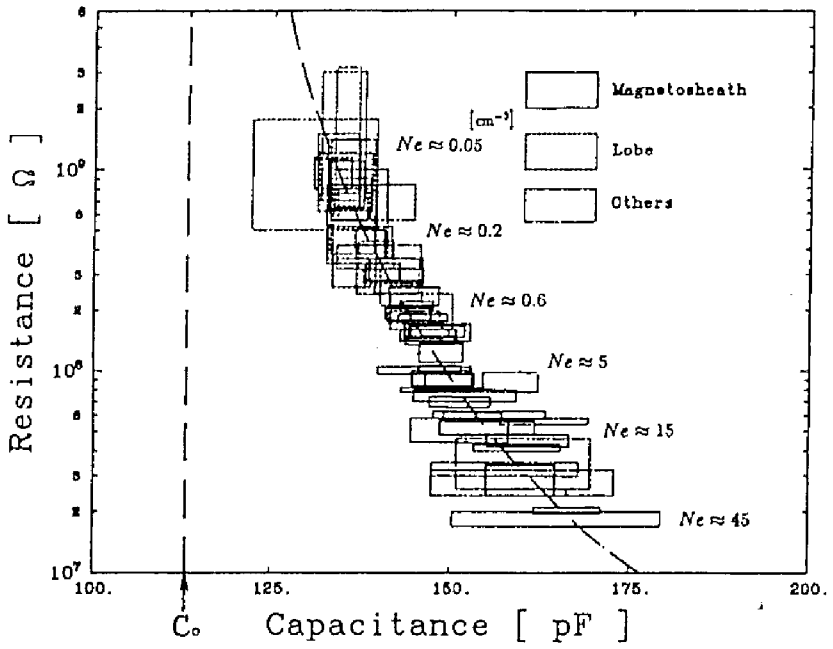

Figure 2.30: A quantitative relation between the resistance and capacitance values derived from WANT impedance measured by the 65 experiments conducted in the Earth's magnetosphere. The height and width between the facing sides of each rectangle indicate fluctuation ranges of the resistance and capacitance values, respectively. C_o, which is shown by the vertical dashed line, is the theoretical value for a linear dipole antenna with one element length of 50 m in a vacuum [*after Tsutsui et al.*, 1997].

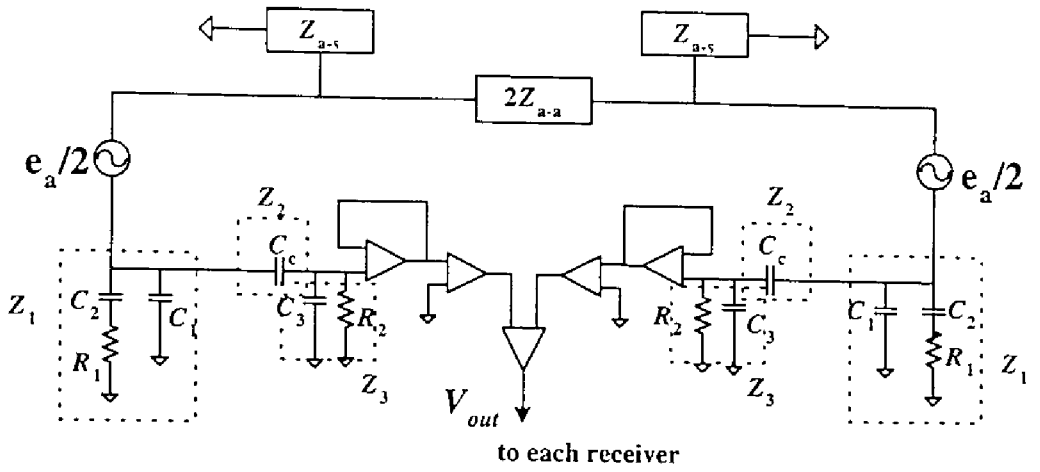

Figure 2.31: Block diagram for the principle of calibrations including the effect of the antenna impedance.

The telemetry data, which are sent back to the Earth, are the digital data. We need to convert these digital data to physical quantitative values, E (electric field) and B (magnetic field) as follows:

$$E(f) = G_{\text{preamp}}(f) \cdot G_{\text{receiver}}(f) \cdot V_{\text{A/D}}(f), \tag{2.9}$$

$$B(f) = G_{\text{sc}}(f) \cdot G_{\text{receiver}}(f) \cdot V_{\text{A/D}}(f), \tag{2.10}$$

where G_{preamp} and G_{sc} are the complex transfer functions of pre-amplifies of WANT/PANT including antenna impedance and of search coils, respectively. G_{receiver} is the transfer function of each receiver and $V_{\text{A/D}}$ mean telemetry values digitized by A/D converters (Note that in the case of the WFC data, we need to conduct Fourier transformation for getting $V_{\text{A/D}}(f)$ and also need the Inverse Fourier transformation for getting calibrated waveforms from $E(f)$ and $B(f)$.).

Among these transfer functions, G_{receiver} in each receiver and G_{sc} are already known from the ground tests before the launch. However, G_{preamp} is complicated, because it includes the effect of the antenna impedance. We need to change G_{preamp} depending on antenna impedance calculated by Eq. (2.7). Figure 2.31 shows the equivalent electric circuit of the preamplifiers and their peripheral circuits including antenna impedance. e_{a} is the voltage induced on the dipole antenna. The other parameters are described in Table 2.4 and Table 2.5.

Using Fig. 2.31, we can calculate effective electric fields from the output level (V_{out}) of the final differential amplifier as follows:

$$\begin{aligned} E &= \frac{e_{\text{a}}}{h_{\text{eff}}} \\ &= \frac{Z_1 + Z_2 + Z_3}{h_{\text{eff}} Z_1 Z_3} \left\{ Z_{\text{a-a}} \parallel Z_{\text{a-s}} + \frac{Z_1(Z_2 + Z_3)}{Z_1 + Z_2 + Z_3} \right\} V_{\text{out}}, \end{aligned} \tag{2.11}$$

where $h_{\rm eff}$ is the antenna effective height, which is theoretically expected to be 50 m. Thus we obtain $G_{\rm preamp}$ as

$$G_{\rm preamp}(f) = \frac{Z_1 + Z_2 + Z_3}{h_{\rm eff} Z_1 Z_3} \left\{ Z_{\rm a-a} \parallel Z_{\rm a-s} + \frac{Z_1(Z_2 + Z_3)}{Z_1 + Z_2 + Z_3} \right\}. \tag{2.12}$$

As stated in the previous section, *Tsutsui et al.* [1997] showed that $Z_{\rm a-a} \parallel Z_{\rm a-s}$ can be replaced by the parallel connection of resistance and capacitance $R \parallel C$, which are derived from the real and imaginary parts of $Z_{\rm a}$ in Eq. (2.7).

2.8 Electromagnetic compatibility (EMC)

2.8.1 Geotail EMC specifications

As shown in Fig. 2.13 and Fig. 2.18, the PWI sensors are significantly sensitive. Therefore, electrical noises emitted from spacecraft or onboard instruments cause severe pollution to the plasma wave observations by PWI receivers. The electrical noises from spacecraft have been also always problems for plasma wave observations in other spacecraft. We need to suppress the noise levels emitted from other instruments until launches of spacecraft. Even if it is impossible to do this, we need to identify noises emitted from spacecraft in order to avoid misunderstanding noises as natural signals.

In order to identify noise sources and to suppress identified noise levels, we have conducted the ElectroMagnetic Compatibility (EMC) tests during the ground tests before the launch. EMC is the ability of equipment and systems to function as designed without degradation or malfunction in its intended operational electromagnetic environment [*White*, 1981]. Geotail is the first Japanese spacecraft which the EMC tests were systematically conducted in.

EMC specifications are classified into 4 groups as follows:

CE: Conducted Emission EMC,

CS: Conducted Susceptibility EMC,

RE: Radiated Emission EMC, and

RS: Radiated Susceptibility EMC.

CE and CS are related to noise emissions on power lines and signal lines, and RE and RS are to noises radiated to free space. CE and RE are the specifications to noise sources and CS and RS are to target equipment (PWI in the present case). The study of the EMC has made progress in the military agencies in United States. They defined the military standard specifications (MIL-STD-461A) for EMC tests as shown in Fig. 2.32. We defined the Geotail EMC specifications referring to this MIL-STD-461A.

Figure 2.33 shows the Geotail EMC specifications, which we used for the Geotail EMC tests before the launch. We defined three types of specifications. They are: CE-01/03, RE-02, and RE-04. CE-01/03 is the same with that in MIL-STD-461A. RE-02 and RE-04 are decided referring to the sensitivities of each PWI receiver. Note that the levels specified

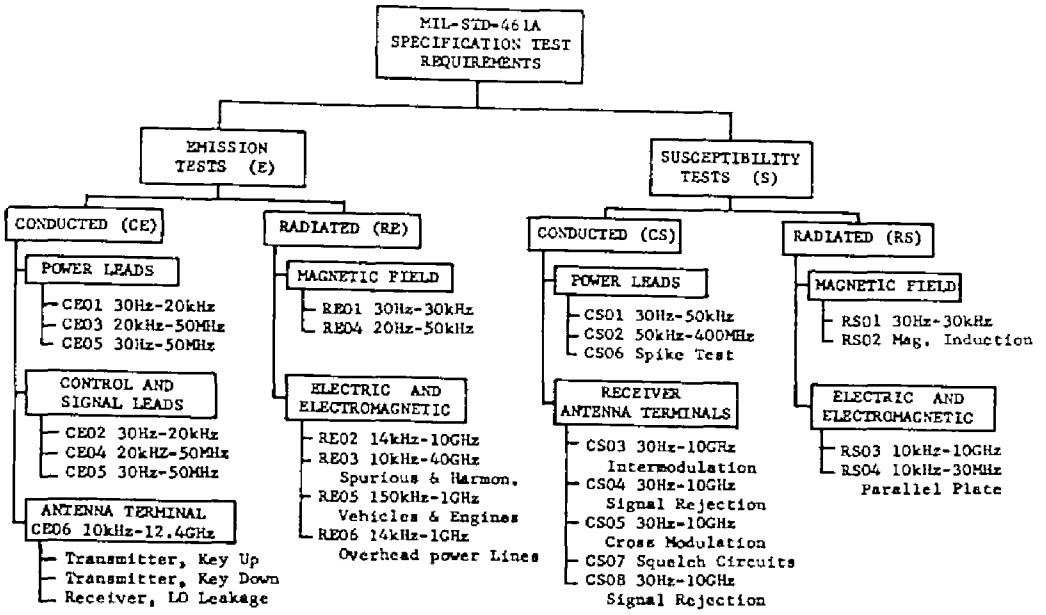

Figure 2.32: Military standard specifications (MIL-STD-461A) [*after White*, 1981].

in RE-02 and RE-04 are values observed at distances of 1 m and 60 cm from a specimen to a sensor, respectively.

All of the Geotail EMC tests were conducted in the magnetic shield spherical chamber with a diameter of six meters at ISAS (see Fig. 2.34). Simultaneously, the EMC tests for DC magnetic field measurements were also conducted by the Japanese MGF team. CE-01/03, RE-02, and RE-04 were measured by the current probe, monopole antenna and tri-axial search coils, respectively. Signals picked up by each sensor are fed to the EMC measurement system. The EMC measurement system consists of three types of spectrum analyzers. One is controlled by the EMC measurement software on the HP computer through the GPIB interface. In this system, collected data are stored on the inner harddrive. Other 2 are the individual spectrum analyzers for low frequency (< 10 kHz) and high frequency ranges (< 1000 kHz). Measurement system and connections of each sensor and spectrum analyzers are shown in Fig. 2.35 and Fig. 2.36.

Two different series were carried out in the Geotail EMC tests. They are "Individual EMC tests" and "System EMC tests." The objective of the Individual EMC tests is to check that each instrument is satisfied with the Geotail EMC requirements shown in Fig. 2.33.

In the individual EMC tests, we carried each instrument to be onboard Geotail into the electromagnetic shield room and conducted the measurements of CE-01/03, RE-02, and RE-04. If we find that the instrument is not satisfied with Geotail EMC specifications, we try to identify the noise sources and their emission mechanisms and to survey countermeasures. Figure 2.37 schematically shows the configuration of the Individual EMC tests in the magnetic shield chamber. The measurement configuration is very similar to that described in MIL-STD-461A [White, 1981]. Each instrument is put on the conductive aluminum plane which lies on the top of the wooden desk. NiCd battery is also located on the same aluminum plane and power is supplied to the instrument through the twisted-pair

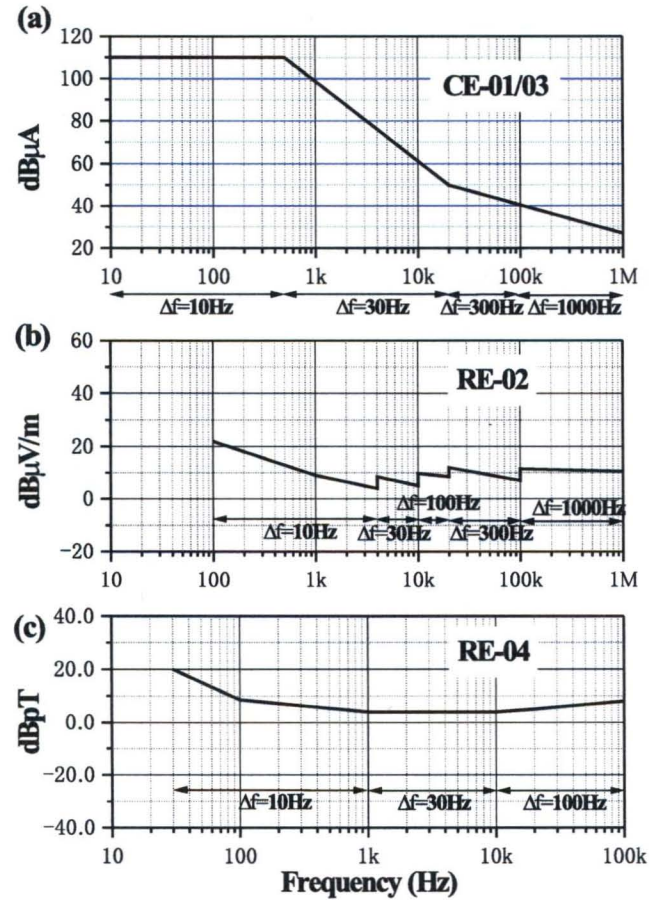

Figure 2.33: Geotail EMC specifications for (a) Conducted emissions, (b) Radiated emissions (electric field) and (c) Radiated emissions (magnetic field).

Figure 2.34: Magnetic shield chamber at ISAS.

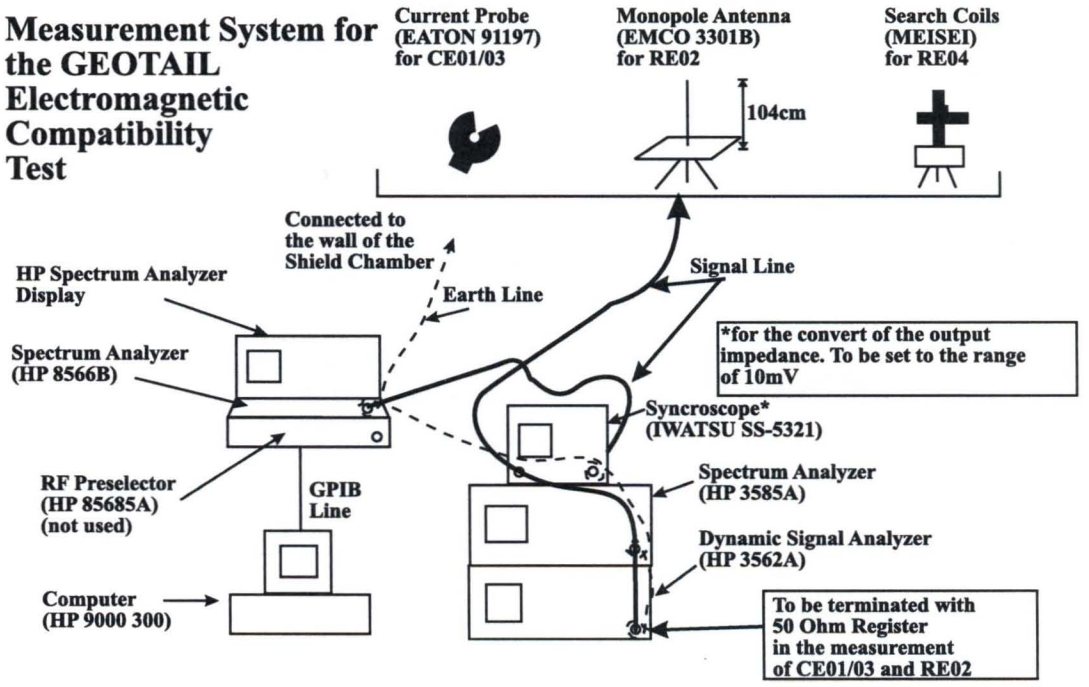

Figure 2.35: Connections of each sensor and spectrum analyzers.

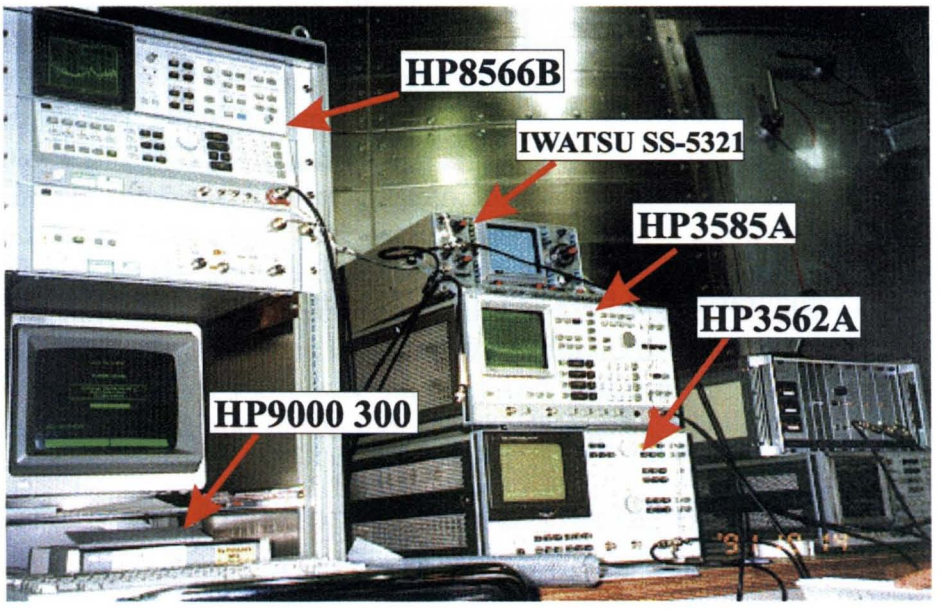

Figure 2.36: EMC measurement system.

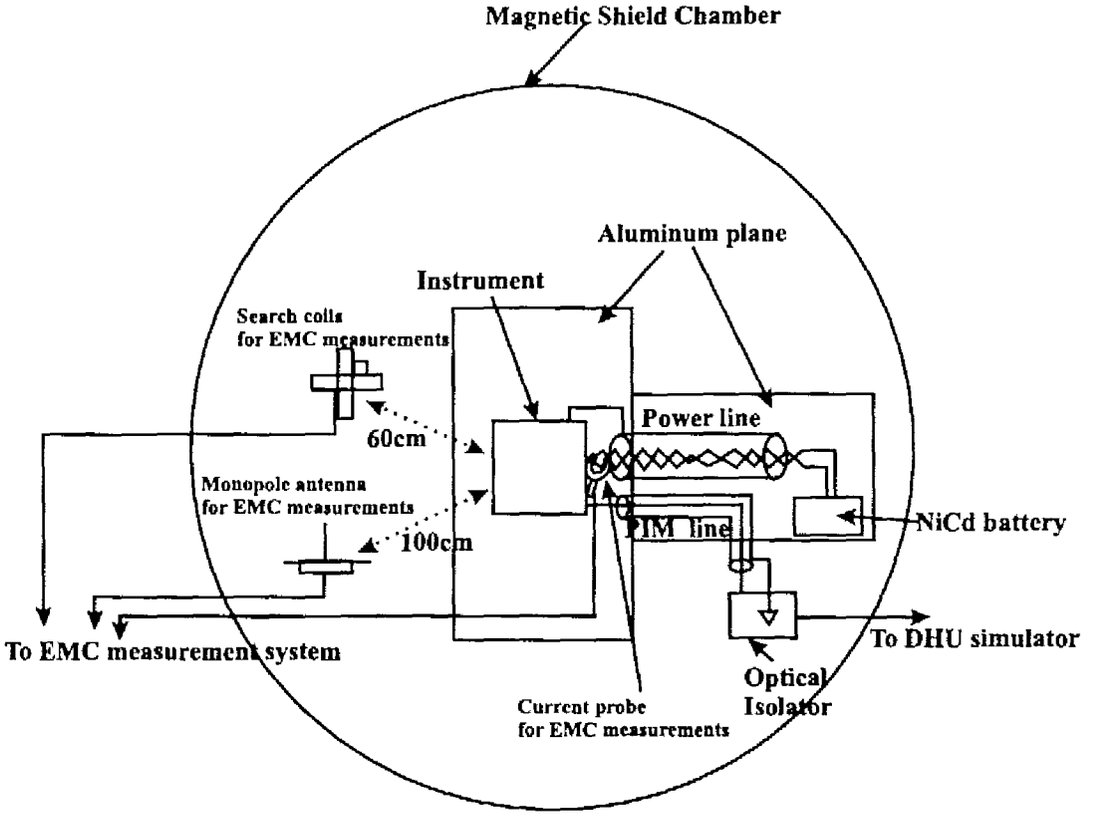

Figure 2.37: Configurations of the Geotail EMC tests in the magnetic shield chamber.

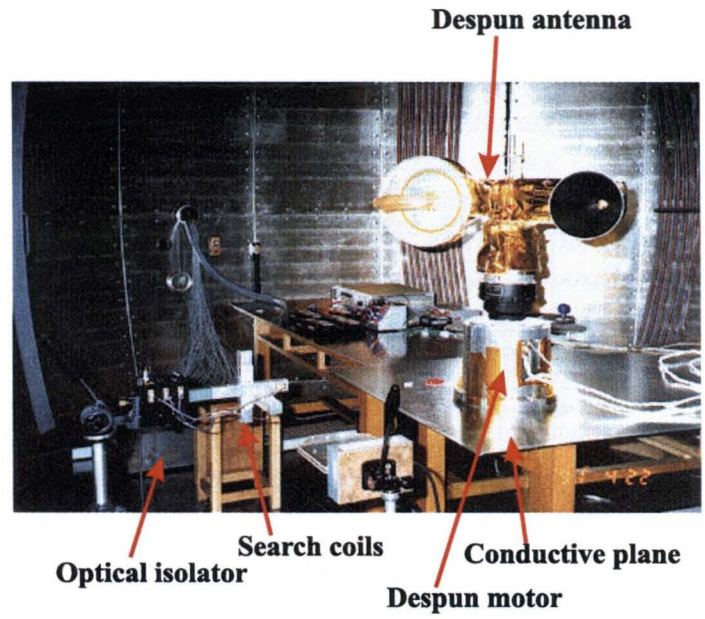

Figure 2.38: Example of the individual EMC test: Despan motor with the Despan antenna.

shielded cable. In order to monitor the status of each instrument and to send commands for changing its operation mode, the instrument should be connected to the DHU (Data Handling Unit) simulator and GSE (Ground Support Equipment). However, since we need to isolate the instrument from others outside the magnetic shield chamber, we insert the newly developed optical isolator between the instrument and the DHU simulator.

Figure 2.38 shows an example of the individual EMC test for the Despan motor with the Despan antenna. The Despan antenna consists of X-band and S-band high gain antennas. Since these antennas must point the Earth on the spinning spacecraft, the Despan motor despins two high gain antennas. Since the Despan motor is driven by pulse signals, we needed to check this drive system emits the noises. As shown in Fig. 2.38, the Despan motor is directly put on the aluminum plane, which is connected to the ground. Of course, the ground line of the NiCd battery is common on the conductive plane.

The system EMC is the test for measuring the emitted noise levels as the total of the spacecraft, therefore, the system EMC is conducted after the assembly completion of the spacecraft. The system EMC is very important in the sense of finding new noises as well as in confirming reduction of noise levels which are found in individual EMC tests, because routes of currents between the power supplies and each instrument are different between in the system EMC tests and in the individual EMC tests.

2.8.2 Strategies for suppressing artificial noises in spacecraft

Figure 2.39 shows an example of the results on the Geotail RE-02 specification which are measured in the individual EMC tests of the Magnetic field measurement instrument (MGF) [*Kokubun et al.*, 1994]. The monochromatic intense spectra of 12 kHz and its harmonics can be seen in panel (a). The fundamental frequency of 12 kHz is equal to the driving frequency of the MGF fluxgate magnetometer. Note that harmonics in the low

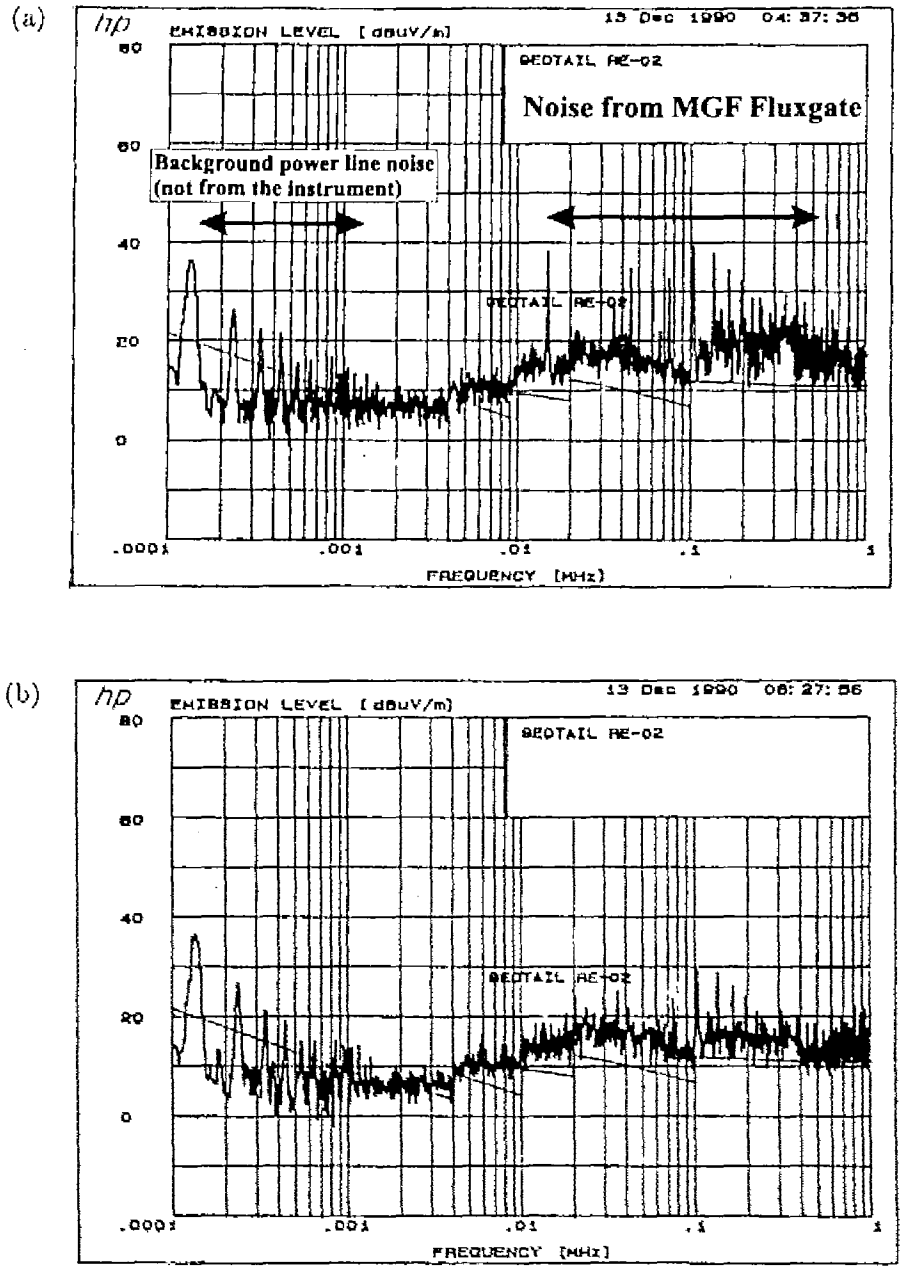

Figure 2.39: (a) Electric field noise emitted from the MGF fluxgate magnetometer. (b) The noise is suppressed by shielding the connectors of the fluxgate magnetometer.

frequency range from 100 Hz to 1 kHz are the background power line noise spectra, which are not emitted from the instrument.

When we found these noises, we suspected that signal lines between the MGF electric circuits and the fluxgate radiate such intense noises. However, since the signal lines are twisted and shielded, there were no radiations from the signal lines. Eventually, the radiation source is found to be the pins of the fluxgate sensor connector where the driving signal is fed from the MGF main circuit. After shielding the connector using the backshell, we found that the noise is significantly suppressed as shown in panel (b). In this case, the pins of connectors behave as a short dipole antenna. As shown in Fig. 2.39(a), even such a short dipole antenna causes severe pollution to the plasma wave measurement.

Figure 2.40 shows an example of the noise found in the individual EMC test on RE-04 for the Sun Aspect Sensor (SAS). The intense peak at 3.5 kHz is radiated from the DC-DC converter of the SAS. Note that the peaks at 9 kHz shown in panels (a) and (b) are not noise. They are the calibration signals radiated from the standard loop antenna.

Since a DC-DC converter has an oscillator in it, noises radiated from the oscillator are frequently problems in spacecraft EMC. In this case, as shown in the lower panel, the significant noise reduction is succeeded to cover the SAS chassis by μ-metal, which is familiar as shield of magnetic field noises

The most serious noise found in the Geotail EMC test is the PIM line noise. PIM stands for Peripheral Interface Module. The PIM lines are the signal lines between each instrument and the DHU. All of the instruments onboard spacecraft are connected to the DHU through these PIM lines. Observed data or status of each instrument are transferred through the PIM lines to the DHU. The commands transmitted from the Earth are transferred to each instrument from the DHU through the PIM lines. Thus, since bursty currents are on the PIM lines, if these currents are unbalanced between hot and return lines, intense magnetic field noises are radiated.

Figure 2.41 shows observed spectra of the PIM line noise (we pick up only PIM line noise by removing the background noise in this figure). The PIM line noise was not detected until the system EMC tests, because in the individual EMC tests, the relative locations of instruments and DHU and wiring configuration between them are different from those in the system EMC tests. Very intense discrete magnetic noises can be seen in Figure 2.41. These noises are caused by the unbalanced signal lines between the subsystem and the DHU. Figure 2.42 shows the connection and the route of signal currents among a subsystem, DHU and PCD. Here, the PCD stands for Power Converter and Distributor, which is the power supply to each subsystem. The problem is that the signal line between the subsystem and the DHU does not have its return line. Therefore, as shown in Fig. 2.42, the signal currents return through the return line of the power line. This means that huge current loops are formed through a subsystem, PCD, and DHU. This huge current loops cause the PIM noise shown in Fig. 2.41.

Tsutsui et al. [1992] analyzed the radiation level of the PIM noise by experiments and numerical calculations using the Finite Element analysis Method (FEM) and showed the radiated noise levels from the PIM lines are strongly affected by the eddy currents induced on conductive planes where the PIM lines are located. Based on their analysis results, we redesigned the configurations of the PIM lines on the spacecraft so that the current loop area by wiring the PIM line for each subsystem together with each power line as much as

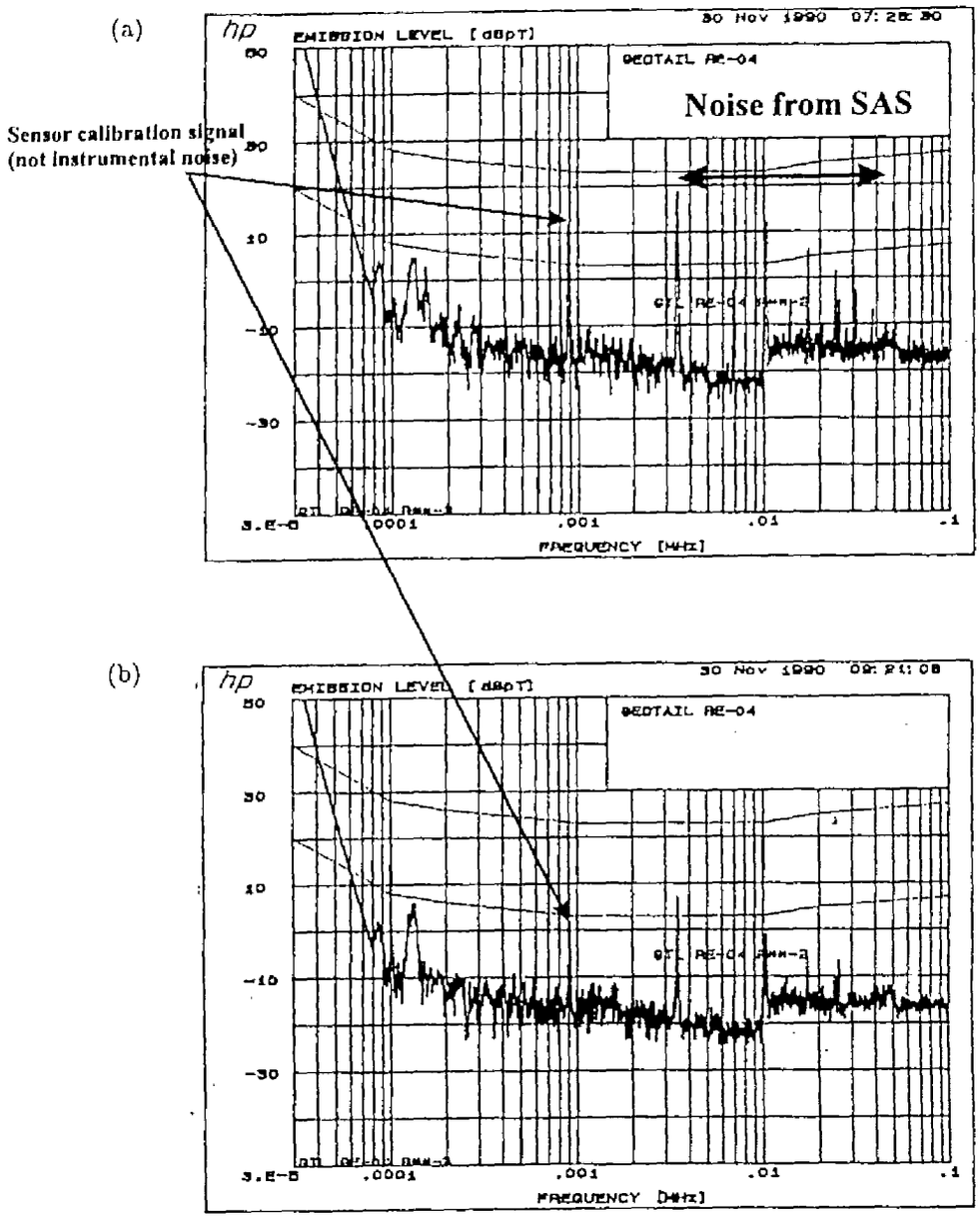

Figure 2.40: (a) RE-04 noise radiated from the DC-DC converter of the SAS. (b) Noise reduction by shielding the instrument with μ-metal. Note that the intense peaks at 9 kHz in both panels are the calibration signals radiated from the standard loop antenna.

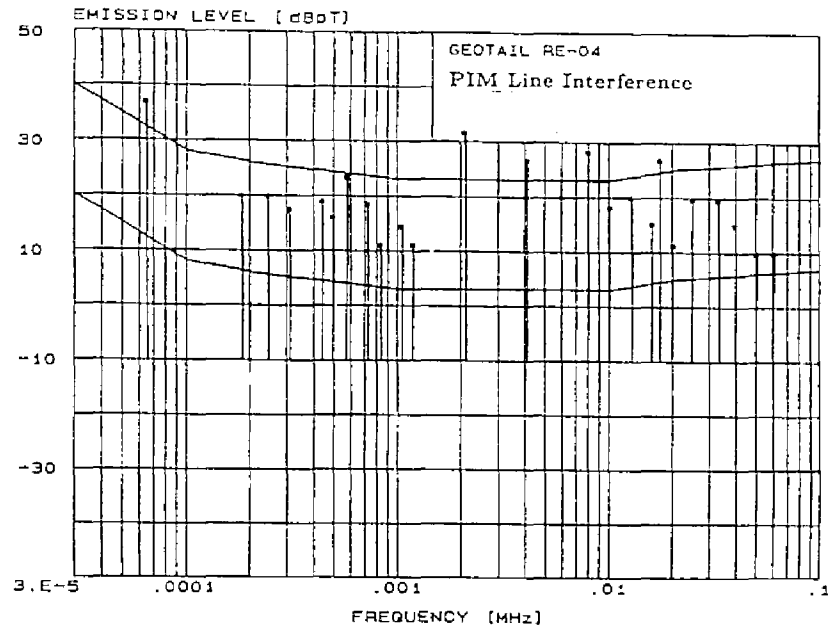

Figure 2.41: Intense magnetic field noise radiated from the PIM lines.

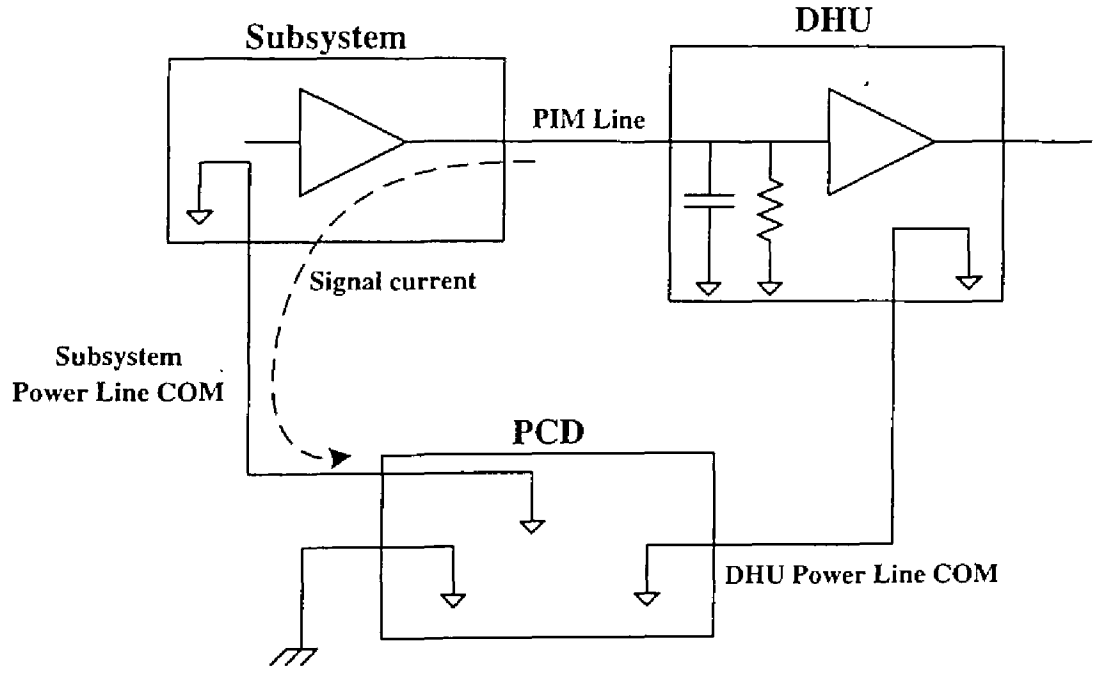

Figure 2.42: Connection and signal current route among a subsystem, DHU and PCD.

possible.

The Geotail EMC tests were conducted more than 100 times. We have succeeded to suppress many types of noises from instruments other than the above-mentioned noises. As mentioned in the beginning of this section, the Geotail is the first spacecraft which the EMC tests were systematically carried out in. We obtained important experiences and knowledge from the Geotail EMC tests. Based on the Geotail EMC tests, we could propose the detailed requirements for the noise reduction in the Mars probe mission called Nozomi, which was launched on July 4, 1998, during an initial phase of the spacecraft design. Followings are the EMC requirements proposed by the Low Frequency Analyzer (LFA) team of the Nozomi spacecraft in 1992.

1. The Low Pass Filter should be inserted between the output lines of the solar cells and the power distributor.

2. All of the power lines and signal lines should be wired in pairs of hot and return lines. They should be twisted and be shielded.

3. The power lines of the antenna deploy system should be connected to the ground after the completion of the antenna deployment.

4. The chassis of each particle sensor should be connected to the ground.

5. All of instruments should use the DC-DC converter with the same frequency oscillator.

6. Connectors with signal lines should be shielded by backshells.

Chapter 3

Plasma wave signatures in the magnetosphere

Plasma wave signatures provide an important clue for identifying the region where the spacecraft is located. Each characteristic region in the magnetosphere is associated with respective wave signatures, because peculiar wave-particle interactions take place in each characteristic region. By combining the density information obtained from the lower cut-off frequency of continuum radiation (CR) with the wave signatures, we can identify the distinct regions in the magnetosphere. In the present chapter, we introduce the plasma wave signatures in each region of the magnetosphere and show the way how we identify the region where the spacecraft is located.

3.1 Solar wind and electron/ion foreshock regions

The solar wind in the interplanetary space is one of the regions where the plasma wave activities are very low. In the nominal state of the solar wind, we observe only weak UHR noise around the local plasma frequency (~20 kHz). However, in the special case such as the encounter with the interplanetary shocks, a drastic change of the plasma wave activities is found. Detailed wave features in the encounter with the interplanetary shock will be discussed latter part of this chapter.

The terrestrial foreshock has been extensively surveyed by the previous spacecraft. It is now well known that the foreshock region is mainly classified into two different characteristic regions called the electron foreshock and the ion foreshock [*Gurnett*, 1985]. *Matsumoto et al.* [1997b] proposed a further division of the electron/ion foreshock regions based on the GEOTAIL low energy particle and plasma wave observations as shown in Figure 3.1. Figures 3.2 and 3.3 show examples of the frequency-time spectrogram observed in the electron and ion foreshock regions, respectively. The proposed subregions are also displayed on the top bar and its color captions in each figure. The spacecraft location and its relative relation to the IMF direction are shown in the upper-right panels.

Matsumoto et al. [1997b] classified the electron foreshock into 3 characteristic subregions. They are: Fast electron beam region; Slow electron beam region; and Electron heat flux region (see Fig. 3.1). The fast electron beam region is characterized by strong Langmuir waves (~ 25 kHz) associated with enhanced low frequency waves below 200 Hz. They

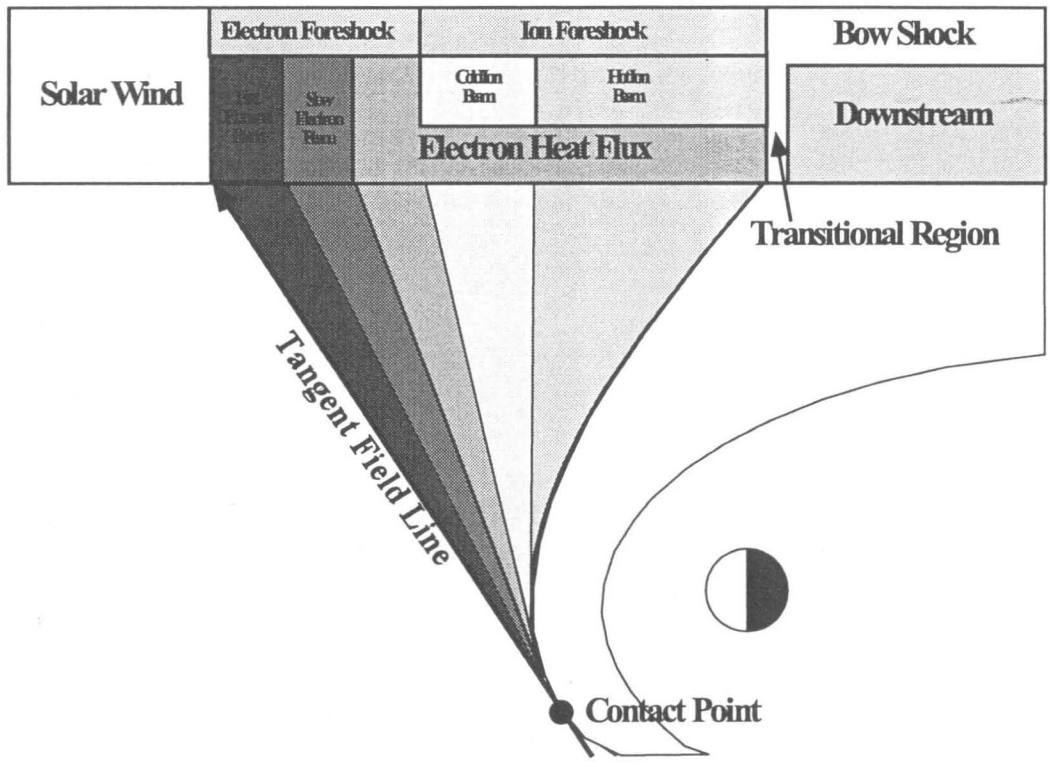

Figure 3.1: Subregions of the foreshock region, which are proposed based on the plasma wave and plasma measurements [*after Matsumoto et al.*, 1997b].

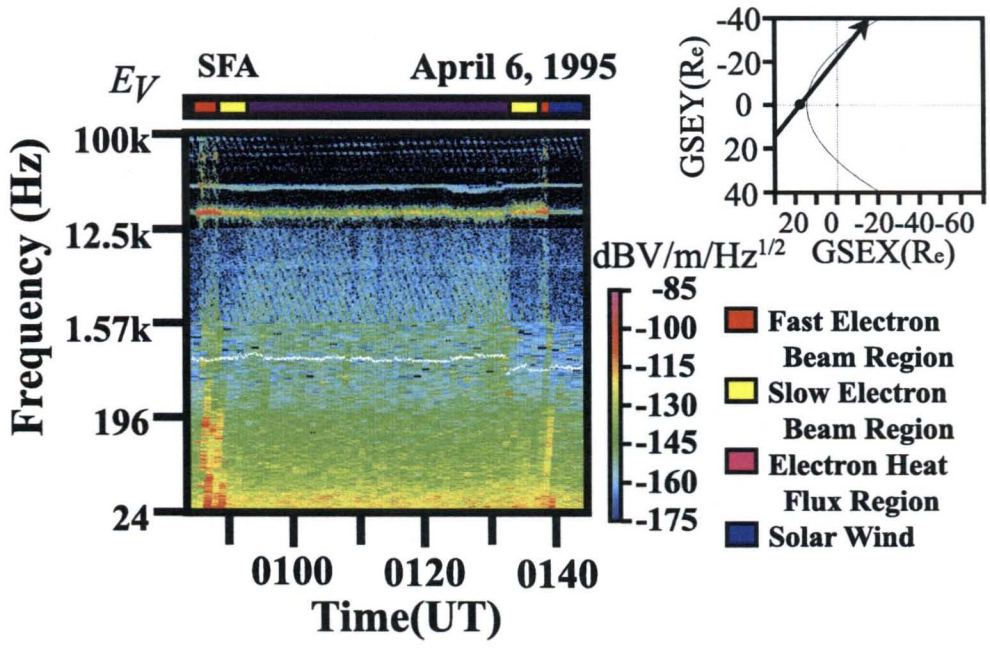

Figure 3.2: Frequency-time spectrogram observed in the electron foreshock. Equivalent subregions are shown in the top panel. The representative wave signature of the electron foreshock is the intense electron plasma waves [*after Matsumoto et al.*, 1997b].

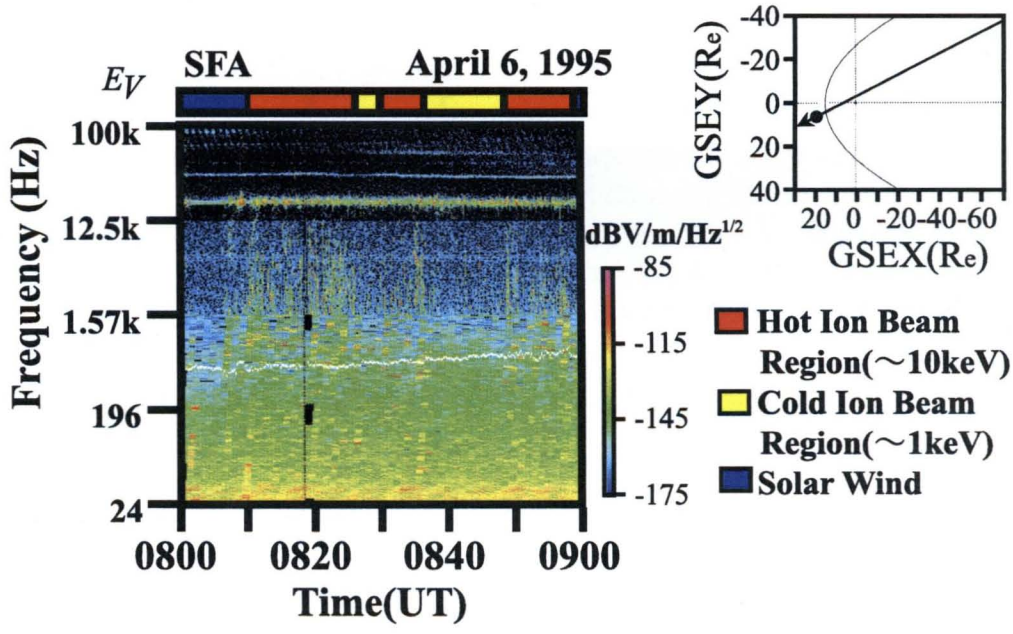

Figure 3.3: Frequency-time spectrogram observed in the ion foreshock. Equivalent subregions are shown in the top panel. The representative wave signature of the ion foreshock is the ion acoustic-like wave [*after Matsumoto et al.*, 1997b].

are excited by electron beams running along the tangent field line which contacts the bow shock. In the slow electron beam region, we see weaker Langmuir waves but see no wave activities below the electron plasma frequency. In the electron heat flux region, we do not find well-defined electron beams, however, there exists a high energy tail with higher temperature in the electron distribution. As shown in Figure 3.2, the electron heat flux region is characterized by weak Langmuir waves and simultaneous weak waves from below 10 Hz up to approximately 20 kHz.

Figure 3.3 is a similar plot to Figure 3.2 for the ion foreshock. The subregion in the ion foreshock proposed by *Matsumoto et al.* [1997b] (see Fig. 3.1) are hot and cold ion beam regions, which are displayed by the horizontal color bar in the top of Fig. 3.3.

In Figure 3.3, we find patchy red or yellow dots. They are very similar to the NEN emissions observed in the magnetosheath and in the tail lobe region, which will be focused on in Chapters 6 and 8. The patchy spectra suggest the quick change of the wave frequency and its intensity relative to the sweep periods of the SFA. The difference between waves in the hot and cold ion regions is the uppermost frequency of these waves. In the hot ion beam region it reaches approximately 10 kHz or more, while in the cold ion beam region, it is below 1 kHz.

3.2 Bow shock

Gurnett [1985] gave a good review of the plasma wave signatures around the bow shock. He pointed out that the bow shock transition layer is characterized by an abrupt burst of electric and magnetic wave components associated with the jump of the ambient magnetic field. *Matsumoto et al.* [1997b] showed further detailed plasma wave structures in the bow shock using the GEOTAIL PWI data.

Figure 3.4 shows a typical wave spectrum observed in the vicinity of the bow shock by GEOTAIL. The spacecraft experienced the bow shock crossings six times (displayed by blue arrows) during the 2 hour period. The intense broadband emission up to 12 kHz seen in the electric field component (upper panel) indicates the bow shock crossing followed by the entry into the downstream region. The edge of such broadband emissions corresponds to the timing of the bow shock crossing. The wave intensity in the downstream of the transition region is almost constant in the frequency range from about 200 Hz to 2 kHz. It is, however, weakened as the distance from the bow shock increases in the frequency range from 5 Hz to about 200 Hz.

The magnetic field components of waves are also enhanced in the bow shock and downstream regions. Especially in the bow shock transition, their uppermost frequencies reach the local electron cyclotron frequency which is shown by the white solid line, while in the downstream region, they remain below 100 Hz and seem to be similar to the MNB spectra.

Matsumoto et al. [1997b] performed the waveform analyses on the plasma waves observed in the vicinity of the bow shock. They showed that in the ramp of the magnetic field of the bow shock both ESW and EQMW types of waveforms are observed and that their wave features rapidly change in a short time scale of a few msec.

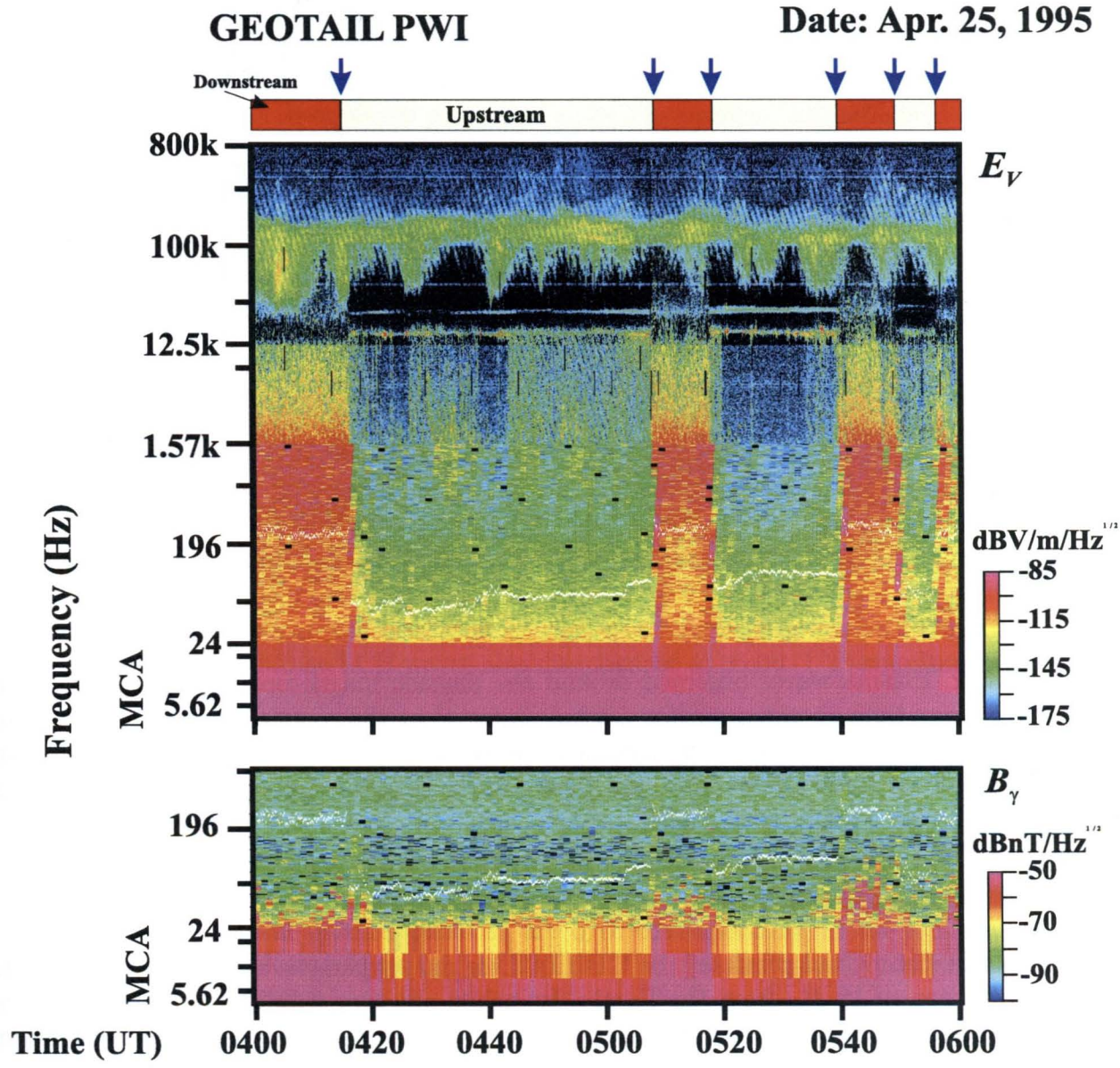

Figure 3.4: Plasma wave signatures in the bow shock crossing. The transition timings of the bow shock are indicated by arrows in the top panel [*after Matsumoto et al.*, 1998].

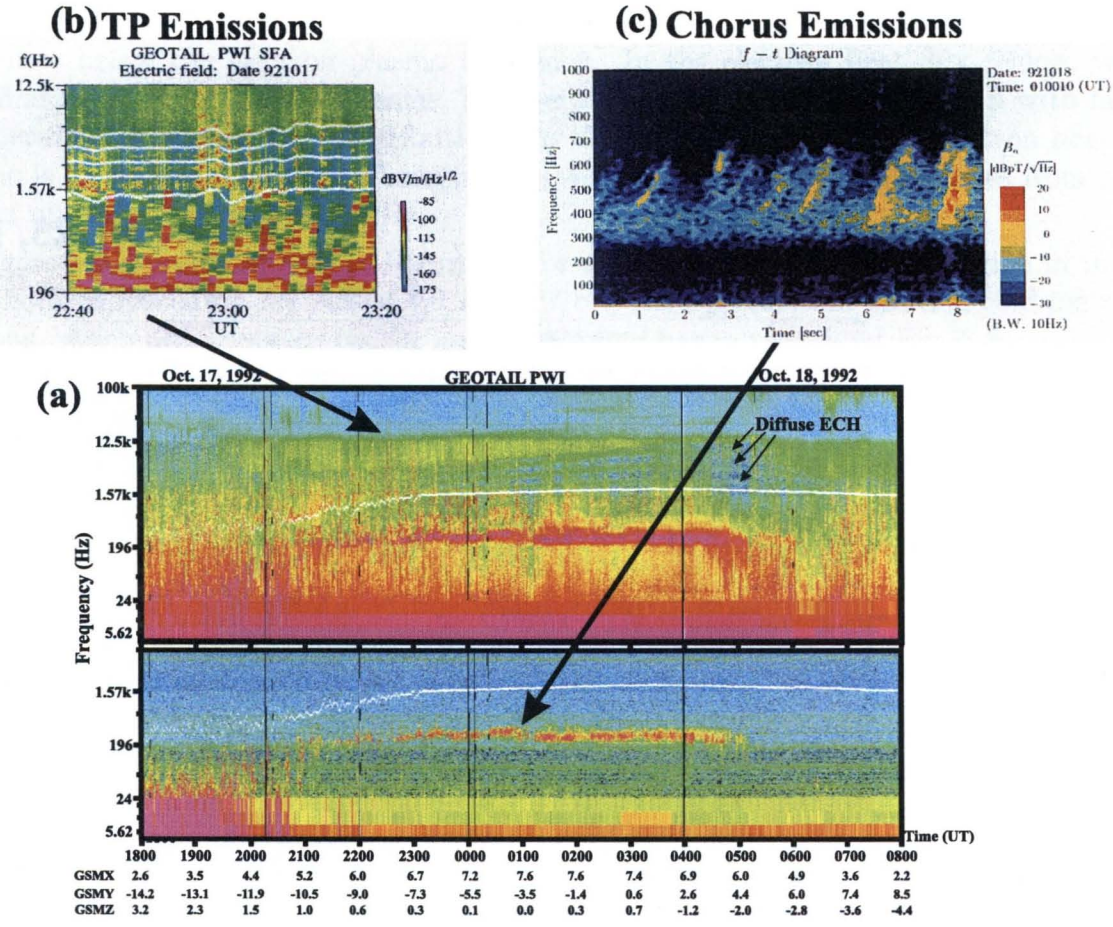

Figure 3.5: Plasma waves observed around the dayside magnetopause. (a) Overview of the frequency-time spectrogram for a whole interval of the magnetopause skimming [*after Matsumoto et al.*, 1998]. (b) Detailed spectra of the Totem Pole emissions (Bursty ECH emissions) [*after Matsumoto and Usui*, 1997a]. (c) Spectral structure of the chorus emissions [*after Nagano et al.*, 1996].

3.3 Dayside outer magnetosphere

During the distant tail phase of the GEOTAIL orbit, its perigee was located around the dayside region of 10 R_E from the Earth. Its orbits are very suitable for the observation of the outer magnetosphere on the dayside and occasionally provided chances of skimming the dayside magnetopause.

GEOTAIL experienced its first dayside magnetopause skimming on October 17-18, 1992. The spacecraft moved from the dawn side of the northern hemisphere to the dusk side of the southern hemisphere. Figure 3.5 (a) shows the frequency-time spectrogram observed in this first magnetopause skimming.

The gradual increase of the electron cyclotron frequency indicated by a white line shows that the spacecraft moved into the magnetosphere during the interval from 20:00 (UT) on October 17 to 05:00 (UT) on October 18. We find bursty electromagnetic waves below 200 Hz during the interval from 18:00 (UT) to 20:40 (UT) (see B component). These low

frequency electromagnetic waves indicate that the spacecraft was located in the magnetosheath region. They are switched on and off repeatedly, which suggests that the spacecraft repeatedly crossed the magnetopause and moved in and out of the magnetosphere several times.

The wave activities in the dayside outer magnetosphere are characterized by the chorus emissions and electron cyclotron harmonic waves. The electromagnetic waves with the frequency range of 200 Hz to 500 Hz observed in the interval from 20:40 (UT) to 05:00 (UT) shown in Fig. 3.5 (a) are the chorus emissions. The detailed structure can be seen in Fig. 3.5 (c). We can see the structure of chorus emissions with rising tone. *Nagano et al.* [1996] showed that these waves propagate along the ambient magnetic field and pointed out that their source region is located around the magnetic equator of the dayside region. The chorus emissions disappear around 05:00 UT and in turn the broadband electrostatic emissions start to appear in the E-component. This fact suggests that the spacecraft moved into the plasma sheet region around 05:00 UT.

The electron cyclotron harmonic (ECH) waves observed in the dayside outer magnetosphere are classified into the bursty ECH waves and the diffuse ECH waves, as discussed in the previous chapter. The bursty Totem Pole emissions (TP emissions) were repeatedly observed during the interval from 21:30 (UT) to 23:00 (UT) [*Matsumoto and Usui*, 1997a]. The frequency spectra of the TP emissions are shown in Fig. 3.5 (b). The bursty harmonic structures are the TP emissions. Based on the statistical analyses, *Usui et al.* [1997] showed that while the diffuse ECH waves broadly appear along the dayside magnetopause, the TP emissions are mainly observed at the dawnside region near the magnetopause. Further, *Usui et al.* [1998] examined the correlation of the TP emissions and plasma measurements in order to identify their generation mechanism.

The diffuse ECH waves were continuously observed during the period from 20:50 (UT) to 05:00 (UT). This diffuse ECH waves also disappeared at 05:00 (UT) simultaneously with the chorus emissions.

3.4 Magnetosheath

The magnetosheath is characterized by very high activities of plasma waves. Typical plasma wave activities in the magnetosheath are represented by BEN, NEN, electron plasma waves, and MNB. The typical plasma densities are 5/cc corresponding to the CR lower cutoff frequency (electron plasma frequency) of 20 kHz. The detailed waveform observations will be discussed in Chapter 8.

Figure 3.6 shows a representative frequency-time spectrogram generated from the SFA data observed in the magnetosheath at (GSM X, GSM Y, GSM Z) = (-86, 39, 1.0 R_E). The above mentioned typical waves are denoted by white arrows in the figure.

The BEN spectra observed in the magnetosheath are very similar to those in the PSBL except its uppermost frequency. Though the uppermost frequency of the PSBL BEN always reaches the local electron plasma frequency ($\sim$ 2 kHz), the frequency of the magnetosheath BEN almost always stays at much lower than the local electron plasma frequency ($\sim$ 20 kHz). This is also proved by the waveform observations of the BEN (see Chapter 8).

On the other hand, the magnetosheath NEN has similar features to the lobe NEN. The interesting point, however, is that the ratio of the local electron plasma frequency and

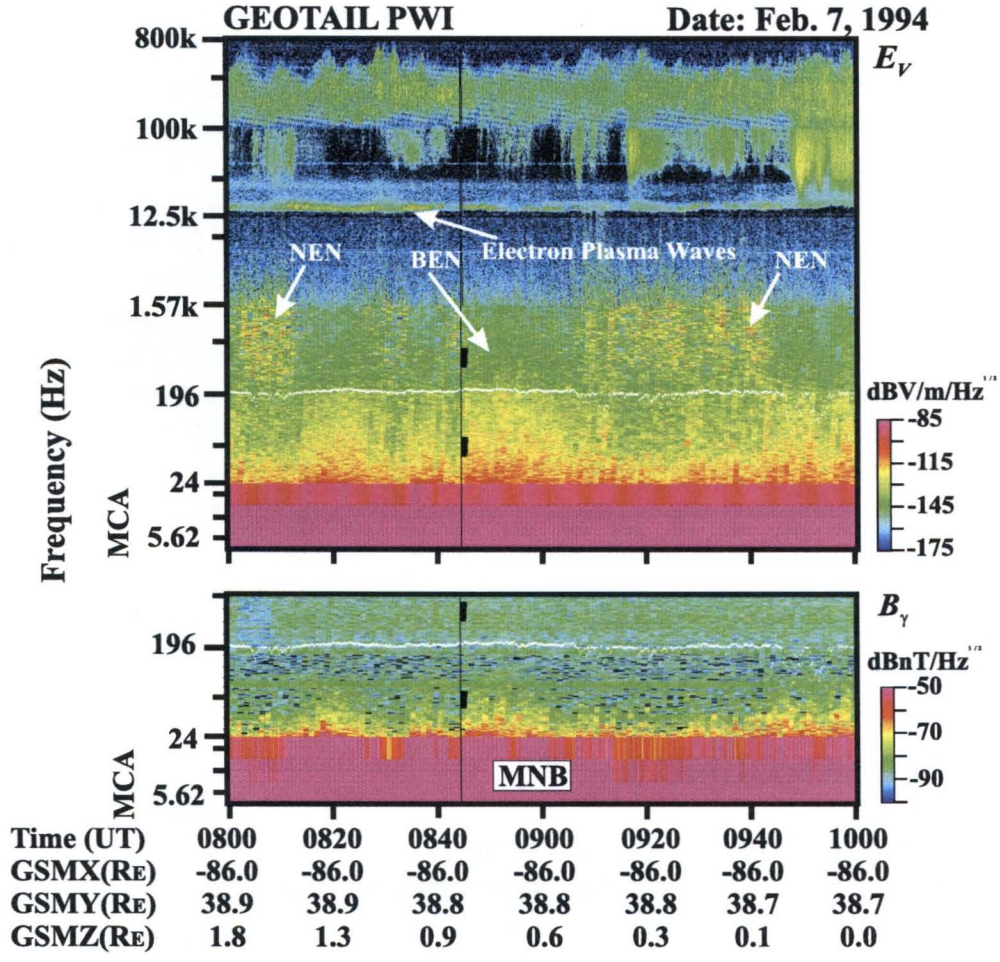

Figure 3.6: Typical plasma wave signatures observed in the magnetosheath region [*after Matsumoto et al.*, 1998].

the center frequency of the NEN in the magnetosheath is almost equal to that of the NEN in the lobe. The typical center frequencies (f_{NEN}) of the NEN in the lobe and in the magnetosheath are 200 Hz and 2 kHz, respectively. Since the typical electron plasma frequencies (f_{pe}) in both regions are 2 kHz and 20 KHz respectively, we find that the ratio (f_{pe}/f_{NEN}) is almost equal to 10. As we have shown in Chapter 8, the waveform characteristics of the NENs in the lobe and in the magnetosheath are very similar to each other. The above observations suggest generation mechanisms of the NENs in the lobe and the magnetosheath are the same or similar.

We will discuss the electron plasma waves observed in the lobe region in Chapter 7. Our waveform observations of electron plasma waves in the lobe region show that they are continuous waves but are strongly modulated in amplitude. Further, we will show that they include both Langmuir waves and ECH waves. The separation of these two waves can be done only by the polarization analysis based on the high time waveform observations, because the UHR frequency is too close to the electron plasma frequency in the lobe region (see detailed discussions in Chapter 7). This situation is similar in the magnetosheath. In order to identify the plasma wave mode of the electron plasma waves observed in the magnetosheath, we need to consult the waveform observations. However, unfortunately, the frequencies of the electron plasma waves in the magnetosheath are normally higher than 4 kHz which is the upper limit frequency of the GEOTAIL WFC. This prevents us to identify the wave mode in the magnetosheath.

The MNB is the most useful wave signature for the identification of the magnetosheath. It can be clearly seen in the magnetic component (lower panel) of Figure 3.6. The MNB is observed in the upstream and downstream of the bow shock as well as in the magnetosheath. The upper frequency of the MNB occasionally reaches the local electron cyclotron frequency, and its lower frequency limit is well below the lowest observable frequency (5.62 Hz) of the PWI.

3.5 Magnetopause boundary

In the view point of the plasma wave signatures, we can classify the magnetopause and its boundary layer into 3 types. They are: Type 1: Magnetopause with a wide and smooth boundary layer, Type 2: Magnetopause with a thin and sharp boundary layer, and Type 3: the low latitude boundary layer (LLBL) in the near tail. Typical wave signatures in these 3 types of the magnetopause boundary are shown in Figures 3.7 and 3.8. The frequency-time spectrogram shown in Figure 3.7 illustrates the above mentioned first two kinds of the typical magnetopause and its boundary. In this figure, we can easily identify the clear magnetopause crossings in 2 intervals from 00:48 to 00:55 (UT) and from 01:35 to 01:40 (UT) judging from the rapid drop or rise of the plasma frequencies and the change in the magnitude of the ambient magnetic field, which is indicated by the change of the electron cyclotron frequency shown by the white solid line. Further, the low frequency MNB indicates that the spacecraft stayed in the magnetosheath during the periods from 00:00 to 00:48 (UT) and from 01:35 to 02:00 (UT).

Two magnetopause crossings displayed in Figure 3.7 have the different features in the time scale. In the first crossing, the spacecraft passed through the magnetopause boundary layer in 15 minutes. The gradual decrease of the CR lower cutoff frequency and the gradual

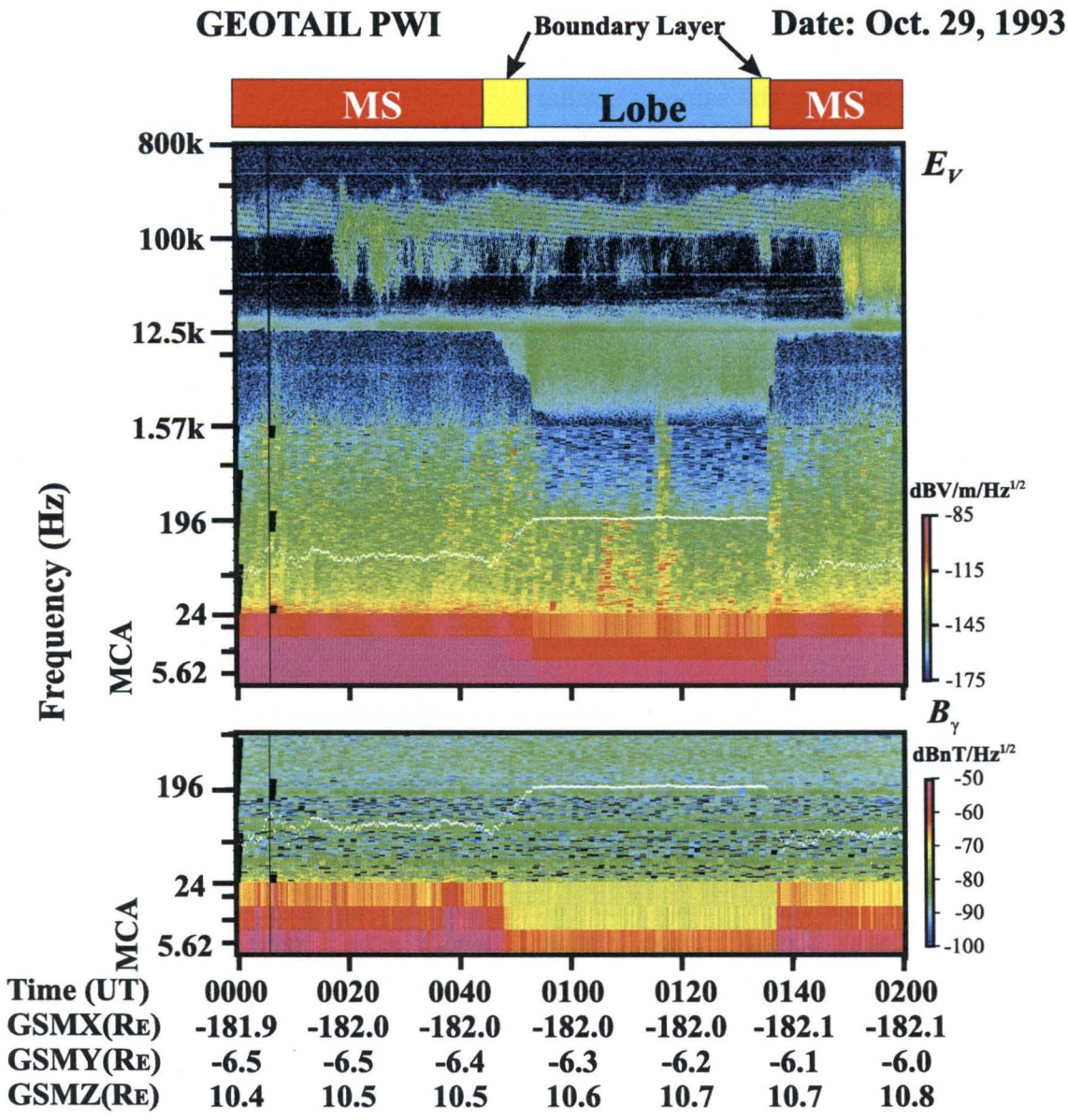

Figure 3.7: Magnetopause crossings of the type 1 and 2. Judging from the time variation of the CR lower cutoff frequency, and of the electron cyclotron frequency displayed by white lines, the spacecraft experienced the very smooth magnetopause crossing (type 1) around 00:55 (UT), while the abrupt magnetopause crossing (type 2) can be observed around 01:38 (UT) [*after Matsumoto et al.*, 1998].

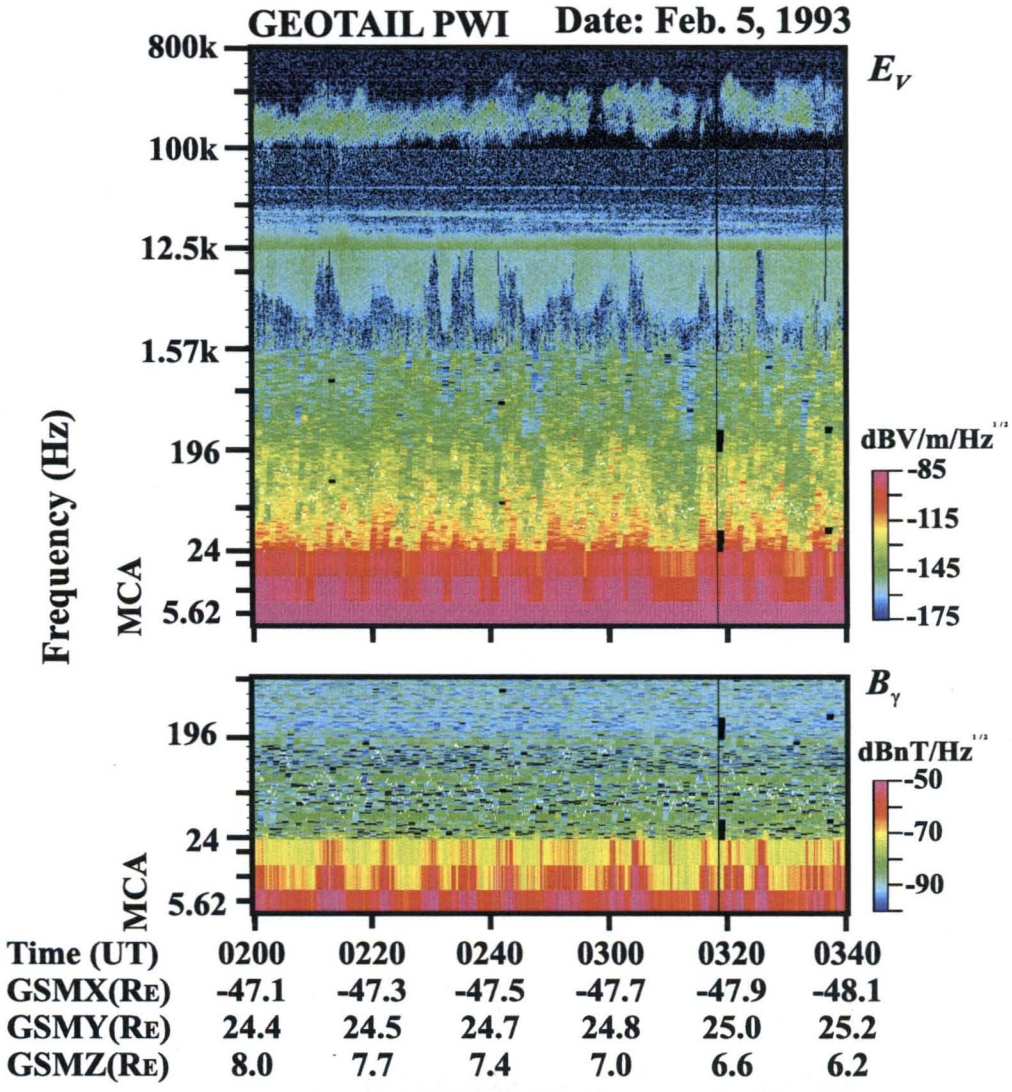

Figure 3.8: Magnetopause crossing of the type 3. We can find that the local plasma density changes repeatedly from the time variation of the CR lower cutoff frequency. Consulting the time variation of the ambient magnetic field, and of the plasma temperature, we conclude that the spacecraft moved around between the plasma sheet and Low Latitude Boundary Layer (LLBL) [*after Matsumoto et al.*, 1998].

increase of the cyclotron frequency from 00:48 to 00:55 (UT) show that the spacecraft moved into the lobe region through the magnetopause boundary layer of Type 1.

On the other hand, in the second crossing, the spacecraft moved back to the magnetosheath through the Type 2 magnetopause boundary. Although the time difference between the first and second cases is only 30 min, we find that the spacecraft moved across the magnetopause boundary in the second crossing more quickly than in the first crossing. The passage time in the second crossing is only one or two minutes. The time difference can be clearly seen in the difference of the time change of the CR lower cutoff frequency around 00:55 (UT) and around 01:38 (UT). Since the velocity of the spacecraft is negligible relative to the dynamic motion of the tail structure, the following two hypotheses can be inferred to explain the time scale difference between these 2 events. (1) The speed of tail flapping or oscillation motions changed during the interval between the 2 crossings. (2) The thickness of the magnetopause boundary is different at the 2 different locations through which the spacecraft passed.

The GEOTAIL PWI occasionally observes such events with different features during a short period as the spacecraft passes through the magnetopause. Unfortunately, since the single spacecraft observation cannot distinguish between the temporal and spatial phenomena, we need to wait for the multiple spacecraft observations in the future to verify the above two hypotheses.

Figure 3.8 shows the third type of the magnetopause crossing observed at (GSM X, GSM Y, GSM Z) = (-48, 25, 7 R_E) on February 5, 1993. The electron density, the intensity of MNB, and the magnetic field change quasi-periodically during the 100 min period. The time period of their variation is about five to ten minutes. The BEN type emissions are also observed simultaneously. The interesting point is that the periods of higher density coincide with the periods of the appearance of the MNB and BEN. On the other hand, in the low density periods, plasma wave activities are low. Consulting with the magnetic field, we found that the azimuthal magnetic field direction often reverses (not shown) and that their amplitudes are lower in the periods of lower density. The above wave signatures in the periods of higher density are quite similar to those in the magnetosheath. However, since the plasma densities in the periods of higher density are about 0.4/cc to 2/cc, these densities are smaller than the average density in the magnetosheath. On the other hand, the signatures of the wave and the ambient magnetic field in the periods of lower density are typical ones in the central plasma sheet. From these results, we infer that the spacecraft stayed in the magnetopause boundary in the low latitude region into which the magnetosheath plasma invades and forms a boundary layer between the magnetosheath and the plasma sheet.

From the observations of the plasma waves, and the magnetic fields, we draw a conclusion that the spacecraft periodically repeated a motion between the LLBL and the plasma sheet for the period of present interest. During this period, the spacecraft was located in the dusk side of the near tail region, which is consistent with the conclusion we have drawn. The moderate plasma density and the observation of the MNB suggest the plasma entry from the magnetosheath to the LLBL region. Such plasma entry to the LLBL has been discussed in detailed based on the Geotail observations by *Fujimoto et al.* [1997] and *Fujimoto et al.* [1998].

3.6 Tail lobe, central plasma sheet and its boundary layer

Figure 3.9 shows the plasma wave signatures of the plasma sheet entry from the lobe observed at (GSM X, GSM Y, GSM Z) = (-205.3, 16.7, -1.9 R_E) on June 8, 1993.

The activities of the plasma waves in the core lobe are low. However, as we will discuss in Chapter 6, the NEN (lobe EQMW) is observed near the magnetopause/plasma sheet boundaries in the tail lobe. In Figure 3.9, the patchy spectra below 200 Hz observed during the periods from 01:00 to 01:15 (UT) and from 01:42 to 02:00 (UT) are the NEN in the lobe. The stable magnetic field corresponding to the electron cyclotron frequency of 200 Hz displayed by a white line is also an indication of the lobe during this period.

The intense broadband spectra with uppermost frequencies around 2 kHz seen in the two periods from 01:18 to 01:22 (UT) and from 01:35 to 01:41 (UT) are the BEN. These BENs suggest that the spacecraft was located in the PSBL during the above two periods.

During the interval between the two PSBL crossings, the wave activities below 2 kHz in the electric component channels (upper panel) become very quiet during the interval from 01:25 to 01:35 (UT). The magnetic field measurements (not shown) indicate that the spacecraft crossed the neutral sheet crossing at 01:25 (UT). Therefore, the spacecraft entered into the central plasma sheet (CPS) around this time. However, one interesting point is that the lower cutoff frequency of the CR remains constant or even lower than the surrounding PSBL and the lobe. This suggests that the plasma temperature must be high in this region to maintain the pressure balance.

Though the plasma wave activities are very low in the central plasma sheet especially around the neutral sheet, we occasionally observe very low frequency component of the electromagnetic waves there. Such electromagnetic waves can be seen in Figure 3.9. The bursty waves below 24 Hz are seen at 01:25, 01:32, 01:35, 01:37, and 01:39 (UT) as shown in the lower panel. The spectral intensity of these EM bursts was very low, but we occasionally observe intense electromagnetic waves even in the central plasma sheet as those in the magnetosheath region.

Another significant wave signature is the electron plasma wave shown by a white arrow in Figure 3.9. As we will discuss in Chapter 7, the electron plasma waves with their frequencies equal to the local electron plasma frequency are observed in the lobe edge contacting the PSBL where BEN is actively observed. Actually the electron plasma waves displayed by the white arrow are observed just before the appearance of the BEN at 01:19 (UT). Therefore, the electron plasma waves provide a good indication to identify the edge of the plasma sheet.

3.7 CME and CIR

Though the main objective of the GEOTAIL spacecraft is to survey the geomagnetic tail region, the spacecraft spends most of the time in the magnetosheath region, specially at far distant toward the deep tail. In the deep tail the difference between the magnetosheath plasma and the solar wind is very small. As we have shown in Section 3.1, there exist only very weak plasma wave activities in the solar wind except for special events such as

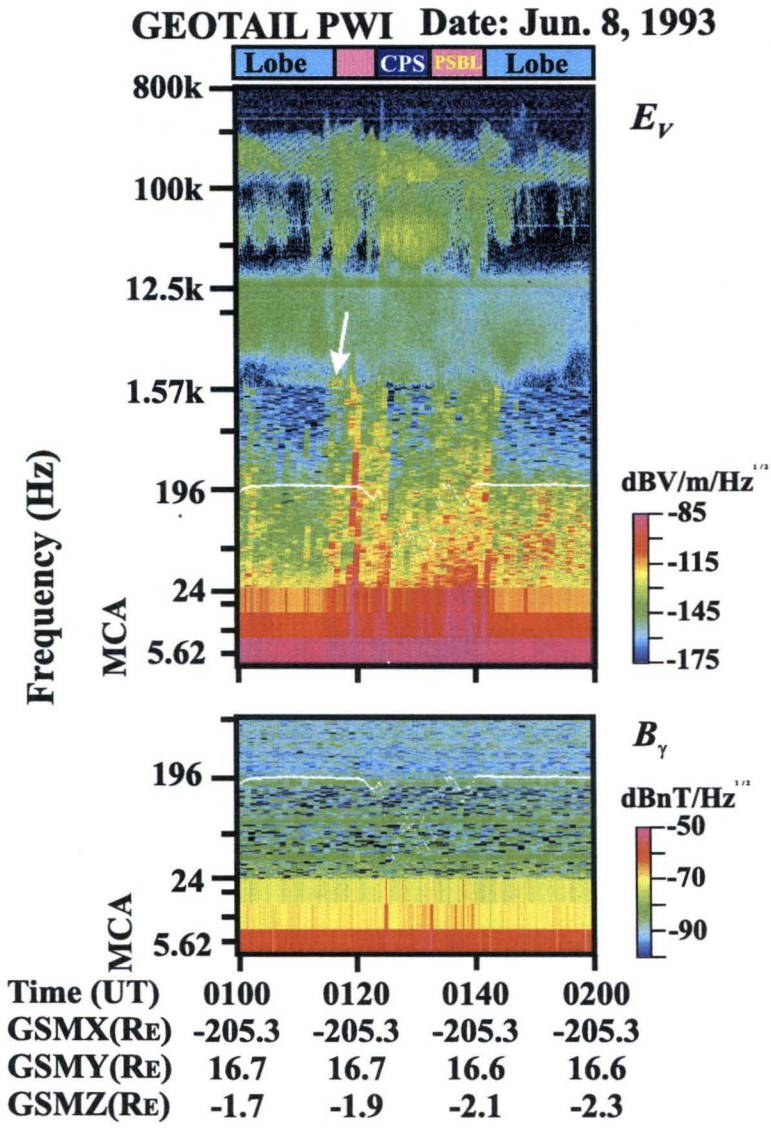

Figure 3.9: Plasma sheet entry from the lobe region. We frequently observe the electron plasma waves at the lobe edge close to the plasma sheet (indicated by a white arrow). The typical wave signature of the plasma sheet boundary layer is the BEN, while in the central plasma sheet especially around the neutral sheet, the plasma wave activity is very low [*after Matsumoto et al.*, 1998].

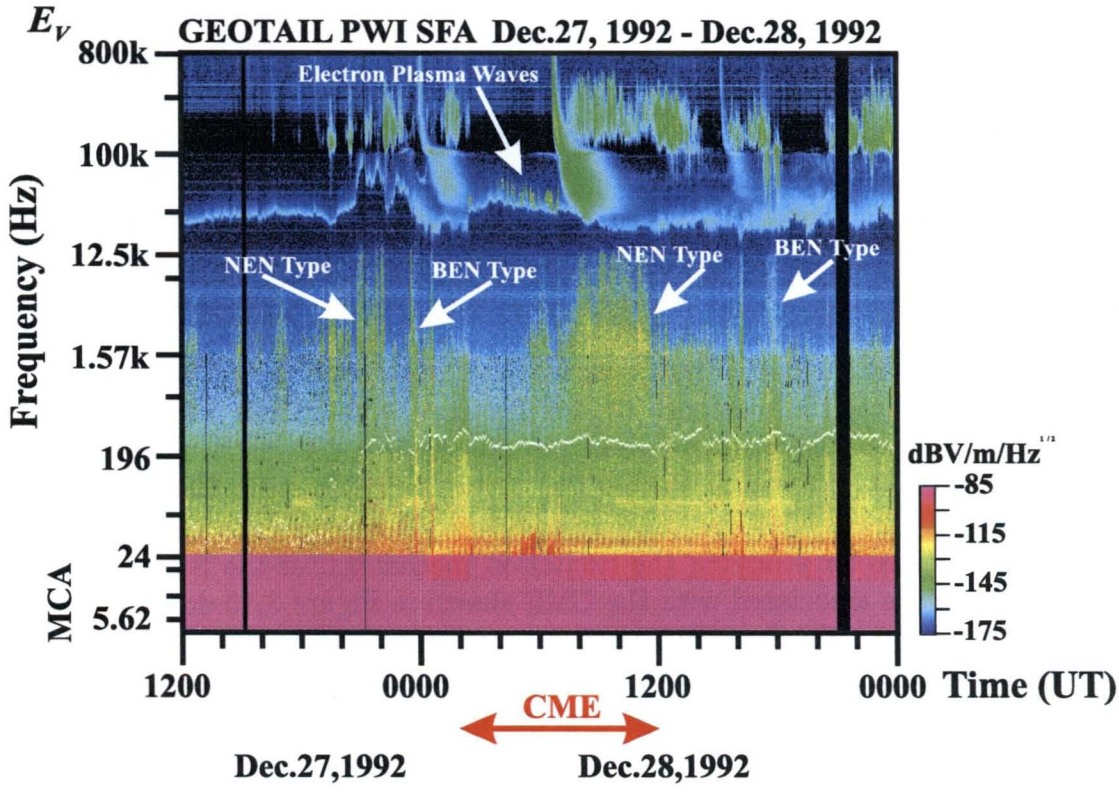

Figure 3.10: Plasma waves associated with the encounter of the CME observed by GEOTAIL [*after Matsumoto et al.*, 1998].

the interplanetary shocks, CME (Coronal Mass Ejection) and CIR (Corotating Interaction Region). The detailed wave signatures in the encounter with interplanetary shocks have been introduced by *Gurnett et al.* [1979], *Kennel et al.* [1982], and *Richter et al.* [1985]. In this section, based on the Geotail observations, we show examples of the plasma waves associated with such transient phenomena in the solar wind.

Coronal Mass Ejection (CME) is a phenomenon causing large interplanetary disturbances by the ejection of a sizable amount of the solar material [*e.g., Gosling et al.*, 1974]. These events have origins near the solar surface in the complex magnetic structure of the coronal streamer belt known to be the origin of the slow solar wind. There are two fundamental categories of CME's: fast CME's and slow CME's. Fast CME's have velocities ranging from 450 to 1200 km/s and are easily identified by a forward propagating shock preceding the CME by approximately 4 to 8 hours. On the other hand, the slow CME is identified by the presence of a bidirectional electron heat flux [*e.g., Gosling*, 1990].

Figure 3.10 shows the wave dynamic spectrum associated with the slow CME event observed in the deep magnetosheath (GSE $X = -152$ R_E) by GEOTAIL on December 27 and 28, 1992. *Hammond et al.* [1995] examined the correlation of this slow CME and the CME event observed by Ulysses spacecraft at ~20°S of GEOTAIL and 5AU from the Sun on January 9 and 10, 1993. From the similarities of the time variation of the magnetic field, they concluded that the same CME was observed by both GEOTAIL and Ulysses. Further, they discussed the latitude dependence of the CME global structure using

observation results of GEOTAIL and Ulysses spacecraft.

The plasma wave activities associated with the encounter with this CME are similar to those in the magnetosheath. The period for the CME event in Figure 3.10 is displayed by the red arrow along the horizontal axis. This period is decided by the rotation of the magnetic field direction, which suggests the passage of the magnetic cloud. Before the encounter with the CME, we see the strong density enhancement (from 11/cc up to 60/cc) associated with the enhancement of the ambient magnetic field amplitude at 21:00 (UT) on December 27, 1992. This seems to correspond to the compressed portion as the precursor of the CME. We find bursty NEN-like and BEN-like emissions at 19:50, 21:30, 23:55 and 00:30 (UT). The density enhancement appears again at 02:00 (UT) when the spacecraft encounters the CME. The electron plasma waves observed from 05:00 to 06:30 (UT) on December 28 suggest the existence of the electron beam in the CME magnetic cloud. Further, the intense NEN-like emissions are observed in the latter portion of the CME from 07:30 to 11:30 (UT) on December 28. As we will discuss in Chapters 6 and 8, the center frequency of the NEN is closely related to the local plasma density. This is one of the important clues for studying the excitation mechanism of the NEN. However, these NEN-like emissions associated with the CME shown in Figure 3.10 do not seem to have a correlation with the local density. This is clear when we compare the NEN-like emissions in the precursor with those in the inner CME. The center frequencies of the two NEN-like emissions are almost the same in spite of the big difference of the density. This is the reason why we do not address these waves in the CME event NEN emissions. We need more detailed analyses for the NEN-like emissions comparing with the real NEN observed in the tail lobe and the magnetosheath.

Another type of the solar wind disturbance arises from the interaction between high and low speed solar wind streams as they propagate radially outward from the solar surface. These are termed Corotating Interaction Regions (CIR's). The mechanism for forming CIR is provided by the interaction between the non-interpenetrable high and low speed solar wind streams. The high speed solar wind overtakes and compresses upstream slow solar wind plasma. Therefore, the stream interface (SI) between these two regions will steepen and form a pair of shocks called the forward shock and the reverse shock [*Gosling et al.*, 1976]. The forward and reverse shocks propagate radially outward and inward from the SI, respectively. The CIR is characterized by an enhancement in the bulk velocity, density, temperature, and magnetic field amplitude at the forward shock followed by a decrease of these at the reverse shock or reverse compression. Figure 3.11 shows the frequency-time spectrogram of plasma waves associated with the CIR observed by GEOTAIL for a period from December 6 to December 8, 1992 at GSM $X = -180R_E$ behind the earth. The periods of the forward shock, stream interface and reverse shock which are judged from the magnetic field and plasma measurements are displayed in the bottom of Figure 3.11. This CIR event was also confirmed by Ulysses at 5 AU after 20 days from the observation by GEOTAIL (*private communication with C. M. Hammond*).

The UHR noise, from which we could read the approximate local plasma densities, shows the gradual density increase by the encounter with the foreshock. At the foreshock encounter, the density is abruptly enhanced at 08:00 (UT) on Dec. 7, 1992. The enhanced density gradually increases until the encounter of the streaming interface. It reaches about 120/cc at maximum. The increase of the density is followed by an abrupt decrease when the

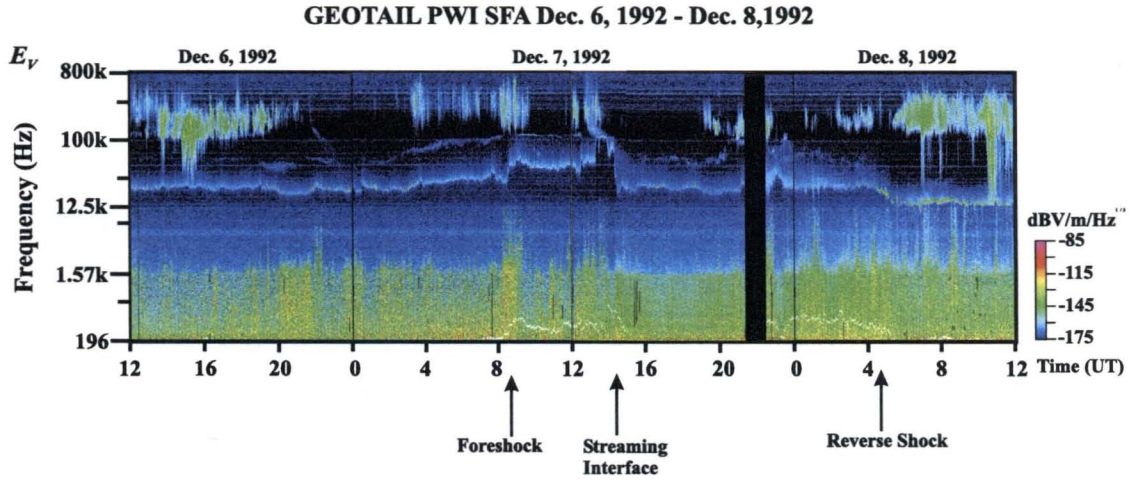

Figure 3.11: Plasma waves associated with the encounter of the CIR observed by GEOTAIL [*after Matsumoto et al.*, 1998].

spacecraft passes the streaming interface. The arrival of the reverse shock is indicated by the small density decrease at about 04:00 (UT) on Dec. 8, 1992. The weak monochromatic waves in the frequency range 70 kHz to 200 kHz are the $2f_p$ emissions, which is excited in the foreshock region. They trace well the variation of the UHR frequency.

Bursty BEN-type electrostatic waves are observed at the encounter with the foreshock, for about 4 hours before the encounter with the streaming interface, and for about 6 hours before the encounter with reverse shock. Unfortunately, no waveform data corresponding to the above BEN-type waves are available. However, judging from their spectral features, they seem to consist of a series of the ESW. The existence of ESW suggests the nonlinear interaction, which will be discussed in Chapter 4, of possible electron beam instabilities.

3.8 Plasmoid

The neutral line model for the substorm needs the near earth neutral point at the substorm onset time [e.g., *Russell and McPherron*, 1973]. The reconnection process at the near earth neutral point results in the ejection of the plasma cloud called "plasmoid." The ejected plasma cloud travels tailward. *Machida et al.* [1994] and *Mukai et al.* [1996] performed detailed analyses on the plasmoid observed by GEOTAIL. In Fig. 3.12, we show the frequency-time spectrogram of plasma waves associated with the same plasmoid event of *Machida et al.* [1994] The spacecraft location is displayed in the bottom.

We see the intense BEN emissions during the period corresponding to the plasmoid. In the magnetic field component, we also find the low frequency MNB during the same period. These BEN and MNB are the typical wave signatures in the body of the plasmoid. These signatures are very close to those of the PSBL (plasma sheet boundary layer). However, in general, the wave intensity of these waves in the plasmoid is higher than those in the plasma sheet boundary.

Machida et al. [1994] reported that the tailward electron and ion beams were observed in

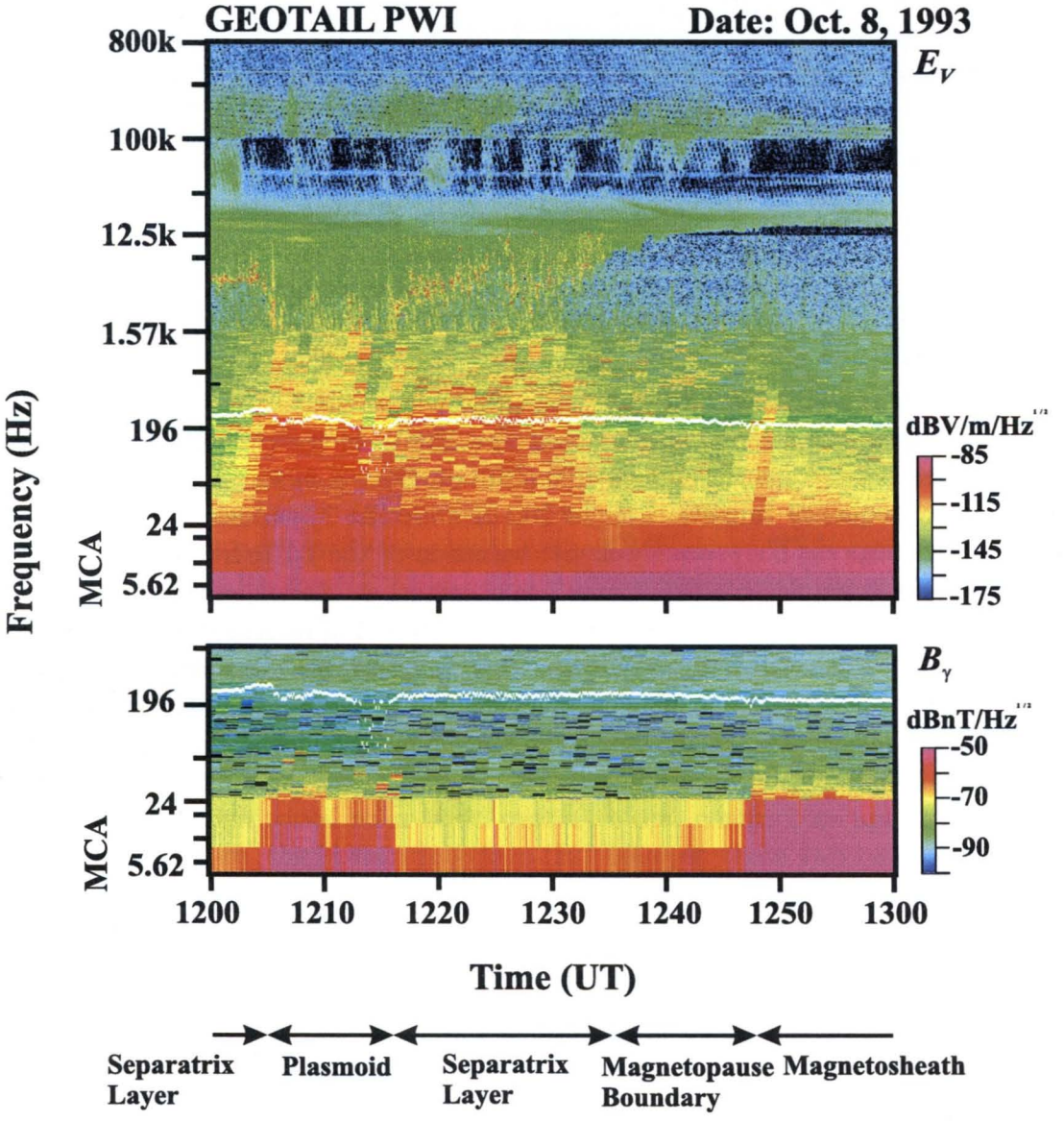

Figure 3.12: Plasma waves associated with the encounter of the plasmoid observed by GEOTAIL [*after Matsumoto et al.*, 1998].

the separatrix layers which are located at both leading and trailing edges of the plasmoid. As shown in Fig. 3.12, the wave activities in the leading and trailing edges are significantly different. The leading separatrix layer during the period from 12:00 to 12:05 (UT) is represented by the electron plasma waves with frequencies equal to 7 kHz. The equivalent plasma density is about 0.6 /cc. This density is higher than the average tail lobe density. This high density could be a result of the compressional effects due to the plasmoid. The observation of the electron plasma waves in this layer is very consistent with the existence of the electron beam. On the other hand, the latter separatrix layer in the trailing edge of the plasmoid shows significantly different wave features. During the period from 12:15 to 12:35 (UT), we see rather intense but scattered waves in addition to the electron plasma waves. The scattered and sparse spectra below 1 kHz seem to represent NEN. It is noted that such spectra are not observed in the leading edge of the plasmoid. *Machida et al.* [1994] showed the velocity distributions of electrons and ions at six time intervals around the plasmoid event. We compared them with our data, but could not find the decisive difference in the electron velocity distributions between the leading and trailing separatrix layers. *Mukai et al.* [1996] have reported the fla-top type electron distribution in the deep inside plasmoids. In Fig. 3.12, we can see intense broadband wave emissions which are confined below the electron cyclotron frequency during the interval 12:05 to 12:15 (UT). We have not concluded these broadband emissions are related to the flat-top type electron velocity distribution. Therefore, we need further comparison studies of wave activities with electron velocity distributions inside plasmoids.

Another plasmoid event observed by GEOTAIL PWI was shown by *Matsumoto et al.* [1994a]. By the comparison of the event shown in Fig. 3.12 with that in *Matsumoto et al.* [1994a], we find that the common wave activities during the plasmoid event are the BEN in the body of the plasmoid, and the electron plasma waves in the edge of the plasmoid.

The intense and sparse spectral components below 1 kHz shown in Fig. 3.12 would be observed only on the special orbit. Similarly monochromatic whistler mode waves are sometimes observed in association with the plasmoid event. The occurrence of these special wave signatures associated with the plasmoid could depend on the spacecraft path through the plasmoid.

3.9 Summary

In this chapter, we have introduced the plasma wave signatures in each characteristic region of the magnetosphere using the data observed by Geotail spacecraft. Figures 3.13 and 3.14 schematically draw the observed plasma wave signatures on the meridian plane and the cross-section of the magnetotail, respectively. As we introduced in Chapter 1, the magnetosphere consists of several different regions and their boundaries. The regions with most active wave activities are the PSBL, magnetosheath, bow shock and regions around them. The common wave activities in these regions are the intense BEN emissions and electron plasma waves. The observations of the BEN and electron plasma waves strongly suggest the existence of electron beams. Electron beams are the highest energy source for the plasma waves in the frequency ranger we focus on in the present thesis.

The interesting point is that similar wave activities as well as the BEN and electron plasma waves are seen in the different regions with different plasma parameters. Wave

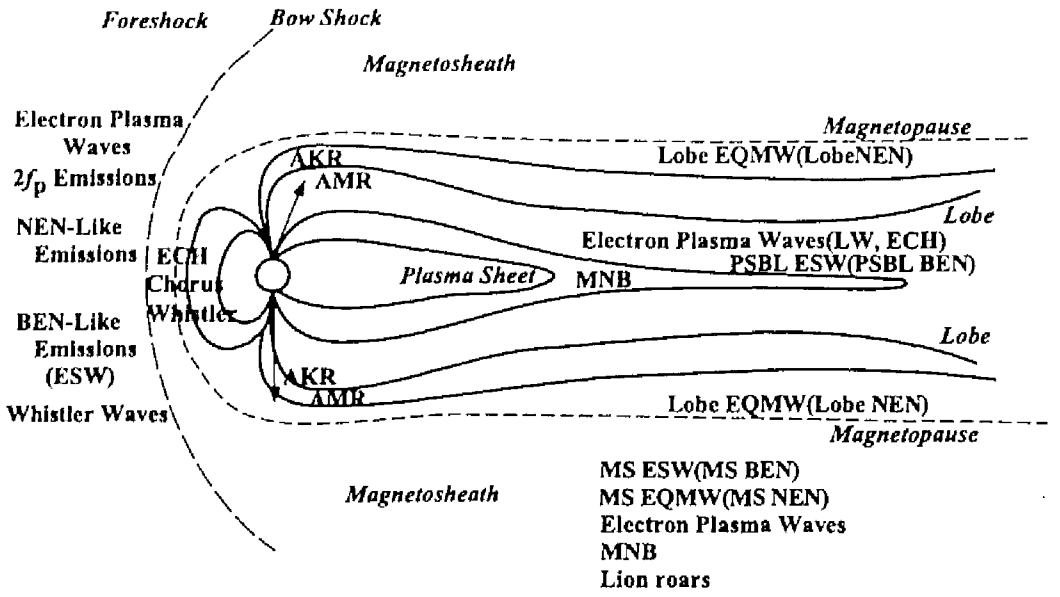

Figure 3.13: Plasma wave signatures illustrated on the meridian plane, based on the Geotail observations.

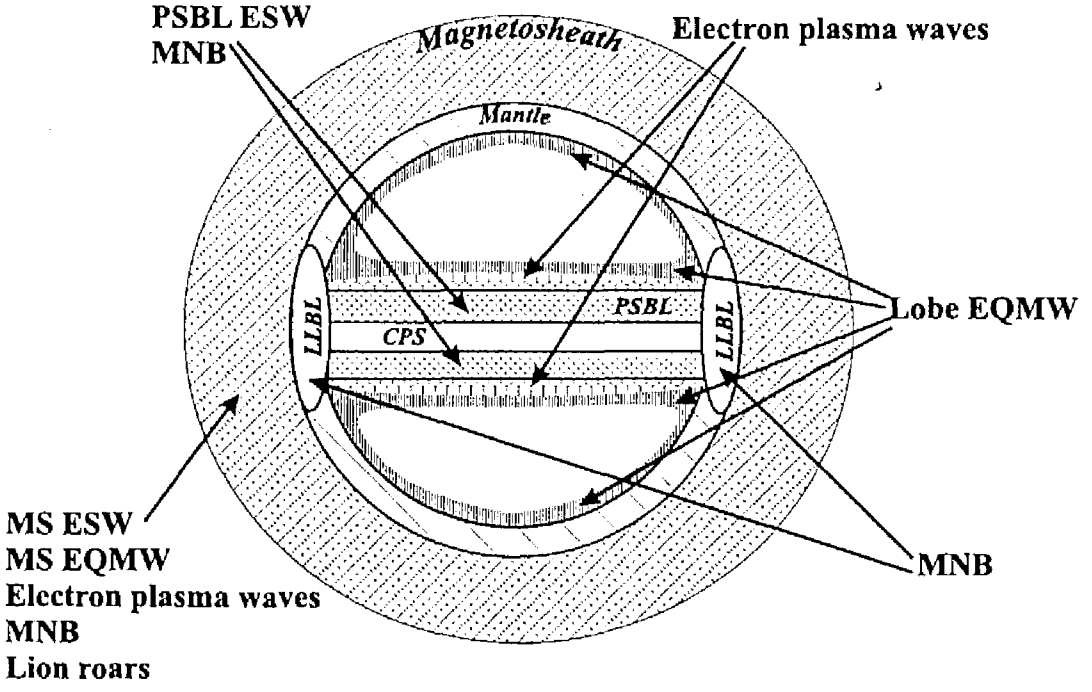

Figure 3.14: Plasma wave signatures illustrated on the tail cross-section.

Table 3.1: Typical parameter related to plasma waves

Parameters	Magnetosheath	Lobe	PSBL	CPS
Number density $n[\mathrm{cm}^{-3}]$	5	0.1	0.1	0.3
Magnetic field B[nT]	5	10	8	5
Electron				
Cyclotron frequency $f_{\mathrm{ce}}[Hz]$	140	280	224	140
Plasma frequency $f_{\mathrm{pe}}[kHz]$	20.1	2.8	2.8	4.9
Ion				
Cyclotron frequncy f_{ci}[Hz]	0.08	0.15	0.12	0.08
Plasma frequency f_{pi}[Hz]	469	66	66	115
UHR frequency f_{UHR} [kHz]	20.1	2.8	2.8	4.9
LHR frequency f_{LHR} [Hz]	3.3	6.5	5.2	3.3

activities observed in each characteristic region of the magnetosphere reflect wave-particle interactions which take place in each region. Therefore, we can classify the wave-particle interactions which occur in the magnetosphere based on the observed waves in each region. We will summarize and classify the generation mechanisms of plasma waves observed by Geotail and extend them to those in other planetary magnetosphere (planetosphere) in Chapter 10. Finally, we summarize typical parameters related to plasma waves in each region of the distant tail in Table 3.1.

Chapter 4

Waveform observations of the broadband electrostatic noise in the plasma sheet

4.1 Introduction

Scarf et al. [1974] discovered the broadband electrostatic emissions around the neutral sheet during the substorms by IMP 7 spacecraft. *Gurnett et al.* [1976] showed that such broadband electrostatic emissions are commonly observed around the plasma sheet. They referred to as broadband electrostatic noise (BEN). The similar broadband emissions are reported in the various regions of the geomagnetosphere, i.e., dayside auroral zone [*Dubouloz et al.*, 1991b], cusp/cleft regions [*Pottelette et al.*, 1990], magnetosheath [*Kojima et al.*, 1997a], and bow shock [*Matsumoto et al.*, 1997]. The BEN is also reported to be observed around the Space Shuttle orbiter [*Shawhan et al.*, 1984].

Gurnett et al. [1976] reported BEN's detailed natures using the plasma wave data observed by IMP 8 spacecraft, which passes through the magnetotail at radial distances ranging from about 23.1 R_E to 46.3 R_E. Figure 4.1 shows a typical spectrum of the BEN reported by *Gurnett et al.* [1976]. The BEN usually occurs over a broad range of frequencies extending from about 10 Hz to a few kHz with intensities ranging from about 50 μV/m to 5 mV/m. The interesting feature shown in Fig. 4.1 is that there exists a quasi-upper cutoff around a few hundreds of Hz. *Gurnett et al.* [1976] pointed out this quasi-upper cutoff frequency is almost equal to the local electron cyclotron frequency (f_{ce}). The above BEN's natures can be more clearly seen in Fig. 4.2. Figure 4.2 shows a frequency-time spectrogram with high frequency time resolutions generated from the wideband receiver data. Intense emissions shown in this figure are the BEN. The very bursty nature of the BEN appears in the lower panel. The BEN consists of many discrete bursts lasting from a few seconds to several minutes.

The above mentioned quasi-upper cutoff frequency can be seen around 400 $\sim$ 500 Hz in the upper panel. This marked decrease in intensity at frequencies above about 400 Hz agrees well with the local electron cyclotron frequency varying from 400 to 500 Hz. Another interesting point shown in a lower panel is the existence of the lower cutoff frequency. *Gurnett et al.* [1976] pointed out these lower cutoff frequencies are equal to the local lower

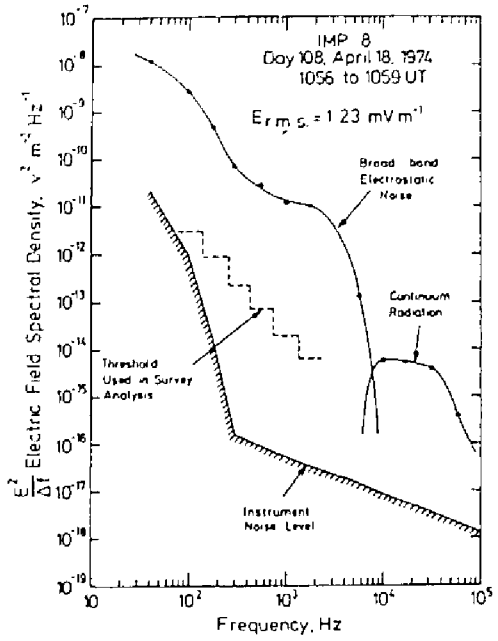

Figure 4.1: A typical frequency spectrum of the broadband electrostatic noise observed by the IMP 8 spacecraft [*after Gurnett et al.*, 1976].

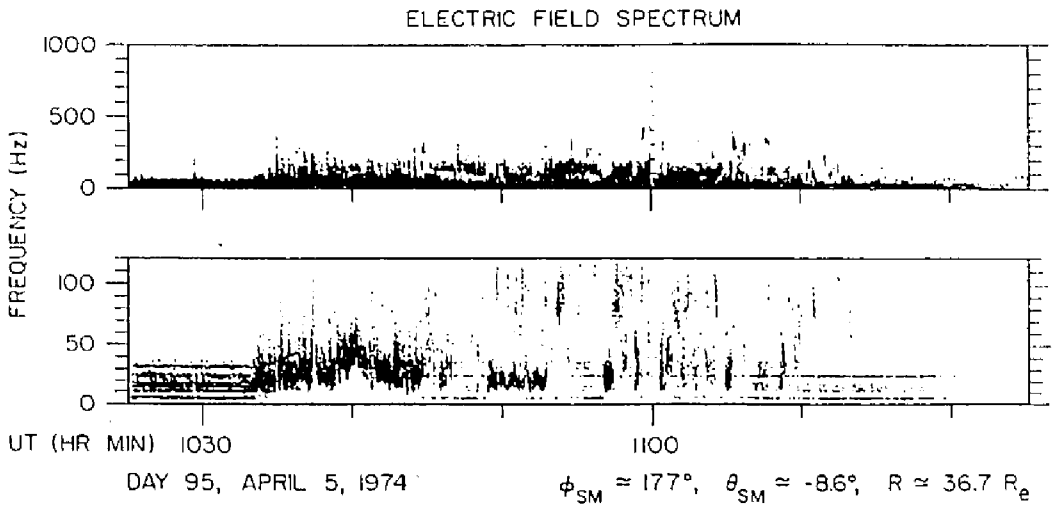

Figure 4.2: High resolution frequency-time spectrogram of the broadband electrostatic noise observed by the wideband receiver [*after Gurnett et al.*, 1976].

hybrid resonance frequencies.

The wave features of the BEN reported by *Gurnett et al.* [1976] are summarized as follows:

1. The noise usually occurs over a broad range of frequency up to the local electron plasma frequency.
2. They consist of many discrete bursts lasting from a few seconds to several minutes.
3. Their spectrum shows a marked decrease in intensity at the electron cyclotron frequency.
4. They have a low frequency cutoff corresponding to the local lower hybrid resonance frequency.
5. The electric field is oriented within $\pm 20^{\circ}$ from perpendicular to the magnetic field.
6. The BEN is usually observed in the plasma sheet boundary.

Gurnett et al. [1976] also reported good correlation of the BEN with ion streams observed in the plasma sheet boundary layer (PSBL). This good correlation leads many theoretical studies on the BEN generation mechanism to the ion beam instabilities such as ion-ion two stream instability [*e.g., Akimoto and Omidi*, 1986; *Schriver et al.*, 1990; *Grabbe*, 1987], the ion beam acoustic instability [*e.g., Dusenbery and Lyons*, 1985; *Omidi*, 1985; *Akimoto and Omidi*, 1986; *Ashour-Abdalla and Okuda*, 1986a, b; *Dusenbery*, 1986; *Grabbe and Eastman*, 1984; *Grabbe*, 1987; *Burinskaya and Meister*, 1989, 1990], the Buneman instability [*Grabbe*, 1985, 1989], and their combinations [*Schriver and Ashor-Abdalla*, 1987; *Schriver and Ashour-Abdalla*, 1990]. *Tsutsui et al.* [1991] considered the ion flow as the plasma bulk flow to provide the Doppler shift and they attempted to explain the broad frequency characteristics of BEN by the Doppler shift of ion acoustic potential bubbles convecting with the plasma bulk flow.

On the other hand, *Parks et al.*, [1984] demonstrated the relation of the BEN and electron beams based on the observations by ISEE-1 spacecraft. Further detailed analyses on the relation of the BEN and electron distributions were conducted by *Onsager et al.* [1993]. They showed that the BEN can be observed in the electron layer of the outer PSBL without energetic ions. They pointed out that the ion streaming is not essential in the excitation of the BEN, and stressed that the BEN has the close relation to the electron dynamics.

The above proposed generation mechanisms originate from destabilized normal modes. However, *Nishida et al.* [1985] pointed out that the high frequency portion ($f > f_{ce}$) of the BEN is not a normal mode. They suggested the possibility that the high frequency portion of the BEN corresponds to a kind of potential structures picked up very closed to electric field antennas. On the generation of the high frequency portion of the BEN observed in the auroral zone, *Dubouloz et al.* [1991] applied the theory of the electron acoustic solitons and showed that it is a plausible generation mechanism.

In spite of the above observational and theoretical efforts, the clear answers to the generation mechanism of the BEN had not been obtained. The main difficulty for explaining the BEN excitation mechanism is originated from the broadness of its spectrum. In order to explain the broadness of the BEN spectra, we need to combine different instabilities.

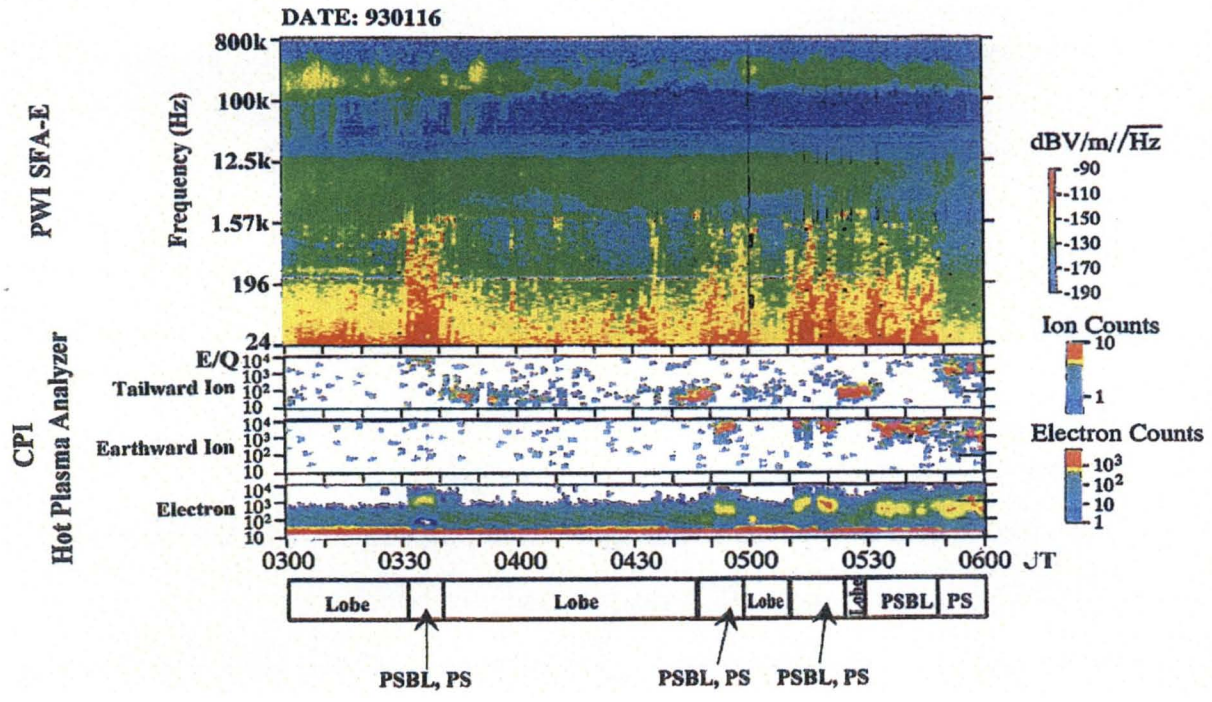

Figure 4.3: Correlation between the BEN and the high energy ion flow [*after Kojima et al.*, 1994].

4.2 BEN observed by Geotail in plasma sheet boundary layer

Data in Fig. 4.3 show a typical example of multiple crossings of the Plasma Sheet (PS) through the PSBL from the Lobe region on January 16, 1993. The GEOTAIL spacecraft was located at (GSM X, GSM Y, GSM Z)=(–65, 6, –2.5 R_E). The top panel shows the frequency-time spectrogram of the electric field component generated from the SFA. The white line shows the electron cyclotron frequency, which is calculated from the MGF fluxgate magnetometer data. Note that the frequency scales in each of the frequency bands are linear, while the boundaries of the individual bands represented by large tick marks are on a logarithmic scale. The second and third panels from the top show the energy-time spectrogram of ions from the Hot Plasma Analyzer of the Comprehensive Plasma Instrumentation (CPI) [*Frank et al.*, 1994]. The energy spectra in these panels correspond to tailward flowing ions and earthward flowing ions, respectively. The fourth panel shows the energy spectra of the omni directional electrons measured in the spacecraft equatorial plane.

In Fig. 4.3, GEOTAIL entries into the PSBL (and/or PS) are repeated 4 times at 03:31, 04:48, 05:10, and 05:30 (UT), respectively. The regions where the spacecraft was located as a function of time are indicated in the bottom of the figure. In the top panel, we can see intense BEN emissions with their uppermost frequency being close to the local plasma frequency ($f_{pe} \sim 2$ kHz) from 03:31 to 03:40 (UT), from 04:48 to 05:00 (UT), from 05:10 to 05:23 (UT), and from 05:30 to 05:49 (UT), respectively. Weaker BEN emissions whose

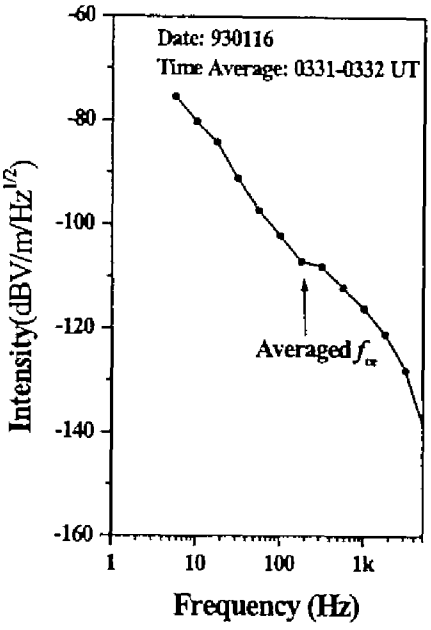

Figure 4.4: Typical frequency spectra of the BEN observed by Geotail in the PSBL.

uppermost frequency is lower than the local electron cyclotron frequency are seen from 03:00 to 03:31 (UT), from 03:40 to 04:48 (UT), from 05:00 to 05:10 (UT), from 05:23 to 05:30 (UT), and from 05:50 to 06:00 (UT), respectively.

All of the intense BEN events mentioned above show a good correlation with the high speed tailward or sunward hot ion flows ($10^3 \sim 10^4$ eV) in the PSBL (and/or PS). On the other hand, weaker BEN emissions show no correlation with the high energy ion flows. Some of these weaker emissions are detected at times when low energy ion flows ($10 \sim 10^2$ eV) in the lobe are observed such as the periods from 03:40 to 04:10 (UT), from 04:40 to 04:50 (UT), and from 05:22 to 05:30 (UT), respectively. We can see that the BEN emissions suddenly disappear at 05:50 (UT). Especially during the interval from 05:50 to 05:54 (UT), high energy tailward flow is observed form 05:50 to 05:54 (UT), however, no corresponding BEN emissions are observed during this interval. The hot ions are seen in both earthward and tailward directions from 05:54 to 06:00 (UT). They are actually not flowing ions but are hot isotropic ions (as proved by other CPI channel data: not shown).

Most of the events shown in Fig. 4.3 confirm the correlation between BEN events and the presence of high energy tailward or earthward ion flows [e.g., Grabbe and Eastman, 1984; Schriver et al., 1990]. However, as shown in Fig. 4.3 (05:50 to 05:54 (UT)), there is also an example of such energy flows which are not associated with BEN emissions. This observation caused us to question the relevance between BEN and ion beam instabilities as suggested in the previous studies. Rather, it suggests the possibility that the BEN is not generated due to an ion beam but have some other source mechanisms.

Figure 4.4 shows an example of the BEN spectral feature observed by Geotail. The

displayed format is the similar to that in Fig. 4.1. The spectrum shown in Fig. 4.4 is generated from one minute average data obtained by the MCA during the time period of 03:31 to 03:32 (UT). The Geotail BEN spectrum shown in Fig. 4.4 is quite similar to that in Fig. 4.1. The marked decrease in intensity around f_{ce} (shown by an arrow) can be also clearly seen in Fig. 4.4. From Fig. 4.3 and Fig. 4.4, we can confirm the BEN natures reported by *Gurnett et al.* [1976].

4.3 Electrostatic solitary waves

All of the observations of the BEN by previous spacecraft were conducted by spectrum analyzers. However, the Geotail PWI succeeded in revealing BEN waveforms in the time domain via the WFC receiver. On the basis of the waveform observations by GEOTAIL, *Matsumoto et al.* [1994b] and *Kojima et al.* [1994] revealed that the BEN includes a series of solitary bipolar waveforms.

Figure 4.5 (a) shows an SFA plot which is the frequency-time spectrogram of the BEN observed in the PSBL at (GSM X, GSM Y, GSM Z) =(−118, 4.3, 0.7 R_E) on April 1, 1993. Figure 4.5 (a) shows clearly intense spectra extending all the way to the electron plasma frequency ($f_{pe} \sim 2$ kHz) during the intervals from 13:30 to 13:36 (UT), from 13:41 to 13:53 (UT), from 13:54 to 14:00 (UT) and from 14:12 to 14:22 (UT). Figure 4.5 (b) shows waveforms observed by the WFC at 13:55:43.241 (UT). The observed waveforms are completely different from those expected by many scientists as incoherent random noises. They are composed, instead, of a series of bipolar pulses. The bipolar signature is characterized by solitary spikes composed of a half sinusoid-like cycle followed by a similar half cycle having opposite a sign. The time span between these isolated pulses varies from pulse to pulse. The pulse width shown here is about 2 msec. One of the interesting points shown in Fig. 4.5 (b) is that observed solitary waves have coherent structures of each electric field channel (E_U and E_V). This characteristic is very important for the potential model which we will introduce later.

Since the most frequently observed BEN emissions have an isolated pulse waveform and no corresponding magnetic component, we term them "PSBL Electrostatic Solitary Waves (PSBL ESW)" [*Matsumoto et al.*, 1994b; *Kojima et al.*, 1997a]. The Fourier analysis of the observed waveform data shows that the frequency of the spectral peak intensity is primarily controlled by the pulse width of the PSBL ESW. The broadband frequency characteristics of the BEN are mainly attributed to the higher harmonics caused by the isolated pulse nature of individual bipolar spikes. However, note that the PSBL ESW mainly contribute to a high frequency portion of the BEN spectra. Wave amplitudes of the ESW as shown in Fig. 4.5 are too small for interpretation of low frequency portions.

In order to study the natures of the PSBL ESW, we examined the waveforms which were captured simultaneously by the two sets of orthogonal electric field antennas. Figure 4.6 shows a comparison of these waveforms. The product of E_U and E_V is plotted as a function of time for two Geotail spin periods as well as schematic drawings on phase relation of E_U and E_V. The two waveforms captured simultaneously by WANT and PANT systematically repeat an "in-phase" and "out-of-phase" relationship synchronizing with a spacecraft spin. Therefore, the signs of the product $E_U \cdot E_V$ shown in panel (a) change every a half of the spin period. This relation is schematically shown in panels (b), (c), and (d). Positive and

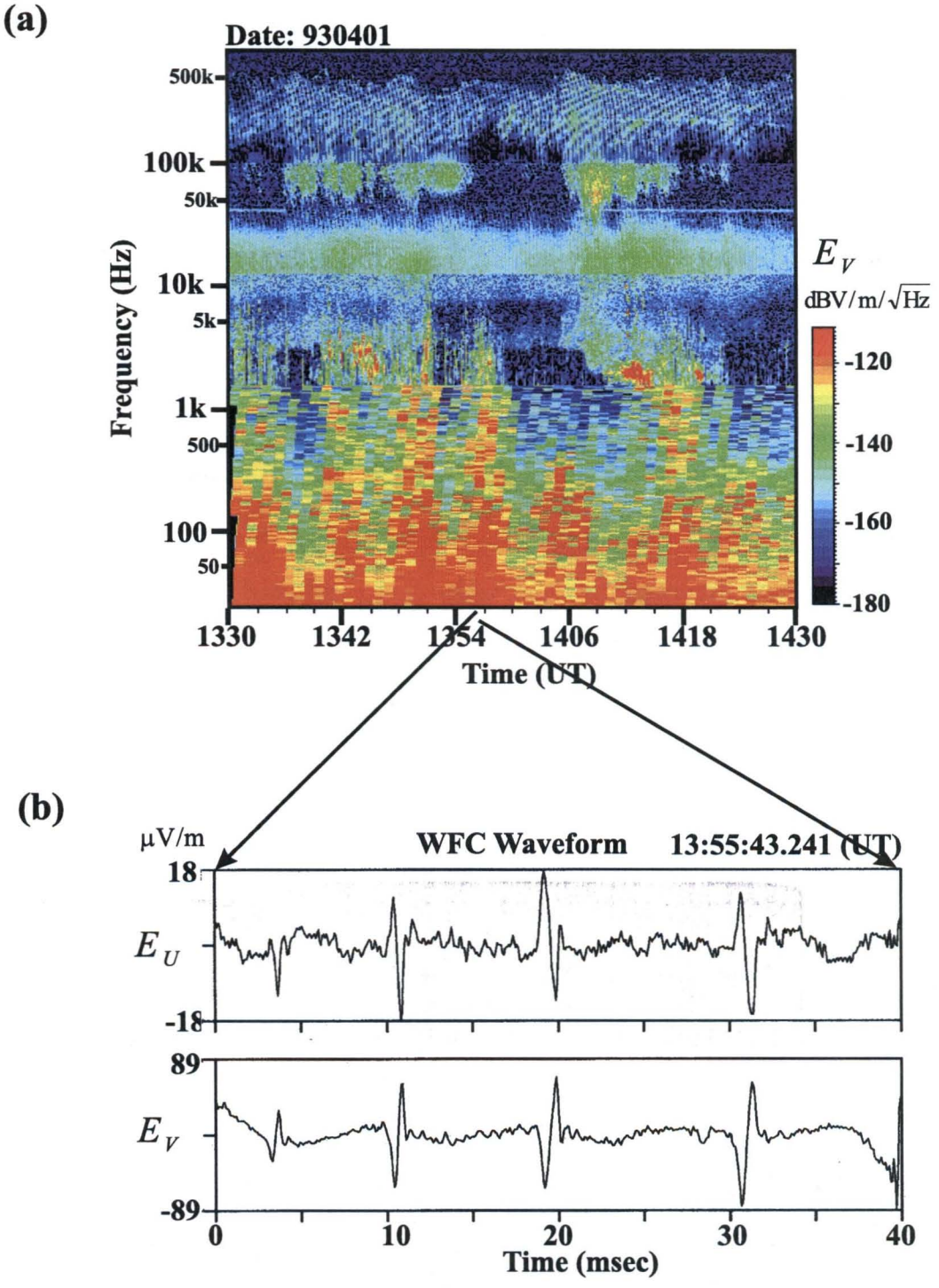

Figure 4.5: BEN spectra observed by Geotail spacecraft (upper) and their waveforms revealed by the WFC receiver (lower).

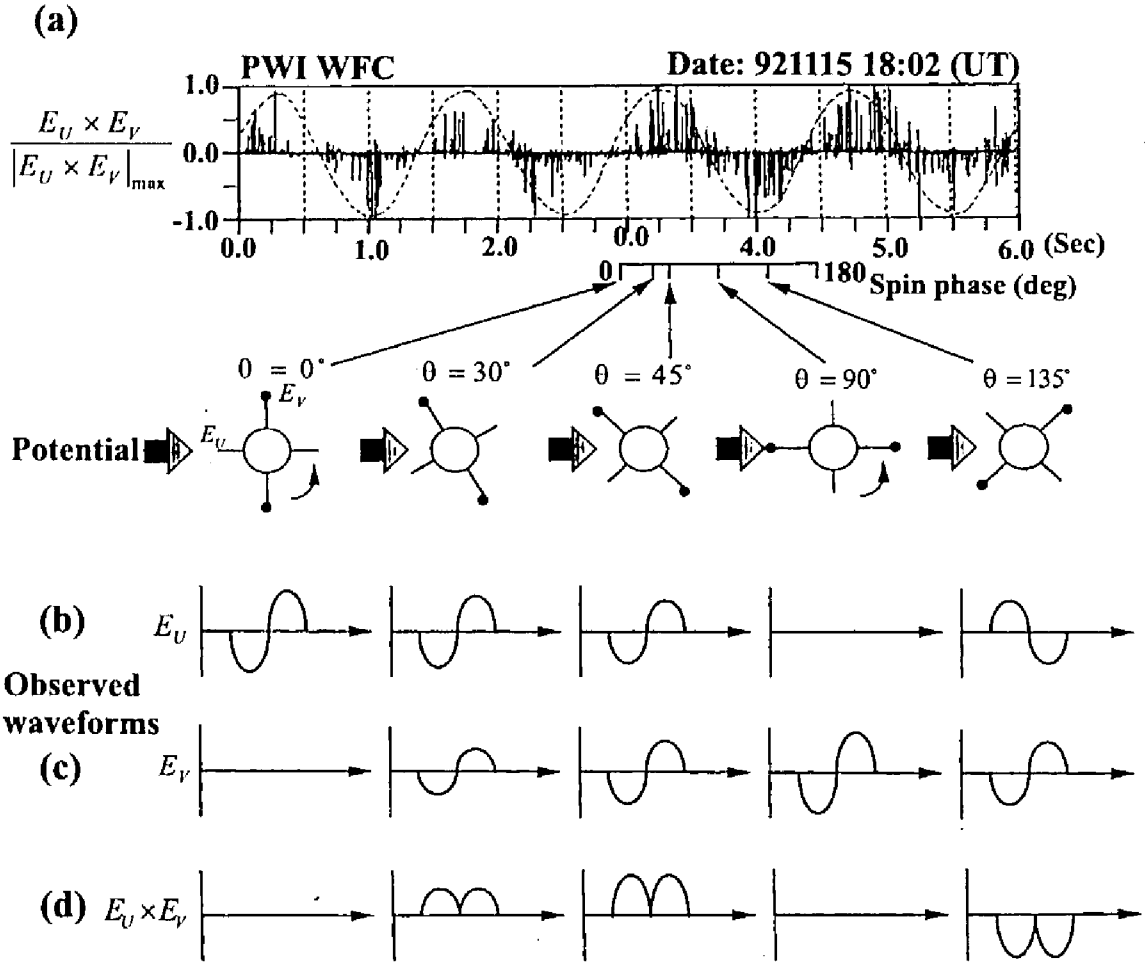

Figure 4.6: Comparison of simultaneously observed ESW waveforms by two orthogonal electric antennas. Their relative phase changes from in-phase to out-of-phase four times per single spin period.

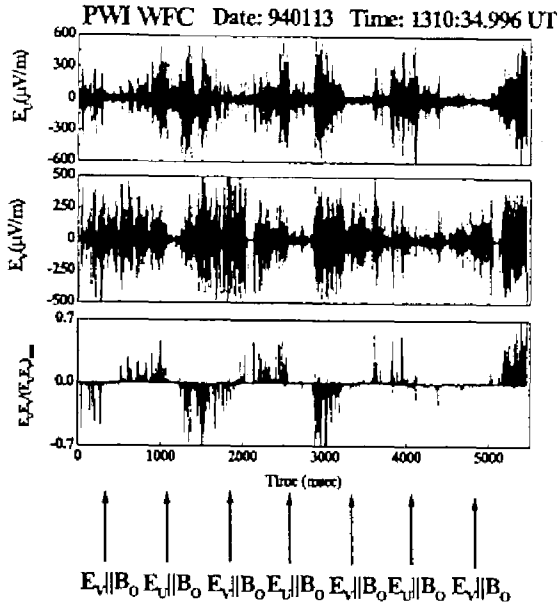

Figure 4.7: Spin dependence of the PSBL ESW. This shown result suggests that the polarization of the PSBL ESW is parallel to the ambient magnetic field [*after Kojima et al.*, 1994].

negative signs of $E_U \cdot E_V$ correspond to in-phase and out-of-phase waveforms, respectively.

This spin dependence of observed wave phases between two components, E_U and E_V, can be understood if we assume that a large, essentially one-dimensional electrostatic potential structure passes over the spacecraft with a transit time which is much shorter than the spacecraft spin period. This situation is illustrated schematically in the lower figures of panel (a) in Fig. 4.6.

Kojima et al. [1997a] examined timing when signs of $E_U \cdot E_V$ change and showed that they change at the time when either electric field antenna of E_U or E_V is parallel to the ambient magnetic field. Figure 4.7 shows that the comparison of the above change timings and relative directions of electric field antennas and the ambient magnetic field for the PSBL ESW observed on the different day. We can see that either the E_U or E_V antenna is almost parallel to the ambient magnetic field, the amplitudes of waveforms detected by another antenna minimize and the signs of $E_U \cdot E_V$ change as shown by arrows. This means that the potential structure of the PSBL ESW is formed along the direction parallel to the ambient magnetic field.

Further, we can confirm that the electric field orientation of the PSBL ESW is parallel to the ambient magnetic field in Fig. 4.8. The best way to identify orientation of electric field components is to draw a hodogram on a fixed plane. Since Geotail has 2 sets of orthogonal electric field antennas on the spin plane, therefore, we can obtain the orientation of the electric fields on $x-y$ plane of the spacecraft coordinate system (see Appendix A). E_x and

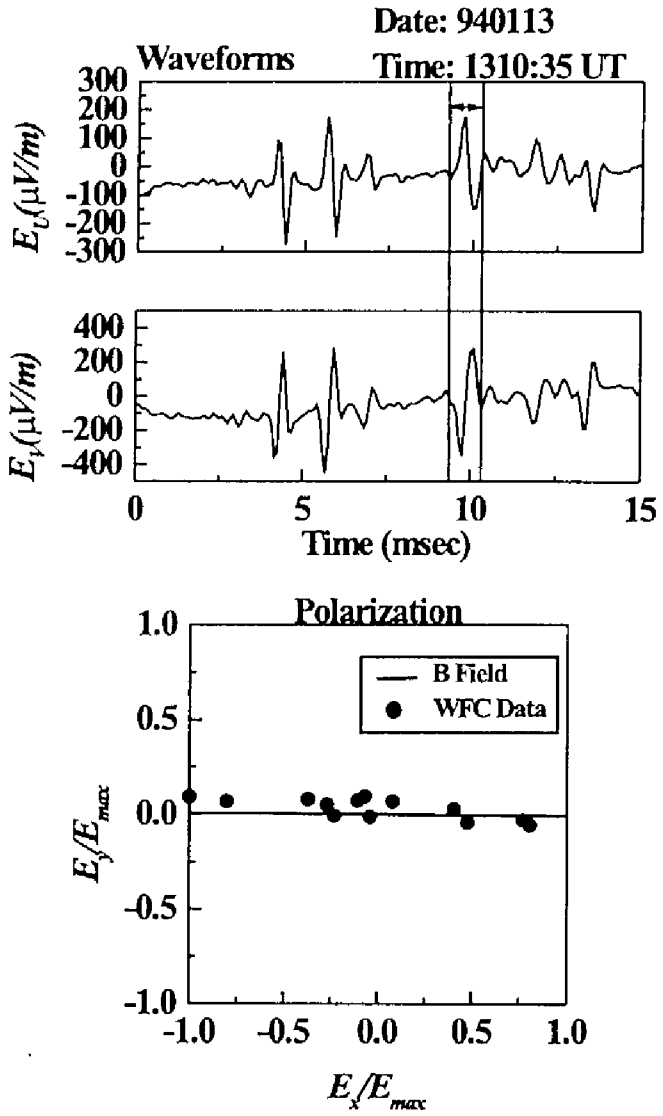

Figure 4.8: Waveforms and corresponding polarizations of the PSBL ESW. From data displayed at bottom, we can confirm the parallel polarization of the PSBL ESW [*after Kojima et al.*, 1997a].

E_y are calculated as follow:

$$\begin{pmatrix} E_x \\ E_y \end{pmatrix} = \begin{pmatrix} \cos\theta & -\sin\theta \\ \sin\theta & \cos\theta \end{pmatrix} \begin{pmatrix} E_U \\ E_V \end{pmatrix}, \tag{4.1}$$

and θ is defined by

$$\theta = \theta_{\text{spin}} - 15^\circ, \tag{4.2}$$

where θ_{spin} is the spin angle, which is defined as the relative angle between the Sun direction and mechanical X axis fixed on the spacecraft (see Fig. 2.9). This method allows us to examine the wave polarization with a very high time resolution, however, we need to calibrate the waveforms very carefully, taking account of the antenna impedance, because the errors of the waveform calibration lead to the distortion of the polarization in the fixed coordinates.

Figure 4.8 (top and middle) illustrates the waveforms detected by two sets of an orthogonal electric field antenna (E_U and E_V). Figure 4.8 (bottom) shows the electric field orientation of the PSBL ESW corresponding to the PSBL ESW shown by arrows in Fig. 4.8 (top and middle). The solid line in Fig. 4.8 (bottom) is the direction of the ambient magnetic field projected on the spacecraft coordinate system. Each dot represents each sampled waveform level, which is converted to the spacecraft coordinate system, of the PSBL ESW waveforms shown by arrows in Fig. 4.8 (top and middle). In Fig. 4.8 (bottom) we find that the converted, sampled PSBL ESW level is scattered along the direction of the ambient magnetic field. This means that the PSBL ESW are polarized along the ambient magnetic field and that since the PSBL ESW are purely electrostatic, the PSBL ESW propagate along the ambient magnetic field.

Based on the above results, we proposed the isolated flowing potential for the model of the PSBL ESW, as shown in Fig. 4.9. In the proposed model, an isolated potential structure propagates in the directions parallel or anti-parallel to the ambient magnetic field and is satisfied with following conditions:

$$\frac{L_2}{V} \ll T_{\text{spin}}, \tag{4.3}$$

$$L_2 \gg L_{\text{ant}}, \tag{4.4}$$

$$L_1 \gg L_{\text{ant}}, \tag{4.5}$$

where L_1, L_2, L_{ant}, and T_{spin} denote perpendicular scale of the potential, potential width, antenna length (= 100 m), and spacecraft spin period ($\sim$ 3 sec), respectively.

The natures of the PSBL ESW are summarized as follows:

1. Pulse widths are from a few milliseconds to a few tens of milliseconds.
2. The orientation of the electric field is parallel to the ambient magnetic field.
3. The PSBL ESW waveform corresponds to a huge potential hump flowing along the ambient magnetic field as shown in Figure 4.9.
4. The PSBL ESW appear very bursty and intermittently. The bursty nature of the BEN especially in a high frequency range is originated from the bursty nature of the PSBL ESW.

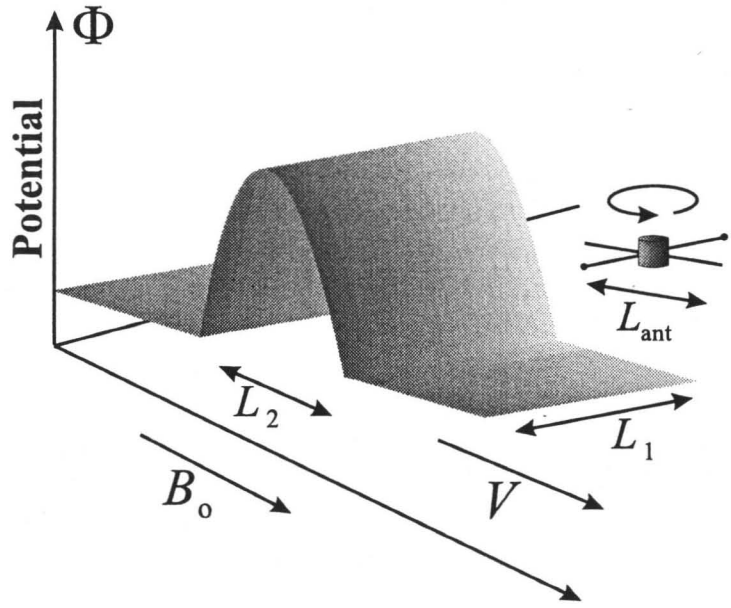

Figure 4.9: Schematic drawing of the PSBL ESW potential. The potential flows along the ambient magnetic field [*after Kojima et al.*, 1997a].

The above mentioned natures of the PSBL ESW agree well with the BEN natures, which were reported by *Gurnett et al.* [1979] except one point. The difference is the electric field orientation. *Gurnett et al.* [1979] reported that the orientation of the electric field of the BEN is almost perpendicular to the ambient field, while we showed that the polarization of the ESW is parallel to the ambient magnetic field. *Onsager et al.* [1993] showed that the high frequency portion of the BEN spectra is polarized along the ambient magnetic field, however, even in their results, when the spectral intensity of the high frequency portions is weak, their wave polarizations are perpendicular to the ambient magnetic field. Their results on the electric field orientation are not consistent with ours. All of the ESW which we have examined are polarized along the ambient magnetic field. We will discuss this difference on the polarization in Section 4.7.

4.4 PSBL ESW with two-dimensional structures

We concluded that the PSBL ESW have one-dimensional potential structure as shown in Fig. 4.9. The main reason for this conclusion is that the observed electric fields do not have perpendicular components relative to the ambient magnetic field in most of cases we examined among waveform data collected in the distant tail region.

As we stated in Section 2.2, since November 1994, Geotail was put on the near tail orbits and we have more opportunities to observe the PSBL in the near tail region. We can see BEN spectra in the near tail PSBL, but we find several different features on the ESW. The most important difference is that the ESW observed in the near tail region

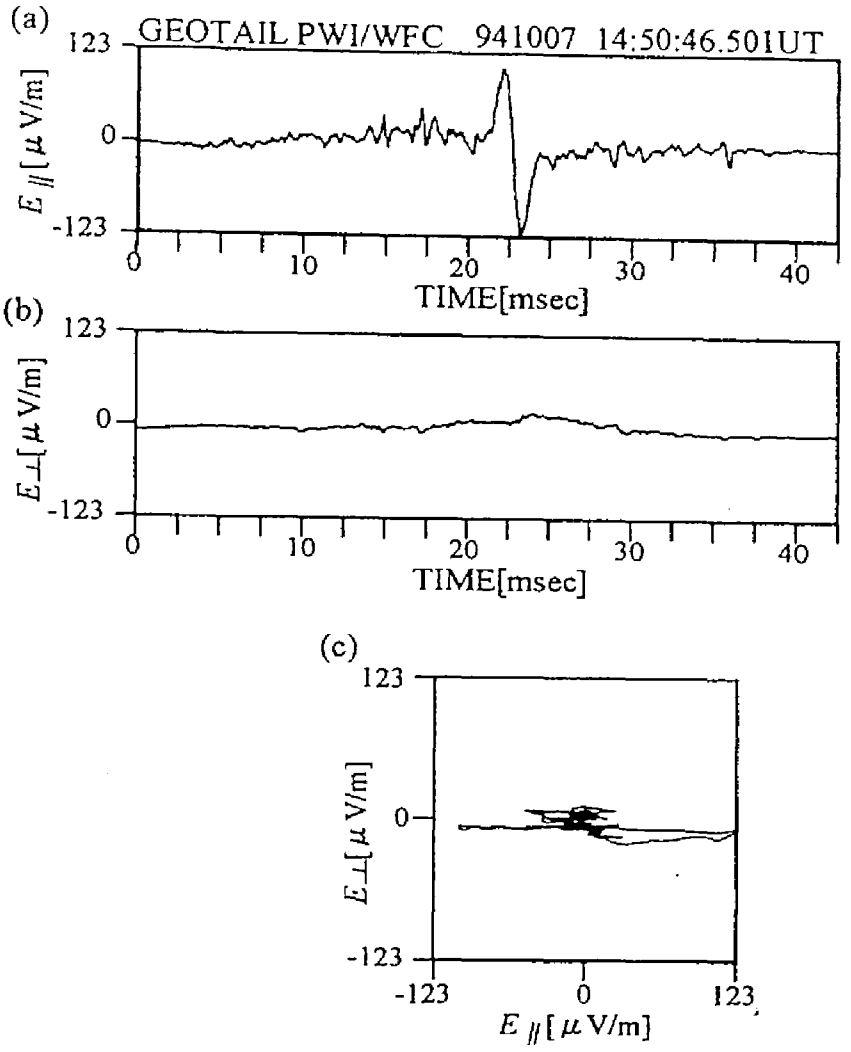

Figure 4.10: ESW waveforms with a one-dimensional potential structure as well as corresponding hodogram.

have the perpendicular components relative to the ambient magnetic field in many cases. The existence of the perpendicular component shows that the potential structure is not one-dimensional.

Figure 4.10 shows waveforms and corresponding hodogram of the ESW with one-dimensional structure, which we focused on in the previous section. The waveforms are observed in the distant tail region at (GSM X, GSM Y, GSM Z)=(−149, -11, 10 R_E). Note that the displayed format is different from previous ones. In Fig. 4.10, we show waveforms of $E_{\parallel}$ and $E_{\perp}$ components, where $E_{\parallel}$ and $E_{\perp}$ mean the electric field components parallel and perpendicular to the ambient magnetic field, respectively. These two components of waveforms are calculated as follow:

$$\begin{pmatrix} E_{\parallel} \\ E_{\perp} \end{pmatrix} = \begin{pmatrix} \cos\theta_{\mathrm{BW}} & -\sin\theta_{\mathrm{BW}} \\ \sin\theta_{\mathrm{BW}} & \cos\theta_{\mathrm{BW}} \end{pmatrix} \begin{pmatrix} E_U \\ E_V \end{pmatrix}, \tag{4.6}$$

where θ_{BW} denotes a relative angle of the direction of the ambient magnetic field and

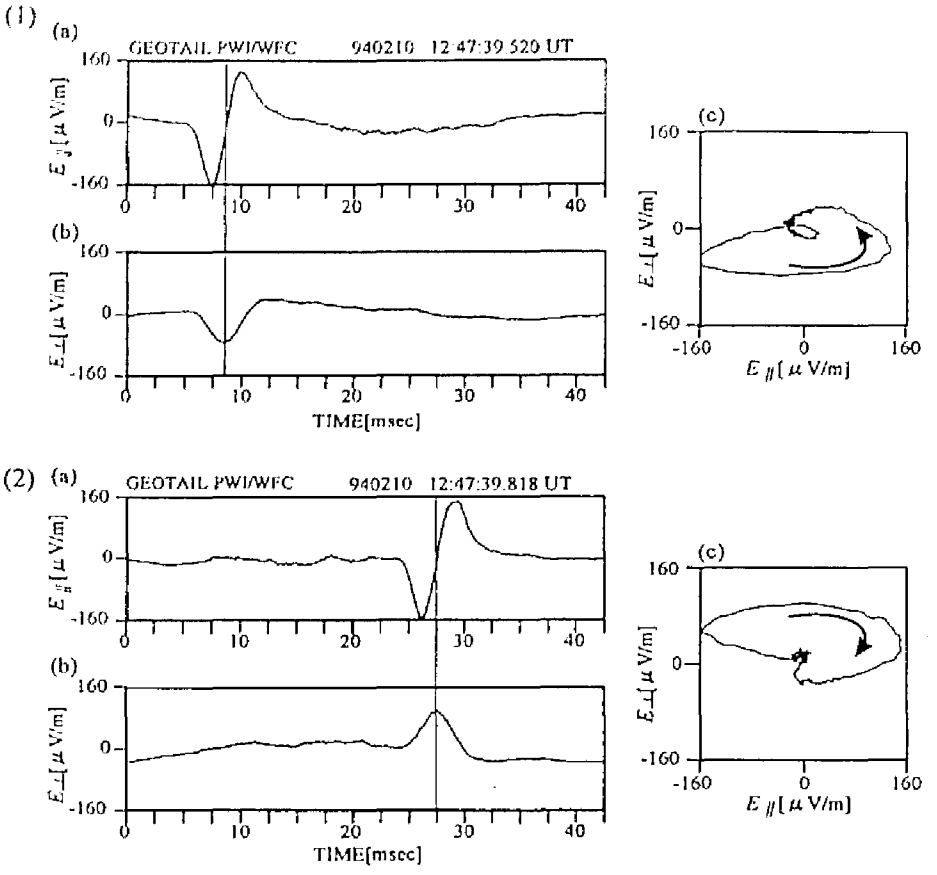

Figure 4.11: ESW waveforms with a two-dimensional potential structure as well as corresponding hodogram.

WANT-B on the spacecraft spin plane. We draw a hodogram using two components of the waveforms as displayed in the lower panel. We can clearly see that the shown PSBL ESW do not have perpendicular component of its electric field. On the other hand, we can see the different features of the PSBL ESW in Fig. 4.11. The ESW shown in Fig. 4.11 were observed in the middle tail region at (GSM X, GSM Y, GSM Z)=(-81, 27, -0.6 R_E). The striking point in this figure is mono-hump or mono-well structure with a large amplitude in $E_\perp$ component. In both cases, the amplitude of $E_\parallel$ component is about 160 μV/m, while $E_\perp$ is about 80 μV/m. Such large amplitudes of $E_\perp$ component cannot be seen in the ESW waveforms with one-dimensional potential structure as shown in Fig. 4.10.

We cannot apply our one-dimensional potential model as shown in Fig. 4.9 to these PSBL ESW with large perpendicular electric field components. The hodograms shown in Fig. 4.11 are very suggestive to the potential model. From the hodograms, we find the orientation of the electric field vectors rotate on $E_\parallel - E_\perp$ plane. This rotation of the electric field suggests the potential structure with a mortar shape. However, note that even when we observe a series of PSBL ESW with large $E_\perp$ component, PSBL ESW without $E_\perp$ component can be found in the same WFC memory sequence of 8.7 sec. Therefore, from this mixture of ESW with and without $E_\perp$ components and the rotation of E vectors,

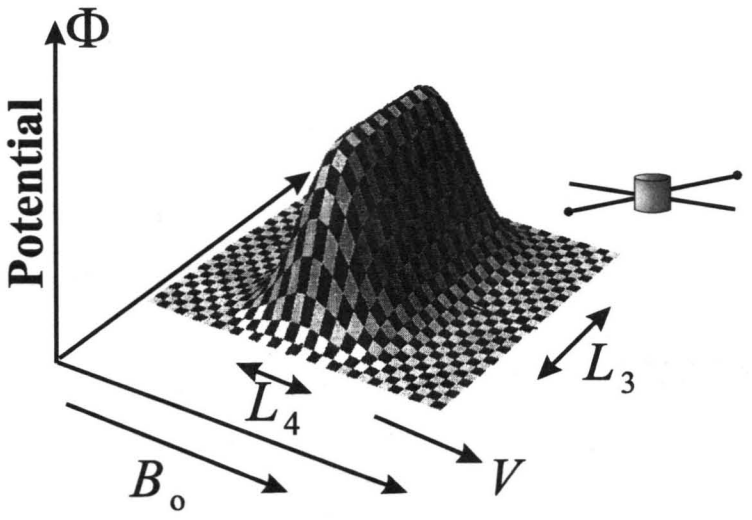

Figure 4.12: Two-dimensional PSBL ESW potential model.

we can propose two-dimensional potential structures as shown in Fig. 4.12. When the spacecraft passes the potential through its portion with the uniform structure indicated by "L_3" in Fig. 4.12, we observed the ESW without perpendicular components, while when the spacecraft encounters the edge of the potential, we can see the PSBL ESW with perpendicular components. Figure 4.13 schematically shows the relation of observed waveforms and relative location of spacecraft and PSBL ESW potential. Green curves and blue arrows display equi-potential lines, and electric field vectors, respectively. As shown in Fig. 4.13, the observed waveforms depend on the relative location of spacecraft and potential structure. This model explains well the mixture of observations for the PSBL ESW with and without $E_{\parallel}$ components.

The main difference of the ESW potentials shown in Fig. 4.9 and Fig. 4.12 is the scale of their structures' uniformity in the perpendicular direction relative to the ambient magnetic field. The relations of the scale of these two types of structures are:

$$L_1 \gg L_3 \tag{4.7}$$

$$L_2 \sim L_4 \tag{4.8}$$

We examined many PSBL ESW observed in both distant and near tail regions. From the preliminary statistical analyses, we found that the observation possibilities of the PSBL ESW with two-dimensional structures are much higher in the near tail region $|X_{\mathrm{GSE}}| < 100\ R_E$ than in the distant tail region. This tendency is very important for studying the generation mechanism and generation source region of the PSBL ESW. We will discuss this tendency in the next section based on the results of computer experiments.

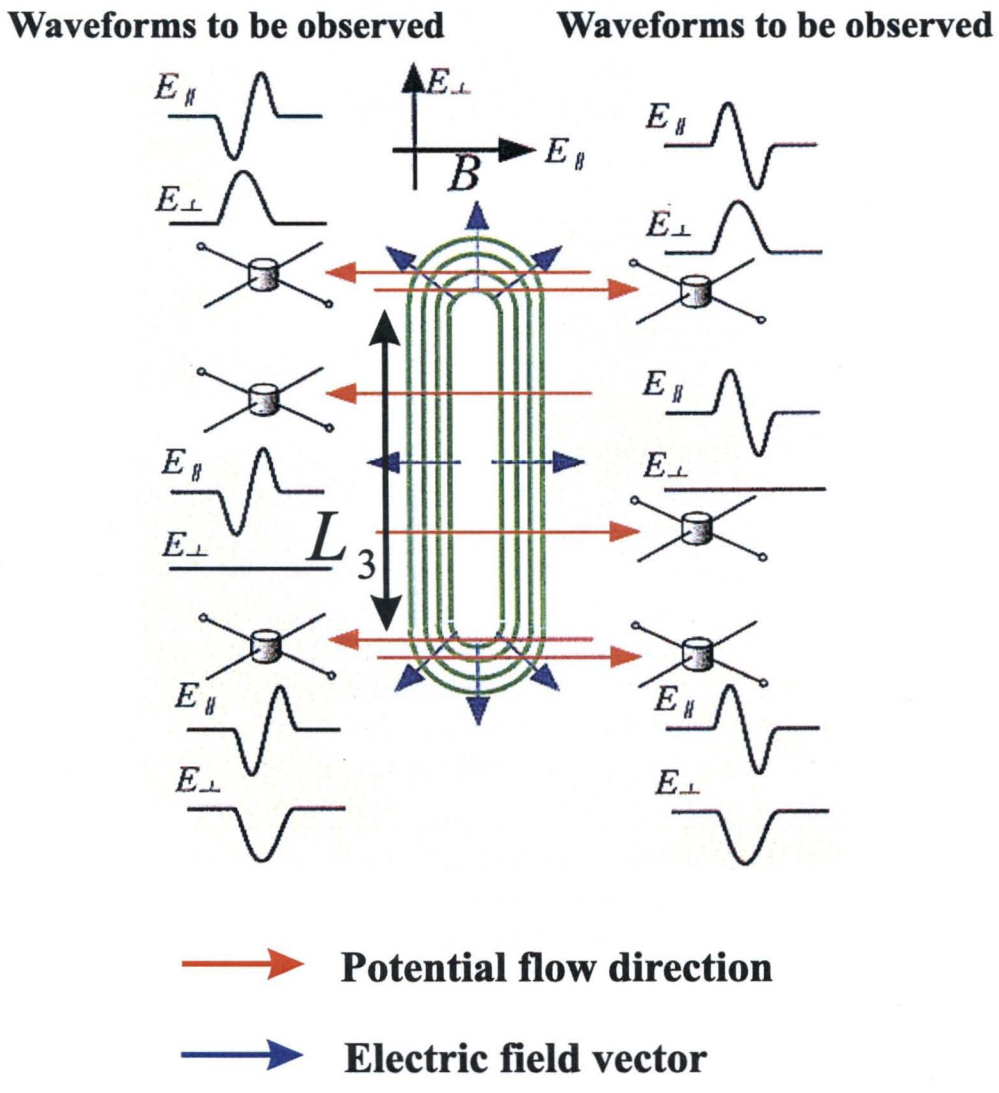

Figure 4.13: Waveforms to be observed when the spacecraft encounters the two-dimensional potential structure.

4.5 Possible generation mechanism of the PSBL ESW

4.5.1 One-dimensional computer experiments

As we introduced in section 4.1, many theoretical attempts have been made for the studies on the BEN generation mechanism and many of them discuss the instabilities on the ion dynamics, because spacecraft observations reported the good correlation between BEN emissions and high energy ion flow in the PSBL. In section 4.2, we also showed the good correlation of the BEN and high energy ion flows using the Geotail observations. However, we also pointed out that there are examples of high energy ion flows which are not associated with the BEN emissions. *Parks et al.* [1984] and *Onsager et al.* [1993] showed that the BEN emissions can be observed even without high energy ion flows and *Onsager et al.* [1993] claimed the importance of the role of electrons for the BEN generation.

Our Geotail waveform observations of the BEN revealed that the BEN spectra consist of a series of bipolar pulses named as PSBL ESW. The PSBL ESW waveforms mainly contribute to the high frequency portions of the BEN spectra. Therefore, in order to study the generation mechanism of the BEN, it is very essential to make clear the generation mechanism of the ESW. We proposed the mono-hump potential structure for the PSBL ESW as shown in Fig. 4.9 and Fig. 4.12. However, since the Geotail PWI does not have a capability to measure the potential polarity, we cannot decide whether the PSBL ESW correspond to the positive potentials or negative ones. The potential polarity depends on whether the potentials are related to electron dynamics or ion dynamics. Figure 4.14 shows an important clue to answer this problem. In Fig. 4.14, we show the waveforms for the PSBL ESW observed on April 1, 1993. The 4 panels show the waveforms from four different intervals collected in one WFC snapshot (8.7 seconds). The horizontal axis for each panel shows the time in milliseconds from the start of the WFC sequence. The bipolar impulsive signatures which are evident in each example are observed in conjunction with many BEN events found in the PSBL. The PSBL ESW pulse widths and their inter-pulse time spans for the four examples shown in each panel are all different. These parameters change quickly even within one WFC snapshot period (8.7 seconds). The pulse widths (w) and repetition periods (τ) in each panel are: $w_A = 16.1$ msec and $\tau_A = 57.1$ msec; $w_B = 11.6$ msec and $\tau_B = 40.1$ msec; $w_C = 6.1$ msec and $\tau_C = 21.9$ msec; $w_D = 3.6$ msec and $\tau_D = 12.3$ msec, respectively. If the pulse width of the PSBL ESW and their repetition periods are controlled by the PSBL ESW potential speed, then the ratio of the pulse width to the repetition period should be of the same order under the assumption that individual wells have essentially the same spatial scales. Using the above numbers for the pulse widths and the repetition periods, we obtain

$$\frac{w_A}{\tau_A} \simeq \frac{w_B}{\tau_B} \simeq \frac{w_C}{\tau_C} \simeq \frac{w_D}{\tau_D} \simeq 0.3. \tag{4.9}$$

Thus, within experimental error, this fact supports the idea that the spatial size of the solitary potentials is almost constant and that the variation in the pulse width with time is controlled simply by the change in the potential speed. This implies the interesting result that the moving velocity of the PSBL ESW potential structure changes on a time scale ranging from a few milliseconds to a few hundreds of milliseconds in the PSBL. Such velocity fluctuations on these time scales cannot be resolved and be picked up by the

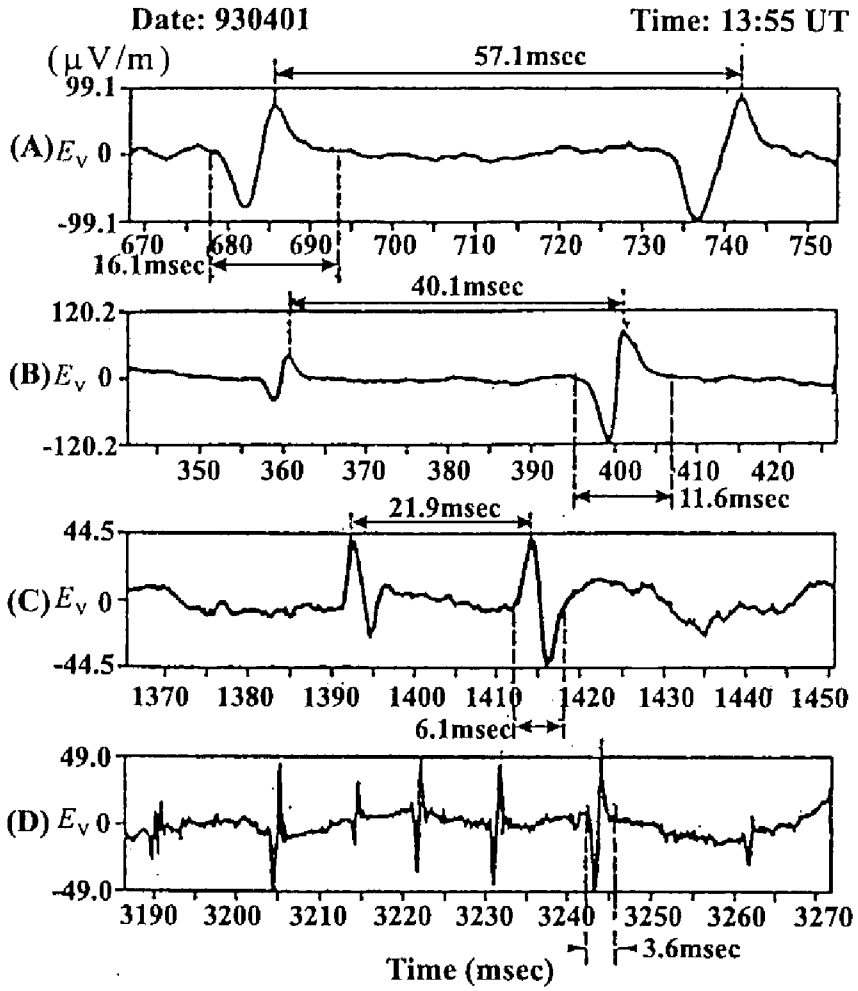

Figure 4.14: Examples of the ESW pulse widths and their repetition periods suggesting that the speed of the ESW potential flow changes very rapidly [*after Kojima et al.*, 1994].

plasma instruments. These rapid variations of the potential flow suggest that the PSBL ESW potentials are not controlled by ion dynamics. Since the typical electron (ion) plasma frequency in the PSBL is about 1 kHz (23 Hz), the typical electron plasma oscillation period is about 1 msec (42 msec). Therefore, the rapid variation of the PSBL ESW in a time scale of a few milliseconds cannot be explained by ion dynamics. Further, since the observed pulse widths of the PSBL ESW are a few milliseconds to a few tens of milliseconds, this fact also suggests the close relation to electron dynamics.

Focusing on electron dynamics, we performed computer experiments on nonlinear evolutions of electron beam instabilities by using one-dimensional full particle electromagnetic simulation code called KEMPO (KyOto university ElectroMagnetic Particle cOde) [*Matsumoto and Omura*, 1985; *Omura and Matsumoto*, 1993]. Since electron beams are frequently observed in the lobe region close to the PSBL, electron beam instabilities are one of the most plausible generation mechanisms for the PSBL ESW. *Matsumoto et al.* [1994a], *Omura et al.* [1994], and *Omura et al.* [1996] succeeded in reproducing the PSBL ESW waveforms in the above computer experiments. They performed simple computer experiments with periodic boundaries. They assume isodensity bistreaming electron beams and found that the nonlinear evolution of the beam excited electron plasma waves leads to the formation of quasi-stable isolated electrostatic potential. Figure 4.15 shows a time evolution of the bistream instability. Left and right panels display the time variation of $x - v_x$ phase diagram of electrons and ions, and corresponding electron velocity distributions, respectively. In this computer experiment, they assumed ions drifting with the same speed with one of electron beams. As shown in the panel at $t = 51$, the bistream electrons excite and form strong static potentials and most of electrons are trapped in excited potentials. As time elapses, the excited potentials start to coalesce and in the final stage at $t = 410$ we see the very stable isolated potential structures. These stable potentials are equivalent to a kind of the Bernstein-Greene-Kruskal (BGK) modes, which were proposed as a stationary nonlinear electrostatic wave by *Bernstein et al.*, [1957]. These two isolated potentials shown in the bottom panel correspond to the PSBL ESW potentials as shown in Fig. 4.9. *Matsumoto et al.* [1994a] show the resemblance of PSBL ESW waveforms observed by Geotail and those reproduced by computer experiments as shown in Fig. 4.16. The upper three panels in Fig. 4.16 show representative ESW waveforms observed by Geotail. On the other hand, the middle three panels are snapshots of spatial waveforms reproduced by computer experiments at three different times. The data in the middle panels are spatial waveforms, but since the corresponding potentials stream with almost the same velocity of electron beam velocity V_d as shown in bottom panels, we can easily transform these spatial waveforms to the temporal waveforms. The results from computer experiments shown in Fig. 4.16 provide a good agreement with the observed PSBL ESW waveforms. Further, we can confirm that the BGK potential appearing as electron vortices in the bottom panels correspond to the PSBL ESW waveforms. It is evident that polarity of these reproduced potentials is positive. Therefore, although we cannot obtain the potential polarity from Geotail observations, we can conclude that the polarity of the PSBL ESW potential model is positive by applying these results from our computer experiments. This conclusion is consistent with above mentioned specification that the PSBL ESW is closely related to electron dynamics.

As stated above, we succeeded in reproducing the ESW waveforms by computer experi-

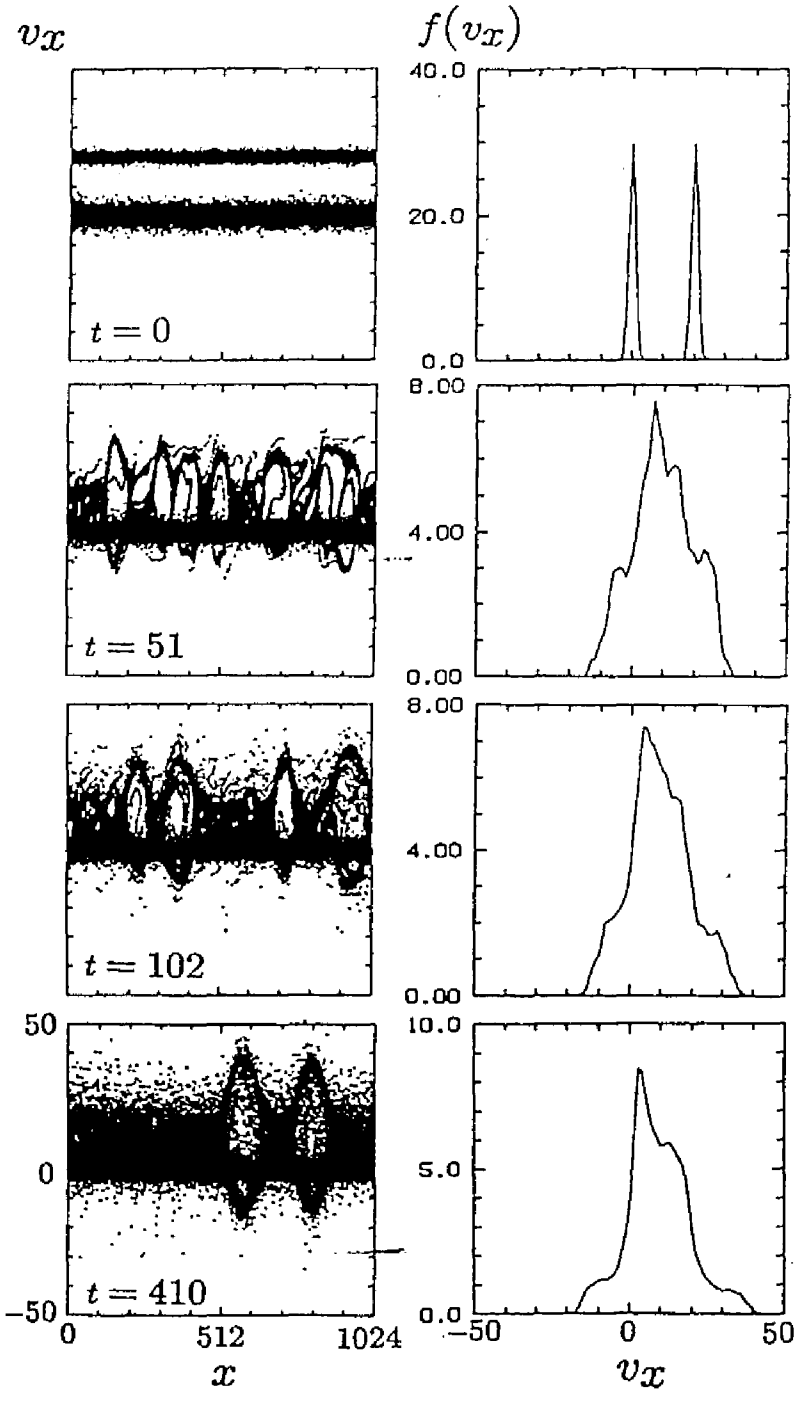

Figure 4.15: Time evolution of the bistream electron beam instability [*after Omura et al.*, 1996].

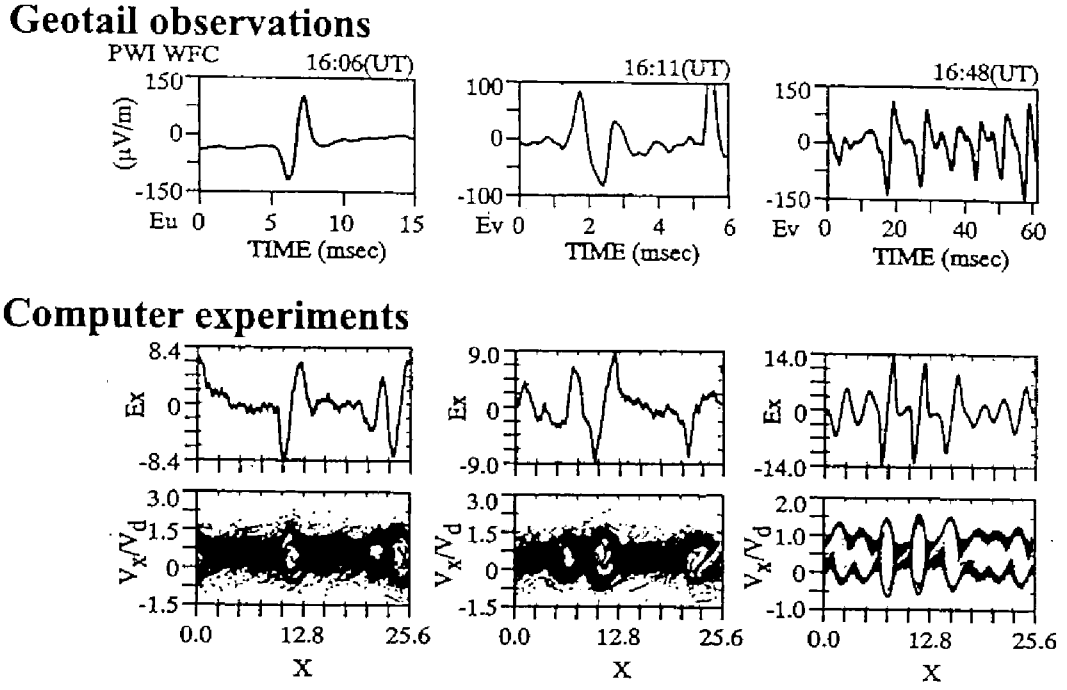

Figure 4.16: Representative PSBL ESW waveforms (upper), spatial waveforms (middle) and corresponding electron distributions in $x - v_x$ phase space (lower) reproduced by a particle computer experiment [*after Matsumoto et al.*, 1994b].

ments on the electron bistream instability. However, the electron distribution shown in the top panel of Fig. 4.15 is not realistic in the PSBL region. We do not observe such bistream electrons in the PSBL.

Omura et al. [1996] extensively performed computer experiments in order to study the parametric dependence of the nonlinear evolution in electron beam instabilities by assuming several types of electron velocity distributions. They concluded that the most plausible generation mechanism of the ESW potentials is the bump-on-tail instability. The initial velocity distribution of electrons is displayed in the top panel of Fig. 4.17.

We can see that the nonlinear evolution of the bump-on-tail instability leads to the formation of the BGK mode as shown in the bottom panel of Fig. 4.17. The bump-on-tail velocity distribution is more realistic than the bistream velocity distribution. Such velocity distributions can be formed around reconnection regions in the geomagnetic tail by acceleration due to intense electric fields at x type neutral points. *Omura et al.* [1996] also point out another important point. Their computer simulations show that the evolution to the BGK mode from the bump-on-tail instability is independent of background ions. In the case of the bistream instability, when ion temperatures are less than electron temperatures, the excited waves are decayed into ion acoustic waves and they do not evolve to the BGK mode. However, in the case of the bump-on-tail instability, there exist no significant influences of ions to their evolution to the BGK mode. This result is contrary to results of correlation between the BEN and high energy ion flows. As we stated before, there do not exist complete one-to-one correlations between the BEN and high energy ion flows, but it is evident that the BEN has some relations to ion flows. *Kojima et al.* [1994] compare the

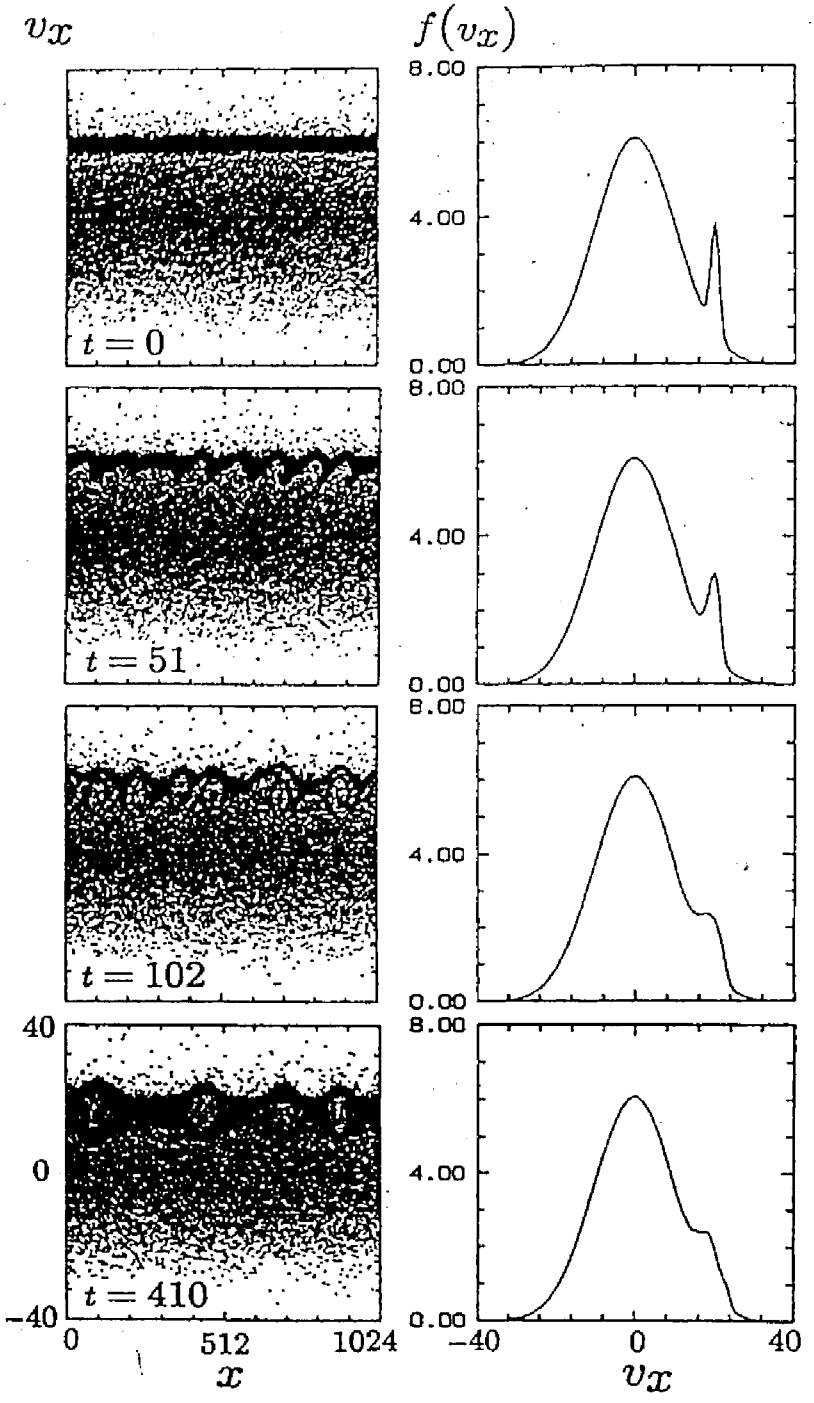

Figure 4.17: Time evolution of the bump-on-tail instability [*after Omura et al.*, 1996].

time variation of the BEN spectra with the variation of ion parameters. In order to study the relation of the BEN to the ion parameters, we can examine the correlation between BEN and the ion (plasma) bulk speed and temperatures shown in Fig. 4.18. The top panel of this figure (a) is a frequency-time spectrogram obtained by the SFA and MCA (below 24 Hz) on September 14, 1993 at (GSM X, GSM Y, GSM Z)=(-71, 22, -5 R_E). The lower two panels (b) and (c) show a time history of the tailward ion bulk velocity and the ion temperature measured along the y-direction in spacecraft coordinates using the Ion Energy Analyzer (EA-i) of the Low Energy Particle experiment (LEP) [*Mukai et al.*, 1994]. During most of the period depicted in Fig. 4.18, GEOTAIL moved into the lobe/mantle region after the multiple entries into the PSBL [*Saito et al.*, 1994].

The SFA frequency-time spectrogram in the top panel shows the intense BEN spectrum. The uppermost frequency ($f_{\max}$) of the BEN from 16:00 to 16:13 (UT) lies around the local electron plasma frequency which is indicated by the lower cutoff frequency of the continuum radiation around 2 kHz. Beginning near 16:12 (UT), $f_{\max}$ smoothly decreases in frequency to a level below the local electron cyclotron frequency. Comparing this behavior with those of the plasma bulk flow and ion temperature data in the middle and bottom panels, we see a correlation between the BEN intensities and the velocity and temperature of the tailward ion flows. The most clear event is the sudden decrease of ion bulk velocity and temperature at 16:11:40 (UT). Around this time, the BEN intensities suddenly decrease.

We cannot ignore this correlation between ions and BEN spectra, however, computer experiments show that the ESW are not directly related to ion parameters. The important point is that the BEN does not consist only of the PSBL ESW. What we stress here is that the PSBL ESW mainly contribute to the high frequency portion of the BEN. The low frequency portion, especially below f_{ce}, is possibly contributed to by another different wave mode. Therefore, we can speculate that the ion parameters control the low frequency portion of the BEN spectra, and that they have no relation to the ESW.

4.5.2 Two-dimensional computer experiments

We showed that the nonlinear evolution of the bump-on-tail instability leads to the formation of the nonlinear BGK mode corresponding to the PSBL ESW potential. We succeeded in reproducing isolated potential structures parallel to the ambient magnetic field, but in order to discuss perpendicular structures, we need to perform two-dimensional computer experiments. As we introduced in sections 4.3 and 4.4, while most of ESW observed in the distant tail region have one-dimensional structures, PSBL ESW with two-dimensional potential structures can be also found more in the near tail region than in the distant tail region. two-dimensional computer experiments also allow us to study two-dimensional structures of the ESW. Figure 4.19 shows the time evolution of the spatial waveforms in the two-dimensional computer experiments conducted by *Miyake et al.* [1998]. The ambient magnetic field is in x direction lying on the simulation $x-y$ plane. They assume the bump-on-tail electron velocity distribution in the initial condition.

The initial stage in panel (a) of Fig. 4.19 shows that Langmuir waves with sinusoidal waveforms are excited due to the bump-on-tail instability. Excited Langmuir waves continue to grow and start to coalesce each other. The final stage shown in a bottom panel of Fig. 4.19 provide the confirmation of PSBL ESW potential formation in two-dimensional simulation system. As seen very clearly, the formed potential has its uniform structure

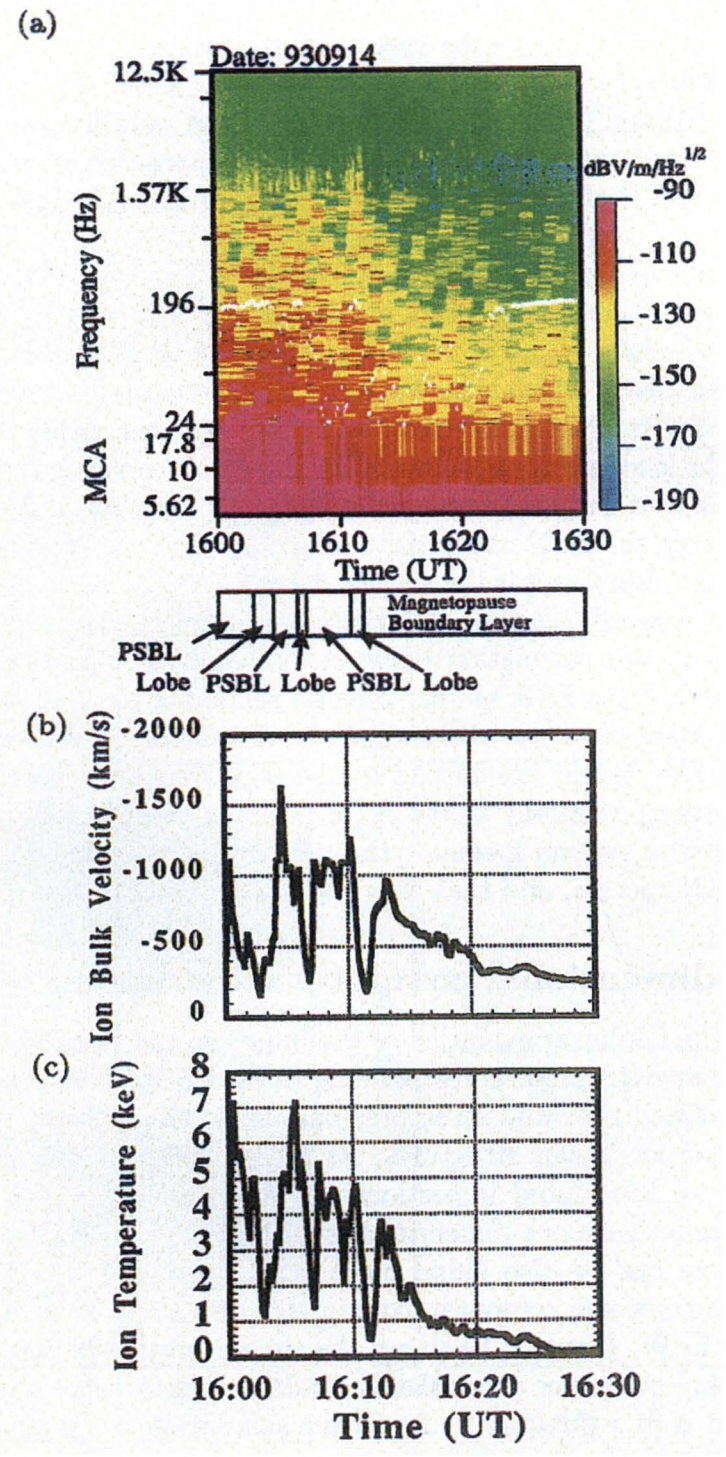

Figure 4.18: Time history of (a) plasma wave spectra, (b) the tailward ion drift velocity, (c) the ion temperature of the y-direction in the spacecraft coordinates [*after Kojima et al.*, 1994].

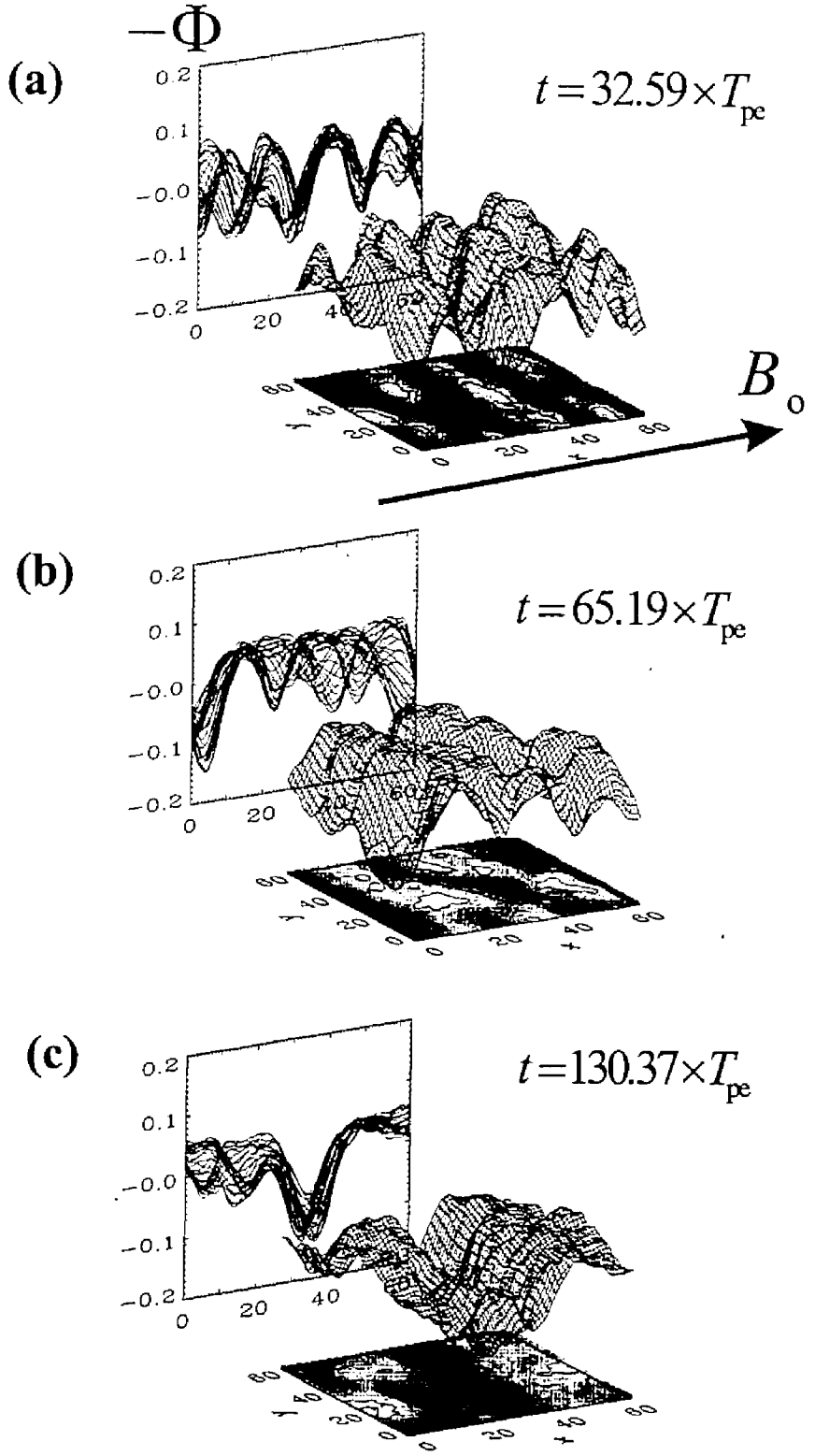

Figure 4.19: Results of two-dimensional computer experiments. Time evolution of spatial waveforms lead to the one-dimensional potential structure through the two-dimensional ones [*after Miyake et al.*, 1998].

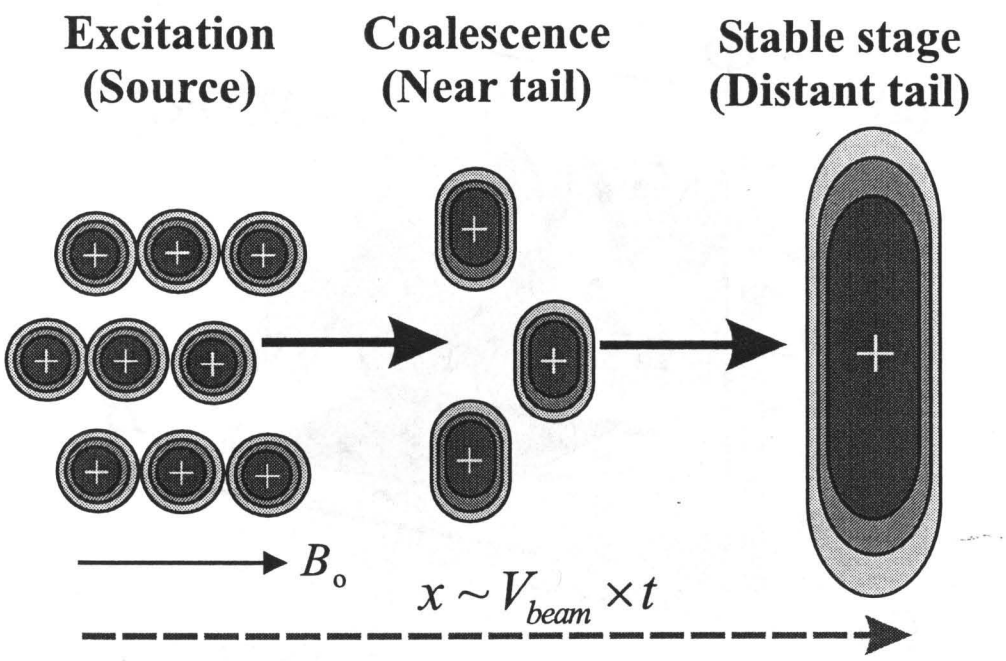

Figure 4.20: Schematic illustration of the time evolution of the ESW potential.

in the perpendicular direction relative to the ambient magnetic field. This result provides a good agreement with the PSBL ESW potential model shown in Fig. 4.9. *Miyake et al.*, [1998] concluded that the uniform perpendicular potentials are formed through the diffusion process due to the electron cyclotron motion at the contact boundary of different potential structures aligned in the perpendicular direction. Another interesting point in this simulation is shown in panel (b) of Fig. 4.19. At this stage of $t = 65.19 \times T_{pe}$, the formed potential structures are isolated in both parallel and perpendicular directions. These potential structures correspond to the two-dimensional PSBL ESW potential structure as shown in Fig. 4.12. Therefore, from the results of the above computer experiment, we can expect that the two-dimensional structure of the PSBL ESW potential is formed in the middle stage of the nonlinear evolution leading to one-dimensional structure at the final stage.

Figure 4.20 schematically shows the scenario of the ESW growing from their excitation through two-dimensional potential to one-dimensional potential structure. In the source region, the bump-on-tail instability takes place and the Langmuir waves are excited. Excited Langmuir waves grow and start to coalesce each other in the parallel direction relative to the ambient magnetic field. The time scale of the electron diffusion due to the cyclotron motions is slower than that of the coalescence in the parallel direction. Therefore, before the formation of the uniform perpendicular structure, isolated structures can be observed. Due to the diffusion in the perpendicular direction, one-dimensional potential structure is formed at the final stage.

As we stated in section 4.4, two-dimensional PSBL ESW are frequently observed in the near tail region. When we apply the above scenario to this result, we can speculate that the two-dimensional PSBL ESW observed in the near tail region is equivalent to the middle stage of the PSBL ESW nonlinear evolution. Since the ESW potentials propagate with

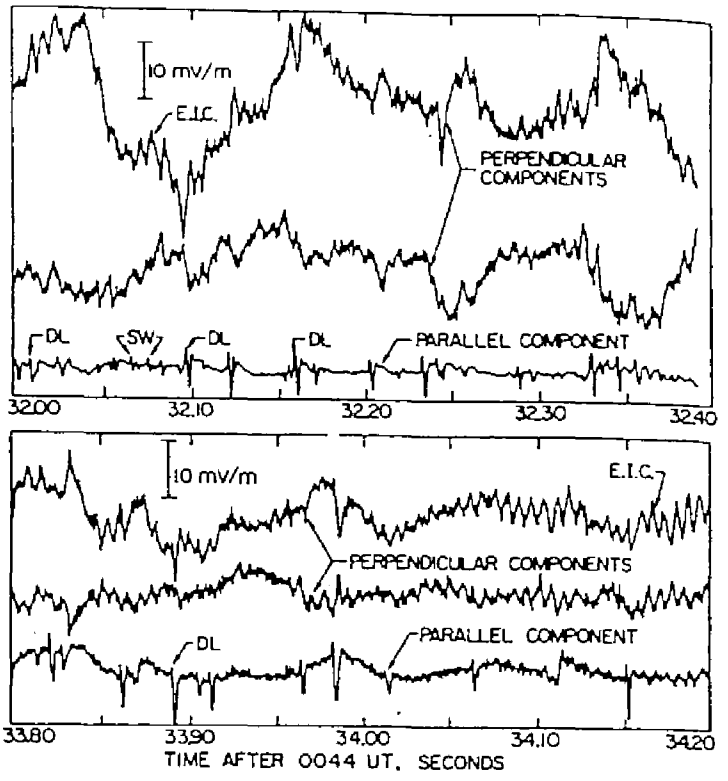

Figure 4.21: Solitary structures observed by the S3-3 satellite in the polar magnetosphere [*after Temerin et al.*, 1982].

almost the same speed of electron beams, the two-dimensional ESW observed in the near tail region suggest that the source region of the ESW is located in the near tail region. This result is very important for identifying source locations of the PSBL ESW.

4.6 Solitary waves observed by other spacecraft

Solitary waves similar to the ESW observed by Geotail have been also observed by other spacecraft. The initial observation of the solitary waves was reported by *Tamerin et al.*, [1982]. They found 2 kinds of solitary structures in the electric field data observed by the S3-3 satellite in the polar magnetosphere at the altitude of 6030 km.

Figure 4.21 shows the observed solitary structures reported by *Temerin et al.* [1982]. The displayed data are composed of two perpendicular and one parallel electric field components relative to the ambient magnetic field. The large amplitude waves in the perpendicular components are the electrostatic ion cyclotron waves. Two kinds of solitary structures can be seen in the parallel component. Since these are purely electrostatic, these structures correspond to the isolated electrostatic potentials. The structures with a net potential drop are refereed to as weak double later (WDL) and those without net potentials as solitary waves (SW). Here, "weak" means that the potential energy of the WDL is smaller than

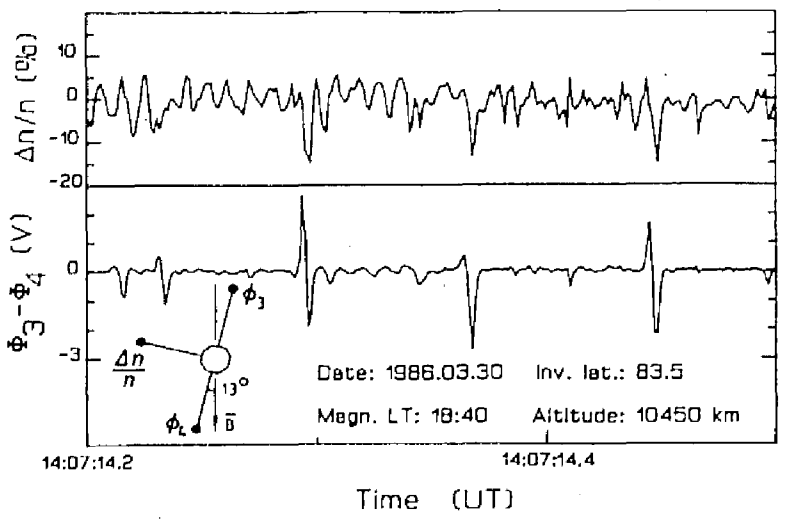

Figure 4.22: Simultaneous density (upper) and electrostatic difference variations (lower) during passage of solitary structures [*after Boström et al.*, 1988].

thermal energies of background electrons as follow:

$$e\phi_{\text{potential}} \leq T_e. \tag{4.10}$$

They pointed out that these solitary structures are correlated with upward ion flows and enhanced loss cone electrons.

Due to the limitation of the instruments onboard the S3-3 satellite, the enough data analyses were not conducted until the observations by the Viking satellite. *Koskinen et al.* [1987] and *Boström et al.* [1988] conducted detailed analyses of the WDL and SW observed by the Viking satellite. They observed similar solitary structures associated with the density depletion as shown in Fig. 4.22. They showed that the observed solitary structures flow upward along the ambient magnetic field with velocities of 5 $\sim$ 50 km/s, and their potential spatial scale is 50 $\sim$ 100 m, which corresponds to about 10 λ_D, where λ_D is the Debye length. They also reported that observed SW and WDL correspond to negative potentials with its amplitude of 2 $\sim$ 3 V. Further, *Koskinen et al.*, [1990], *Mälkki et al.*, [1993] and *Mälkki et al.*, [1994] performed statistical surveys on the solitary structures using the Viking data. They showed that these structures are mostly observed at altitudes between 7000 and 11000 km and mean value for measured net potential drops varies between -0.6 and $+0.1$V. Further, the close relation between these structures and beams of moderate-energy upward flowing ions are revealed by their surveys.

Similar solitary structures are detected in the lower altitude of the polar region by the Freja spacecraft [*Dovner et al.*, 1994]. The data collected at the altitude of 1748 km resemble the previous waveforms observed by the S3-3 and Viking satellites, but solitary structures by the Freja propagate perpendicular to the ambient magnetic field with a very slow velocity of 4 km/s. This characteristic is completely different form that of the solitary structures observed by other spacecraft instead of the similarity of the waveforms.

The report of the ESW from the Geotail is followed by 2 different spacecraft observations

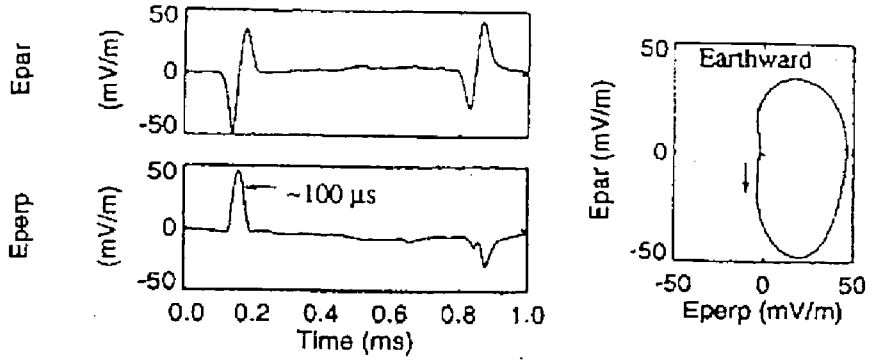

Figure 4.23: Solitary waves observed by FAST spacecraft. The right plot is $E_{\parallel}$ versus $E_{\perp}$ of the solitary waves [*after Ergun et al.*, 1998].

in the polar region. The FAST satellite found solitary waves in the bursty broadband VLF emissions in the downward current region of the mid-altitude auroral zone ($\sim$ 3000 km). Figure 4.23 shows the solitary waves observed by FAST spacecraft.

The display format of Fig. 4.23 is similar to that of Fig. 4.11. The features of observed solitary waves are very similar to those of two-dimensional ESW observed in the near tail region, but their pulse width is about $\sim$ 100 μsec, which is much shorter than that in the typical PSBL ESW. Since the FAST satellite has a capability for measuring with very high time resolutions, *Ergun et al.* [1998] revealed the modulation of upgoing electron fluxes of $\sim$ 100 eV synchronizing with appearance of solitary waves. This modulation is consistent with the result that the estimated positive potential amplitude of solitary waves is about 100 V. They report that the observed solitary structures propagate upward with velocity of $\sim$ 4500 km.

Solitary waves in the high altitude polar region are observed by Polar spacecraft [*Franz et al.*, 1998]. *Franz et al.* [1998] observed solitary waves shown in Fig. 4.24 at radial distances of 2.02 to 8.5 R_E. In Fig. 4.24, the top panel shows waveforms of the perpendicular electric field component. Waveforms shown in lower two panels are observed by two monopole antennas parallel to the ambient magnetic field at this observation time. We can find that these observed solitary waves also have two-dimensional potential structures. The observed solitary waves correspond to positively charged potentials propagating at velocities of the order of 1000 km/s in the parallel direction relative to the ambient magnetic field. These features are very similar to those of solitary waves observed by FAST satellite, but while the solitary waves of the FAST propagate in the upward direction, those of the Polar spacecraft in both directions. This difference will be discussed in Chapter 5 referring to the Geotail observations. Polar spacecraft also succeeded in detecting solitary waves in lower altitude auroral zone of $\sim$ 5000 km [*Mozer et al.*, 1997].

The above introduced solitary structures are observed in the polar region. Another satellite "ISEE-1" detected the similar waveforms at the magnetic ramp of the bow shocks as shown in Fig. 4.25 [*Wygant et al.*, 1987]. *Anderson et al.* [1982] also reported the very bursty electrostatic waves called "spikes" during the bow shock crossings. They examined only spectrum data, but their "spikes" might be the similar waves to those of *Wygant*

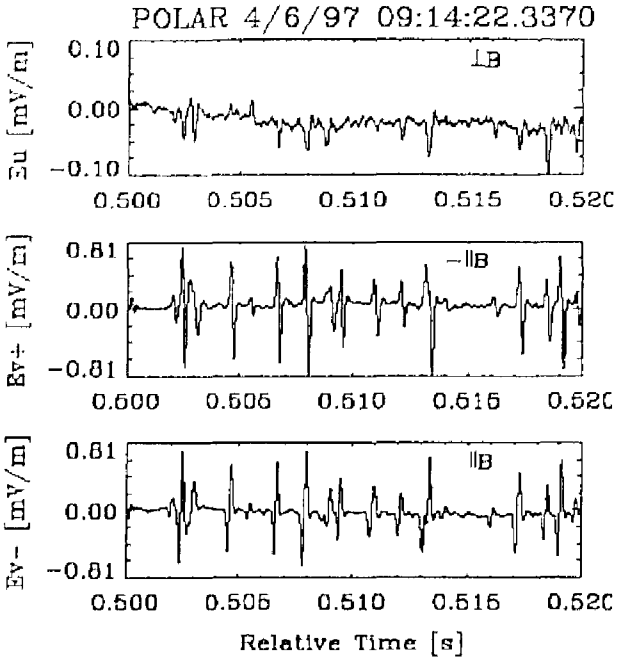

Figure 4.24: Solitary structures observed by POLAR spacecraft. The E_u antenna is roughly perpendicular to B_o, while the E_{v+} and E_{v-} antennas are roughly parallel to B_o [*after Franz et al.*, 1998].

et al. [1987]. Geotail PWI also observed the ESW at the bow shock transition layer [*Matsumoto et al.*, 1997b]. Figure 4.26 shows a representative ESW waveforms observed by Geotail at the bow shock. When we compare the ESW by Geotail with the solitary waves by ISEE-1, we find that both amplitudes are the same order of a few tens of mV/m but the pulse widths are different. While the typical pulse width of solitary waves from ISEE-1 is about 100 msec, the ESW pulse width from Geotail is about 1 msec. This difference suggests that the coexistence of different size of isolated potential structures at the bow shock transition layer.

We also found the ESW in the distant magnetosheath region [*Kojima et al.*, 1997a]. The ESW in the magnetosheath will be discussed in Chapter 8.

As we stated in this section, solitary structures are common plasma phenomena in space plasmas. The characteristics of each solitary structure observed by several spacecraft are summarized in Table 4.1.

4.7 Summary and discussions

In this chapter, we discussed waveform observations of the BEN in the PSBL. The WFC receiver revealed that the BEN spectra consist of a series of isolated pulses which we addressed ESW. The ESW waveforms are isolated bipolar pulses, and they mainly contribute to the high frequency portions of the BEN spectra. The ESW are purely electrostatic and they correspond to isolated potential structure propagating along the ambient magnetic field. The structure of the ESW in the distant tail seems to be one-dimensional with a

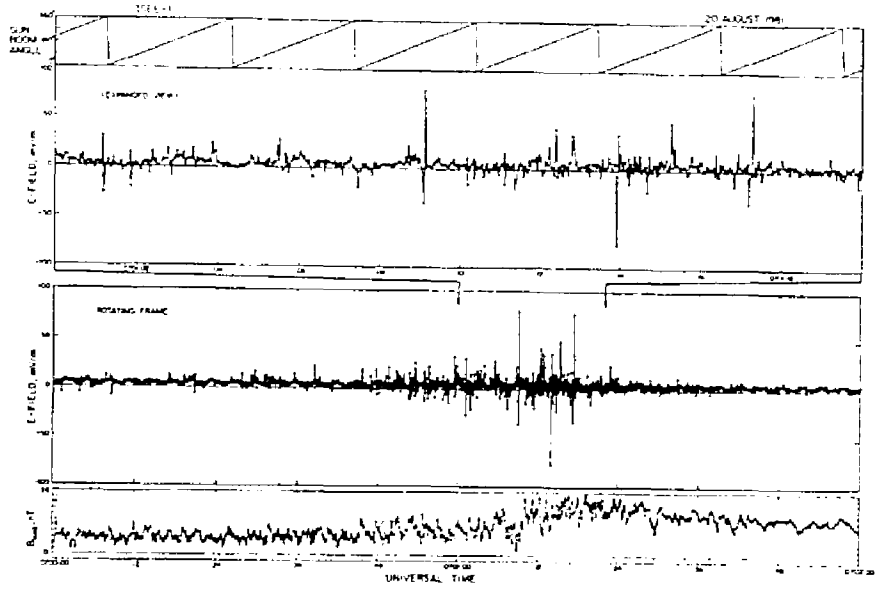

Figure 4.25: Single component, raw electric field data and magnetic field (bottom) magnitude data as well as antenna spin phase (top) from ISEE-1 bow shock crossing [*after Mozer*, 1990].

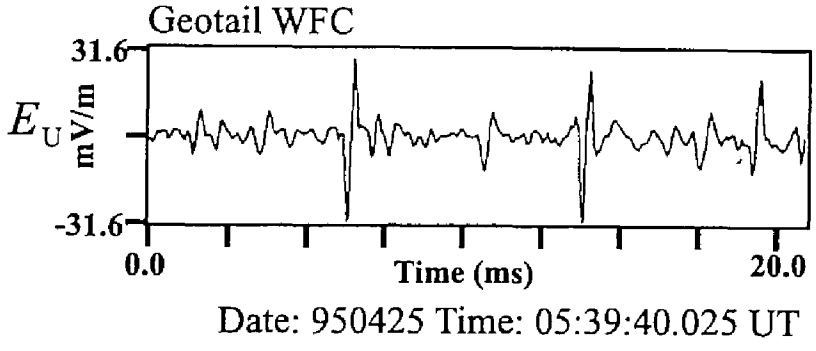

Figure 4.26: ESW observed by Geotail at the bow shock transition layer [*after Matsumoto et al.*, 1997].

Table 4.1: Characteristics of the solitary waves observed in the various regions.

Region	Polar region				Bow shock(MS)		Near tail	Distant tail
Spacecraft	S3-3/Viking	Freja	FAST	POLAR	ISEE-1	Geotail	Geotail	Geotail
Pulse width	~ 20msec	~ 5 msec	~ 100μ sec	< 1msec	~ 100msec	~ 5msec	1 msec ~ 10 msec	1 msec ~ 10msec
Amplitude (Peak-to-peak)	~ 100mV/m	~ 10 mV/m	1~ 100mV/m	1mV/m~10 mV/m	~ 100 mV/m	~ 100 mV/m	< 1mV/m	< 1mV/m
Flow direction to B_0	parallel	perpendicular	parallel	parallel	?	parallel	parallel	parallel
Flow speed	5 ~ 50 km/s	4km/s	~5000km/s	500~1000km/s	?	?	~10000km/s	~10000km/s
Sign of potential	negative	negative	positive	positive	?	positive	positive	positive
Potential Structure	2D	?	2D	2D	?	1D	2D/1D	1D
Net potential	0~ 1V	?	~ 0V ?	~0V	?	0V	0V	0V
Potential depth	a few eV	?	~100eV	~ 1eV	?	?	a few eV	a few eV

uniform perpendicular structure, but many of them observed in the near tail region are likely to be two-dimensional.

The one-dimensional computer experiments on the nonlinear evolution of electron beam instabilities succeeded in reproducing the ESW waveforms. We found that electron beam instabilities lead to quasi-stationay BGK mode in the final stage. The potential corresponding to the BGK mode is very isolated and propagate along the magnetic field. Reproduced waveforms agree well with the PSBL ESW waveforms. We examined several electron beam instabilities for the formation of the BGK mode in several initial parameters, and found that the most plausible generation mechanism is the bump-on-tail instability. The computer experiments also showed that nonlinear evolution of the bump-on-tail instability has no relation to ion dynamics. Further, by performing two-dimensional computer experiments, we showed that the uniformity of the perpendicular structure of the ESW potential depend on the growing phase of the PSBL ESW.

By combining the above results from spacecraft observations and computer experiments, we can describe a following scenario for the observation of the ESW.

1. The bump-on-tail instability takes place at some regions around electron acceleration points and Langmuir waves are excited.

2. Langmuir waves propagate along the ambient magnetic field. When the excited Langmuir waves reach the nonlinear stage, their corresponding potentials start to coalesce each other in the parallel direction. When spacecraft observe the ESW in this stage, the potentials of the observed ESW have two-dimensional structures, because the uniformity in the perpendicular direction due to diffusion process has not been completed at this stage.

3. The ESW potentials in the previous stage continues to propagate at the almost same speed with those of electron beams as the free energy source.

4. During the ESW propagation, they continue to grow and to coalesce. On the other hand, the diffusion processes due to cyclotron motions of electrons complete to make the perpendicular structure uniform at the final stage. At this final stage, spacecraft observe the ESW with one-dimensional structures.

As we stated in section 4.6, the solitary waves can be observed in various regions, and they are common plasma phenomena in space plasmas. Can we apply our model for the PSBL ESW to other solitary waves ? Table 4.2 provide a clue to answer to this question. In our model of the bump-on-tail instability, the excited waves are Langmuir waves. Therefore, even after the coalescence, observed pulse widths should be related to local electron plasma oscillation period. Therefore, it is an interesting attempt to compare ratios of observed pulse widths ΔW to electron plasma oscillation periods $(1/f_{\mathrm{pe}})$.

Table 4.2 shows the comparison of the characteristic time scales of solitary structures observed by Geotail, Polar, Viking and FAST spacecraft. In the table, ΔW, f_{pe}, and f_{pi} denote observed pulse widths, local electron plasma frequencies, and local ion plasma frequencies, respectively. $\Delta W \cdot f_{\mathrm{pe}}$ and $\Delta W \cdot f_{\mathrm{pi}}$ mean ratios of observed pulse widths to plasma oscillation periods of electrons and ions, respectively. In this table, we can see that the ratios in solitary waves observed by Geotail in PSBL, Polar and FAST spacecraft show

Table 4.2: Characteristic time scales of solitary waves observed by different spacecraft.

	$\Delta W \cdot f_{pe}$	$\Delta W \cdot f_{pi}$
Geotail (PSBL)	**1~10**	**0.02~0.23**
Geotail (Bow shock)	**20~40**	**0.5~0.9**
Geotail (Magnetosheath)	**20~**	**0.5~**
Polar	**4.5~9**	**0.1~0.2**
Viking	**~400**	**~9**
FAST	**~3**	**~0.07**

Positive potential

Negative potential

almost the same order of values. The ratios in solitary waves by Viking spacecraft are significantly different from others. The ratios from Geotail in the bowshock and magnetosheath show moderate values.

The group of Geotail PSBL ESW, Polar solitary waves, FAST solitary waves have the values of $\Delta w \cdot f_{\mathrm{pe}}$ are almost between 1 and 10. This means that these solitary waves are closely related to electron dynamics, because these values mean their pulse widths are in the order of electron plasma oscillation periods. Further, what we stress here is that these solitary waves were reported to correspond to positively charged potentials. We note that while the positive polarity of the GEOTAIL PSBL ESW potentials is inferred by the results of computer experiments, Polar and FAST spacecraft directly measured positive potentials. These agreements and consistencies suggest the possibility that the solitary waves observed by Polar and FAST spacecraft are also the BGK potentials equivalent to electron vortices which are the results of the nonlinear evolution of electron beam instabilities.

On the other hand, the value of $\Delta W \cdot f_{\mathrm{pe}}$ for the Viking solitary waves shows a huge value of 400. This means that the pulse width is much larger than the time scale of electron dynamics. However, the value of $\Delta W \cdot f_{\mathrm{pi}}$ has a reasonable value of nine. This result is very suggestive to the relation of the Viking solitary waves to ion dynamics. Since Viking spacecraft found that the solitary wave potentials are negatively charged, the result is very consistent as the counter part case of solitary waves observed by Geotail, Polar, and FAST spacecraft.

Since the discovery of the solitary waves by S3-3 and Viking spacecraft, many theoretical attempts have been made for explaining their generation mechanisms. The candidates for their generation mechanisms are mainly classified into 2 kinds of waves. They are ion acoustic solitons and ion hole instability. The ion acoustic soliton is proposed as the nonlinear evolution of beam driven ion acoustic instabilities [*e.g., Lotko and Kennel*, 1983; *Marchenko and Hudson*, 1995]. On the other hand, the quasi-stationary BGK mode is also proposed for generation mechanisms of solitary waves observed by Viking spacecraft. The nonlinear evolution to the BGK mode is addressed as phase-space ion hole instability, which is driven by ion-ion two streams or electron currents [*Dupree*, 1982; *Hudson et al.*, 1983]. This phase-space ion hole model is the counter part of our ESW potential models consisting of phase space "electron hole" (vortices). In the above both mechanisms, the formation of

solitary waves has been confirmed. *Mälkki et al.* [1989] compared observation results from S3-3/Viking spacecraft with the results of computer experiments focusing on the above two generation mechanisms. Since the velocities of observed solitary structures are much smaller than velocities expected by the theory of ion acoustic solitons, they concluded that it seems that the theory of nonlinear ion hole instability is in best agreement with the observations.

Before concluding this chapter, we need to discuss low frequency components of the BEN. As we stated in this chapter, the ESW mainly contribute to the high frequency portion of the BEN spectra. This point can be clearly seen in Fig. 4.27. Figure 4.27 shows the frequency-time spectrogram generated from the WFC data (upper panel) as well as 2 snapshots of waveforms and corresponding Fourier spectra (lower 4 panels). The shown data are observed at (GSM X, GSM Y, GSM Z)=(−12.5, 0.5, 0.7 R_E) on April 15, 1995. We pay our attention to the latter part of the upper panel of Fig. 4.27. The intense broadband emissions gradually start at 4.25 sec. Especially spectra after 5 sec show the broadband nature. We find that the ESW can be observed during the period after 5 sec in the upper panel.

The observed waveforms and corresponding Fourier spectra are displayed in lower panels. While waveforms observed at 16:51:11.732 (UT) are the ESW (shown in lower right panels), those observed at 16:51:10.708 (UT) are low frequency quasi-sinusoidal waves superposed by small amplitude high frequency waves. The difference between two snapshots is clear in the Fourier spectra shown in 2 bottom panels. By comparing these 2 Fourier spectra, it is evident that the ESW contribute the high frequency portion (beyond about a few hundreds of Hz in this case) of the BEN spectra. Further, the quasi-sinusoidal waves shown in left lower panel mainly contribute to the low frequency portions. Since the waveforms are not complete sinusoidal and are distorted, their Fourier spectra show the broadbandness in the frequency range of 10 Hz to a few hundreds of Hz.

Figures 4.28 and 4.29 show the waveforms of $E_{\parallel}$ and $E_{\perp}$ components and hodograms in the similar display format of Fig. 4.10 and Fig. 4.11. Most of the ESW of shown data in Fig. 4.28 are one-dimensional, but three ESW have perpendicular components. The interesting feature can be seen in the lower panel of Fig. 4.29. The shown data are the low frequency component of the BEN. The electric fields of the quasi-sinusoidal low frequency component oscillate in the perpendicular direction. This means that the low frequency component is completely different wave mode from the ESW.

Gurnett et al. [1979] reported that the electric field orientation of the BEN is almost perpendicular to the ambient magnetic field. We pointed out the disagreement with our ESW observations in Section 4.3. However, since Gurnett et al. [1979] examined the electric field orientation using the frequency averaged spectrum intensities, we can expect that their obtained electric field orientation is strongly affected by the low frequency component with larger wave intensities and perpendicular polarizations relative to the ambient magnetic field.

On the other hand, Onsager et al. [1993] reported that the intense high frequency portions of the BEN are oscillating in the parallel direction to the ambient magnetic field, but weak ones have the perpendicular polarizations. We think that they confuse high frequency portion of the BEN with electron plasma waves observed around the local electron plasma frequencies. We will discuss these electron plasma waves in Chapter 7.

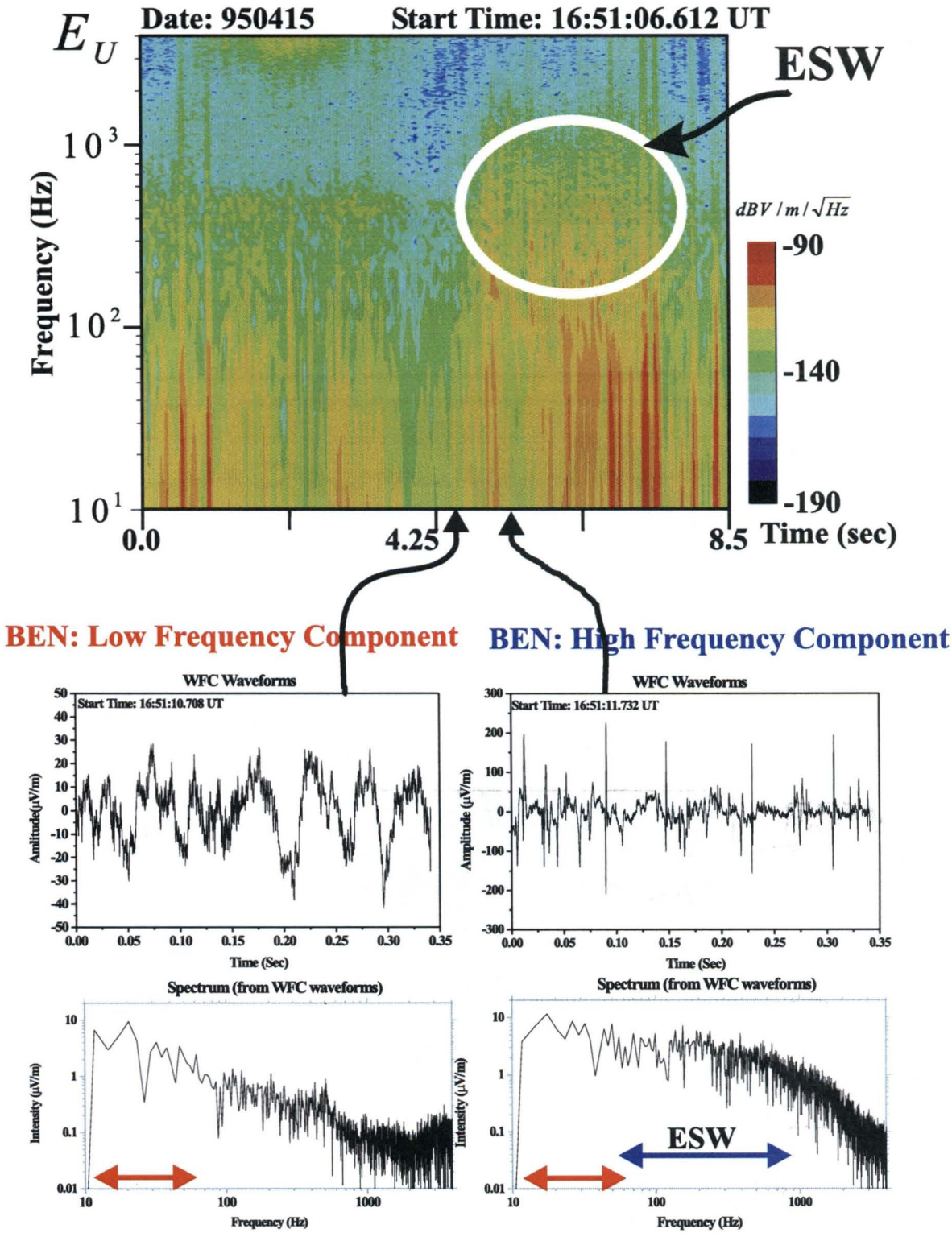

Figure 4.27: Frequency-time spectrogram]generated from the WFC data (top), snapshots of waveforms and corresponding Fourier spectra observed at two different times. We can clearly see that the PSBL ESW mainly contribute to the high frequency component of the BEN.

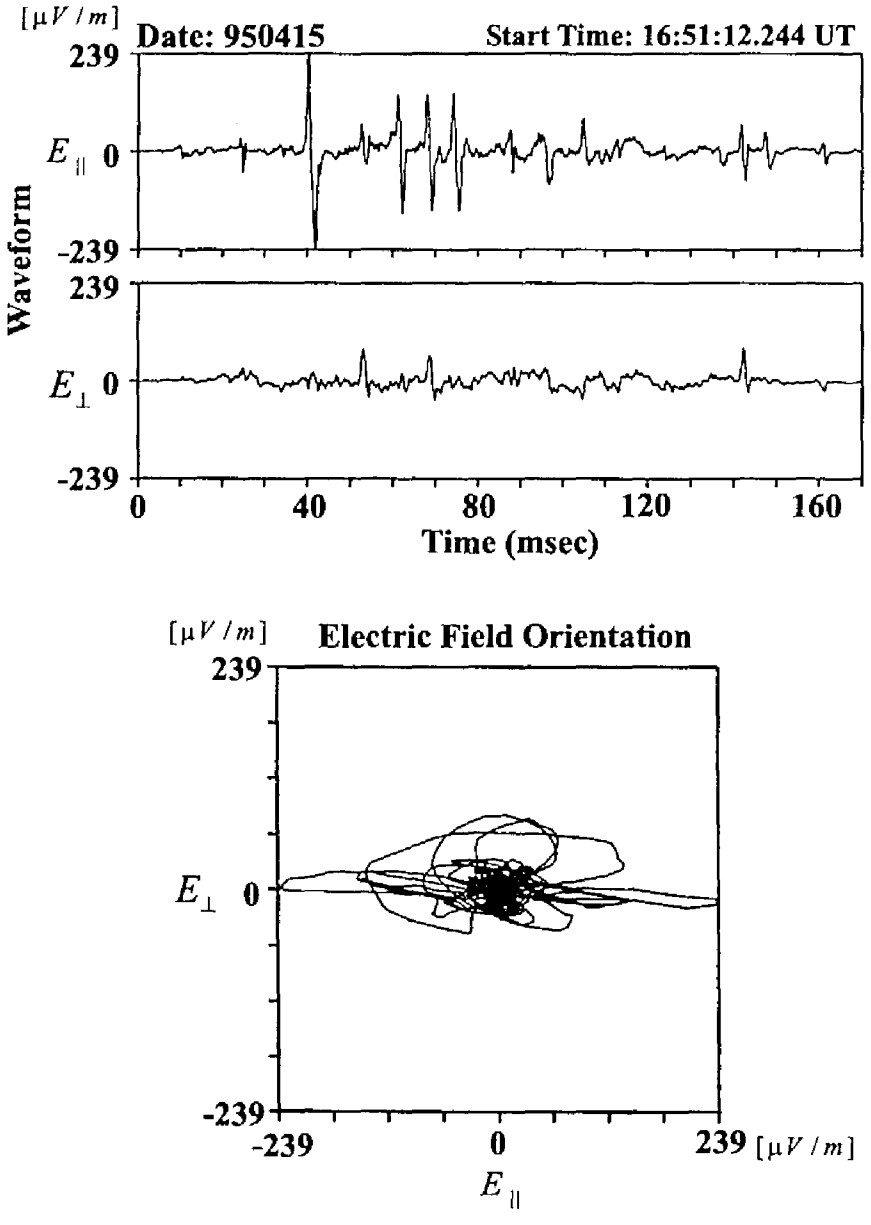

Figure 4.28: Waveforms and electric field orientation of the PSBL ESW.

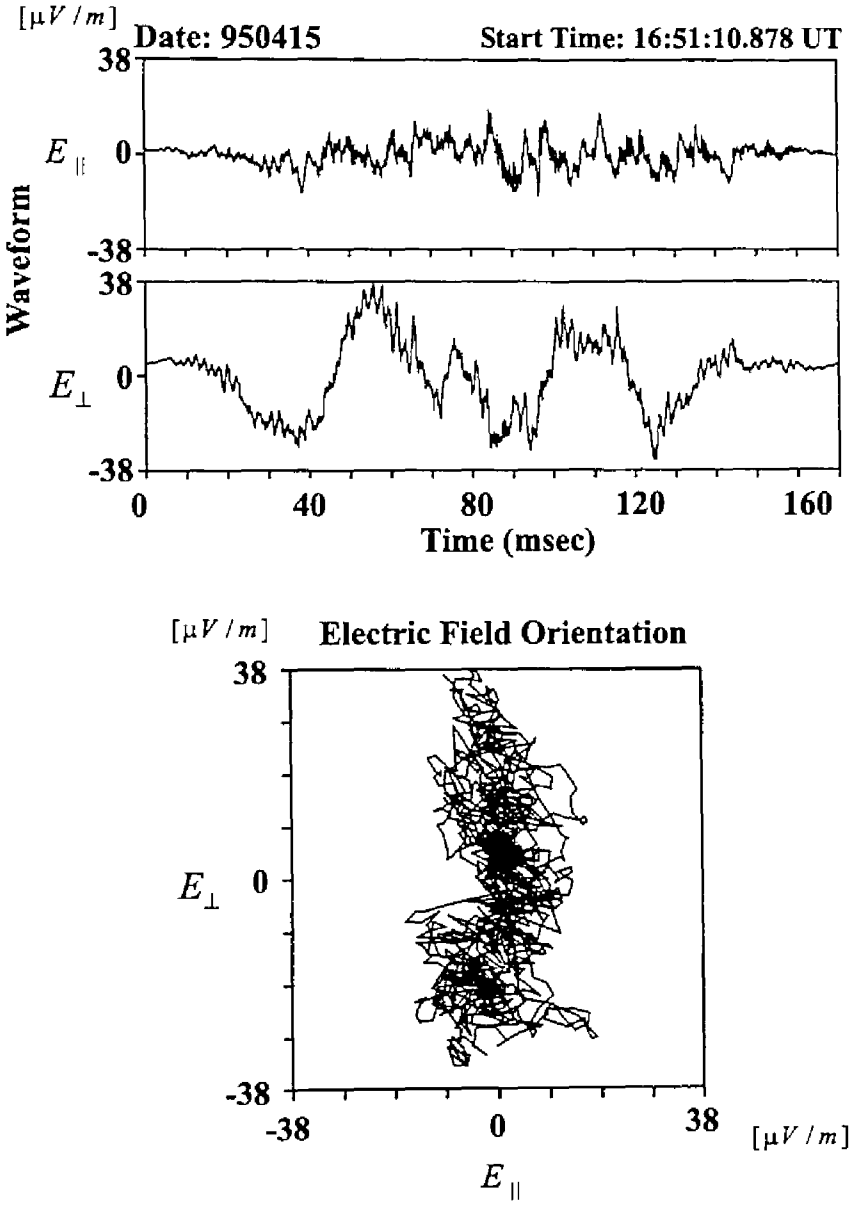

Figure 4.29: Same as Fig. 4.28 but for low frequency component.

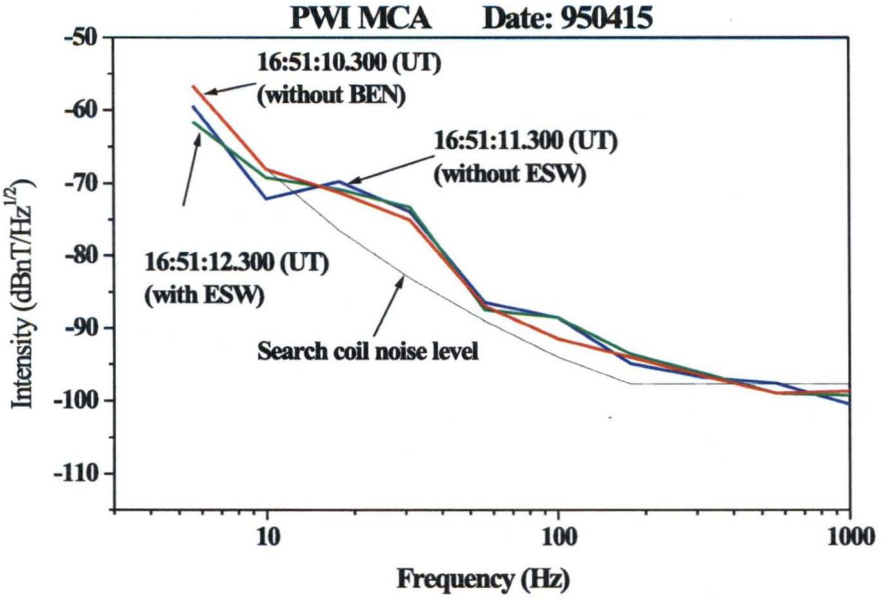

Figure 4.30: Magnetic field spectra observed by the MCA. There exist no differences in the observed spectra in the cases of PSBL ESW, without PSBL ESW, and without BEN.

We do not find any evidence for these low frequency waves to have magnetic field components. Figure 4.30 shows the difference of the magnetic component spectra observed by the MCA. We plot spectra of B_α component at three different times. Three spectra correspond to following timings: (1) Very weak BEN eimissions at 16:51:10.300 (UT), (2) BEN emissions without ESW (only low frequency component) at 16:51:11.300 (UT), (3) BEN emissions with ESW at 16:51:12.300 (UT). We also plot the theoretical search coil noise level. It is evident that there exist no difference in spectral features among above three cases. The weak peak around 20 Hz seems to be the artificial noise. This means that the low frequency component is not accompanied with the magnetic component or that expected magnetic component is below the noise level of search coils.

From the frequency range, the most plausible wave mode is the whistler mode. We roughly estimated the refractive index of whistler mode described as

$$n^2 = 1 + \frac{f_{\rm pe}^2}{f(f_{\rm ce}\cos\theta - f)}. \tag{4.11}$$

In this event, $f_{\rm pe}$ and $f_{\rm ce}$ are 2.846 kHz, and 1.0 kHz, respectively. In the assumption of $\theta = 0°$, we obtain refractive index n is equal to 16 at $f = 30$ Hz. From this refractive index, we can expect the magnetic field intensity at 30 Hz as –66dBnT/$\sqrt{\rm Hz}$. This level is enough higher than the search coil noise level. However, we cannot see corresponding spectra in Fig. 4.30.

Since the refractive index in oblique whistler mode at a fixed frequency becomes larger than that of the parallel whistler mode, oblique propagation whistler modes should have

larger wave amplitudes of the magnetic component. Therefore, we do not have clear explanations about very low amplitude of magnetic components of low frequency BEN. The polarizations are very important clue to identify wave modes, but unfortunately, Geotail does not have the third electric field component along the spin axis, it is very difficult to find the polarizations.

In this section, we only demonstrated the one case study. If we collect more events and performed some statistical analyses, we will obtain important information for the mode identification for the low frequency portions of the BEN in the future.

Recent waveform observations with high time resolutions revealed that solitary waves are commonly observed in space plasmas. Further, the progress of the technique in computer experiments allows us to analyze nonlinear evolutions of excited plasma waves. Computer experiments show us that the BGK mode is the best candidate for generating solitary waves. However, as we discussed in this section, solitary waves observed by Viking are related to ion dynamics, on the other hand, ones observed by Geotail, Polar, and FAST spacecraft are related to electron dynamics. Therefore, we need to explain the comprehensive generation mechanism including both electron and ion dynamics. The comprehensive theory will be proposed under the collaboration of spacecraft observations and computer experiments near future.

Chapter 5

Propagation analyses of the PSBL electrostatic solitary waves

5.1 Introduction

In Chapter 4, we discussed the generation mechanisms of the PSBL ESW observed in the geomagnetic tail region consulting the results from computer experiments on nonlinear evolution of electron beam instabilities. We concluded that the most plausible generation mechanism of the PSBL ESW is the bump-on-tail instability and we can apply this mechanism to the solitary waves observed in the polar region.

What we are interested in the next is to identify the source regions of the PSBL ESW. Our computer experiments show that the nonlinear evolution of the bump-on-tail instability leads to the formation of the BGK potentials. Generally, purely electrostatic waves do not propagate in long distance away. However, since the BGK potentials are very stable, they can propagate to far points from their source regions. Therefore, in order to identify the source locations, propagation analyses of the PSBL ESW are very important. In our BGK potential model, the generated potential structures propagate in the same direction of electron beams. Therefore, the comparison of the propagation direction of the PSBL ESW with electron beam direction detected by plasma measurements provides us with confirmation of our BGK potential model.

The propagation analyses have been made for the solitary waves observed by other spacecraft in the polar region. While *Koskinen et al.* [1987] showed that the solitary waves and weak double layers observed by Viking spacecraft propagate in the upward direction, *Ergun et al.* [1998] showed that the solitary waves observed by FAST spacecraft also propagate in the upward direction. On the other hand, the solitary waves observed by Polar spacecraft at higher latitude polar region are reported to propagate in both upward and downward directions by *Franz et al.* [1998].

Propagation directions for the above solitary waves have been decided by observation time difference between two monopole electric antennas. Unfortunately, Geotail PWI does not have such a capability to detect the time difference. However, by using our results from spacecraft observations and computer experiments, we can identify propagation directions of the PSBL ESW in the Geotail data. In the present chapter, we will demonstrate the propagation directions of the PSBL ESW using Geotail data and discuss their source

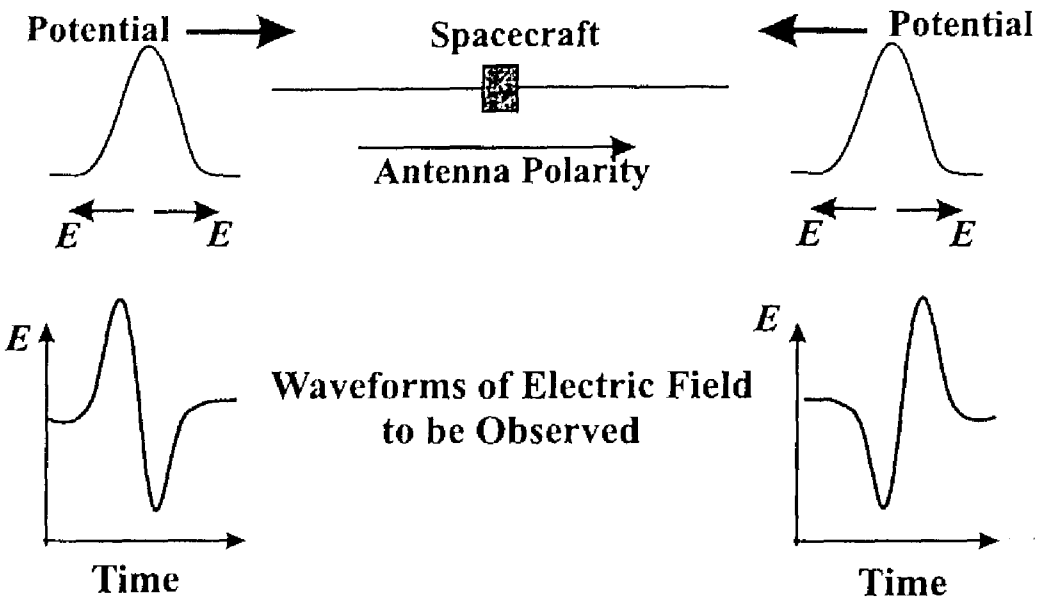

Figure 5.1: Schematic illustration on the method of propagation analyses.

locations.

5.2 Method

Generally, it is very difficult to identify propagation directions of purely electrostatic waves. However, in the case of the PSBL ESW, if we assume following points, we can identify their propagation directions using the waveforms of the ESW and antenna polarities. Followings are conditions in the propagation analyses of the PSBL ESW:

1. The polarity of the PSBL ESW potentials is positive.
2. The ESW potentials propagate along the ambient magnetic field.
3. Polarities of electric field antennas are known in the ground tests.

Condition No. 1 is satisfied in our BGK model shown in Fig. 4.9 and Fig. 4.12. No. 2 is confirmed by Geotail observations as we showed in Chapter 4. The polarities of electric field antennas are shown in Fig. 2.4. The arrows displayed with components of E_U and E_V correspond to the positive directions of each antenna. We confirmed these antenna polarities in the ground system tests, therefore, the condition No. 3 is also satisfied.

Figure 5.1 shows a schematic illustration on the method of propagation analyses. We assume a spacecraft spin phase that the positive polarity of one component of electric field antenna (E_U or E_V) is in the right direction on Fig. 5.1 as shown by an arrow. At this spacecraft spin phase, if a positive potential propagates from the left side to spacecraft, the onboard receiver detects a positive amplitude first, and later it detects a negative amplitude. When a potential propagates from the right side to spacecraft, the receiver detects a negative amplitude first. Thus, the observed waveforms in each case are drawn

as shown in a bottom part in Fig. 5.1. When we apply this method to waveforms observed by each component of antennas, we can uniquely identify the propagation direction of the PSBL ESW. This method makes use of characteristic of isolated waveforms and it is very useful for surveying source locations of the PSBL ESW. However, we note that if the polarity of the PSBL ESW potential is negative, the identified propagation directions become inverse. We show examples to demonstrate the appropriateness of the above method in Fig. 5.2 and Fig. 5.3. The waveforms shown in upper panels of Fig. 5.2 and Fig. 5.3 are the ESW observed at (GSM X, GSM Y, GSM Z)=(-118, 4.3, 0.7 R_E) on April 1, 1993. The lower panels illustrate the spacecraft spin phase and its relation of antenna polarities. The arrows corresponding to each antenna mean the positive polarity direction. Figure 5.2 is the case at 13:55:41.064 (UT). At this time, the spacecraft spin phase ($\theta_{\rm spin}$) and the azimuthal angle (θ_B) of the ambient magnetic field in the spacecraft coordinate system are 34° and 220°, respectively.

Since E_V component is close to the perpendicular direction to the ambient magnetic field at this snapshot, the detected amplitude of E_V component is small, but we can see the ESW waveforms in both E_U and E_V components. As shown in upper 2 panels, at this time, both waveforms of E_U and E_V appear negative amplitudes first. These waveforms can be explained by the potential propagating in the anti-sunward direction along the ambient magnetic field as shown in the lower panel.

About 2 seconds later, the observed waveforms of E_U and E_V appear positive and negative amplitudes first in Fig. 5.3, respectively. This result is different from the previous one, but since the spin phase at this time is about 270° as shown in the lower panel of Fig. 5.3, they can be also explained by the potential propagating in the anti-sunward direction. We can conclude that these PSBL ESW propagate from the Earth side to the spacecraft.

In the above 2 examples, the result on the propagating direction is unchanged even in the different phase angles. This means that this propagation analysis is reasonable. Further, we can confirm that the PSBL ESW propagate in parallel direction relative to the ambient magnetic field.

Solitary waves observed by Geotail as well as by other spacecraft are sometimes suspected of the artificial effects from instruments [e.g., Vago et al., 1993]. However, the above consistent change of waveforms is one of the proofs that the ESW are purely natural waves.

5.3 Counterstream PSBL ESW

We showed that the propagation direction of the PSBL ESW can be consistently identified by using the antenna polarity and observed PSBL ESW waveforms in the previous section.

We applied this method to many PSBL ESW and identified their propagation directions. When we can identify the propagation direction of PSBL ESW, we know the relative location between spacecraft and PSBL ESW source regions. For example, in the case in Figs. 5.2 and 5.3, since the ESW propagate from the Earth side to the spacecraft, we can expect that the source region of the observed ESW is located closer to the Earth than the spacecraft.

In the BGK potential model, the start point is the excitation of the Langmuir waves due to the bump-on-tail instability. Therefore, we need electron beams in the source region.

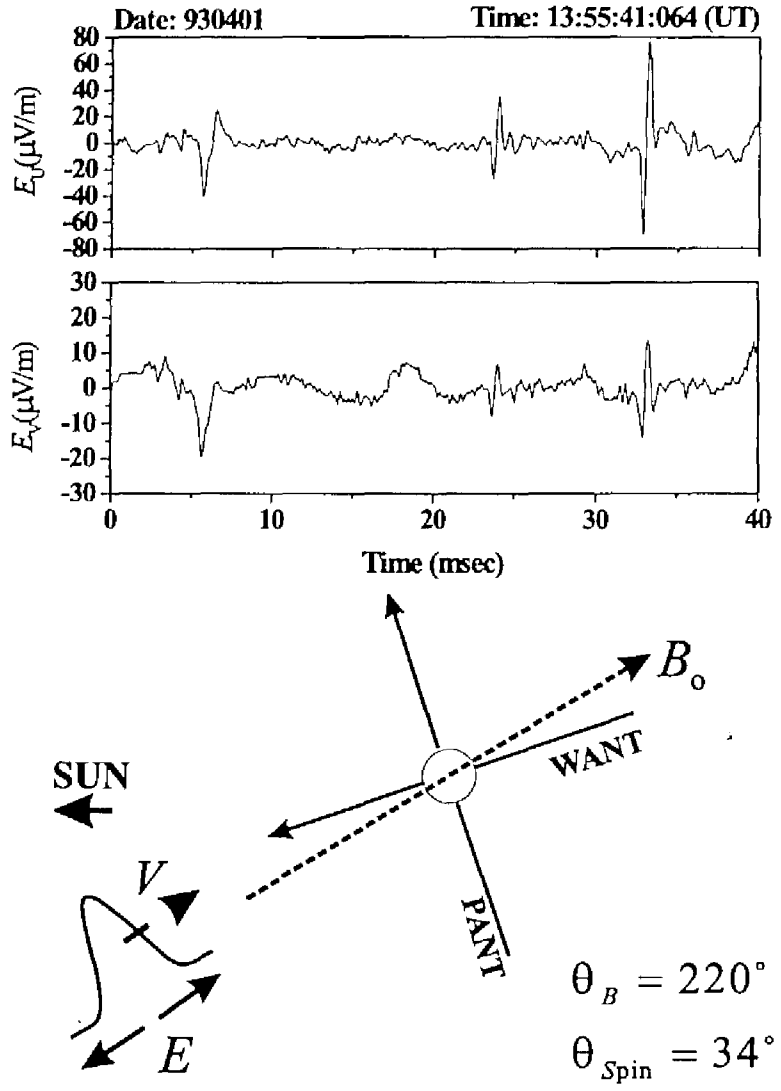

Figure 5.2: An example of PSBL ESW propagation analysis. Upper two panels show observe waveforms of E_U and E_V component. The lower panel is schematic drawing for configuration of antenna polarity and potential flow direction at this time.

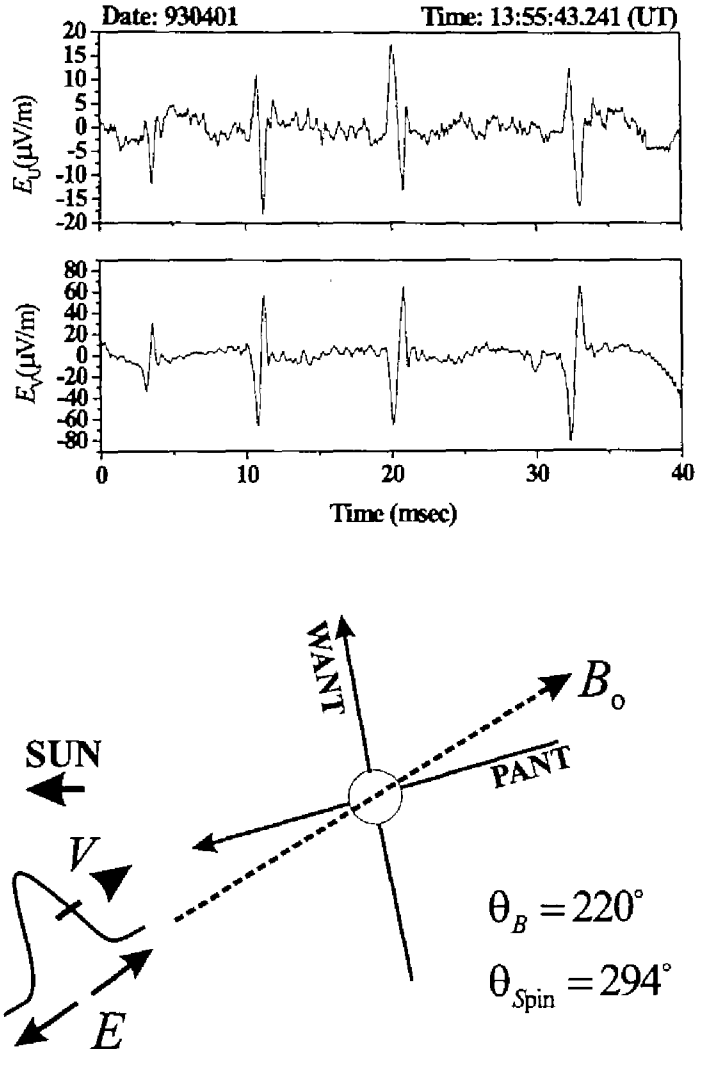

Figure 5.3: Same as Fig. 5.2 but for different spin phase.

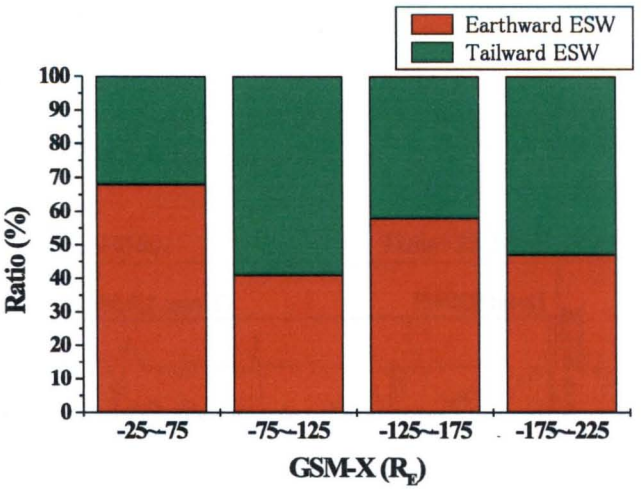

Figure 5.4: Statistical analyses on the ESW propagation directions.

The best candidate for the generation of electron beams is the x type neutral point in the magnetic reconnection. Many scientists believe that the x type neutral point is located at two deferent distances behind the Earth as introduced in Section 1.1. They are the distant neutral line and the near earth neutral line. The distant neutral line is believed to be located around X = -100 R_E. On the other hand, the near earth neutral line is believed to appear in the southward IMF at X = -30 R_E to -60 R_E. In order to identify the distance of the near earth neutral line, many observations and computer experiments have been conducted. We also attempted to identify the distance using the plasma wave signatures observed by Geotail and concluded that the near earth neutral line is distributed around X = -60 R_E [Murata et al., 1995]. Since particles are believed to be accelerated at x type neutral point, these two points are the candidates for the ESW source region.

In order to identify the source region using the ESW propagation analysis method, we performed preliminary statistics on the propagation direction of the PSBL ESW. Figure 5.4 shows that the preliminary statistical analysis results on the ESW propagation directions. The total number of examined ESW is 3937. The red and green bars mean the ratio for observing earthward and tailward propagating ESW in four different areas from the Earth, respectively.

We see that in all of regions both earthward and tailward propagating PSBL ESW are observed. Because of the bad spatial resolution of observation points (resolution of X), concluding the clear spatial dependence of the PSBL ESW observations is difficult, but what we stress here is that the ratio of the earthward propagating ESW is the highest in the range of X = -25 R_E to -75 R_E. If the near earth neutral line is located around X = 30 R_E to 60 R_E, only earthward propagating PSBL ESW should be observed in the region of the earth side relative to the near earth neutral line. On the other hand, in the region between the near earth neutral line and the distant neutral line, there exists the possibility that both earthward and tailward propagating PSBL ESW can be observed. Therefore, the highest ratio of the earthward ESW observation in the range of X = -25 R_E to -75 R_E

is a good signature for the model that the ESW are excited around the near earth neutral line. However, the earthward propagating PSBL ESW in the deep tail of X = -175 R_E to 225 R_E cannot be explained by the distant neutral line. In this model, there exist no regions where electrons are accelerated in the earthward direction. Therefore, we cannot apply the distant neutral line model for the earthward PSBL ESW observed in the deep tail. Instead of this fact, we believe the existence of the distant neutral line based on one interesting result shown below.

Figure 5.5 shows the frequency-time spectrogram of the BEN observed at a kind of PSBL entry at (GSM X, GSM Y, GSM Z)=(-95, 11, -4 R_E) on January 13, 1994. *Saito et al.* [1995] suggested that this event is the encounter of the heart-shape plasmoid. However, in this case, the plasma wave signature is almost the same with those in the normal plasma sheet entry (Typical plasma wave signatures of plasmoids are discussed in Section 3.8). Figure 5.5(a) shows clearly intense BEN spectra extending all the way to the electron plasma frequency ($f_{pe} \sim 2$ kHz) during the interval from 13:10 to 13:15 (UT). High time resolution MCA spectrum shown in Figure 5.5(b) shows the bursty nature of the BEN. In this event, pulse widths of the PSBL ESW are equal to about 1 msec as shown in Fig. 5.5. The propagation analyses for this event show the existence of counterstream PSBL ESW.

Figure 5.6 shows snapshots of the ESW waveforms observed at three different time periods. Waveforms in the top panel of Fig. 5.6 are observed at 13:10:35.166 (UT). From the propagation analyses, we found that these PSBL ESW propagate in the tailward direction. The panel (b) shows the waveforms observed after about 2 seconds. The interesting feature shown in this panel is that the ESW with 2 different pulse widths are observed at this time. Two observed pulse widths are equal to about 1 msec and 5 msec. Further the phase relation of these ESW is out-of-phase. This means that these two ESW propagate in the opposite direction. By applying the propagation analysis method, we found that the short pulse and long pulse ESW propagate in the tailward and earthward directions, respectively. This counterstream ESW suggests that two different source regions are located at the earth side and the tail side of the spacecraft. Further, about 300msec later, all of the observed ESW propagate in the earthward direction as shown in Fig. 5.6 (c) and their pulse widths are short and in the almost same order of the short pulse ESW shown in Fig. 5.6 (a).

Figure 5.7 shows the time chart of the observations of tailward or earthward ESW as well as the observation of Langmuir waves in this WFC observation sequence during 5 sec. As shown in Fig. 5.7, the dominant waves are the tailward ESW. The earthward ESW are very intermittently observed. We occasionally find such counterstream ESW in the Geotail data. We will discuss the observations of such counterstream ESW and corresponding electron velocity distribution referring to the results of the computer experiments in the following section.

5.4 Discussions

In this chapter, we showed that we can obtain the propagation direction of the PSBL ESW using the antenna polarity and their waveforms. The propagation analyses are very important in order to identify the source location of the PSBL ESW. We performed preliminary statistical analyses on the propagation directions of ESW and found that the observation probability of the earthward ESW is highest in the near tail region. This result is very

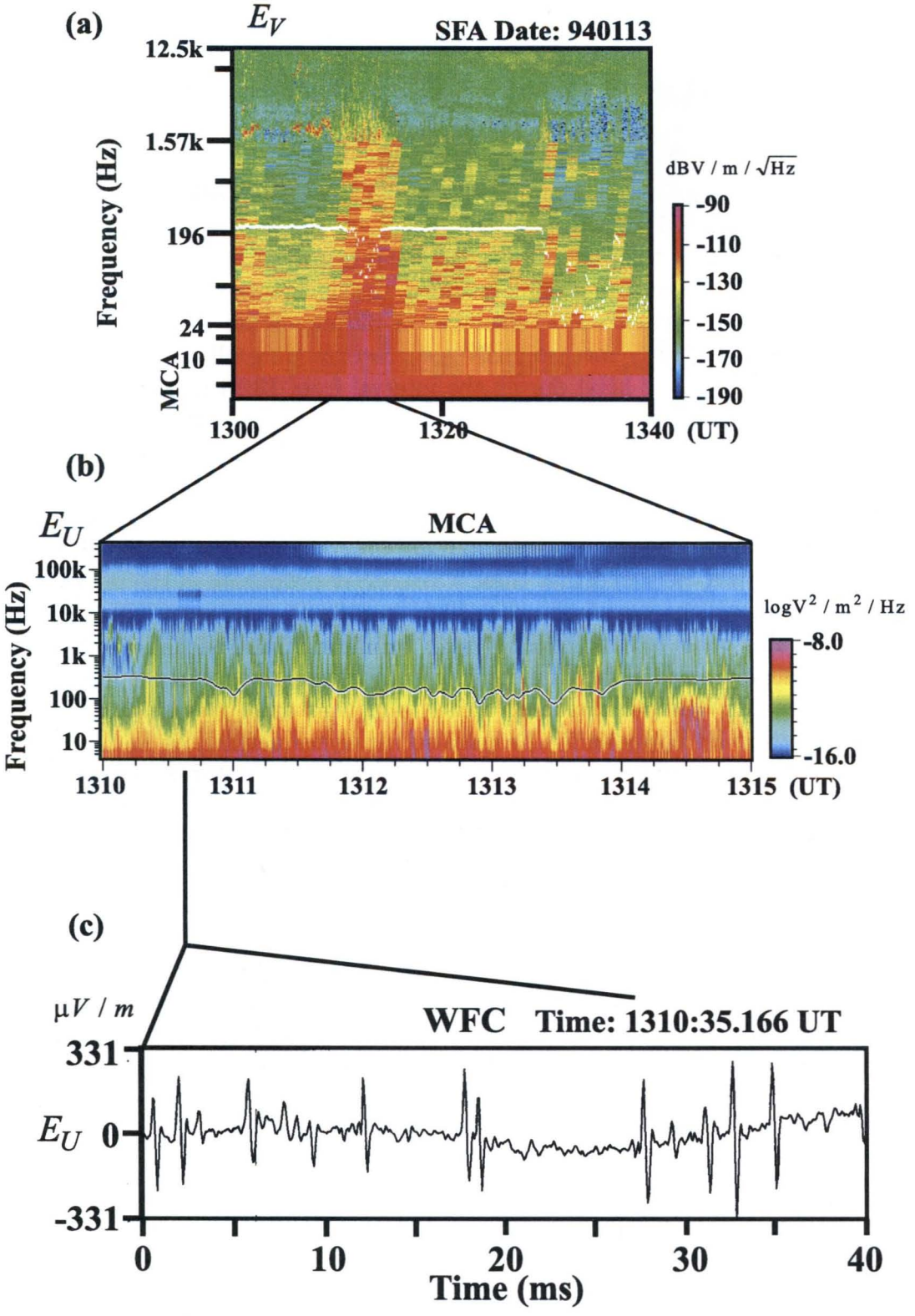

Figure 5.5: Frequency-time spectrogram generated from SFA (a), and MCA(b) and representative waveforms (c) [*after Kojima et al.*, 1997a]

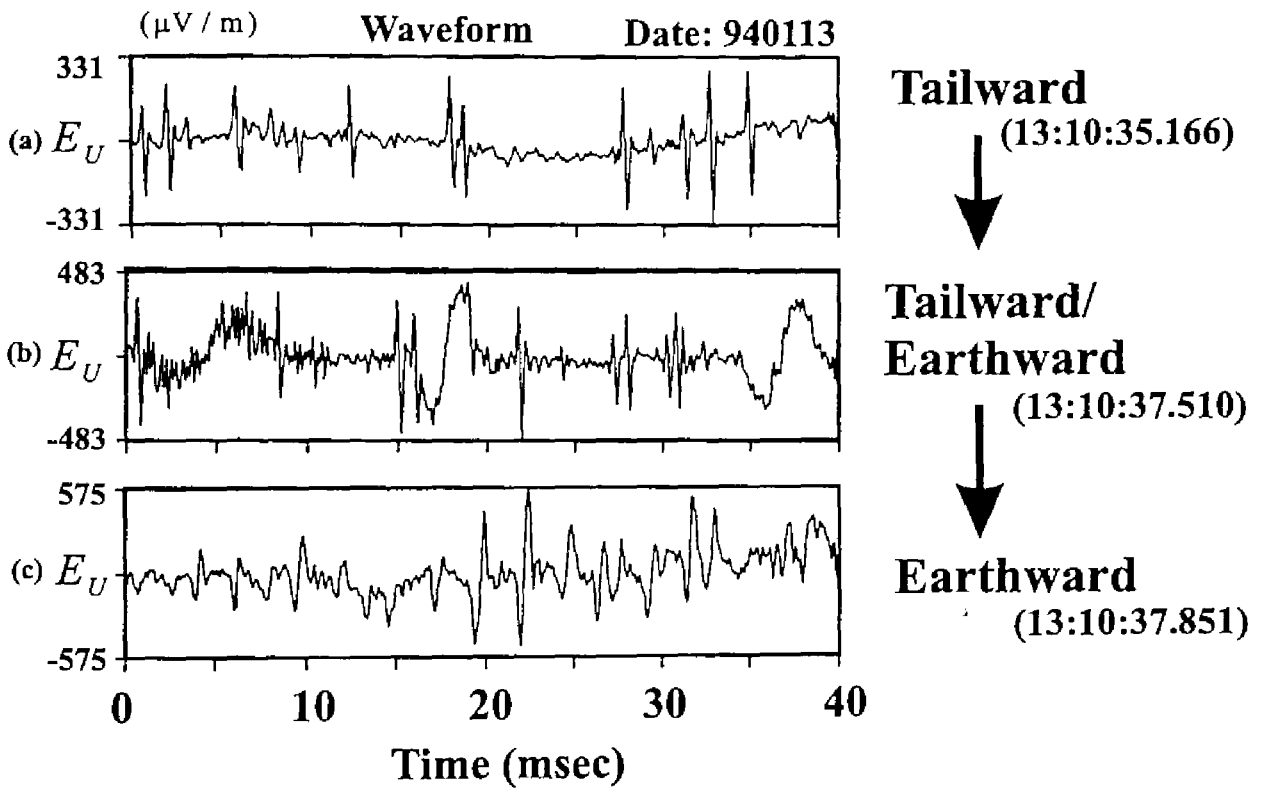

Figure 5.6: Snapshots of the ESW observed at three different time periods. The tailward ESW are observed in the initial phase of one WFC sequence. However, after that as shown in the middle panel, both earthward and tailward ESW are observed simultaneously, and finally only the earthward ESW can be observed.

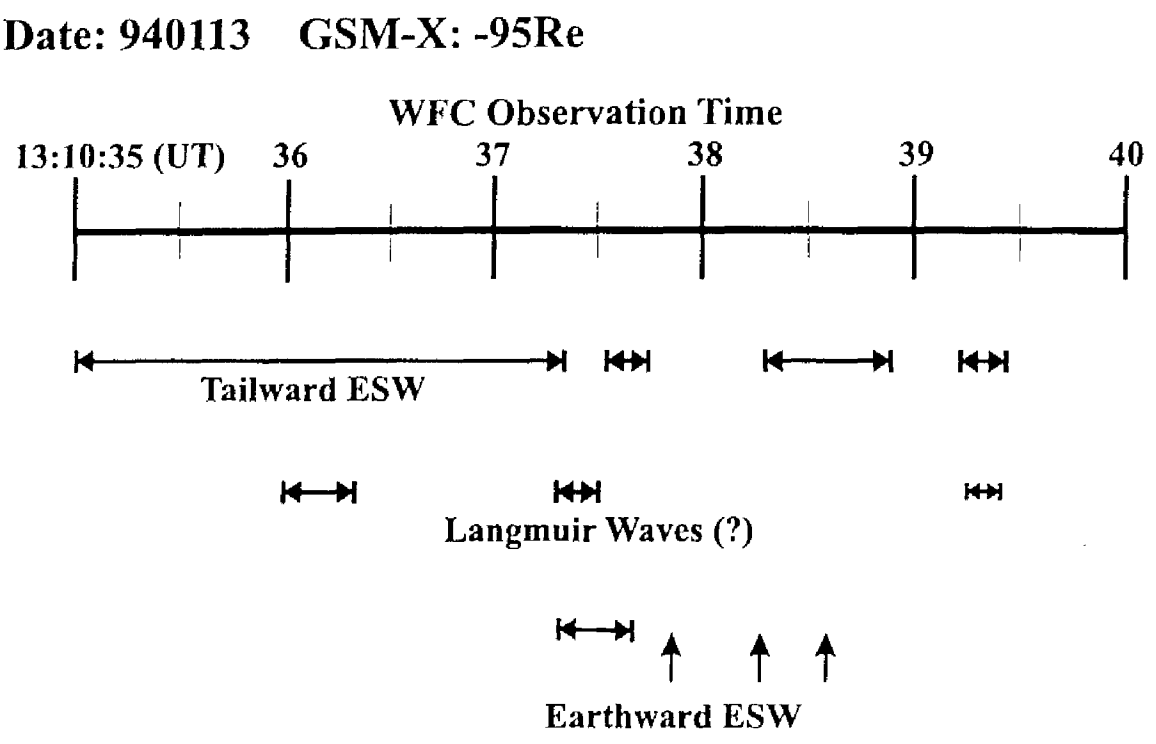

Figure 5.7: Time chart of the observations of tailward or earthward ESW as well as the observations of Langmuir waves.

suggestive to the existence of the near-earth neutral line and acceleration of electrons at this point.

Further, we showed an interesting event that both earthward and tailward ESW are observed in one WFC observation sequence. The observed ESW at one snapshot are only tailward or earthward ones but at another snapshot, both tailward and earthward PSBL ESW are simultaneously observed. Such *Franz et al.* [1998] also observed such counterstream solitary waves by Polar spacecraft in the high altitude of the polar region.

Omura et al. [1996] show that counterstream BGK mode can be existed in the system of counterstream electron beams by computer experiments. Figure 5.8 shows the time evolution of the bi-stream instability. Two couterstream electron beams drift relative to the hot ions in this computer experiments. In the second panel, bi-stream electron instability takes place and electrons are trapped in potentials moving with the same velocity of ions. The electron trapping is affected by ions and the BGK potential is displaced from the ion drift velocity. In the final stage, we can see the formation of both forward and backward propagating BGK potentials. Since the condition that these potentials survive is not to affect each other, it is necessary that the drift velocity of each potential is well separated beyond the trapping velocity of each BGK potential.

The counterstream PSBL ESW need the counterstream electron beams. We examined the existence of the counterstream electron beams consulting the LEP plasma measurement data. Figure 5.9 shows the electron velocity distributions observed by LEP in the same time period which we discussed in the previous section. Note that since electron velocity distributions are obtained every 12 second, velocity distribution shown in Fig. 5.9

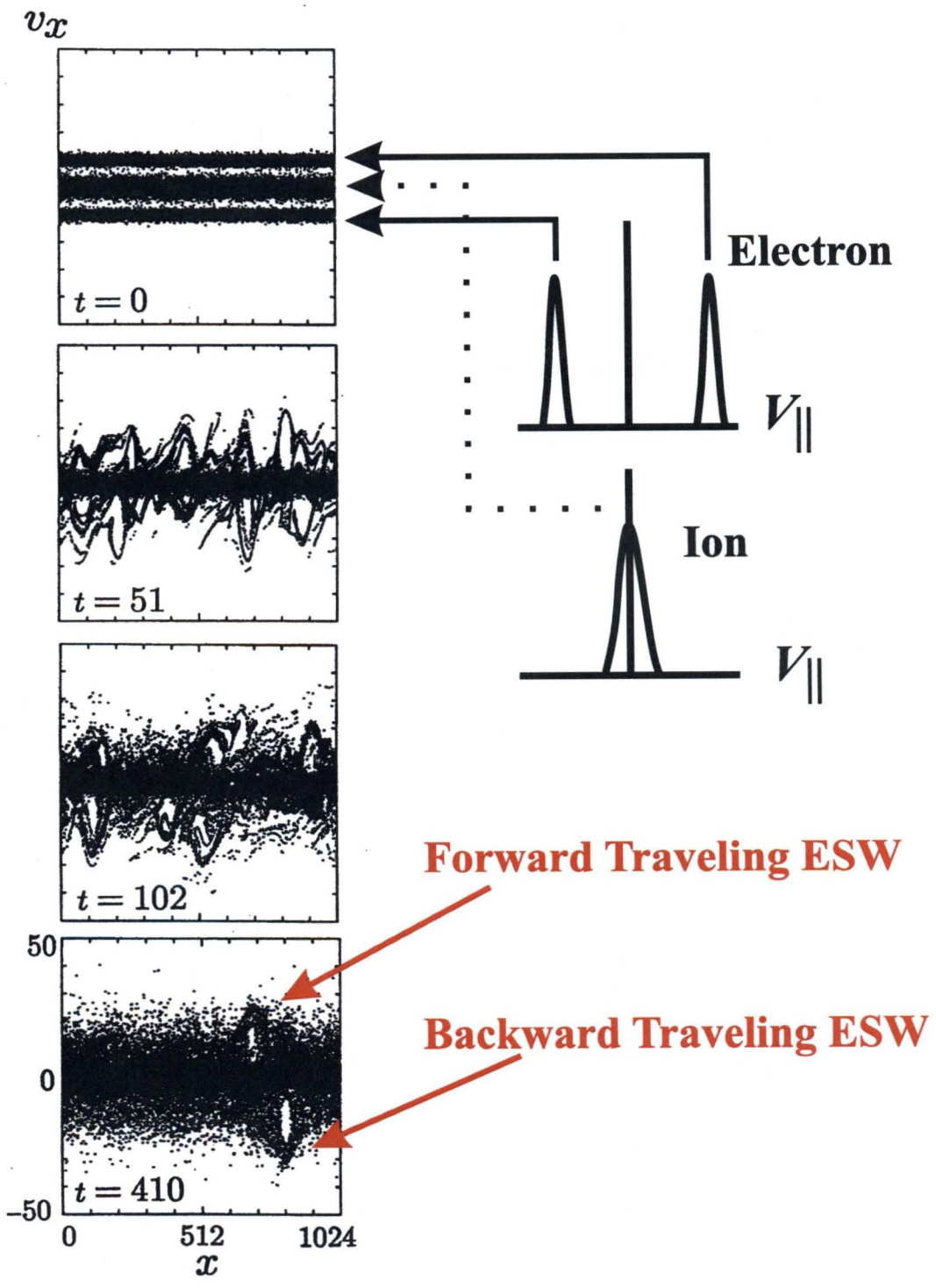

Figure 5.8: Computer experiment on counterstream BGK potentials excited by counterstream electron beams [*after Omura et al.*, 1996].

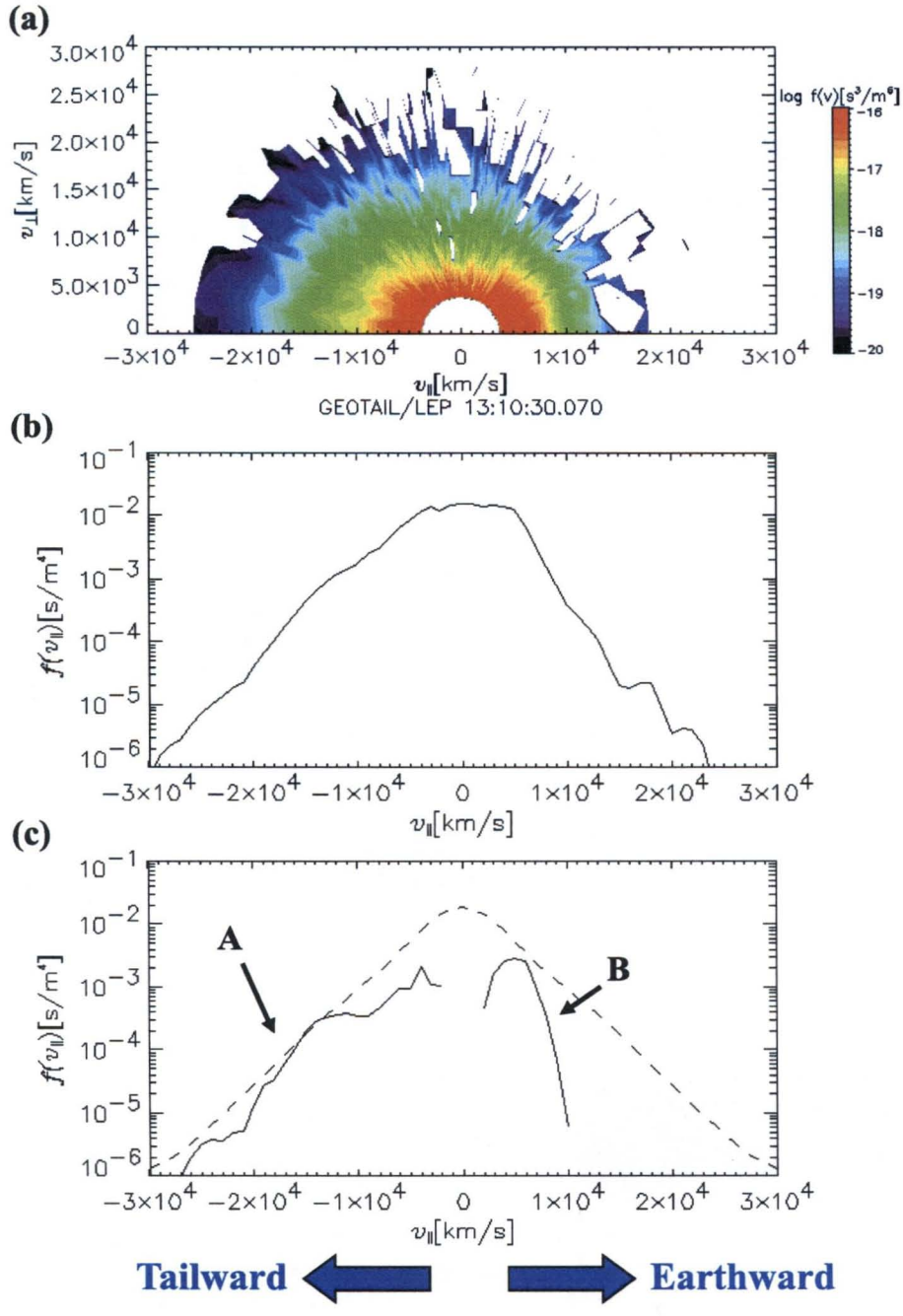

Figure 5.9: Electron velocity distribution observed by LEP. (a) Color coded electron velocity distribution on $v_{\parallel} - v_{\perp}$, (b) reduced velocity distribution, and (c) beam components extracted from the reduced velocity distribution shown in panel (b).

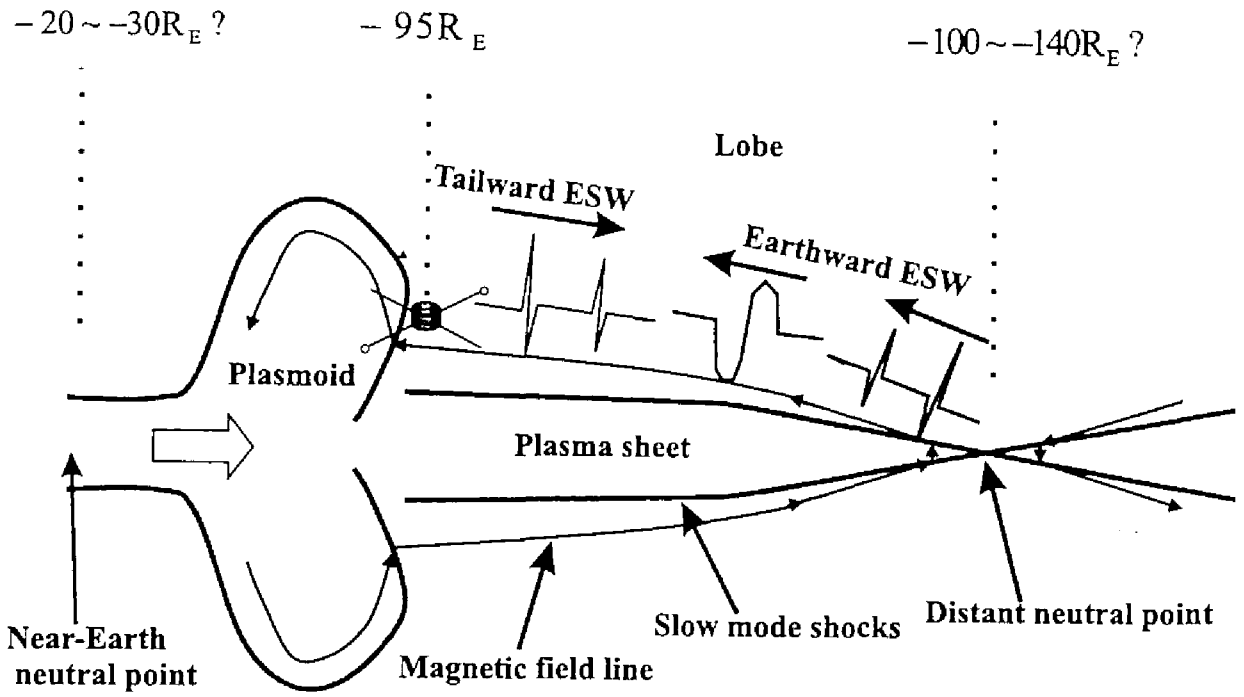

Figure 5.10: Schematic drawing for observations of the couterstream PSBL ESW.

includes whole period of discussed WFC data sequence. The panel (a) shows the color contour of observed electron velocity distribution on $V_{\parallel} - V_{\perp}$ plane. After the integration of $V_{\perp}$ component, we obtain the reduced velocity distribution of $V_{\parallel}$ component as shown in panel (b). By subtract uniform Maxwell distribution from the distribution shown in panel (b), we obtain beam components embedded in observed velocity distribution (see panel (c)). Detailed technique for picking up beam components is described in *Omura et al.* [1998]. In this plot, a positive velocity corresponds to the earthward direction.

The obtained electron beam components consist of 2 groups (A and B) as shown in Fig. 5.9 (c). The beam component A corresponding to high energy tail beyond $V_{\parallel} = -1 \times 10^4$ km/s of this electron velocity distribution stream in the tailward direction. Such a high energy tail is frequently observed with the PSBL ESW and its direction agrees with the ESW propagation direction. In this case, we believe that the beam component A corresponds to electrons trapped in the tailward propagating ESW potentials shown in Fig. 5.6. Such coincidence of high energy electron beam component and the PSBL ESW has been also confirmed by *Matsumoto et al.* [1998].

On the other hand, relatively lower energy beam component B around $V_{\parallel} = 6 \times 10^3$ km/s streams to the earthward direction. This component electrons are believed to be carried by the earthward propagating PSBL ESW shown in Fig. 5.6. However, we cannot decide whether this beam component corresponds to the short pulse width ESW or the long pulse width ones. The important point is that couterstream ESW are observed with counterstream electron beams. This result is consistent with our BGK potential model for the PSBL ESW.

Figure 5.10 schematically shows the configuration of the counterstream PSBL ESW ob-

servations which we discussed in this chapter. *Saito et al.* [1995] claimed that this event is satisfied with the slow mode shock condition. Further, this slow mode shock is formed in the front of the heart-shaped plasmoid. As we stated in the beginning of this section, we do not find significant difference of plasma signatures in this event from those in plasma sheet entries without an encounter of plasmoids. However, according to the plasma measurement result [*Saito et al.*, 1995], Fig. 5.10 includes the heart-shaped plasmoid in the left side of this figure.

The spacecraft is located just in front of the plasmoid. In the earlier WFC sequence, we observe the tailward PSBL ESW with short pulse widths of about 1 msec. About 2 seconds later, the earthward ESW reach the spacecraft and after that, they are intermittently observed. While the earthward ESW which reach spacecraft first have long pulse widths of about 5 msec, the short pulse widths earthward PSBL ESW reached the spacecraft after the long pulse ones (see Fig. 5.6).

The most plausible source region of the earthward ESW is the distant neutral line as shown in Fig. 5.10, which is expected to be located in the distance from -100 R_E to -140 R_E down the tail [*e.g., Nishida et al.*, 1997]. The earthward ESW propagate along the ambient magnetic field which is connected to the distant neutral point. When the spacecraft move across that magnetic field line, we can observe the earthward ESW. On the other hand, concluding that the source region of the tailward ESW is the near-earth neutral line is difficult, because the distance between the expected near-earth neutral point and spacecraft location is about 30 R_E to 90 R_E. If the ESW are assumed to propagate with the velocity of 1×10^4 km/s referring to Fig. 5.9, it takes about 20 sec to 40 sec. Since the characteristic time scale of electrons is electron plasma oscillation period of about 1 msec, the traveling time corresponds to a few tens of thousands oscillation times. This time scale is too long for electron dynamics. Therefore, it is a reasonable idea that the source region of the tailward PSBL ESW is located around the plasma sheet boundary close to the spacecraft or the plasmoid. Up to now, we do not know any electron acceleration mechanisms around the above region. However, we have not fully understood microscopic phenomena related to electron dynamics around plasma sheet and plasmoids as well as x type neutral point. Further theoretical studies are needed in the microscopic scale.

Chapter 6

Waveform observations of the narrowband electrostatic noise in the lobe region

6.1 Introduction

In the previous Chapters 4 and 5, we have discussed the waveform observation results on the BEN in the plasma sheet boundary.

The BEN is the very common emission in the tail region. However, *Scarf et al.* [1984b] reported a separate component of electrostatic noise observed around the slow mode shocks in the plasma sheet boundary.

Figure 6.1 shows the typical spectra observed around the slow mode shocks by ISEE-3 spacecraft [*Scarf et al.*, 1984b]. The top panel displays the time variation of magnetic field magnitude, while the lower panel the time variation of plasma wave electric field spectra observed by the MCA onboard ISEE-3 spacecraft. The emissions in the frequency range from 300 Hz to 1 kHz start at 19:20 (UT) while the spacecraft staying in the foreshock region. It is evident that the spectral feature of these emissions is different from that of the BEN (see Fig. 4.1 and Fig. 4.4). *Scarf et al* [1984b] interpret these emissions as ion acoustic noise. The monochromatic spectra seen around 5 kHz are the electron plasma oscillations. Since the frequency of the electron plasma oscillation is equal to the local electron plasma frequency ($f_{\rm pe}$), the ion plasma frequency ($f_{\rm pi}$) can be calculated to be 117 Hz. The important characteristic of this emission is the frequency range between $f_{\rm pe}$ and $f_{\rm pi}$. There exists no standard parallel propagating electrostatic modes in the frequency range between $f_{\rm pe}$ and $f_{\rm pi}$. *Scarf et al.* [1984b] explained the problem of this frequency range by the Doppler shifted ion acoustic waves. *Tsutsui et al.* [1991] also proposed the explanation of the broadness of the spectra using the Doppler shift of the ion acoustic wave. After the spectral feature of these emissions, *Coroniti and Ashour-Abdalla* [1989] addressed them as "Narrowband Electrostatic Noise (NEN)."

Scarf et al. [1984a] also found similar electrostatic emissions in the magnetopause boundary layer. Figure 6.2 shows the representative electric field spectra observed in the magnetopause boundary layer (top) and those observed in the plasma sheet. The spectra in each panel are plotted for the data collected at the different radial distances from the Earth.

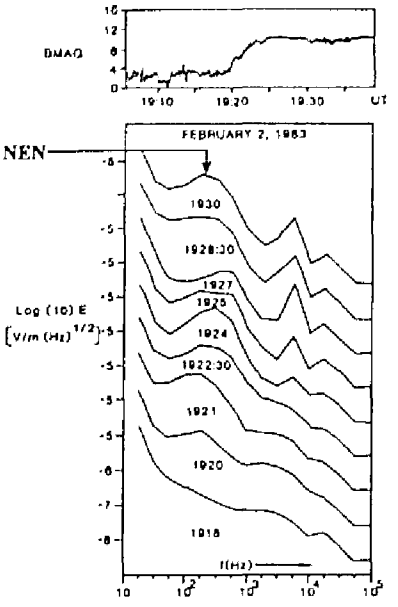

Figure 6.1: Typical wave spectra around the slow mode shocks as well as the variation of the ambient magnetic field [*after Scarf et al.*, 1984b].

The emissions seen in the frequency range between 100 Hz and 1 kHz are very similar to the above-mentioned NEN spectra (The intense spectra shown in the lower panel are the BEN). *Scarf et al.* [1984a, b] did not mention the similarities between the NEN and electrostatic waves in the magnetopause boundary. However, based on the polarization analyses, they concluded that the electrostatic waves in the magnetopause boundary are the doppler-shifted ion acoustic waves. They examined the polarizations of these magnetopause boundary waves using the spacecraft spin as shown in Fig. 6.3. They claimed that the shown weak polarization parallel to the ambient magnetic field is the evidence that the waves are Doppler-shifted ion acoustic waves. *Coroniti et al.* [1990] also observed similar emissions in the magnetopause boundary by ISEE-3 spacecraft. They pointed out the similarity of the magnetopause boundary waves comparing with the NEN, but they claimed that the NEN is not related to ion beams which cause such as Doppler shifted ion acoustic waves, because dense ion flows are not expected to exist in the magnetopause boundary. However, unfortunately, since ion detectors onboard ISEE-3 spacecraft did not function, they could not confirm their claims.

The theoretical studies about the NEN emissions are very few. The papers based on the spacecraft observations except *Coroniti et al.* [1990] conclude that the NEN is the Doppler-shifted ion acoustic wave. But the essential condition $T_e/T_i > 1$ for the excitation of ion acoustic waves is not always satisfied in the tail region, where T_e and T_i are electron and ion temperatures, respectively.

Coroniti and Ashour-Abdalla [1989], and *Ashour-Abdalla et al.* [1989] proposed a new nonstandard electrostatic mode called "Electron velocity space hole mode." *Coroniti et al.* [1993] examined the detailed parametric dependence of this mode. The electron velocity space hole mode is destabilized by a positive slope in $f(v_{\|})$ and/or a weak, energetic ion beam. Such a velocity distribution can be formed by mixtures of different plasmas due to

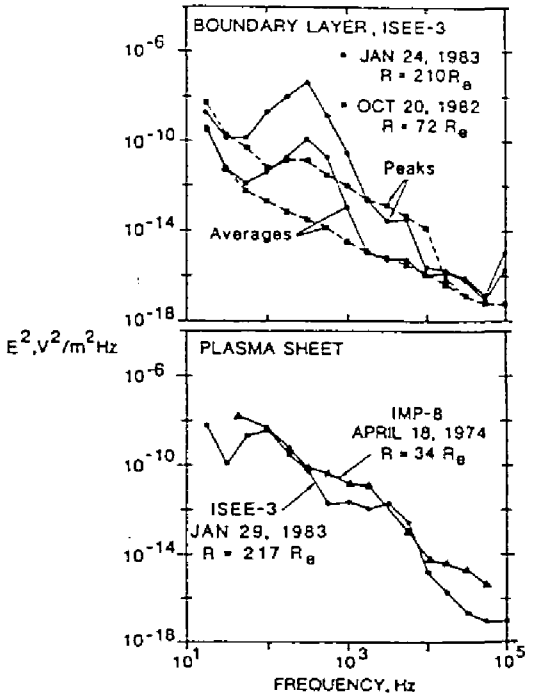

Figure 6.2: Variation with radial distance of electric field spectra in the magnetopause boundary layer (top), and those in the plasma sheet (bottom) [*Scarf et al.*, 1984a].

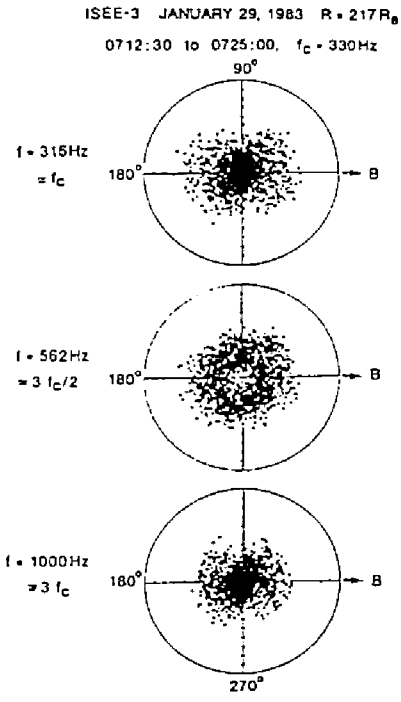

Figure 6.3: Polarizations of electrostatic waves observed in the magnetopause boundary layer [*Scarf et al.*, 1984a].

the interaction between different global structures such as boundary layers. The study of the NEN started in the connection with the slow mode shocks, but ISEE 3 also detected similar waves in the magnetopause boundary layer.

In this chapter, we show the waveform observations of the NEN in the tail lobe region. The detailed waveform analyses revealed the quasi-sinusoidal waveforms and their natures. Further, we discuss the generation mechanism of the NEN based on our computer experiment results.

6.2 Lobe electrostatic quasi-monochromatic waves

Figure 6.4 (a) shows the frequency-time spectrogram of the NEN observed in the tail lobe at (GSM X, GSM Y, GSM Z)= (-192, 20, -10 R_E) on May 29, 1993. During this shown interval, spacecraft moved across the magnetopause three times at 11:35, 12:21, and 12:32 (UT). The intense low frequency emissions observed during the periods from 11:30 to 11:35, and from 12:21 to 12:32 (UT) are the BEN and Magnetic Noise Burst (MNB) emissions in the magnetosheath region. In this case, the magnetopause boundary layer seems to be much thinner, therefore it is difficult to identify it by the SFA with coarse time resolutions. The magnetopause boundaries shown in Fig. 6.4 belong to the type 2 boundary which we showed in Fig. 3.7 of Chapter 3. The spacecraft stays in the lobe region during other periods shown in Fig. 6.4 (a). The multiple magnetopause crossings suggest that the spacecraft is located very close to the magnetopause boundary.

The spectra seen as the patchy structure in Fig. 6.4 (a) are the typical NEN spectra observed by Geotail spacecraft. The shown spectra have a lower limit at 24 Hz and an upper cutoff at 196 Hz. It is easier to compare the MCA data shown in Fig. 6.4 (b) with previous observation results show in Fig. 6.1. We can see the narrowband intermittent spectra of the NEN in the frequency range below 200 Hz.

The most striking difference from the BEN is seen in Fig. 6.4 (c) where we plot the time series of the electric field E_U from the WFC data. The BEN waveform is characterized by a series of bipolar pulses as shown in Fig. 4.5. On the other hand, since the NEN is narrowbanded, we expect its waveform to be more monochromatic. This is indeed the case as shown in Fig. 6.4 (c). We see that the NEN is not noise, but its waveform is rather quasi-monochromatic. These waveforms cause some broadness of the NEN spectra which are shown in Fig. 6.4 (b). The broadness of the NEN spectra is caused by following characteristics:

1. The waveforms are not completely sinusoidal. Some waveform distortions cause the broadness of the NEN spectra.

2. As will be shown later, the frequency of the NEN quickly changes. The continuous frequency change is similar to the Frequency Modulation (FM). Such a frequency modulation can be the reason for the broadness of the NEN spectra.

On the other hand, when we observe the NEN with the above waveform natures by the SFA with coarse time resolutions, the characteristic of these oscillations results in the patchy (grain-like) structure shown in Fig. 6.4 (a). After these waveforms of NEN, we term them as lobe electrostatic quasi-monochromatic waves (lobe EQMW). In this section we showed

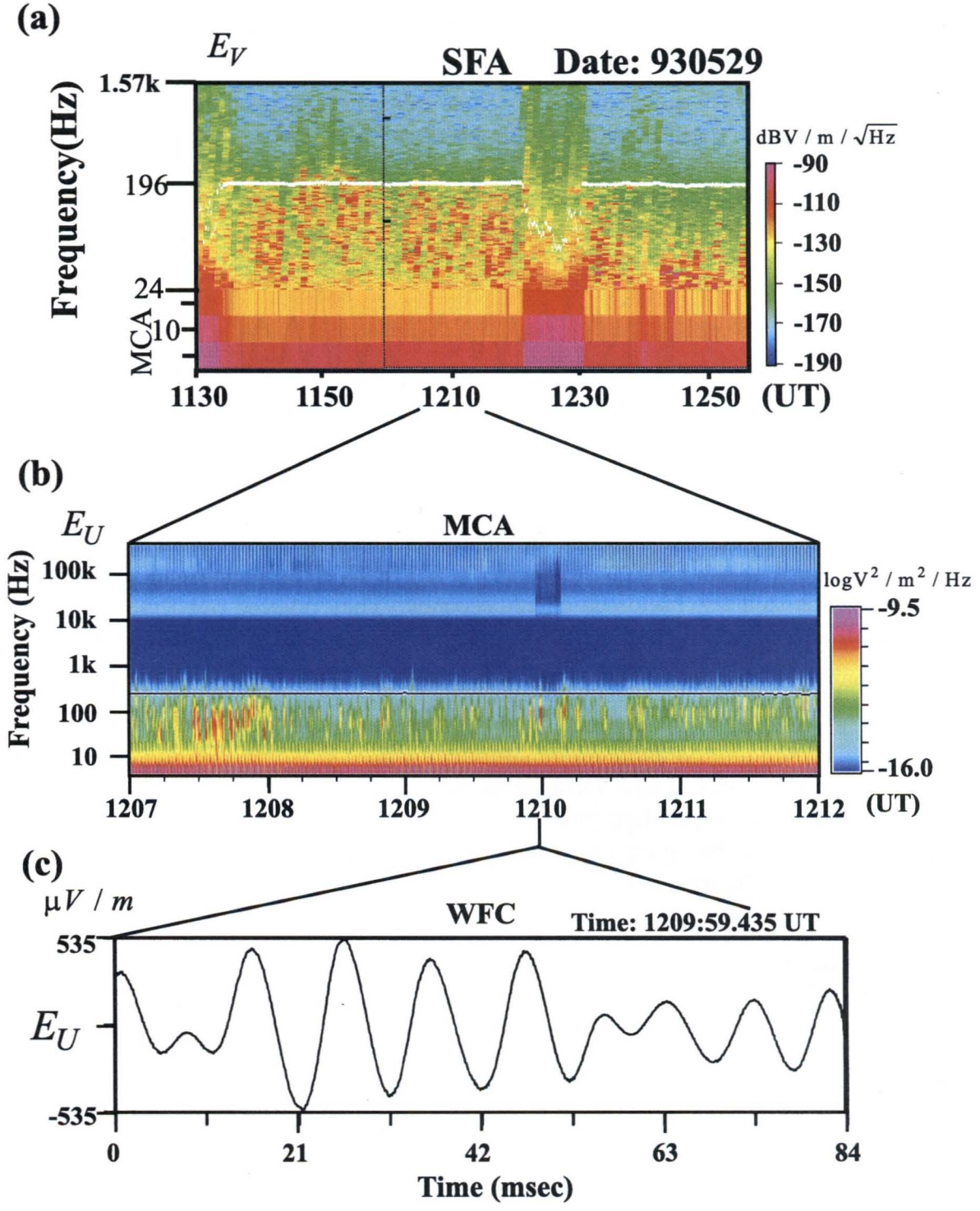

Figure 6.4: Frequency-time spectrograms from (a) SFA and (b) MCA and (c) waveforms from WFC of the narrowband electrostatic noise (NEN) observed in the tail lobe on May 29, 1993. [*after Kojima et al.*, 1997a].

the waveforms of the NEN. These emissions have been considered as noise ever since they were discovered because the broadness of their spectra reminds us of random noise, which consists of the superposition of incoherent waves with various frequencies. However, our waveform observations showed that these NEN emissions are not random noise.

While BEN and NEN are named after their frequency spectra, the ESW and EQMW are named after their waveforms. As we stated above, the observations using the spectrum analyzer alone are misleading, especially for the waves with the broadband spectra and bursty nature. The information on the waveforms provides us with a significantly important clue for studying their generation mechanism.

6.3 Bursty Nature of the Lobe EQMW

The burstiness is one of the interesting natures of the PSBL ESW. Here the burstiness means that their amplitudes, pulse widths, and interpulse time spans change very quickly as well as that they suddenly appear or disappear. *Kojima et al.* [1994] showed that the propagation speed of the ESW potential structure changes on a time scale ranging from a few milliseconds to a few hundreds of milliseconds. They pointed out that the burstiness of the PSBL ESW implies that the PSBL ESW is closely related to electron dynamics.

To compare the characteristics of the lobe EQMW with those of the PSBL ESW, we examine time variation of their waveforms starting at 19:23:30 (UT) on October 26, 1992, when Geotail was in the lobe.

Figure 6.5 shows a part of an 8.7 s observation sequence in the WFC data with each panel lasting 85 ms. The corresponding spectra calculated with the Fast Fourier Transform (FFT) method are shown to the right. The rapid changes in the waveform of the lobe EQMW are very evident in this figure.

In Fig. 6.5 (a), we can see the clear quasi-monochromaitc waves with the peak frequency of 200 Hz. They last until 122 ms in Fig. 6.5 (b) and suddenly disappear after that. The sharply peaked spectra of the lobe EQMW in Fig. 6.5 (a) and Fig. 6.5 (b) are correspondingly replaced by weak broadband spectra in Fig. 6.5 (c). In Fig. 6.5 (d) the EQMW restore their quasi-monochromatic waveforms, however, their peak frequency is about 300 Hz, which is higher than that in Fig. 6.5 (a) and Fig. 6.5 (b). In this case, the lobe EQMW change their frequencies, waveforms, and amplitudes during the time interval of only 340 ms.

The bursty nature of the lobe EQMW is very similar to that of the PSBL ESW. These waveforms rapidly change in a time scale of a few tens of milliseconds. This burstiness has not been able to be detected by the spectrum receiver. The bursty nature is the important clue for discussing the excitation mechanism of the lobe EQMW. The observations suggest the possibility that the free energy source of these waves changes very quickly, of the order of a few milliseconds to a few tens of milliseconds. This means that the electron dynamics play a more important role than the ion dynamics in the generation of both waves.

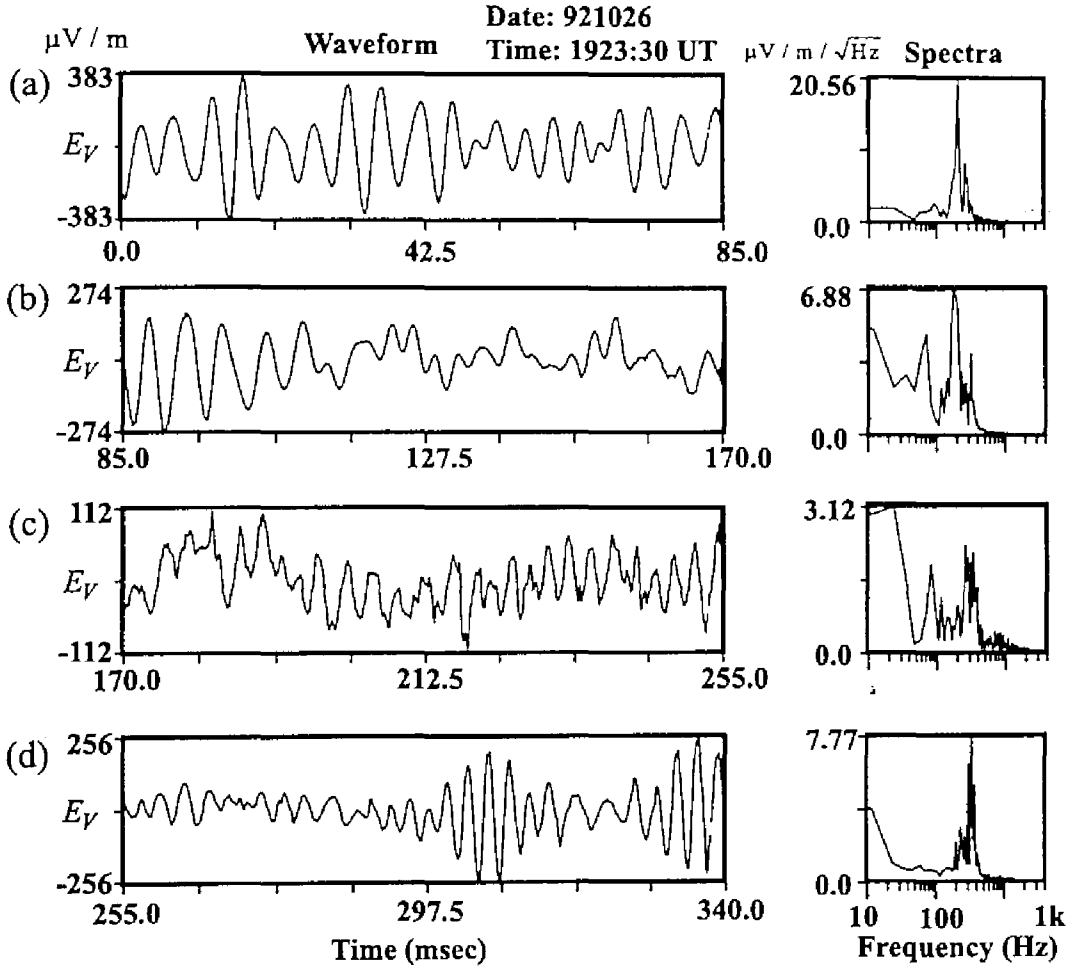

Figure 6.5: (left) Time series of the lobe electrostatic quasi-monochromatic waves (EQMW) waveforms observed by the WFC. (right) Corresponding spectra calculated with the fast Fourier transform (FFT) method. [*after Kojima et al.*, 1997a].

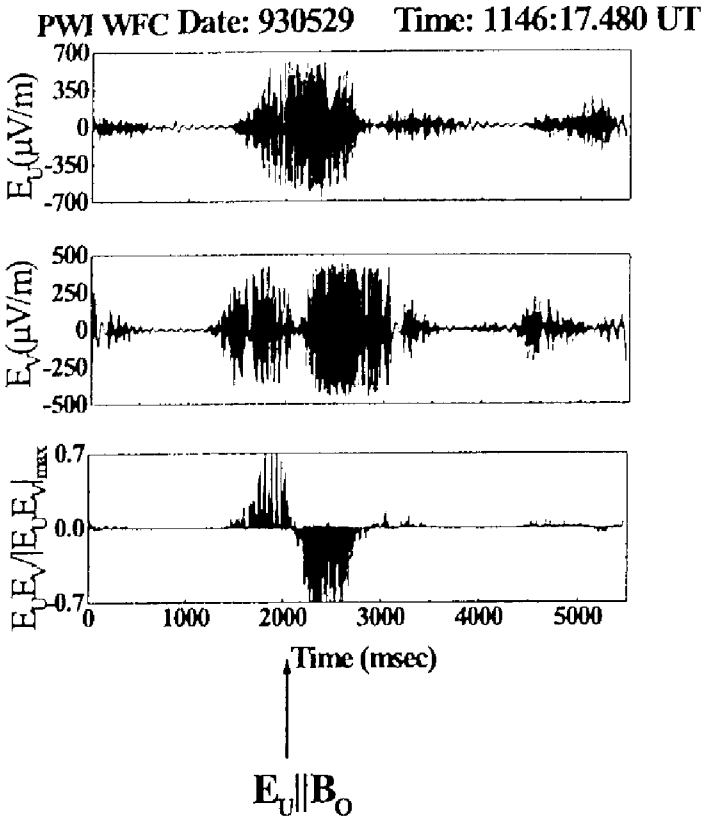

Figure 6.6: Spin dependence of the lobe EQMW waveforms during the interval from 1200 to 3100 ms for (a) E_U and (b) E_V: (c) Variation of the product of E_U and E_V components. When E_U (E_V) is parallel (perpendicular) to the ambient magnetic field at 2050 ms, we can see the minimum amplitude of E_V component in panel (b) and the change of signs of $E_U \times E_V$ in panel (c). [*after Kojima et al.*, 1997a].

6.4 Polarization of the lobe EQMW

Since the WFC receiver can simultaneously collect the waveforms detected by two sets of the orthogonal dipole antennas, we can estimate the potential structure of observed electrostatic waves. This can be easily done by examining the spin dependence of the phase difference between the waveforms observed by each dipole antenna. We applied this method to the PSBL ESW and showed that they have parallel electric field components relative to the ambient magnetic field in Fig. 4.7 and proposed the isolated ESW potential model shown in Fig. 4.9. Using the MCA receiver onboard ISEE-3 spacecraft, *Scarf et al.* [1984a] performed similar polarization analyses, but only weak polarization parallel to the ambient magnetic field (see Fig. 6.3). Figure 6.6 shows the spin dependence of the lobe EQMW observed at (GSM X, GSM Y, GSM Z) =(−192, 20, −10 R_E) on May 29, 1993 in the similar display format of Fig. 4.7. Figure 6.6 (a) and (b) are the waveforms detected by the two orthogonally crossed sets of electric field antennas, E_U and E_V. The product of

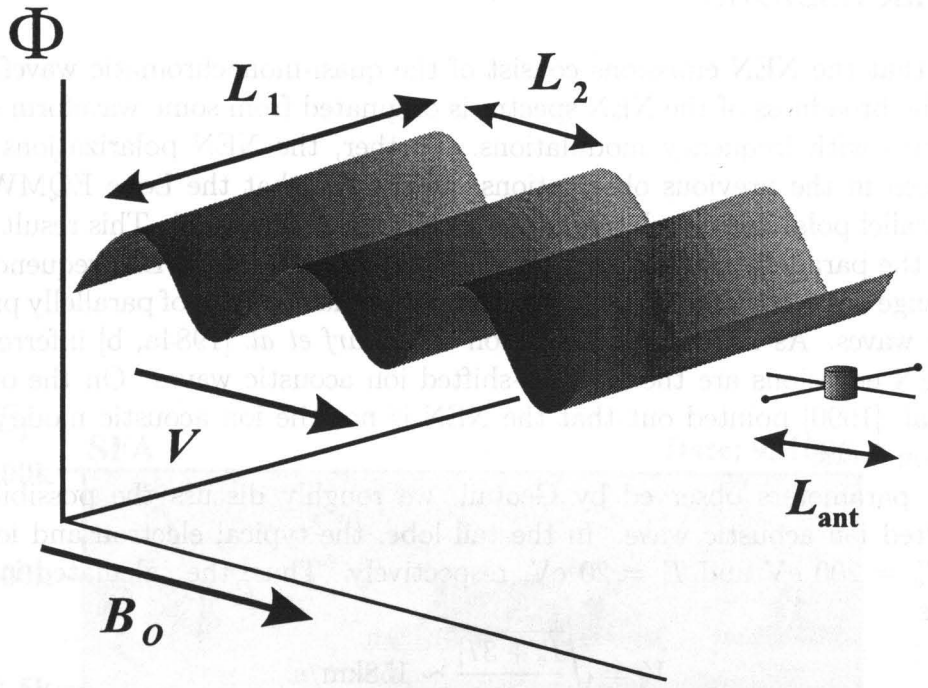

Figure 6.7: Schematic drawing of the lobe EQMW potential. The spin dependence of the lobe EQMW shows that the lobe EQMW are the plane waves which propagate along the ambient magnetic field B_o [*after Kojima et al.*, 1997a].

these two components is shown in Fig. 6.6 (c). The arrow at 2050 ms marks the time when the E_V (E_U) electric field antenna was perpendicular (parallel) to the ambient magnetic field. Taking account of the polarity of each antenna, the positive and negative values in Fig. 6.6 give the phase relationship between the E_U and E_V components. Positive values indicate that the signals are in-phase, while negative values mean they are out-of-phase.

The bursty waves observed from 1200 to 3100 ms are the lobe EQMW. The amplitude of the E_V component waveforms is zero at the exact time when the E_V (E_U) component antenna is perpendicular (parallel) to the ambient magnetic field. This means that the electric field vector of the lobe EQMW is parallel to the ambient magnetic field. In Fig. 6.6 (c), before 2050 ms, the product of the E_U and E_V components are positive, while after 2050 ms, it is negative. This phase relation means that the potential structure in the direction perpendicular to the ambient magnetic field is almost uniform over the scale of the antenna length (100 m).

On the basis of this spin dependence, the potential structure of the lobe EQMW should be as shown in Fig. 6.7. In Fig. 6.7, L_1 and L_2 are the lengths of the uniform scale in the perpendicular direction to the ambient magnetic field, and the potential width, respectively. $L_{\rm ant}$ is the electric field antenna length. Based on the waveforms and spin dependence of the lobe EQMW shown in Fig. 6.6, we find that L_1 and L_2 should be much larger than $L_{\rm ant}$. Thus we conclude the lobe EQMW is a purely parallel propagating plane wave and that sinusoidal potential structures such as those shown in Fig. 6.7 pass through the spacecraft.

6.5 Discussions

We showed that the NEN emissions consist of the quasi-monochromatic waveforms (lobe EQMW). The broadness of the NEN spectra is originated from some waveform distortions and waveforms with frequency modulations. Further, the NEN polarizations could not be clearly seen in the previous observations, we showed that the Lobe EQMW have the complete parallel polarization relative to the ambient magnetic field. This result means the EQMW are the parallelly propagating waves. However, since the NEN frequency is in the frequency range between f_{pe} and f_{pi}, there exist no standard modes of parallelly propagating electrostatic waves. As introduced in Section 6.1, *Scarf et al.* [1984a, b] inferred that the observed NEN emissions are the Doppler-shifted ion acoustic waves. On the other hand, Coroniti et al. [1990] pointed out that the NEN is not the ion acoustic mode because of the lack of ion flows.

Using the parameters observed by Geotail, we roughly discuss the possibility of the Doppler-shifted ion acoustic wave. In the tail lobe, the typical electron and ion temperatures are $T_e = 200$ eV and $T_i = 20$ eV, respectively. Thus, the calculated ion acoustic velocity V_s is

$$V_s = \sqrt{\frac{T_e + 3T_i}{m_i}} \sim 158\text{km/s}. \tag{6.1}$$

Since destabilized ion acoustic waves are in the frequency range below f_{pi}, when we assume that the maximum frequency of expected ion acoustic waves is f_{pe}, the wave number is calculated as $k \sim 2 \times 10^{-3}\text{m}^{-1}$ using the above V_s and typical f_{pi} of 50 Hz . When we use the NEN frequency (f_{NEN}) of 200 Hz, we can estimate the needed bulk velocity v_b for the ion acoustic wave to be observed as NEN frequency due to the Doppler shift as follow,

$$v = \frac{2\pi(f_{NEN} - f_{pi})}{k} \sim 471\text{km/s}. \tag{6.2}$$

From the above estimation, we need the bulk velocity more than 470 km/s at least. However, we have never seen bulk flows with such a high velocity in the lobe region. Therefore, it is impossible to make the frequency of ion acoustic wave shift to the NEN frequency due to the Doppler shift. Before discussing another plausible mechanism of the NEN generation, we show another important nature of the NEN in Fig. 6.8. Figure 6.8 shows a frequency-time spectrogram observed on October 6, 1993. Focusing on the interval between 02:50 and 03:00 (UT), we note intense lobe EQMW (NEN) during that interval. As well known, the lower cutoff frequency of the continuum radiation emphasized by the black solid line is almost equal to the local electron plasma frequency. We note that the lower cutoff frequency of the continuum radiations shown in Fig. 6.8 has increased from 2 to 8 kHz during that time interval. This means that the local plasma density is increased from $0.05/\text{cm}^3$ to $0.8/\text{cm}^3$. The interesting point is that the maximum frequency of the lobe EQMW tracks the local plasma frequency. This fact indicates that the frequencies of the lobe EQMW are closely related to the local plasma density. This nature is consistent with the following generation mechanism related to electron dynamics.

The bursty nature of the EQMW suggests that they are related to the electron dynamics. *Coroniti and Ashour-Abdalla* [1989] and *Ashour-Abdalla et al.* [1989] proposed a new nonstandard electrostatic mode called "Electron velocity space hole modes." They

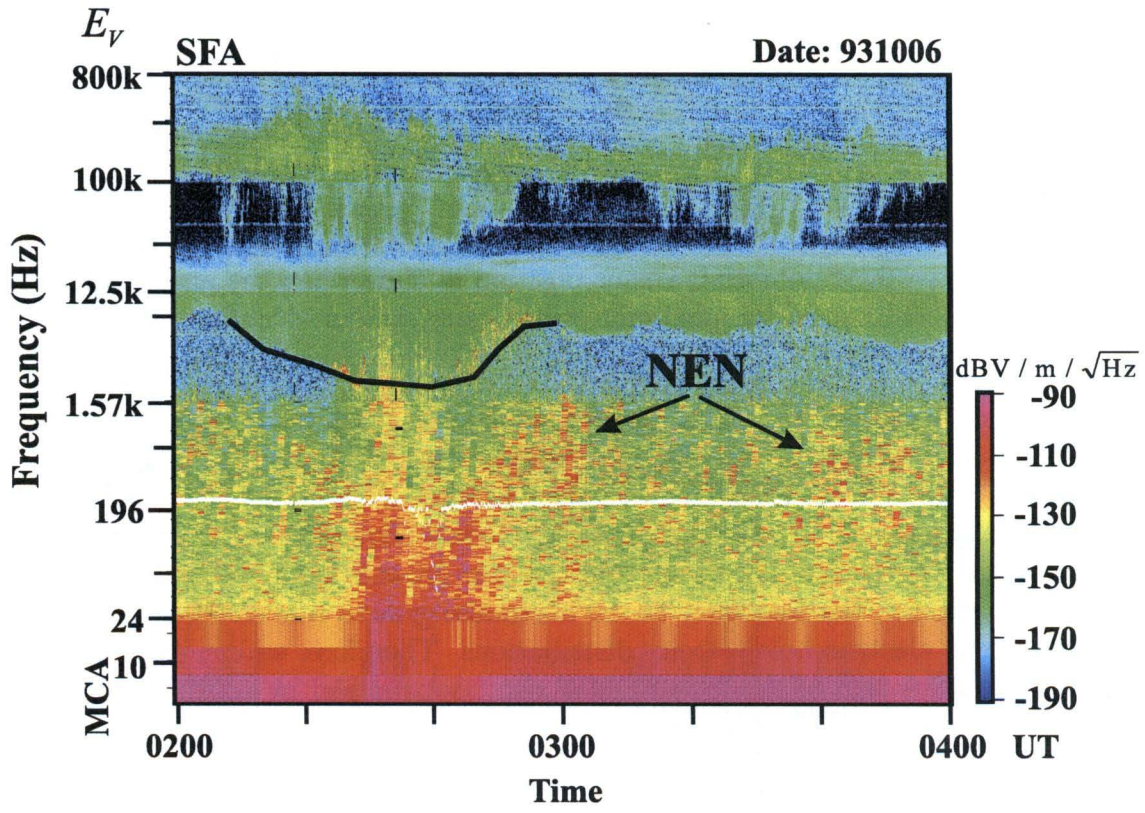

Figure 6.8: Relation between the frequencies of the lobe NEN and the local plasma frequencies. Their clear correlation can be seen during the interval from 02:50 to 03:00 (UT) [*after Kojima et al.*, 1997a].

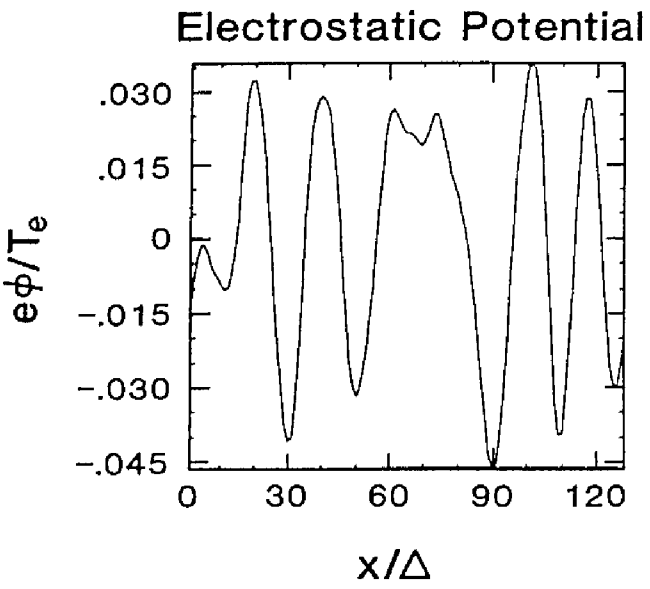

Figure 6.9: Electrostatic potentials versus position at time when the amplitude of excited most unstable mode reaches its maximum value [*after Ashour-Abdalla et al.*, 1989].

showed that some structures with a positive slope in electron velocity distributions destabilize this mode. Since the maximum linear growth rate is confined in the frequency range $10^{-2} < f/f_{pe} < 10^{-1}$, it is consistent with the NEN frequency range. *Coroniti et al.* [1993] examined the parametric dependence of this mode and showed that the growth rate is emphasized by the existence of ion beams and that the growth rate maximizes at the parallel propagation. Further, the frequency at the maximum growth rate changes depending on β and structures of electron hole velocity distributions. Therefore, we can expect that a kind of frequency modulation of the lobe EQMW can be explained by continuous variation of the electron velocity hole distribution.

Ashour-Abdalla et al. [1989] performed computer experiments on the electron velocity space hole mode, and showed the quasi-sinusoidal waves with their frequencies between f_{pe} and f_{pi}. Figure 6.9 shows spatial electrostatic potentials produced in their one-dimensional electrostatic particle computer experiments. They assume the initial electron velocity distribution with a hole in the low energy part of electrons. The excited waves saturate in about 50 times of electron plasma oscillation periods. When we use the typical $f_{pe} \sim 2$ kHz in the tail lobe, the saturation time is about 25 msec. This value is consistent with the bursty time scale of the lobe EQMW. The formed electrostatic potential structure shown in Fig. 6.9 is quasi-sinusoidal and it is easy to imagine the EQMW waveforms from such a potential structure.

The electron velocity space hole mode seems to be the most plausible generation mechanisms of the NEN observed in the lobe region. In order to examine the possibility of the electron velocity hole mode, we examined the relation of the NEN spectra and electron velocity distributions detected by the CPI plasma measurements.

Figure 6.10 shows the time variation of the NEN intensities observed in five different MCA

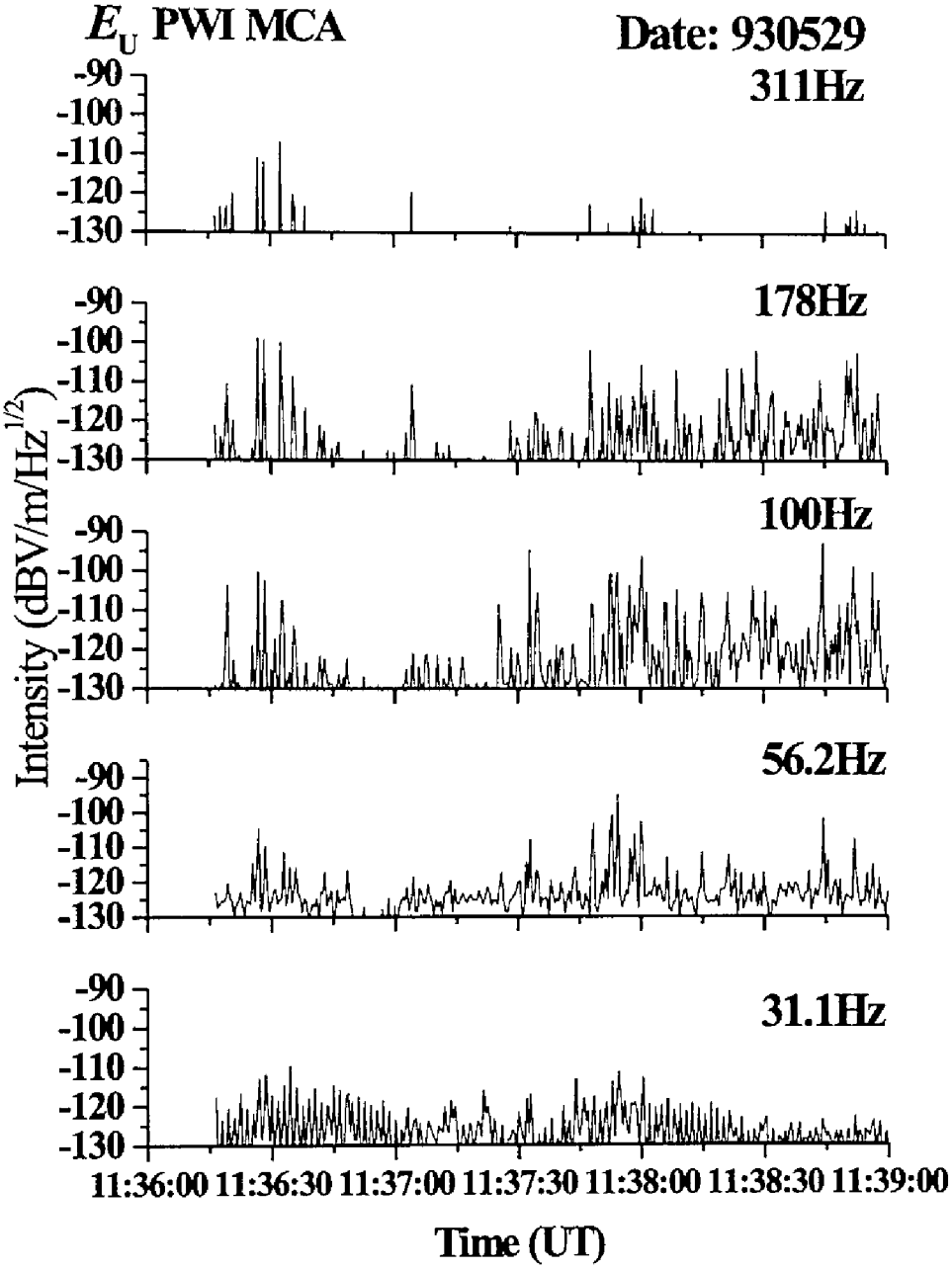

Figure 6.10: Time variation of the NEN intensities observed in five different frequency channels of the MCA.

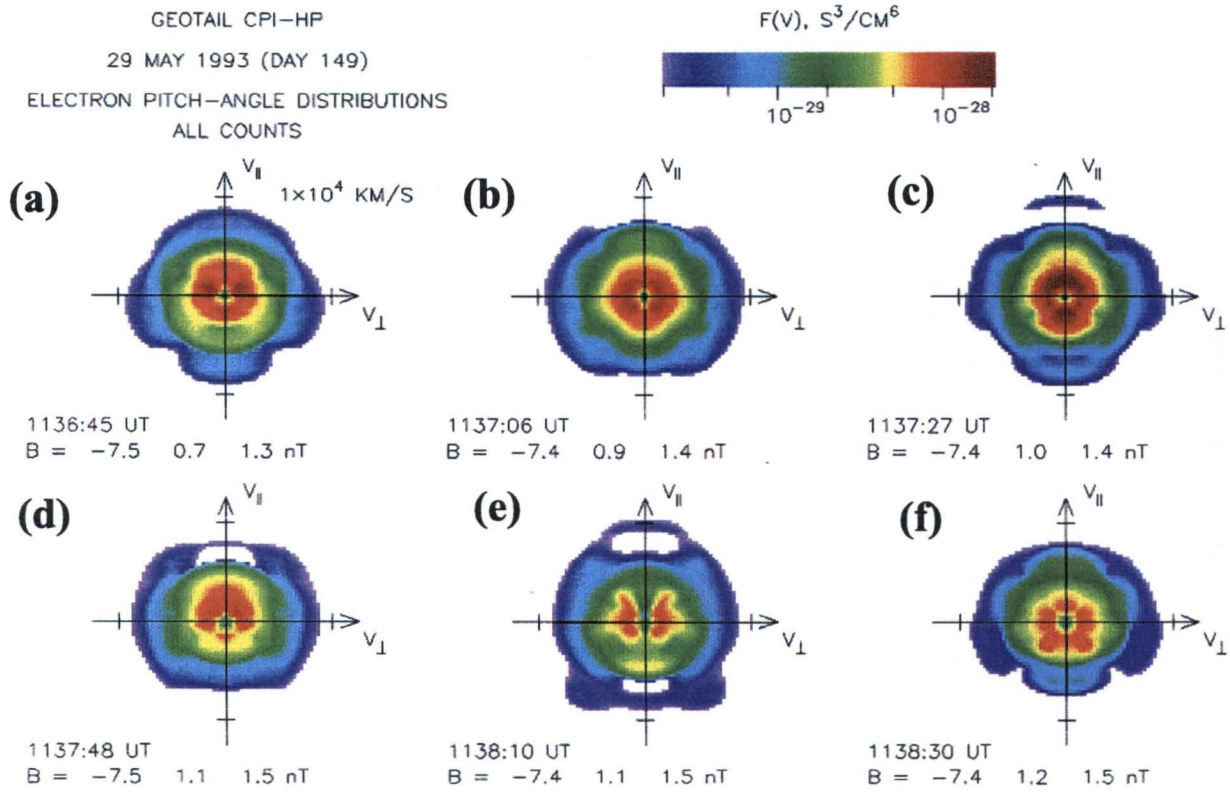

Figure 6.11: Time series of the Electron velocity distributions observed by the CPI. The color coding denotes the phase space density of electrons on $v_{\parallel} - v_{\perp}$ plane.

electric field channels. The NEN emissions shown in Fig. 6.10 is the same in Fig. 6.4 (a). Figure 6.11 shows a time series of electron velocity distributions observed by the CPI. The color coding denotes the electron phase density in $v_{\parallel} - v_{\perp}$ plane. In Fig. 6.10, the NEN emissions intermittently appear in the shown 5 channels. Especially during the interval from 11:37:45 to 11:39:00 (UT), the most intense emissions are observed in the channels of 56.2, 100, and 178 Hz. On the other hand, we can confirm that the electron velocity distributions shown in Fig. 6.11 have some structures except (b). It seems to be difficult to examine the structures quantitatively, but it is evident that the velocity distribution shown in (b) has fewer structures. Further, it is also clear that the velocity distributions of (e) and (f) have more structures. Now we compare these 2 figures. The velocity distribution (b) with fewer structures is observed at 11:37:06 (UT). We note that the shown velocity distribution is generated by the data accumulation during 6 seconds corresponding to 2 spacecraft spins starting from displayed time in each panel. Around the 11:37:06 (UT), the observed wave intensities are much less than those in other period shown in Fig. 6.10. On the other hand, in the time interval after 11:37:45 (UT) when the most intense emissions are observed, we can see the velocity distribution with much structures. The above coincidence can be also found in the next example.

Figures 6.12 and 6.13 show an another example for examining the coincidence between the NEN emissions and structures in electron velocity distributions. The display format

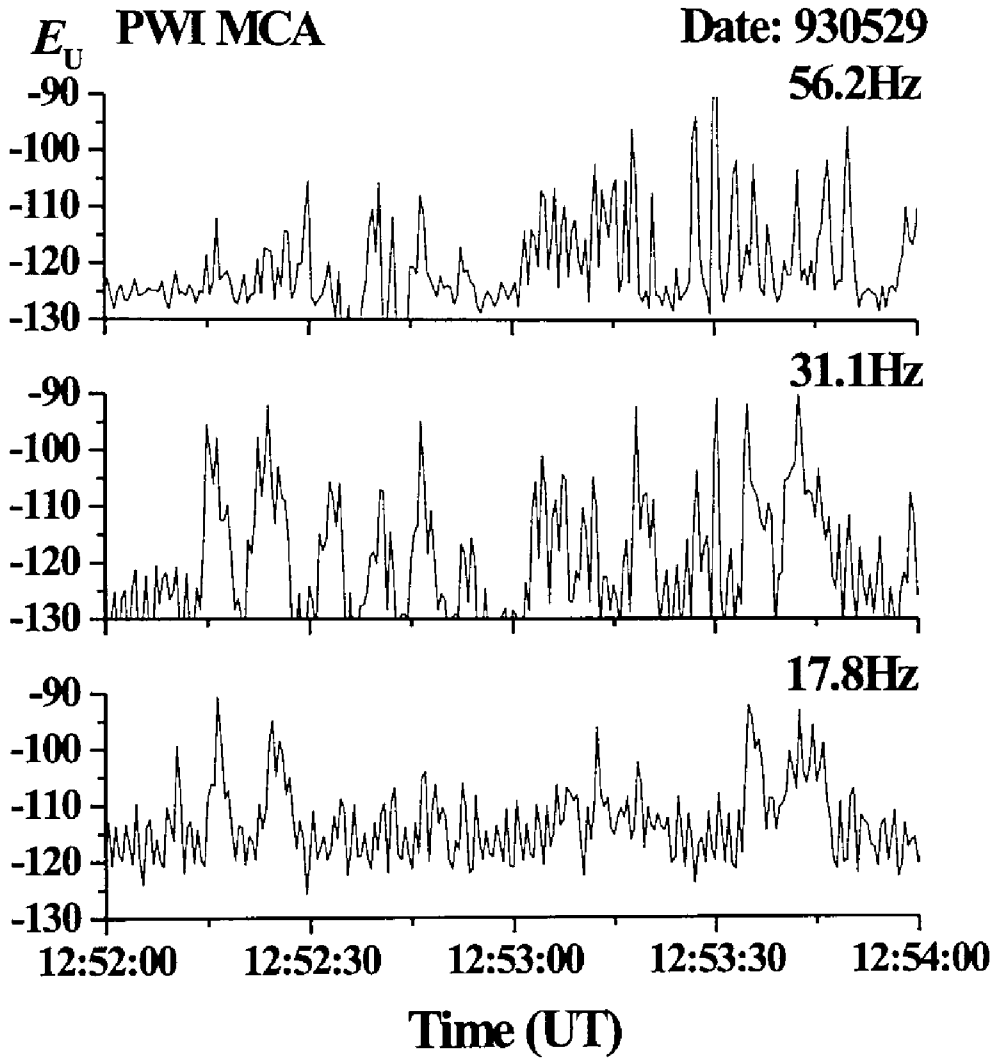

Figure 6.12: Same as Fig. 6.10 but for the different time interval.

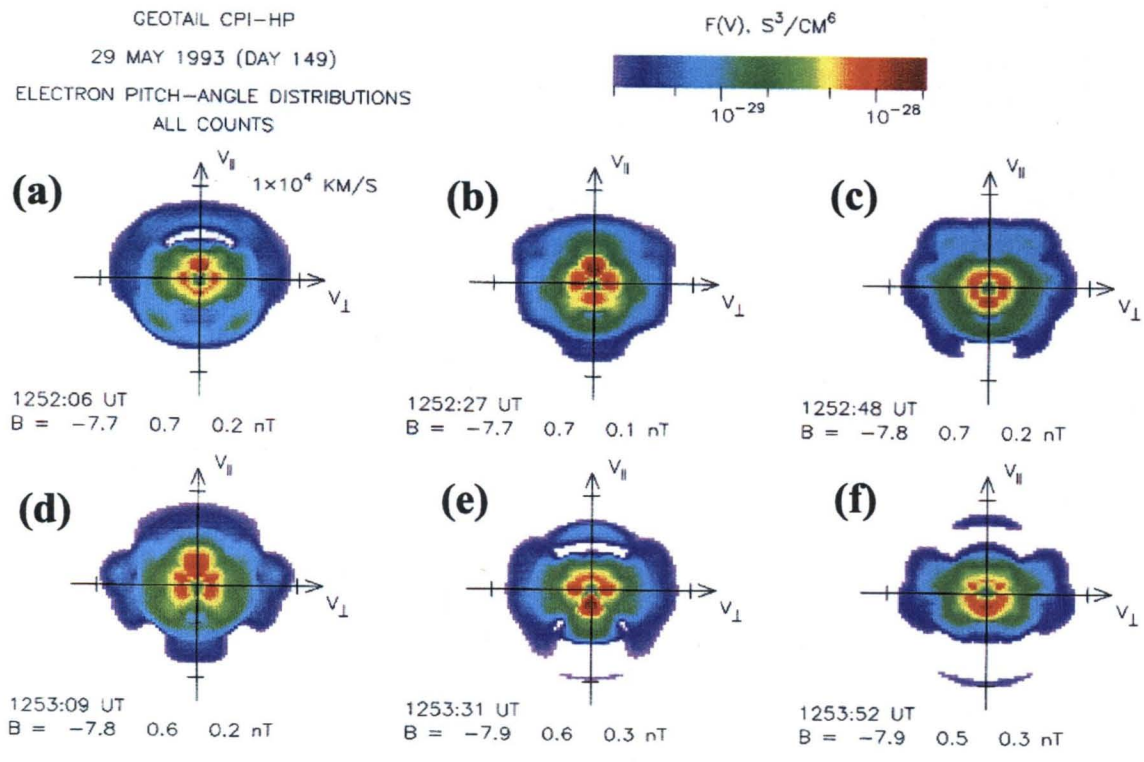

Figure 6.13: Same as Fig. 6.13 but for the different time interval.

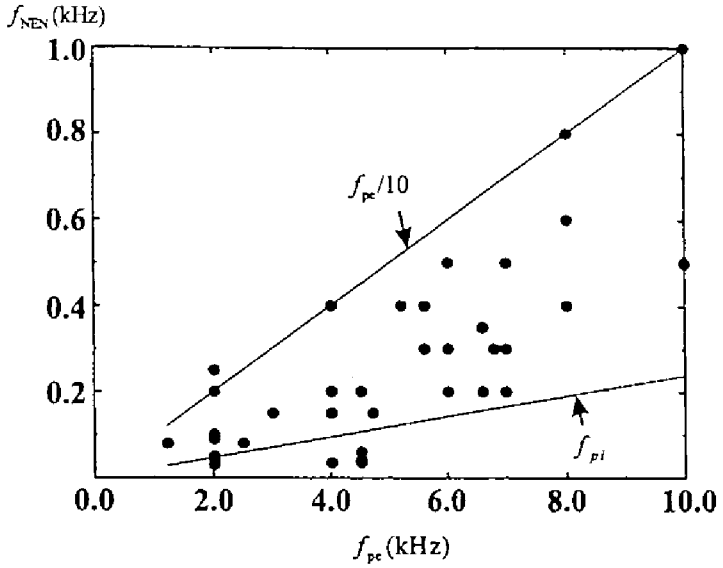

Figure 6.14: Relation of NEN frequencies and local electron plasma frequencies. It is evident that the NEN frequencies focus on the frequency range below $0.1 f_{pe}$.

is the same with that in Fig. 6.10 and Fig. 6.11. This case seems to be more complex. However, we can see that the fewer structure distributions can be seen in (a) 12:52:06 and much structure one in (d) 12:53:09, (e) 12:53:31, and (f) 12:53:52 (UT). The wave intensities in Fig. 6.12 appear the least activity during the interval from 12:52:00 to 12:52:30 (UT). Further, the most intense emissions are observed after 12:53:00 (UT). We also find the coincidence of the NEN intensities and structures of electron velocity distributions. This coincidence strongly suggests that the structure of electron velocity distributions (electron velocity space hole) play an important role for the generation of the NEN.

Coroniti and Ashour-Abdalla [1989] showed that the electron velocity space hole mode becomes most unstable in the frequency range of $10^{-2} < f/f_{pe} < 10^{-1}$. We picked up NEN events and examined the relation of their frequencies and electron plasma frequencies. The results are shown in Fig. 6.14. The two solid lines represent the one tenth of local electron plasma frequencies and ion plasma frequencies versus f_{pe}, respectively. It is clearly seen that the NEN frequencies are well confined in the frequency range below $f_{pe}/10$. This result is also consistent with the theory of the electron velocity space hole mode.

The structures in the velocity space are formed due to the mixture of different plasmas. Therefore, we expect such velocity distributions with structures around the boundary region, where the different plasmas interact each other. As we have shown in Fig. 3.14, the lobe EQMW can be observed in the lobe region close to the magnetopause boundary and/or plasma sheet. In the case of Fig. 6.4, the spacecraft moved across the magnetopause three times and in other interval, the spacecraft stays in the lobe region. This means that the spacecraft was located in the region close to the magnetopause. Therefore, the above fact on the observation region of the NEN is also consistent with the theory of the electron velocity space hole mode. Based on the above results, we can conclude that the NEN (EQMW) observed in the lobe region is the electron velocity space hole mode.

Omura et al. [1996] also confirmed the destabilization of the electron velocity space

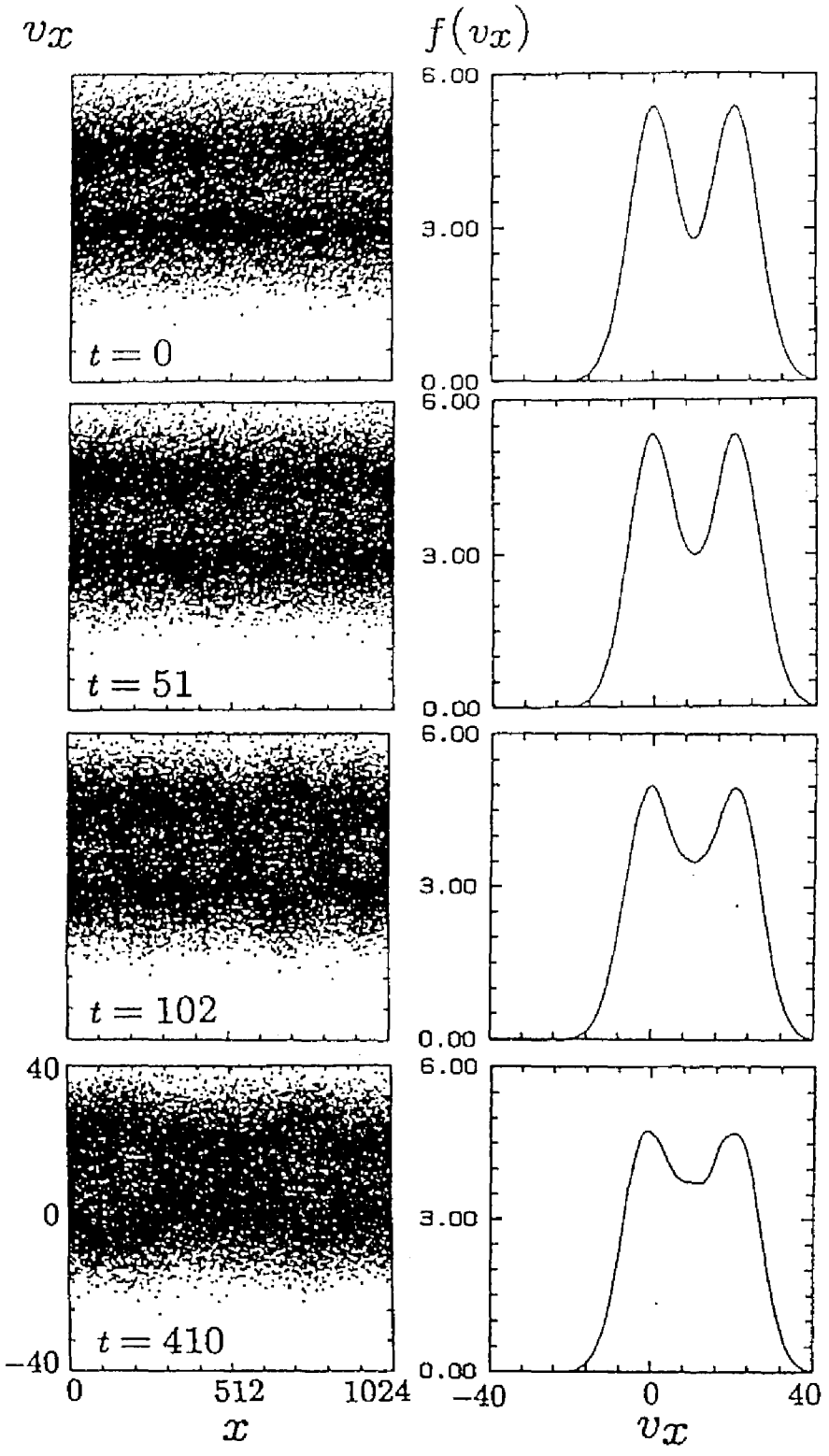

Figure 6.15: Time evolution of the electron velocity space hole instability in the same display format of Fig. 4.15 and Fig. 4.17 [*after Omura et al.*, 1996].

hole mode by their computer experiments as shown in Fig. 6.15. Although it is hard to see detailed structures of potentials in a series of left panels, we can find that electrons are trapped and several vortices are formed. *Omura et al.* [1996] found that the formed potentials are very stable at the final stage of computer experiments. They examined particle motions in the phase space at the final stage and they concluded that the stable potentials formed due to the electron velocity space hole mode is the BGK mode. This means that the electron velocity space hole mode can also generate the ESW. However, they claimed that the velocity of this BGK mode is very slow. Therefore, potential amplitudes estimated from the observed pulse width are too small. Such too small potentials do not trap electrons. Thus, they concluded that the PSBL ESW are generated by the bump-on-tail instability but not by the electron velocity space hole mode.

Chapter 7

Modulated electron plasma waves in the lobe region

7.1 Introduction

Electrostatic waves with amplitude modulations have been observed in the various regions [*Gurnett et al.*, 1981; *Gurnett et al.*, 1993; *Hospodarsky et al.*, 1994; *Stasiewicz et al.*, 1996; *Kellogg et al.*, 1996]. They are believed to be the Langmuir waves excited by electron beams, because their frequencies are almost equal to local electron plasma frequencies. They were initially detected by the Voyager spacecraft in the upstream region of the Jovian bow shock [*Gurnett et al.*, 1981]. They introduced two types of modulated Langmuir waves as shown in Figs. 7.1 and 7.2. They are the beat-type modulated waveforms (shown in Fig. 7.1) and the very isolated wave packets (shown in Fig. 7.2). As easily imagined from their waveforms, their spectra consist of two discrete spectral components with different frequencies. One of these spectra is generated by electron beams emitted from the Jovian bowshock, however, the another one no longer resonants with electron beams. *Gurnett et al.* [1981] claimed that the beat-type modulated waveforms are the results of the nonlinear parametric wave-wave interaction of beam-driven Langmuir waves with a preexisting background of ion acoustic waves. For the isolated wave packets, they pointed out the possibility of the Langmuir wave soliton.

Similar waveforms of the Langmuir waves in the solar wind at 0.98 AU were reported by *Gurnett et al.* [1993] using the plasma wave data of the Galileo spacecraft. They discussed the relation between modulated Langmuir waves and the type III solar radio bursts. Figure 7.3 shows the frequency time spectrogram of the observed type III solar radio bursts (a), high resolution waveform data of the Langmuir waves observed with the type III solar radio bursts (b), and Fourier spectra (c) corresponding to the waveforms of the third snapshot of (b).

It has been known that type III solar radio bursts are produced by energetic electron ejected by solar flares [*e.g., Gurnett and Frank*, 1975]. They are produced in the two step processes. 1. The Langmuir waves are excited by the ejected solar flare electrons and 2. They are converted to electromagnetic radiation with frequencies of $2f_{\rm pe}$ by nonlinear processes. In Fig. 7.3 (a), we can see the Langmuir waves associated with the type III solar radio bursts. The lower cut off frequency is two times higher than the Langmuir

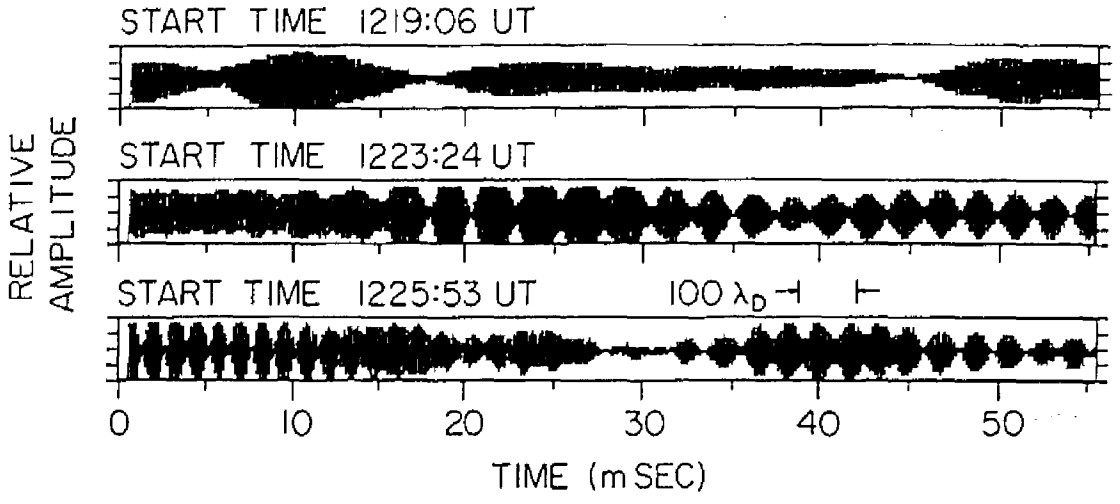

Figure 7.1: Three representative electric field waveforms of the beat-type modulation observed by the Voyager 1 spaceprobe in the upstream region of the Jovian bowshock [*after Gurnett et al.*, 1981].

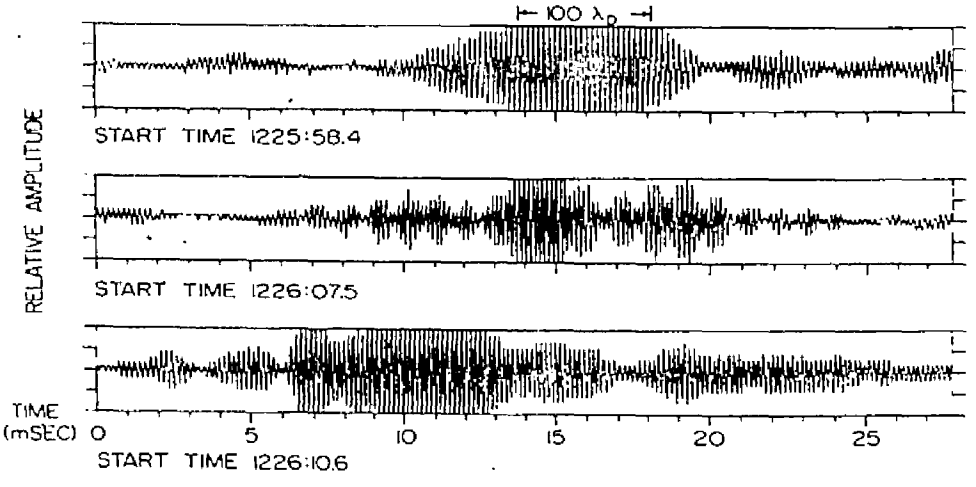

Figure 7.2: Electric field waveforms of the isolated wave packet type [*after Gurnett et al.*, 1981].

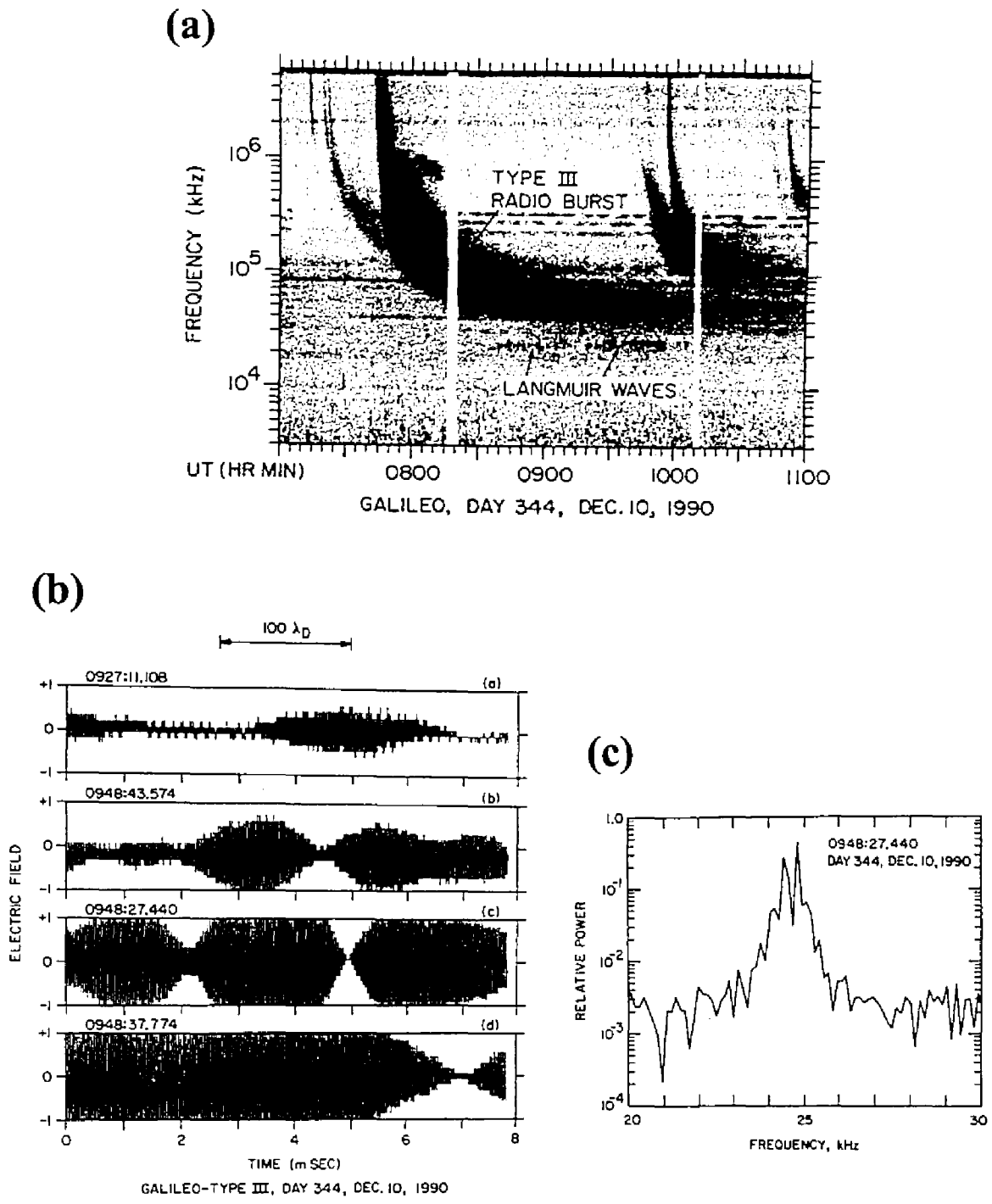

Figure 7.3: Frequency time spectrogram of the observed type III solar radio bursts with the Langmuir waves (a), high resolution waveform data of the Langmuir waves observed with the type III solar radio bursts (b), and Fourier spectra (c) corresponding to the waveforms of the third snapshot of (b) [*after Gurnett et al.*, 1993].

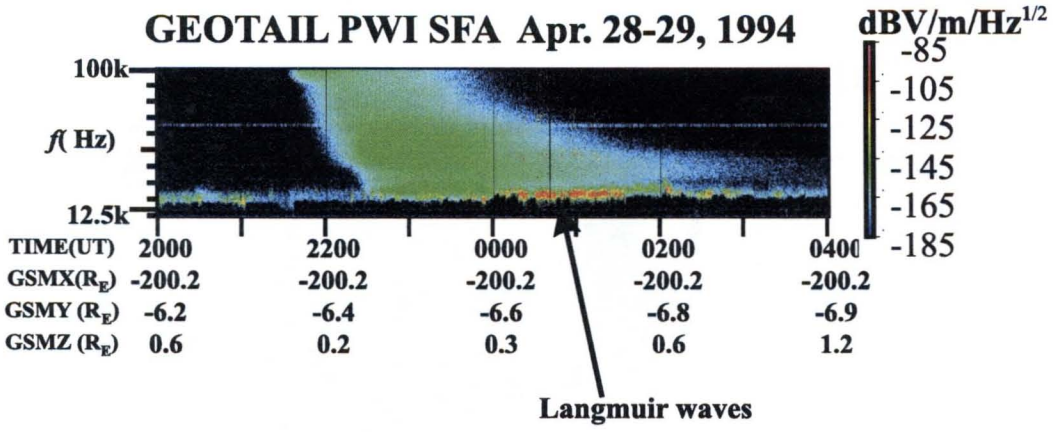

Figure 7.4: Geotail observations of the type III solar radio bursts and associated Langmuir waves [*Matsumoto et al.*, 1998].

wave frequencies. This is consistent with the theory of mode conversion from f_{pe} to $2f_{pe}$. Geotail also observes the many type III solar radio bursts and associated Langmuir waves as shown in Fig. 7.4 [*Matsumoto et al.*, 1998] but we note that the lower cutoff frequency of the type III solar burst shown in Fig. 7.4 is almost equal to Langmuir wave frequencies. This suggests that the low frequency portion of this type III solar burst is electrostatic.

Since unfortunately the Langmuir wave frequencies $\sim$ 20 kHz are beyond the upper limit of the WFC receiver, we cannot see their waveforms, but the Galileo digital wideband receiver showed that amplitudes of these Langmuir waves are strongly modulated as shown in Fig. 7.3 (b). The shown waveforms are quite similar to those in the case of the Jovian bowshock in Figs. 7.1 and 7.2. A representative spectrum corresponding to waveforms of third snapshot of panel (b) is shown in Fig. 7.3 (c). We can confirm that the modulation is caused by a beat between two waves of slightly different frequencies but comparable amplitudes. In this case, the frequency gap is about 300 Hz. *Gurnett et al.* [1993] claimed that the modulated Langmuir waves are also caused by the nonlinear parametric instability. However, they could not find one-to-one correlation between the modulated waves and the low frequency ion acoustic waves that should be excited simultaneously as the result of the nonlinear parametric process.

They also attempted to explain the isolated wave packets as the envelope soliton. However, they found that the amplitudes of the observed waves are not large enough to explain the phenomenon by the nonlinear wave theory.

The Geotail WFC receiver detected, in the geomagnetic tail region, modulated waveforms similar to the modulated Langmuir waves detected by earlier spacecraft. The observed modulated waves have a frequency almost equal to the local electron plasma frequency. In the present thesis, we call these electrostatic waves with a frequency close to the local electron plasma frequency as "electron plasma waves." They are frequently observed in the lobe region close to the PSBL.

In the present thesis, we report the results of the waveform analyses of the electron plasma waves observed in the lobe close to the plasma sheet, discuss their wave features, and compare them with previous observations of the modulated Langmuir waves.

7.2 Electron plasma waves observed in the lobe region

Figure 7.5 shows typical plasma wave signatures at the time of the plasma sheet entry (plasmoid entry which we discussed in Chapter 5) from the lobe region observed at (GSM X, GSM Y, GSM Z) = (–95, 11, –4 R_E) on January 13, 1994. Figure 7.5 (a) illustrates the frequency-time spectrogram generated from the Sweep Frequency Analyzer (SFA). The superimposed white line indicates the electron cyclotron frequency (f_{ce}) calculated from the fluxgate magnetometer data provided by the MGF team. Figure 7.5 (b) shows the time variation of the ambient magnetic field amplitude and its azimuthal direction in the spacecraft coordinate system.

During the interval from 13:00 to 13:10 (UT), as the white line for f_{ce} and B_o show, the ambient magnetic field is very stable and has the magnitude of 12 nT. After 13:10 (UT), the magnitude starts to decrease and to fluctuate. It recovers to the stable magnitude after 13:14 (UT). Judging from the azimuthal angle shown in the lower panel of Fig. 7.5 (b) the spacecraft was located in the north lobe region during the interval of 13:00 to 13:10 (UT) and reached to the south lobe region at 13:14 (UT) after passing through the central plasma sheet (center of the plasmoid). The intense broadband emissions are observed below 4 kHz during the interval of 13:10 to 13:14 (UT) in Fig. 7.5 (a). This broadband emission is the BEN, which was discussed in Chapters 4 and 5.

The monochromatic spectra (indicated by two white arrows) around 3 kHz are "electron plasma waves" which we discuss in the present chapter. The weak emission observed continuously above 3 kHz during the whole period in the frame, is the Continuum Radiation (CR). The lower cutoff frequency of the CR corresponds to the local electron plasma frequency (f_{pe}) as we introduced in Section 1.3.2 [*Gurnett and Shaw*, 1973; *Nagano et al.*, 1994]. Since the frequencies of the observed electrostatic waves are almost equal to the lower cutoff frequencies of the CR, they are the emissions with frequencies around f_{pe}. As clearly seen in this figure, the electron plasma waves are observed just before the plasma sheet (plasmoid) entry at 13:10 (UT).

The WFC detected the waveforms of these electron plasma waves at 13:05:54.321 (UT), as shown in Fig. 7.5 (c). The detected waveforms are highly modulated in amplitude. The frequency of the monochromatic sinusoidal waves is approximately 3 kHz, while the modulation frequency of the wave envelope is very irregularly changing. Such amplitude modulation is the result of superposition of several spectral components with different frequencies. With the SFA alone, however, we cannot resolve the frequency difference of these spectra, because of its insufficient frequency resolution. Therefore, it is very important to perform Fourier analyses of the high time resolution data by the WFC (see Section 7.4).

The waveforms shown in Fig. 7.5 (c) are very similar to those of the Langmuir waves observed by Voyager, Galileo, Freja, and Wind spacecraft (see Fig. 7.1, Fig. 7.2, and Fig. 7.3). It is very interesting that the similar waveforms are observed in different regions.

In the following section, we show the results of detailed data analyses of the modulated electron plasma waves observed in the tail lobe focusing on their polarizations, and spectral structures.

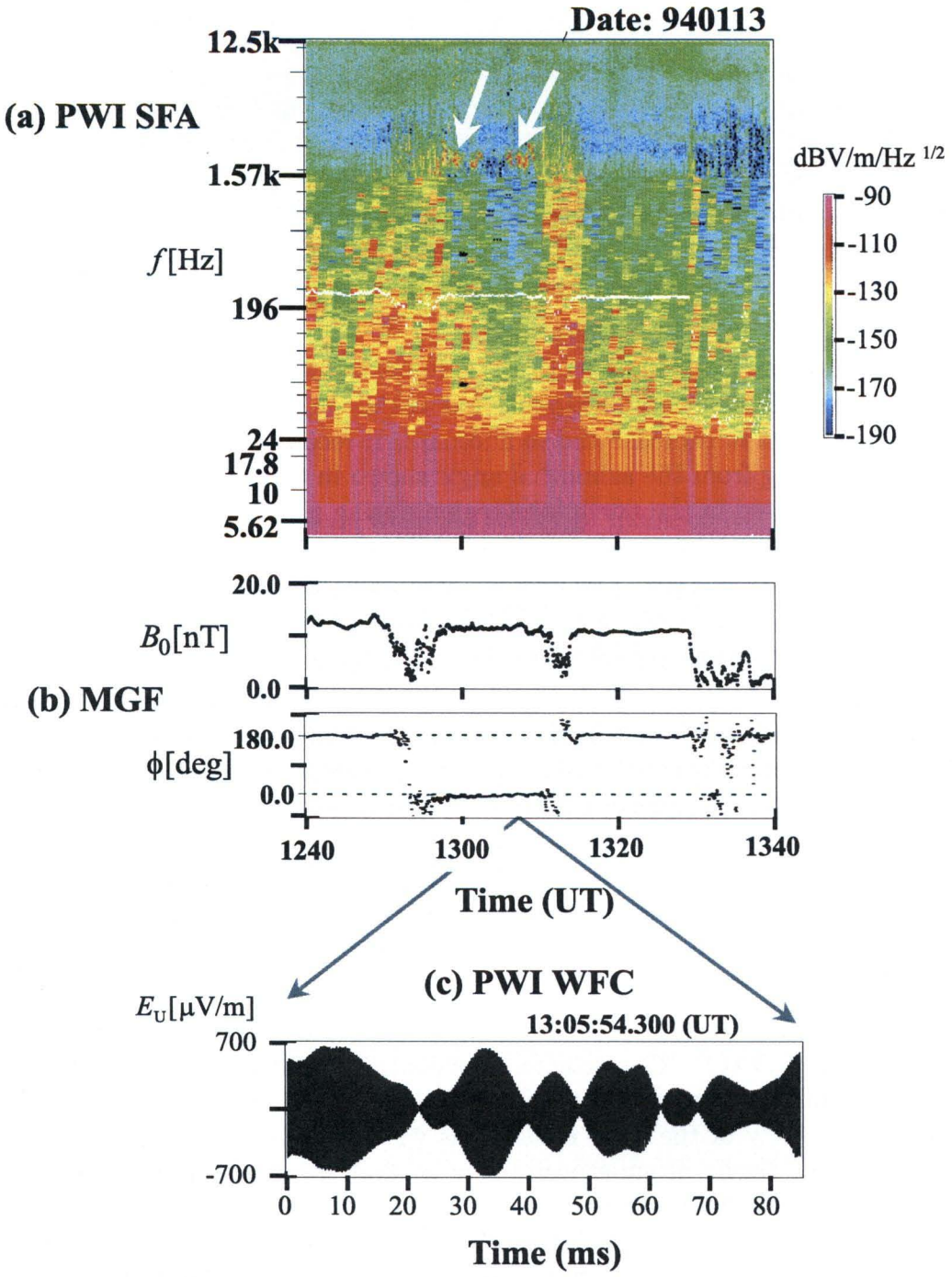

Figure 7.5: Electron plasma waves observed in the lobe close to the plasma sheet. (a) Frequency-time spectrogram generated from the SFA, (b) time variation of the magnetic field magnitude and its azimuthal direction, and (c) modulated waveforms of the electron plasma waves shown in panel (a).

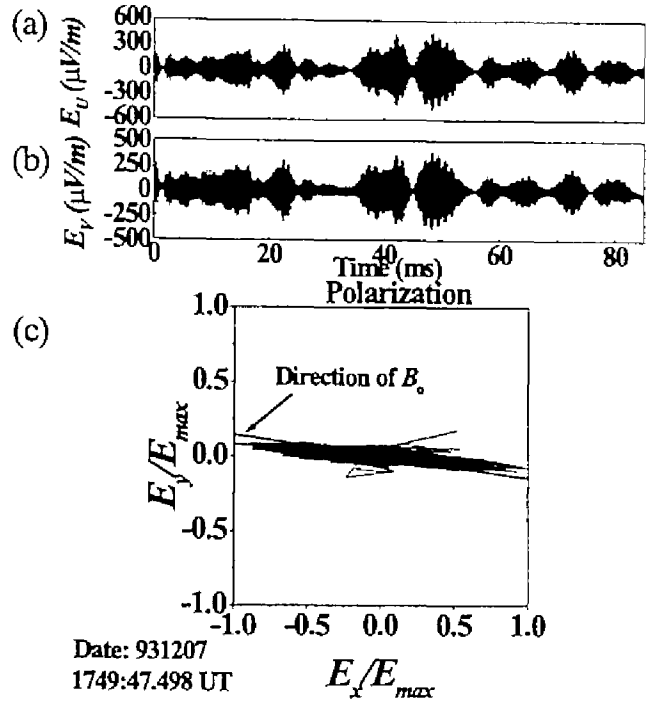

Figure 7.6: Example of waveforms ((a) and (b)) and polarization ((c)) of the modulated electron plasma waves [*after Kojima et al.*, 1997b].

7.3 Polarization analyses

As the WFC simultaneously samples the waveform data of 2 orthogonal electric field components (E_U and E_V) in the spin plane, which is almost equal to the ecliptic plane, we can identify the polarization of the electric field in the spin plane as shown in Fig. 4.8. By converting the observed waveforms E_U and E_V into 2 electric field components (E_x, E_y) in the spacecraft coordinates by using Eq. (4.1), we examined the polarization of the electric field for the observed modulated electron plasma waves, and found that they include two different polarizations relative to the ambient magnetic field B_0.

Figures 7.6 and 7.7 show the 2 components of the waveforms ((a) and (b)) and polarizations ((c)) of the electron plasma waves observed in the lobe region on December 7, 1993, and November 8, 1993, respectively.

Two different modulations of the electron plasma waves can be identified by comparing the upper panels of Figs. 7.6 and 7.7. The shape of the waveform envelope shown in Fig. 7.6 is very asymmetric and its modulation frequency changes in a short time, while the amplitude modulation shown in Fig. 7.7 is very regular. Further, we can see the significant difference in their polarizations shown in the lower panels. We have plotted the time variation of the observed electric field vectors in the $E_x - E_y$ plane. The data are normalized to the maximum value of either E_x or E_y. The data points consist of all values sampled by the WFC over the entire time period displayed in the upper panels in Fig. 7.6

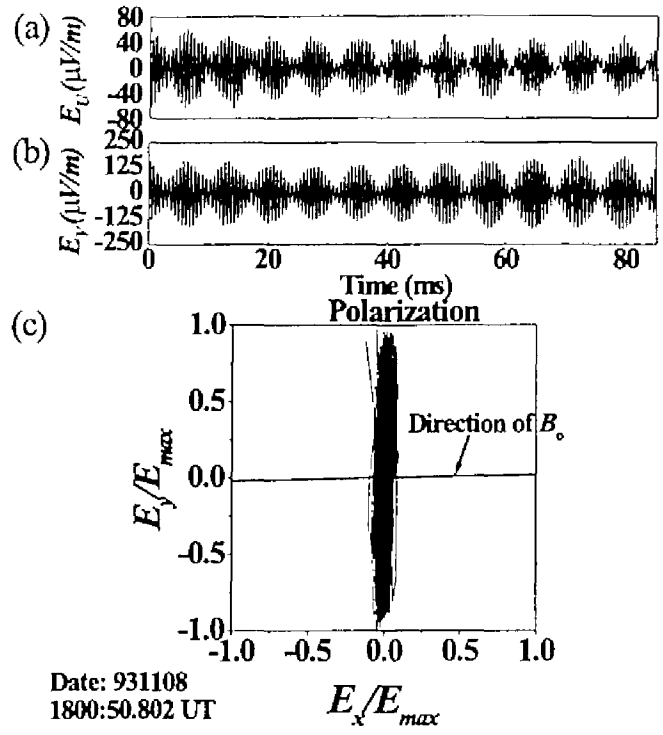

Figure 7.7: Another example of the waveforms and polarizations of the modulated electron plasma waves [*after Kojima et al.*, 1997b].

or Fig. 7.7. The solid lines indicated by arrows in lower panels display the parallel direction relative to B_0 in the $E_x - E_y$ plane. As clearly seen in these figures, orientations of the polarizations plotted in Fig. 7.6 (c) and Fig. 7.7 (c) are almost parallel and perpendicular to B_0, respectively.

As we have introduced in the previous section, the frequencies of the modulated electron plasma waves are almost equal to the local electron plasma frequencies. Therefore, the parallel polarized electron plasma waves shown in Fig. 7.6 are the Langmuir waves. On the other hand, the modulated electron plasma waves shown in Fig. 7.7 are likely to be Electron Cyclotron Harmonic (ECH) waves. This speculation will be confirmed in the analysis on their detailed spectral structure, which will be introduced in the next section.

7.4 Classifications of the modulated electron plasma waves

We have examined the observed waveforms of the modulated electron plasma waves based on the 15,300 waveform samples, where the 85 ms waveform dataset is counted as one sample. As we have shown in the previous section, the modulated electron plasma waves are classified into two groups: (I) Parallelly polarized waves relative to B_0 and (II) Per-

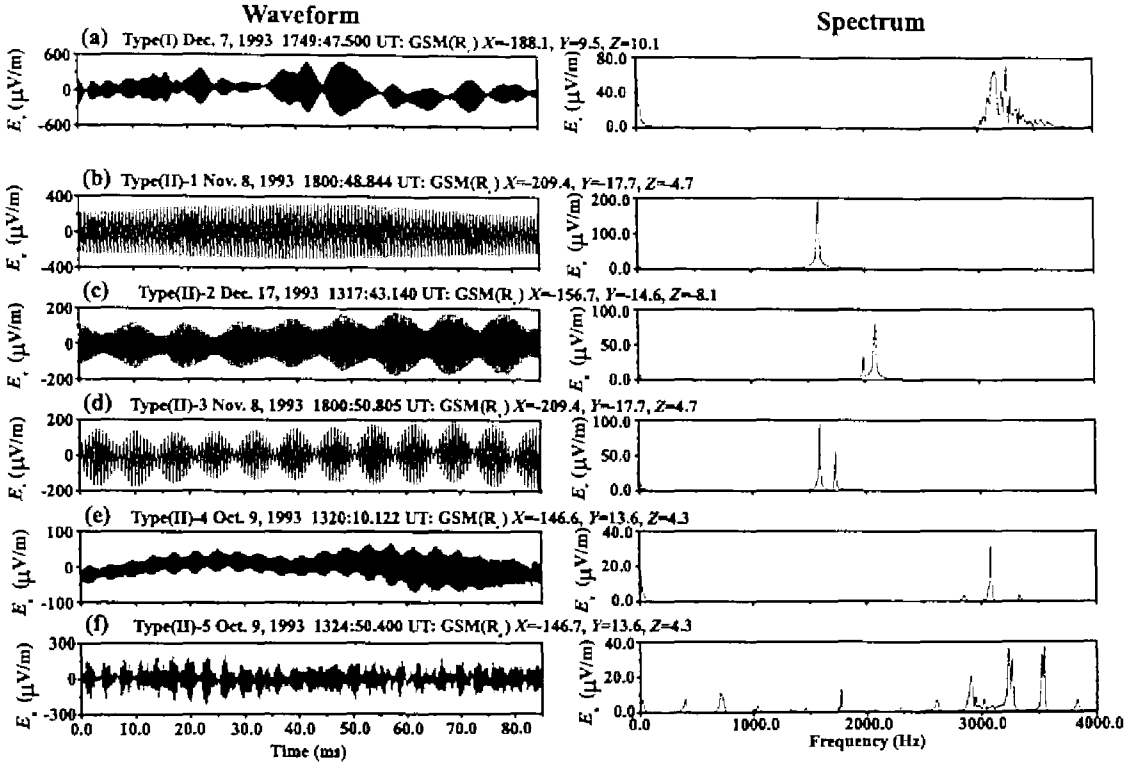

Figure 7.8: Classification of the modulated electron plasma waves. Left and right panels illustrate the waveform and corresponding Fourier spectra in each type of the modulated electron plasma waves, respectively [*after Kojima et al.*, 1997b].

pendicularly polarized waves. Based on the analyses for the spectral structures of the modulated electron plasma waves, we found that waves belonging to the group (II) are further classified into five types, as shown in Fig. 7.8.

Figure 7.8 shows the classified waveforms (left panels) and the corresponding Fourier spectra (right panels). The group (I) (panel (a)) is the modulated Langmuir wave, which electric fields oscillate along the ambient magnetic field. As shown in the right panel, it has a broader frequency spectrum than those of the group (II). From the irregular amplitude modulation shown in (a), we can easily imagine such a broader spectrum, because the irregular amplitude means the quick change of frequencies of superposed waves.

The waveforms in the group II are classified into 5 types based on the differences of the spectral structures. As shown in the frequency spectra of Fig. 7.8 (b)-(f), the spectra of the group II consist of several discrete spectrum components. Here we define the most intense spectrum component as the main spectrum and others as its sideband spectra. Type(II)-1 is monochromatic and its spectrum has no sidebands. The sideband spectrum of the Type(II)-2 appears on the slightly lower frequency side of the main spectrum, while that of the Type(II)-3 appears on the higher frequency side. The Type(II)-4 has both the lower and higher sideband spectra. Though the Type(II)-5 does not show a clear wave envelope, it consists of multiple sideband spectra.

All of the spectra in the group II except Type(II)-1 have discrete sideband spectra. It is noted that a simple superposition of the main and sideband components causes the

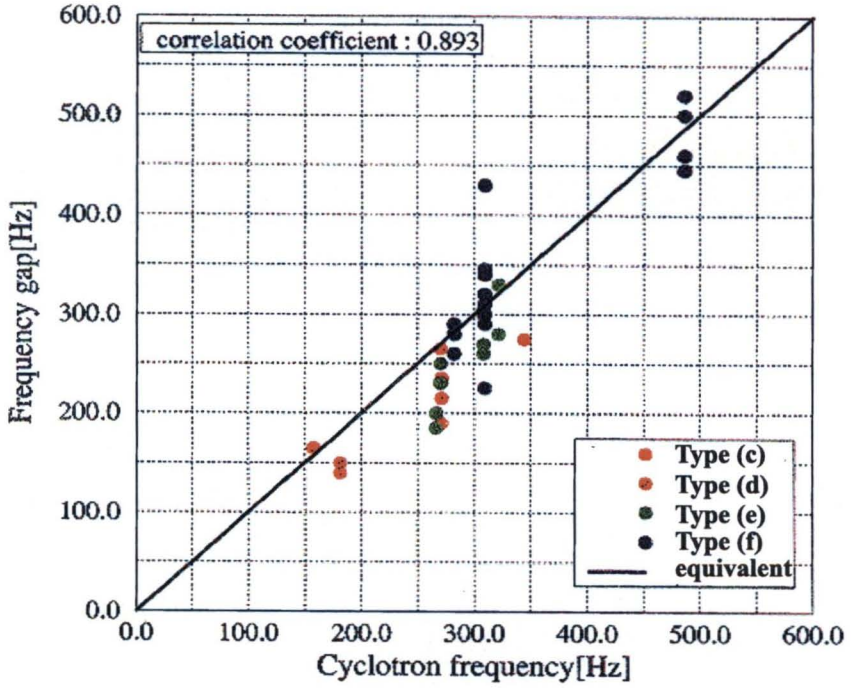

Figure 7.9: Relation between frequency gaps of each spectrum in the type(II)-2 to type(II)-5 and local electron cyclotron frequency.

modulated waveforms. To understand the discrete spectra, we measured the frequency gaps between each spectral peak in the group II. Figure 7.9 shows the relation between local electron cyclotron frequency and frequency gaps of each spectral component in the type(II)-2 to type(II) 5. From this figure, it is evident that the frequency gaps of these types are almost equal to the local electron cyclotron frequency. These results strongly suggest that the modulated waves of the Type(II)-2 $\sim$ 5 are family members of ECH waves. This result is consistent with the result from the polarization analyses discussed in the previous section. Thus, we conclude that the electron plasma waves belonging to the group (II) are the ECH waves.

7.5 Discussions

We have examined the waveforms of the electron plasma waves observed in the tail lobe region. The Geotail waveform observations have revealed that their amplitudes are strongly modulated. We have examined the polarization direction of these waves, and found that they include parallelly polarized waves relative to B_0 (group (I)) and perpendicularly polarized waves (group (II)). We also showed that the group (II) is classified further into 5 types from the view point of the spectral structure. From the results of the polarization and spectral structure analyses, we conclude that the modulated electron plasma waves in the group (II) are the ECH waves. On the other hand, the group (I) waves are the Langmuir waves.

In the tail lobe region, typical electron cyclotron frequencies ($f_{ce} \sim 300$ Hz) are much smaller than the typical electron plasma frequencies ($f_{pe} \sim 2$ kHz). Therefore, the typical upper hybrid resonance (UHR) frequency ($f_{pe} \sim 2.02$ kHz), where the ECH waves are most unstable, is close to f_{pe}. This fact easily misleads to confusion of ECH waves around the UHR frequency with Langmuir waves. Without the determination of their propagation direction, distinguishing the above 2 wave modes is difficult.

Likewise in the solar wind at 1.0 AU, the typical electron plasma frequency ($f_{pe} \sim$ 20 kHz) is much higher than the typical electron cyclotron frequency ($f_{ce} \sim 200$ Hz). *Gurnett et al.* [1993] reported that the modulated Langmuir waves observed in the solar wind at 0.98 AU using the Galileo plasma wave data (see Fig. 7.3). They showed the poor correlation between the modulated Langmuir waves and the ion acoustic waves which are expected from the nonlinear parametric instabilities. They explained the above poor correlation by the lack of sensitivity of the receiver for the observations of the expected ion acoustic waves. However, our result from the Geotail observation in the tail lobe suggests one alternative possibility that their observation may have included the ECH waves because they have not shown the polarization analysis. In the solar wind, since the typical f_{pe} and f_{ce} are equal to 20 kHz and 300 Hz, respectively, UHR frequency is typically equal to 20.002 kHz. It is also difficult to distinguish the UHR waves from the Langmuir waves without the examination of their polarizations. Further, the waveforms shown in Fig. 7.3 are very symmetric and their modulation is very regular. These features are the same as those of our ECH waves. In addition, since the frequency gap of the twin spectral peaks shown in Fig. 7.3 (c) is about equal to 300 Hz, it is very close to the typical f_{ce} in the solar wind. From these discussions, we believe that it is highly possible that the Galileo data as shown in Fig. 7.3 include ECH waves. Since the modulated waveforms of the ECH waves do not need any nonlinear processes, we do not need ion acoustic waves. We can explain the poor correlation between the ion acoustic waves and modulated electron plasma waves by observations of the ECH waves.

Nonetheless, we need to explain the modulation of the Langmuir waves (group I) by some nonlinear processes. Previous theoretical attempts to explain the modulated Langmuir waves were to consider nonlinear parametric instabilities. However, there still remains the problems of the poor correlation of the Langmuir waves with the ion acoustic waves. We also do not see the clear correlation between ion acoustic waves and modulated Langmuir waves. Figure 7.10 shows an example for poor correlation of the modulated Langmuir waves and ion acoustic waves. The panel (a) consists of frequency-time spectrogram generated from $E_{\|}$ component of the WFC data (a-1), waveforms (a-2) and magnified waveforms corresponding to the Langmuir waves (a-3). The data shown in this figure are observed at (GSM X, GSM Y, GSM Z) = (−194.5, 38, 0.9 R_E) on April 11, 1994. The spectral intensities of $E_{\|}$ gradually increases from 13:18:34 (UT) in the shown period and they reach maximum amplitudes after 13:18:41 (UT). The detailed waveforms can be seen in panel (a-3). The irregular amplitude modulations are one of the characteristics of the modulated Langmuir waves. If the shown modulated Langmuir waves are generated by the parametric instabilities, the correlation with intensities of ion acoustic waves should be seen in the low frequency portion of the spectrum. The panel (b) focuses on the low frequency portion of the frequency-time spectrogram of panel (a). The modulated Langmuir waves start to be intensified from 13:18:34 (UT), but we cannot see any significant changes of the spectra

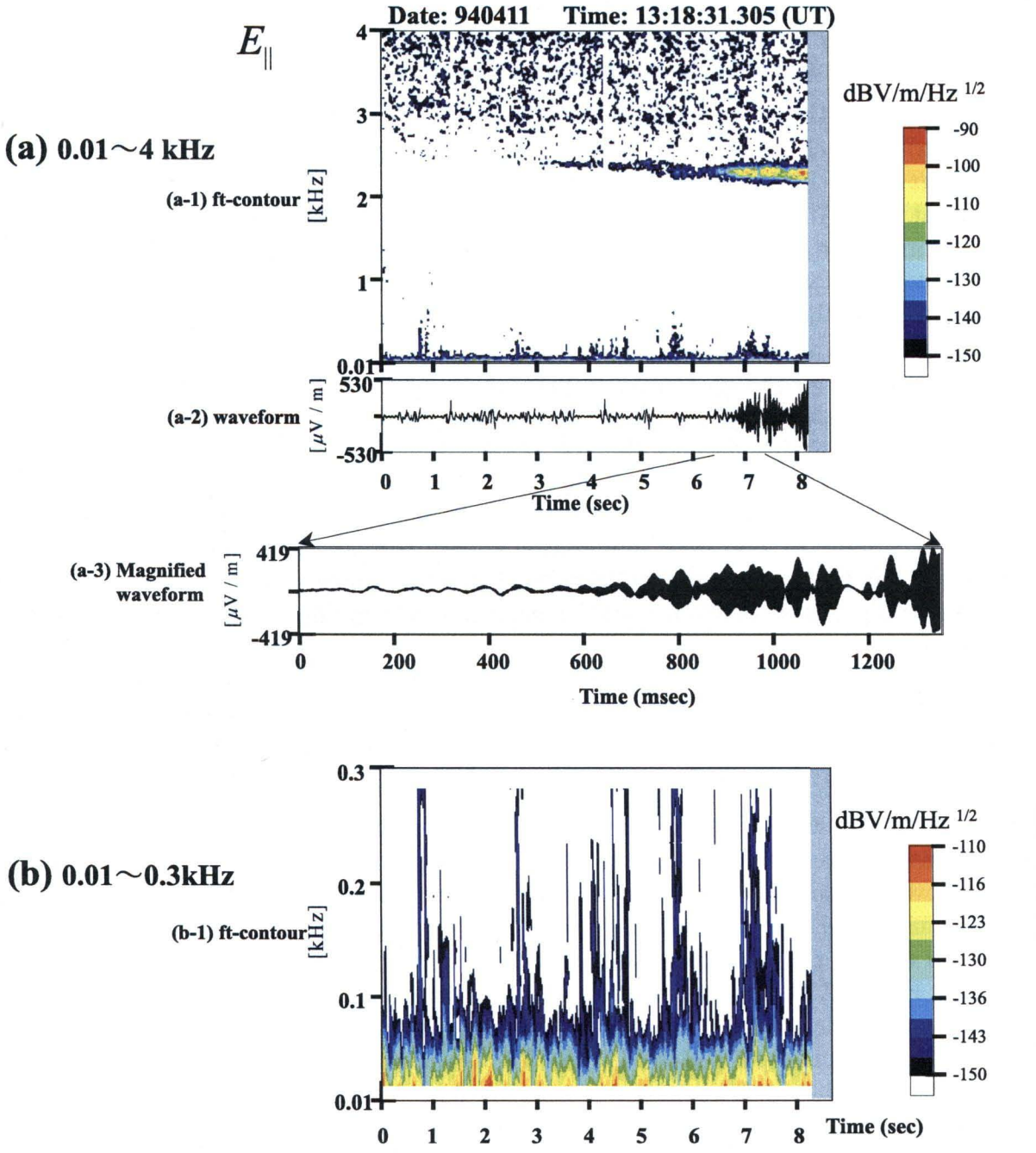

Figure 7.10: Relation of low frequency emissions as ion acoustic waves and the modulated Langmuir waves. (a) Frequency-time spectrogram generated from the WFC data for the modulated Langmuir waves and their waveforms, (b) Frequency-time spectrogram focused on the low frequency portion of the above spectrogram.

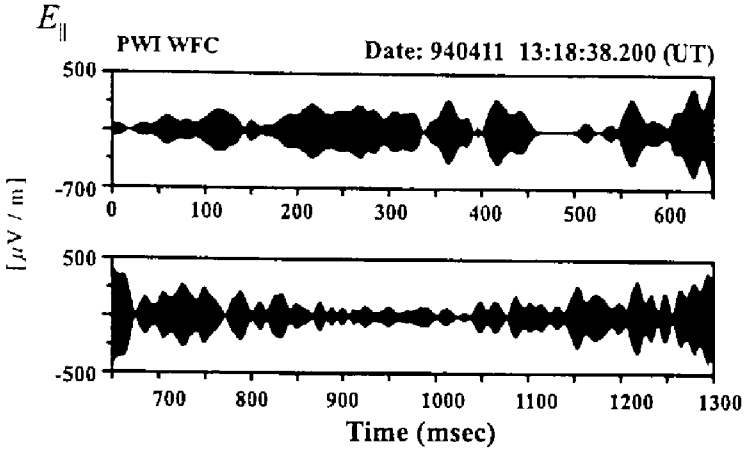

Figure 7.11: Quick change of amplitude modulations in the Langmuir waves.

shown in the panel (b). We have the same discrepancy between the observations and the theory of the parametric instability.

Akimoto et al. [1996] demonstrated that the Langmuir wave packets can be generated without the nonlinear parametric instabilities. On the basis of the particle simulations, they showed that Langmuir waves excited by electron beams are strongly modulated in space by the effect of the nonlinear spatial trapping. They pointed out that this spatial nonlinear trapping effect is converted to the temporal amplitude modulation as discussed in the present paper. If the nonlinear spatial trapping uniformly takes place along the ambient magnetic field, the length of the wave packet reflects the spatial static potential flow velocity, which is equivalent to electron beam velocity. Figure 7.11 shows snapshots of the modulated Langmuir waves for a longer time period. We see that packet lengths drastically change several times in time scales of a few hundreds of milliseconds. For example, during the duration of the first 850 msec, the packet length is about a few tens of milliseconds, while during the duration of next 600 msec, it is about 20 msec or less. If we apply the nonlinear trapping model to this quick change of packet length, we can expect that the electron beam velocities quickly change in a time scale of a few hundreds of milliseconds. This result is very important, because such fast phenomena with a time scale of a few hundreds of milliseconds cannot be detected by the plasma measurements onboard Geotail spacecraft. Since plasma wave observations in general have the highest time resolutions, and they are the most sensitive, they allow us to clarify phenomena with very short time scales.

The nonlinear spatial trapping model proposed by *Akimoto et al.* [1996] is the most plausible model for the modulated Langmuir waves. Since we need the nonlinear parametric instability in this model, the discrepancy between observations and theories is resolved by this model. Further, this model can be applicable for other electrostatic wave modes such as ion acoustic waves as well as Langmuir waves. We frequently observe the moderate amplitude modulation in the EQMW, which we discussed in Chapter 6, and ion acoustic-like waves observed in the foreshock region [*Matsumoto et al.*, 1997]. Therefore, explaining these amplitude modulations by the spatial nonlinear trapping model is possible. We need further studies on the modulation mechanism of the Langmuir waves, which we discussed above,

under the collaboration of computer experiments. The generation mechanism of the ECH waves is not clear. We need to explain which excites ECH waves and which mechanisms switch over from Langmuir waves to ECH waves or vice versa. We consult electron velocity distributions in order to examine the difference of the plasma environment between the case of Langmuir waves and ECH waves. Figure 7.12, and Figure 7.13 show the waveforms (panel (a)), frequency-time spectrogram (panel (b)), and electron distributions (panel(c)) when we observe the Langmuir waves and ECH waves as dominant waves, respectively.

The electron velocity distributions are shown in the cases without Langmuir waves or ECH waves (panel c-1) and with them (panel c-2). Further, we show the electron velocity distributions on the meridian plane including spacecraft spin axis and sunward vector (upper), and on the spin plane (lower).

We see intense Langmuir waves in $E_{\parallel}$ panel of Fig. 7.12 and ECH waves in $E_{\perp}$ panel of Fig. 7.13. In both Fig. 7.12 and Fig. 7.13, we clearly see the beam components streaming in the tailward direction as indicated by arrows. It is well known that the Langmuir waves are excited by electron beams, while it is not still clear that the relation of the ECH wave excitation and electron beams. However, as shown in both figures, electron beam components seem to be important for the excitation of both Langmuir waves and ECH waves. However, we cannot see the significant difference between the electron distributions for the Langmuir waves and the ECH waves. The switch process between the Langmuir waves and ECH waves is one of the important problems which are remained unresolved in this thesis.

Discussing the competing processes among the 2 groups of modulated electron plasma waves is also very important. One example which shows such competing or switching process is shown in Fig. 7.14. Figure 7.14 (c) is the frequency-time spectrogram deduced from the WFC data. The spectrum structure of the modulated electron plasma waves can be seen in the frequency range between 1.5 kHz and 2.1 kHz. Figure 7.14 (a) and (b) are hodograms at 13:11:15.892 (UT) and 13:11:16.799 (UT) with the period of 85 ms in the same format as those in Fig. 7.7, respectively. Surprisingly, the wave polarization changes from the perpendicular direction to the parallel direction relative to B_0 in a short time within only 1 sec. We confirmed that the direction of B_0 does not change during this short period using high time resolution fluxgate data (*T. Yamamoto and S. Kokubun, private communication*). This interesting result means that small difference in the plasma environment, especially in the electron distribution, may control the types of the modulated electron plasma waves. Though we need to compare the waveforms with the plasma measurement, the coarse time resolution of the particle detector does not allow it. Therefore, we need to develop a computer simulation to understand such sudden change of the wave properties in a short time. This will be reported in the future.

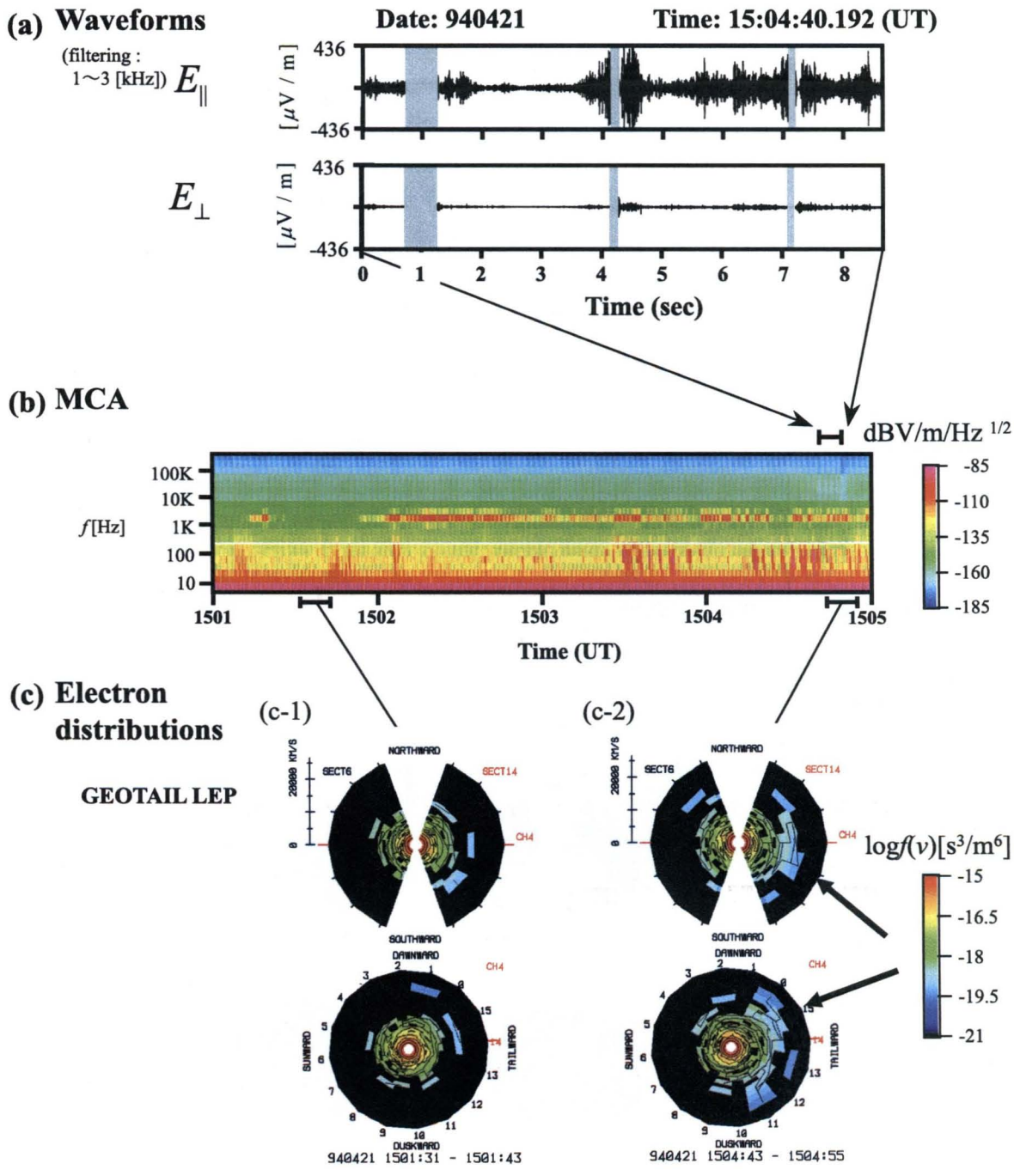

Figure 7.12: Comparison of the modulated Langmuir waves and electron velocity distributions. (a) waveforms of modulated Langmuir waves, (b) frequency-time spectrogram generated from the MCA, and (c) electron velocity distributions detected by the LEP.

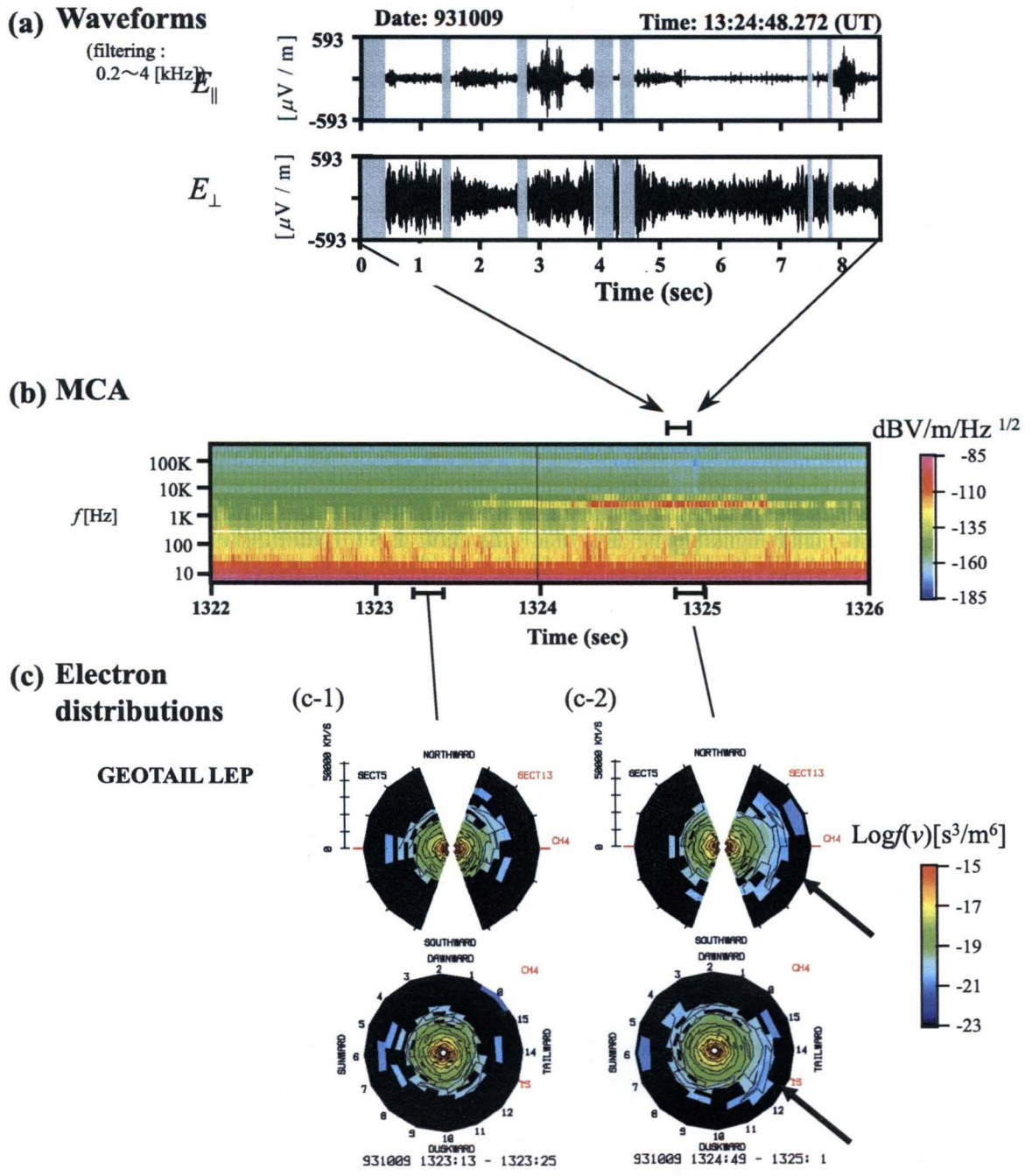

Figure 7.13: Same with Fig. 7.12 but for the ECH waves.

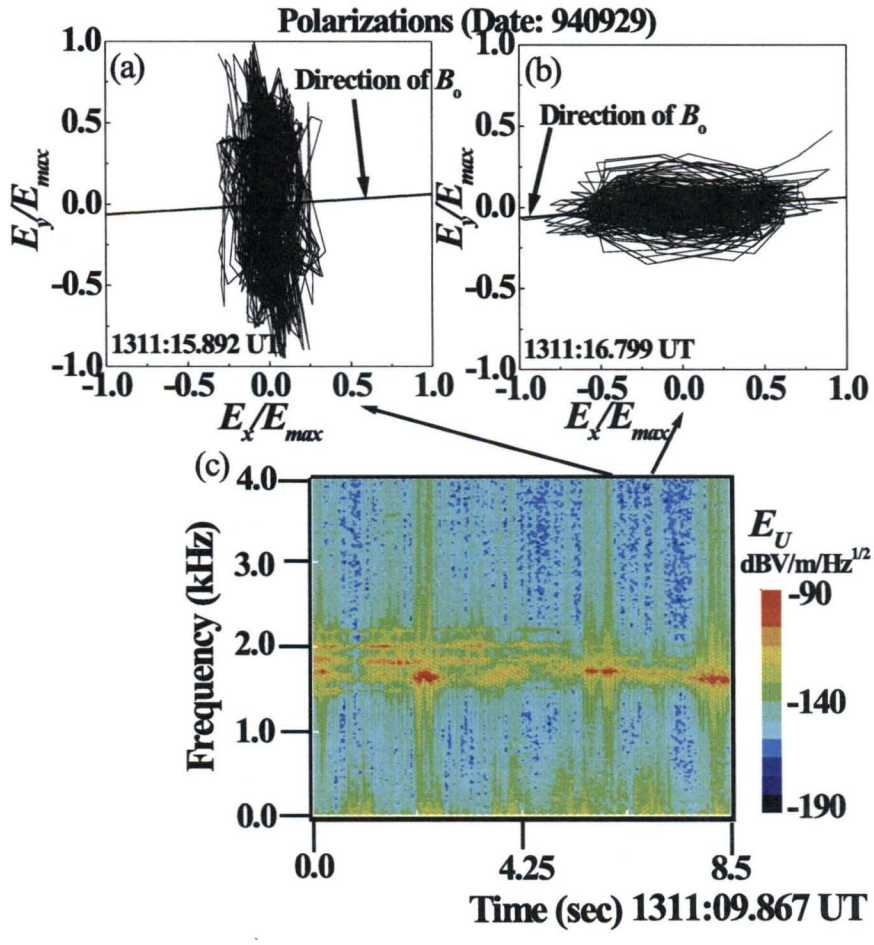

Figure 7.14: Quick change of the polarizations. The polarization changes from the perpendicular direction to the parallel one relative to the ambient magnetic field in a short time scale less than 1 sec [*after Kojima et al.*, 1997b].

Chapter 8

Electrostatic waves in the magnetosheath

8.1 Introduction

The magnetosheath is one of the regions where the plasma wave activities are very high. The first comprehensive observation of plasma waves in the magnetosheath was conducted by *Rodriguez* [1979]. He reported three types of electrostatic waves based on the observations by Imp 6 satellite in the near-earth magnetosheath ($< 30\ R_E$) as follows: 1. Electron plasma oscillations, 2. low frequency component with a broad intensity maximum below the nominal ion plasma frequency, 3. intermediate component in the frequency range $f_{\rm pi} < f < f_{\rm pe}$. Figure 8.1 shows the sample of spectra observed in the magnetosheath by IMP 6 satellite. In each panel, average spectra (AV) are 5.46 min averages and peak spectra (PK) are 0.1 s averages. We can see the above three types of spectra.

Onsager et al. [1989] also studied the generations of electrostatic waves in the near-earth magnetosheath using the plasma wave data of the AMPTE IRM satellite. They pointed out that observed electrostatic waves cannot be explained only by the Langmuir waves (electron plasma oscillations) and Doppler-shifted ion acoustic waves. They discuss the possibility of the electron beam mode in addition to the above two wave modes.

The distant magnetosheath beyond 150 R_E from Earth was investigated by ISEE-3 first. *Coroniti et al.* [1994] confirmed the similar electrostatic emissions can be observed even in the distant magnetosheath region. Further, they reported the clear correlation exists between these electrostatic emissions and cone angle ($\theta_{\rm xB}$), which is the relative angle of the magnetic field and the plasma flow velocity.

Figure 8.2 is an example for showing the above relation between wave intensities and cone angles. The upper four panels present the one-minute average components and magnitude of the ambient magnetic field. The center panel is a color-coded display of the electric field frequency-time spectrogram. The bottom panel show the cone angle and the longitude and latitude of the ambient magnetic field in the GSM coordinates. In this figure, The intense bursty wave spectra shown in Fig. 8.2 correspond to the intermediate component in the frequency range $f_{\rm pi} < f < f_{\rm pe}$, which was introduced by *Rodriguez* [1979]. *Coroniti et al.* [1994] pointed out the dropout of these intermediate components during large cone angles. This tendency can be clear at 02:00, 05:00, 07:00 (UT) in Fig. 8.2. *Coroniti et*

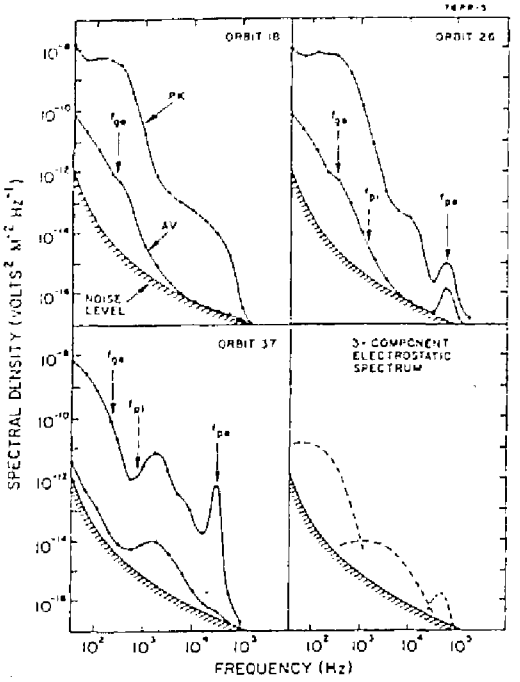

Figure 8.1: Sample of magnetosheath spectrum observed by IMP 6 satellite. The three components of spectra are schematically display in the right-bottom panel [*after Rodriguez*, 1979].

al. [1994] statistically confirmed this relation as shown in Fig. 8.3. They claimed that this tendency is not affected by the relative angles between antennas and magnetic field direction, or the Doppler-shift. We will compare this result with ours in Section 8.5.

In this chapter, we discuss the waveform observations of the electrostatic waves in the distant magnetosheath comparing with previous observations and our observations in the magnetotail.

8.2 Waveform observations of the ESW and EQMW in the Distant Magnetosheath

In this section we look at the electrostatic waves in the magnetosheath. Figures 8.4 (a) and 8.5 (a) show frequency-time spectrograms observed in the distant magnetosheath at (GSM X, GSM Y, GSM Z)=(-208, 11.3, 1.3 R_E) and (−160, 81, 1.2 R_E) on June 23, 1993, and March 16, 1994, respectively. Upper and lower spectrograms in Figs. 8.4 (a) and 8.5 (a) show the electric and magnetic fields observed with the SFA, respectively. Both figures demonstrate typical plasma wave events in the distant magnetosheath region.

In Fig. 8.4 (a) we find BEN type emissions below the electron plasma frequency ($f < f_{pe} = 30$ kHz) similar to those observed in the PSBL. These emissions appear at 16:05-16:13, 16:19-16:38, and 16:52-16:55 (UT). Their uppermost frequencies are several kilohertz; however, intermittently they reach the local electron plasma frequency ($f_{pe} \sim 30$ kHz). This tendency of the BEN type emission in the magnetosheath is different from that of

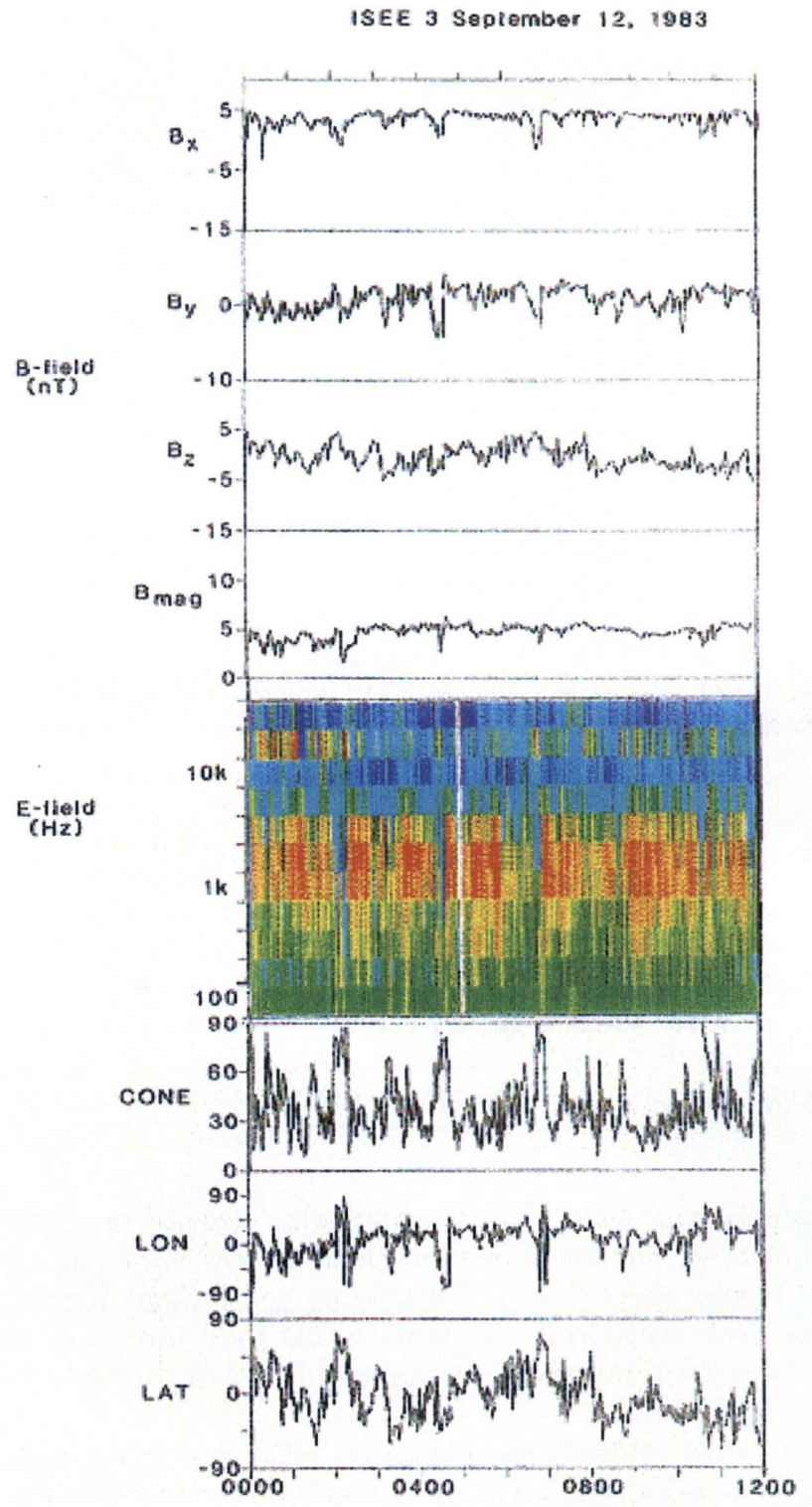

Figure 8.2: ISEE-3 measurements on 00:00 to 12:00 (UT) on September 12, 1983. The upper four panels present the one-minute average components and magnitude of the ambient magnetic field. The center panel is a color-coded display of the electric field frequency-time spectrogram. The bottom panel show the cone angle and the longitude and latitude of the ambient magnetic field in the GSM coordinates [*after Coroniti et al.*, 1994].

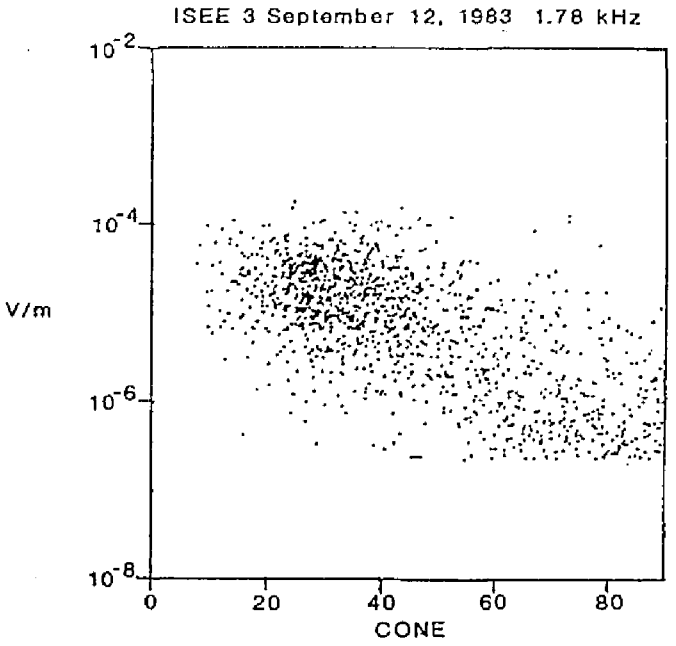

Figure 8.3: A scatter plot of the plasma wave electric field amplitude versus cone angle [*after Coroniti et al.*, 1994].

the BEN in the PSBL. The uppermost frequency of the BEN in the PSBL mostly reach the local electron plasma frequency; however, in most of the BEN type emissions in the magnetosheath, their uppermost frequencies are below the local electron plasma frequency.

We cannot judge whether these electrostatic emissions have the frequency components below the electron cyclotron frequency, because of the superposition of intense electromagnetic waves called MNB, which is the typical wave signature of the magnetosheath region as introduced in Chapter 3. In the magnetic spectra shown in Fig. 8.4 (a) (bottom), we can see the intense MNB at 16:04-16:38 and 16:50-16:55 (UT). The best way to confirm the existence of the low-frequency part of these electrostatic emissions is to consult their waveforms.

Figure 8.4 (c) shows a snapshot of the waveforms detected by the electric field dipole antennas. The observed waveforms are very similar to those of the PSBL ESW. They consist of the isolated bipolar spiky signals. Since we do not find any bipolar signals like these in the magnetic field components, we conclude that these waves are purely electrostatic. Therefore we term these waveforms as magnetosheath electrostatic solitary waves (MS ESW).

As *Matsumoto et al.* [1994b] discussed on the ESW waveforms, such spiky waveforms have the broadband spectra up to the uppermost frequency which is decided by the pulse width of the ESW. Therefore we can conclude that these waves correspond to the BEN type spectra and that in their low-frequency parts, the MNB spectra are superposed on the MS ESW spectra.

The pulse width of the MS ESW in Fig. 8.4 (c) is almost 1 - 2 ms. The observed pulse width of the MS ESW is always a few milliseconds, while that of the PSBL ESW is a

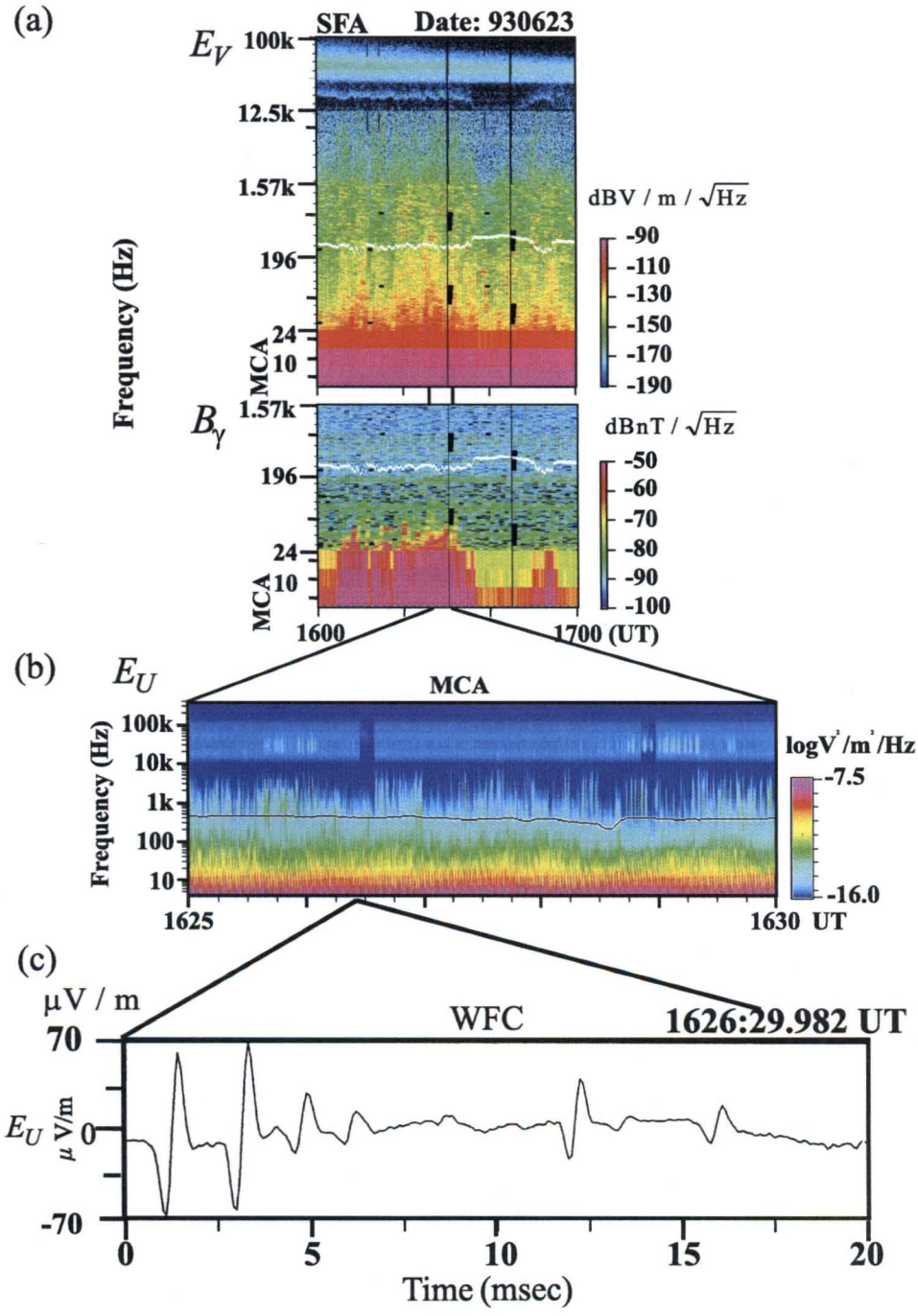

Figure 8.4: The frequency-time spectrograms for (a) SFA and (b) MCA and (c) waveform of the magnetosheath ESW observed on June 23, 1993. Panel a (bottom) shows the magnetic component spectra observed with the search coil magnetometer. The low-frequency electromagnetic waves below 100 Hz are called the MNB, which is the typical wave signature of the magnetosheath [*after Kojima et al.*, 1997a].

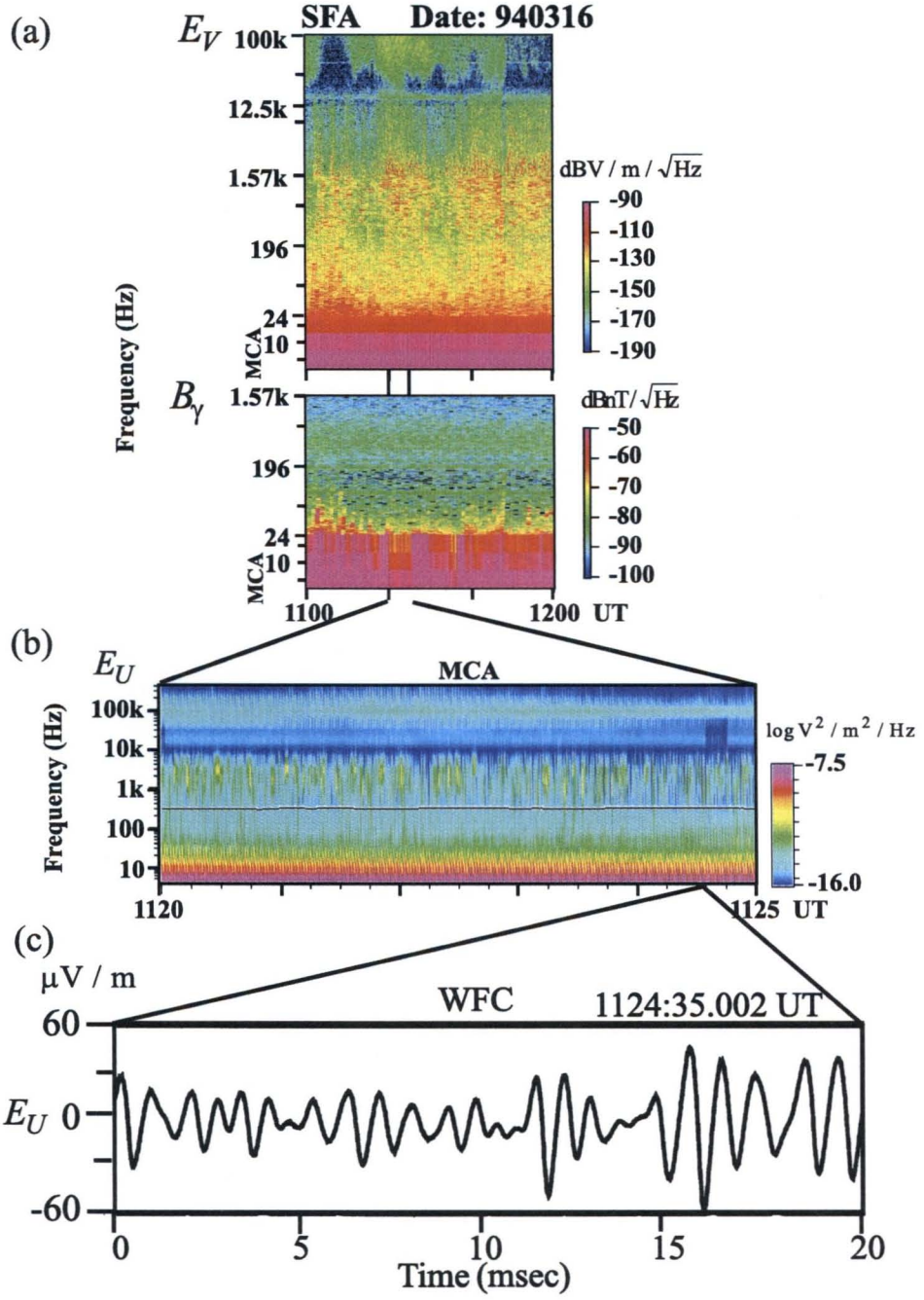

Figure 8.5: Same as Fig. 8.4, but for magnetosheath EQMW [*after Kojima et al.*, 1997a].

few milliseconds to a few tens of milliseconds. This fact is reasonable since the uppermost frequencies of the MS ESW spectra are higher than those of the PSBL ESW spectra. Further, we note that the occurrence possibility of the MS ESW is very rare relative to that of the PSBL ESW.

In Fig. 8.5 (a) we can see the patchy electrostatic emissions above the electron cyclotron frequency (300 Hz). These events are observed throughout the entire interval, except from 11:00 - 11:02, 11:11 - 11:19, 11:29 - 11:34, and 11:46 (UT). They look like the spectra of the lobe EQMW, except their frequency range. This can more clearly be seen in Fig. 8.5 (b). Their center frequency is approximately 2 kHz and is almost 10 times higher than that of the lobe EQMW.

From these spectra we expect that their waveforms are similar to those of the lobe EQMW. Figure 8.5 (c) illustrates the waveforms detected by the electric field antennas at 11:24:35.002 (UT). Although the waveforms are rather deformed comparing with those in the lobe (Fig. 6.4 (c)), their quasi-monochromatic nature reminds us of the lobe EQMW. Thus we term these waves as magnetosheath electrostatic quasi-monochromatic waves (MS EQMW).

Rodriguez [1979] and *Coroniti et al.* [1994] performed the detailed data analyses of the broadband electrostatic emission ($f < 1$ kHz) observed in the near-Earth magnetosheath ($<30\ R_E$) and in the distant magnetosheath ($\sim 150\ R_E$) using IMP 6 and ISEE-3 data, respectively. The electrostatic emissions below 1 kHz they observed are possibly the same as the MS EQMW; however, they did not discuss their waveforms.

8.3 Switching between MS ESW and MS EQMW in short time scales

Figure 8.6(left) illustrates the time variation of the MS ESW and MS EQMW waveforms as well as corresponding frequency spectra (Fig. 8.6 (right)) observed for an extended interval at 09:25:32.731 (UT) on September 30, 1993. Note that we eliminate the low-frequency component below 300 Hz using a numerical filter in order to remove the effect of the MNB.

In Fig. 8.6, we see that the MS ESW and MS EQMW are also bursty, like their counterparts in magnetotail. The continuous quasi-monochromatic waveforms in Figs. 8.6 (a), and 8.6 (c)-(f) correspond to the MS EQMW. On the other hand, the isolated bipolar waveforms seen in Figs. 8.6 (a) and (b) correspond to the MS ESW.

The frequencies of the MS EQMW change very quickly. This is especially evident in Fig. 8.6 (right). We can find that the frequencies of the spectra with peak values corresponding the MS EQMW change in each panel every 85 ms. This wave nature is very similar to that of the lobe EQMW, but the time scale of the waveform change is much faster in the magnetosheath.

The MS ESW are even more bursty than in the magnetotail. As shown in Fig. 8.6, there exist only six big pulses of the MS ESW which we can clearly see (shown by arrows in Fig. 8.6 (a) and (b)). This burstiness demonstrates the difficulties in analyzing the natures of the MS ESW. Since the magnetosheath is the very turbulent region, the isolated potential structure cannot exist stably. This is one of the candidates for explaining the

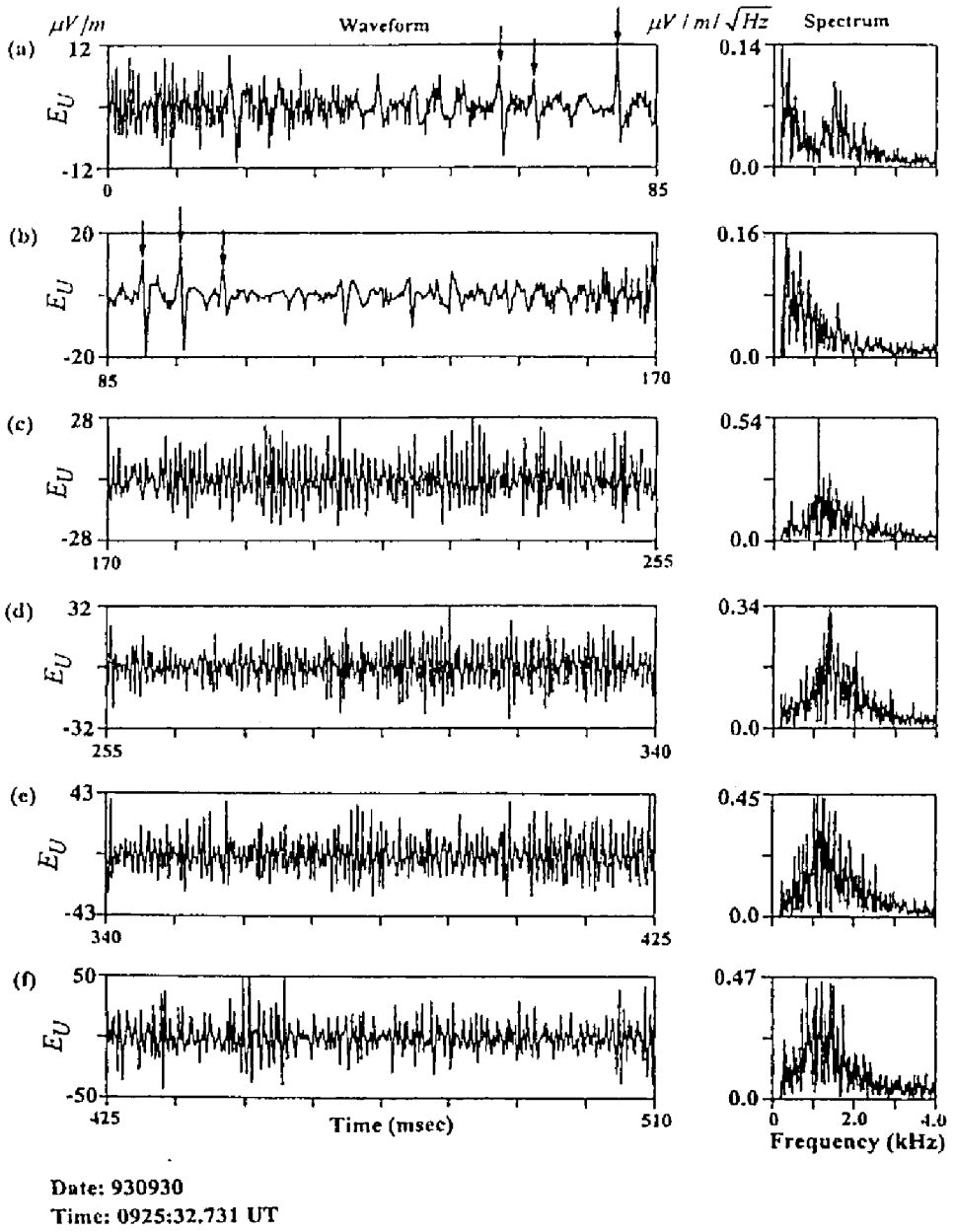

Figure 8.6: Time series of the waveforms and corresponding spectra observed in the magnetosheath. We can see the rapid switching between the MS EQMW and MS ESW in panel (a) and panel (b). As shown by arrows, the six clear pulses of the MS ESW appear in panels (a) and (b), and in other intervals, the MS EQMW are dominant [*after Kojima et al.*, 1997a].

more burstiness of the MS ESW. Their waveforms are quite similar to those of the PSBL ESW; however, we do not have clear proofs that their wave mode is the same. We need to collect more samples of the MS ESW in order to make clear the natures of the MS ESW.

8.4 Polarization of the MS ESW and the MS EQMW

As mentioned before, in the magnetosheath, we observe the intense MNB as well as the electrostatic emissions whose waveforms are referred as the MS ESW and MS EQMW. Its waveforms are always embedded in those of the MS ESW and MS EQMW. Therefore we cannot simply apply the method of multiplying the waveforms detected by the orthogonal antennas in order to examine the spin dependence of the phase difference between E_U and E_V components, which is used in the polarization analysis of the PSBL ESW and lobe EQMW (see Fig. 4.7 and Fig. 6.6). However, we can examine the spin dependence of the MS EQMW if we remove the low-frequency part in the frequency space using the FFT analyses and convert the rest of the frequency components into the time domain waveforms.

This method is applicable only to the MS EQMW. Since the waveforms of the MS ESW are more bursty than other waves, we have not succeeded in detecting the spin dependence of the MS ESW. Therefore we will apply another method, which we also used in order to examine the electric field direction of a single PSBL ESW pulse as shown in Fig. 4.8, for examining the polarization of the MS ESW in the latter part of this section.

Figures 8.7 (a)-(c) show the waveforms detected by two sets of an orthogonal electric dipole antenna and their product observed at (GSM X, GSM Y, GSM Z)=(-86, 39, 0.1 R_E) on February 7, 1994, respectively. During this interval the azimuthal angle ϕ of the ambient magnetic field is equal to 152° in the spacecraft coordinates. Each arrow displays the timing when each component of the electric field antenna is parallel (perpendicular) to the ambient magnetic field.

In order to remove the MNB waveforms, the low-frequency part below 700 Hz is eliminated in Figs. 8.7 (a) and (b) using the above method. The bursty wave packets shown in both panels are the MS EQMW. In Fig. 8.7 (c), we can see the same spin dependence as that of the lobe EQMW and PSBL ESW shown in Figs. 4.7 and 6.6. The sign of the product of E_U and E_V change synchronizing with the timing when each antenna is parallel (perpendicular) to the ambient magnetic field. For example, before 2950 ms, the product of E_U and E_V is negative, while after 2950 ms it is positive. Further, we can see that the wave amplitude of E_U is almost equal to zero around 2950 ms. This spin dependence is quite similar to that of the PSBL ESW and lobe EQMW.

Thus we conclude that the MS EQMW have the same potential structure of the lobe EQMW illustrated in Fig. 6.7. The condition for the relation of L_1, L_2, and $L_{\rm ant}$ should also be satisfied.

As mentioned above, we need to apply another method for examining the polarization of the MS ESW which are more bursty than other waves.

Figure 8.8 shows the hodograms of the MS ESW. Figure 8.8 (top and middle) illustrates the waveforms detected by two sets of an orthogonal electric field antenna (E_U and E_V). Figure 8.8 (bottom) shows the polarization of the MS ESW corresponding to the ESW shown by arrows in Fig. 8.8 (top and middle). The solid line in Fig. 8.8 (bottom) is the direction of the ambient magnetic field projected on the spacecraft coordinate system, in

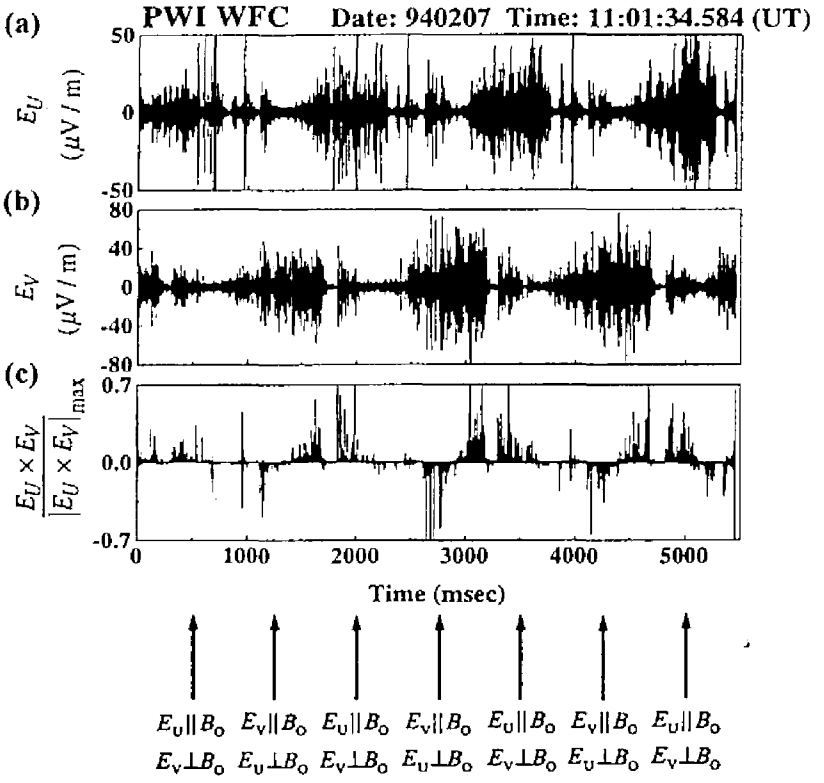

Figure 8.7: Spin dependence of the MS EQMW. In order to avoid the effect of the MNB superposing on the MS EQMW, we eliminate the waves below 700 Hz, making use of the FFT. We can see the same tendencies on the relation of the wave amplitudes and the change of signs of $E_U \times E_V$ with those of the PSBL ESW and lobe EQMW [*after Kojima et al.*, 1997a].

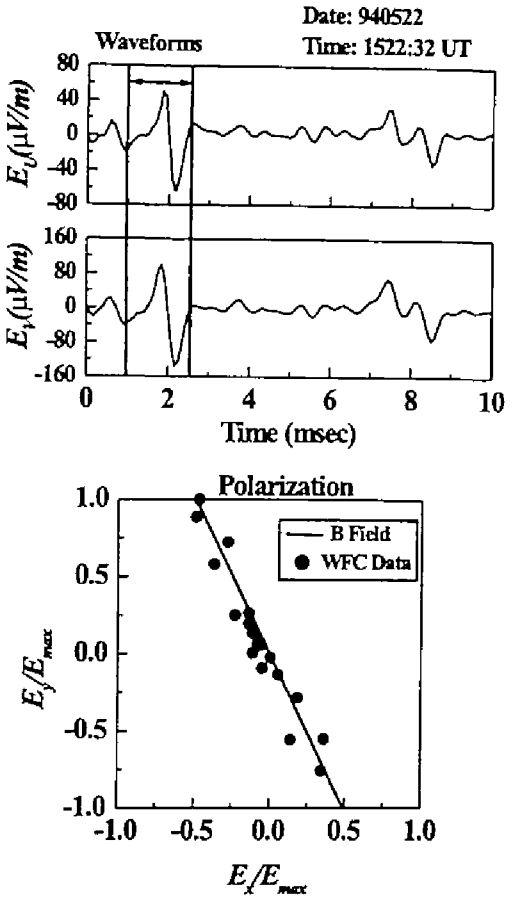

Figure 8.8: Waveforms and corresponding polarization of the MS ESW, with waveforms of the MS ESW detected by two sets of an orthogonal electric dipole antenna (top) E_U and (middle) E_V. (bottom) Polarization of the MS ESW shown by arrows above, with each dot representing sampled waveform level in the spacecraft coordinates. The solid line is the ambient magnetic field line on this plane [*after Kojima et al.*, 1997a].

Table 8.1: Summary of wave natures

	BEN		NEN	
	PSBL ESW	MS ESW	lobe EQMW	MS EQMW
Frequency	$f_U \leq f_{pe}$	$f_U < f_{pe}$	$f/f_{pe} \approx 0.1$	$f/f_{pe} \approx 0.1$
Waveform	solitary	solitary	quasi-sinusoidal	quasi-sinusoidal
Polarization	$E \parallel B_o$	$E \parallel B_o$	$E \parallel B_o$	$E \parallel B_o$
Occurrence rate	frequent	rare	frequent	frequent

which the x axis is oriented to the Sun and the z axis is parallel to the spin axis (see Appendix A). Each dot represents each sampled waveform level, which is converted to the spacecraft coordinate system, of the ESW waveforms shown by arrows in Fig. 8.8 (top and middle). In Fig. 8.8 (bottom) we find that the converted, sampled ESW level is scattered along the direction of the ambient magnetic field. This means that the MS ESW are polarized along the ambient magnetic field and that since the ESW are purely electrostatic, the MS ESW propagate along the ambient magnetic field. Thus we can conclude that we can apply the ESW potential model as shown in Fig. 4.9 to the MS ESW.

8.5 Discussions

We demonstrated the waveform observations of electrostatic waves in the distant magnetosheath. The observed waveforms are classified into the MS ESW and MS EQMW. The detailed natures of these waves are very similar to those of the PSBL ESW and Lobe EQMW, but the MS ESW and MS EQMW are more bursty. The comparisons of these waves are shown in Table 8.1, where f_U in this table denotes the uppermost frequency.

The natures of the MS ESW is quite similar to those of the PSBL ESW, but the striking difference is the pulse width. The typical pulse widths of the MS ESW are slightly shorter than those of the PSBL ESW, but they are the same order. If the MS ESW are generated by electron beam instabilities just like the PSBL ESW, expected pulse widths of the MS ESW should be much shorter than those of the PSBL ESW, because electron plasma frequencies in the magnetosheath are 10 times higher than those in the PSBL. This inconsistency can be seen in Table 4.2. The value of $\Delta W \cdot f_{pe}$ for the PSBL ESW is equal to $1 \sim 10$, while the value for the MS ESW is about 20. In order to make clear this difference, we need to perform some statistical analyses, but since the occurrence rate of the MS ESW is very rare, we have not succeeded in identifying the relation of the pulse width and electron densities in the magnetosheath. Therefore, we have not concluded that the MS ESW are also the BGK mode, which is excited by electron beams.

On the other hand, the frequency ratios of the MS EQMW and electron plasma frequencies are almost equal to those for the lobe EQMW as shown in Table 8.1. This result is very suggestive to the same generation mechanism of the MS EQMW and lobe EQMW. However, previous papers claimed that the waves between f_{pi} and f_{pe} observed in the magnetosheath is the Doppler-shifted ion acoustic wave [*Rodriguez*, 1979; *Onsager et al.*, 1989; *Coroniti et al.*, 1994], while we concluded that the lobe EQMW are generated by electron velocity space hole instability but not by the Doppler-shifted ion acoustic waves.

Using the similar way to that in Chapter 6, we roughly estimate the Doppler-shift ve-

locities of ion acoustic waves as follows. The typical electron and ion temperatures in the magnetosheath are T_e = 45 eV, and T_i = 90 eV. Therefore, the ion sound velocity V_s is calculated to be 113 km/s. We substitute $f_{\rm NEN}$=2000 Hz, and $f_{\rm pi}$=467 Hz to Eq. (6.2) and obtain minimum bulk velocity for the Doppler-shift is 370 km/s. The difference between the lobe and magnetosheath regions is the existence of the continuous bulk flow in the magnetosheath. The typical bulk velocity in the magnetosheath is about 500 km/s. Therefore, the above estimation for the Doppler-shift velocity is very reasonable. This estimation leads us to the idea that the MS EQMW are the Doppler-shifted ion acoustic waves. However, we stress that this Doppler-shifted ion acoustic wave model is not consistent with the cone angle dependence of the wave intensities shown in Fig. 8.2.

We show the same nature on the cone angle dependence of the MS EQMW (MS NEN) in Fig. 8.9. Figure 8.9 (a) shows the frequency-time spectrogram observed at (GSM X, GSM Y, GSM Z)=(-86.3, 39.0, 0.3 R_E) on February 7, 1994. We can see the MS NEN spectra during the intervals of 08:00 to 08:10, 08:29 to 08:31, 08:43, 09:10 to 09:43 (UT). These MS NEN observations can be more clearly in panel (c), which show the spectral power obtained by the integration of SFA E2 spectra. Figure 8.9 (b) shows the elevation angles of the ambient magnetic field in the spacecraft coordinates. Comparing with these panels, we find the MS NEN is intensified during the small elevation angles. This result is very similar to that of *Coroniti et al.* [1994]. What we stress here in Fig. 8.9 is that the MS NEN frequency band seems to be almost constant during the whole period in Fig. 8.9 even in the change of elevation angles shown in panel (b). We have confirmed that the azimuthal angle of the ambient magnetic field is almost constant before 09:30 (UT). This result is not consistent with the Doppler-shifted ion acousitc wave model. As shown in this chapter, the orientation of the electric fields of the MS EQMW is parallel to the ambient magnetic field. Since the MS EQMW is purely electrostatic, they propagate along the ambient magnetic field. The Doppler-shifted frequencies strongly depend on the velocity component along the spacecraft spin plane, because Geotail can observe only two components of electric field by 2 sets of orthogonal antennas lying on the spin plane. If the MS NEN is the Doppler-shifted ion acoustic wave, its frequency should change depending on the change of the ambient magnetic field orientation. However, the MS NEN frequency band is almost constant as shown in Fig. 8.9. It is clearly seen in the period during 09:10 to 09:30 (UT). This result suggests that the MS NEN (MS EQMW) are not the Doppler-shifted ion acoustic wave. Further, typically, ion temperature $T_{\rm i}$ is larger than electron temperature $T_{\rm e}$ in the magnetosheath, it is unlikely that ion acousitc waves become unstable. Therefore, the previous observations reported that the MS NEN (MS EQMW) is the Doppler-shifted ion acoustic waves, but we conclude that they are not the ion acoustic waves.

In order to examine the cone angle dependence of the MS EQMW intensities, we make a similar scatter plot of Fig. 8.3 as shown in Fig. 8.10. The data shown are collected from the WFC data. We see that intense MS EQMW amplitudes are confined in the range of 10° to 60°. The tendency seems to be very similar to that shown in Fig. 8.3.

We excluded the possibility of the Doppler-shifted ion acoustic waves for the MS NEN (MS EQMW), but we cannot conclude an alternative generation mechanism. The most plausible generation mechanism is the electron velocity space hole mode. We can explain the conservation of the ratio $f_{\rm pe}/f_{\rm NEN}$ by the electron velocity space hole mode.

In the magnetosheath, ions are frozen in the ambient magnetic field, and mobility of

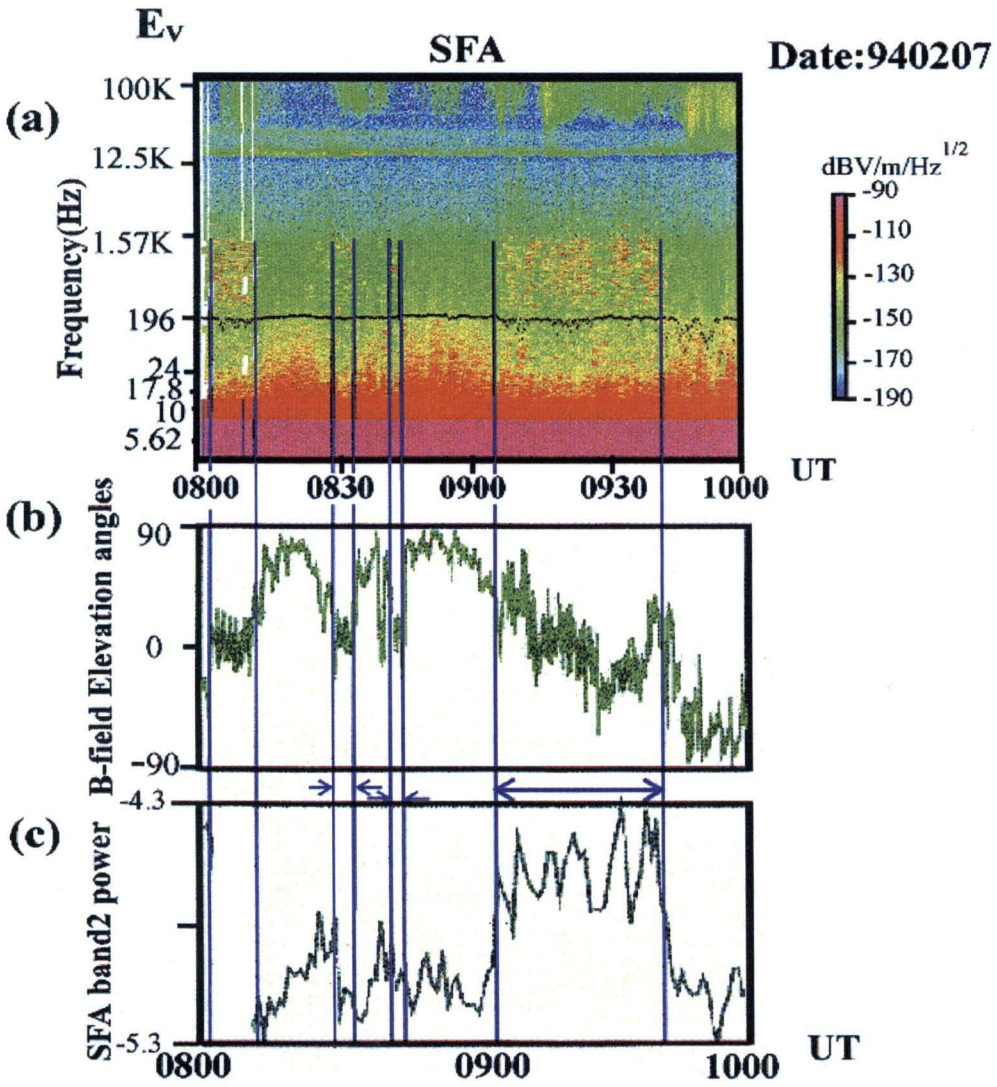

Figure 8.9: The relation of NS NEN intensities and orientations of the ambient magnetic field. (a) frequency-time spectrogram observed on February 7, 1994 in the distant magetosheath. (b) elevation angle of the ambient magnetic field. (c) power of the MS NEN observed in the frequency range of the SFA-E2.

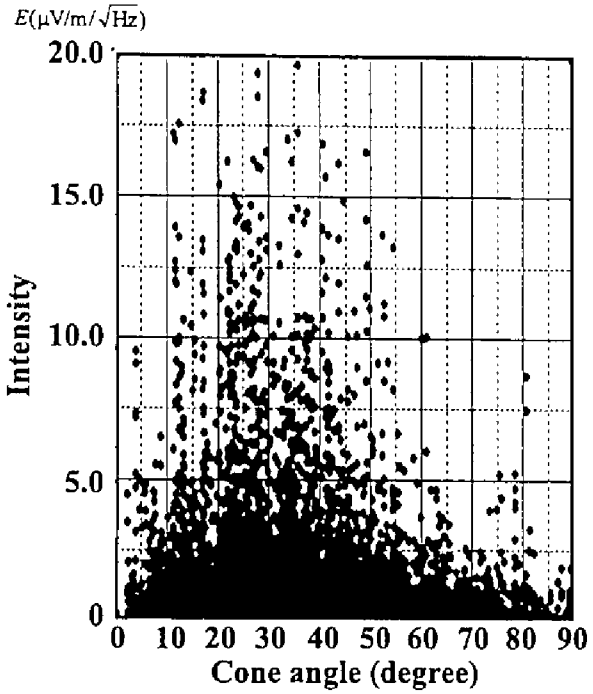

Figure 8.10: Cone angle dependence of the EQMW intensities observed by the Geotail.

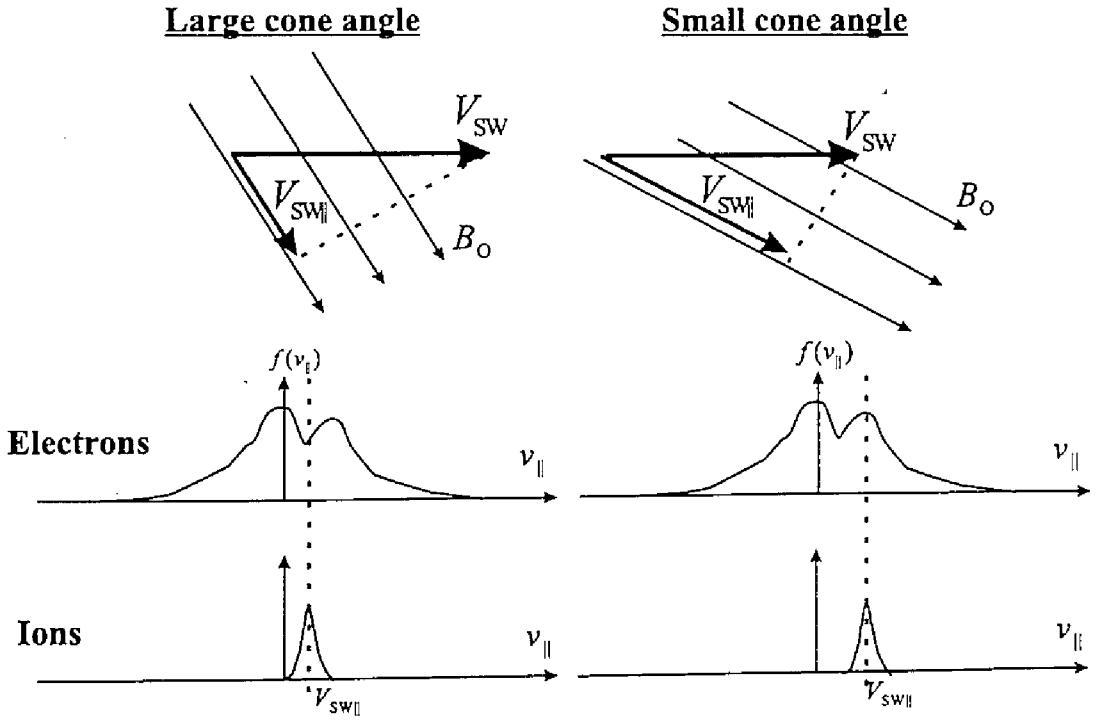

Figure 8.11: Schematical drawing on the relation of velocity distributions and cone angles.

electrons along the ambient magnetic field is much larger than that of ions. Therefore, velocity difference along the ambient magnetic field between electrons and ions can be expected. The velocity component of ions along the ambient magnetic field depends on the cone angle. Since *Coroniti and Ashour-Abdalla* [1989] show that the ion beam along the ambient magnetic field intensifies the electron velocity space hole mode, the role of ions in the electron velocity space hole mode is important. Further, *Omura et al.* [1996] pointed out that when phase velocities of excited electron velocity space hole mode are close to ion beam velocities, the excited waves are damped due to interactions between ions and waves. Phase velocities of electron velocity space hole mode are decided by velocities corresponding to velocity space holes. Thus, the relative velocity of velocity holes and ion beam velocities are also important. The above condition is schematically displayed in Figure 8.11. Upper two panels represent the configuration of ambient magnetic fields (B_o) and solar wind bulk velocities (V_{sw}). As we discussed above, since electron mobilities along the ambient magnetic field are much higher than those of ions, we expect the velocity difference between electron velocities parallel to the ambient magnetic field and ion beam velocities ($V_{sw\parallel}$) are the solar wind bulk velocities projected on ambient magnetic field lines. The relation of electron velocity space hole and ion beam velocities are displayed in lower panels. We assume that electron velocity space hole is formed in a low energy range as shown in Fig. 8.11. If the cone angle is large and $V_{sw\parallel}$ is close to the hole velocity, the excited electron velocity space hole mode is damped. However, Since in small cone angles, $V_{sw\parallel}$ is much different from the hole velocity, the excited waves are maintained and can be observed by spacecraft. This model is very consistent with observation results on the relation of cone angles and MS NEN emissions shown in Figs. 8.3 and 8.10. However, we cannot confirm the existence of some structures in electron velocity distributions which destabilize the electron velocity space hole mode. We also need to explain how such structures can be existed in the very turbulent magnetosheath plasmas.

Chapter 9

Magnetotail structures studied by the plasma wave observations

9.1 Introduction

In the present chapter, we attempt to use plasma wave data in the different way from other chapters. As we discussed in previous chapters, plasma waves sensitively reflect the microscopic plasma phenomena such as wave-particle interactions. On the other hand, since the magnetotail consists of several different distinct regions and boundaries, different kinds of microscopic phenomena take place and different kinds of waves are excited in each region. This means that each distinct region is characterized by plasma wave signatures. We demonstrated this point in Chapter 3 by summarizing plasma wave signatures in each region. As shown in Chapter 3, we can identify the region where the spacecraft is located only using plasma wave signatures. Therefore, by processing plasma wave signatures statistically, we can see averaged structures in each region of the magnetotail. Further, since local plasma densities can be calculated from the CR lower cutoff frequency, we can obtain spatial distributions of plasmas in the magnetotail.

In this chapter, we statistically process plasma densities, intensities of the Magnetic Noise Burst (MNB), and electron plasma waves and discuss their results comparing with a stationary magnetotail model introduced in Chapter 1.

9.2 Plasma density profiles

As we showed in Chapters 1 and 3, we can calculate electron plasma densities from lower cutoff frequencies of the continuum radiation (CR), because its lower cutoff frequency is believed to be equal to a local electron plasma frequency.

We sampled lower cutoff frequencies every one hour in the Geotail orbits during September 18, 1992 to February 17, 1994 and calculated electron densities from sampled lower cutoff frequencies. Since we do not always see clear lower cutoff frequencies of the CR, we do not sample them in the case of weak continuum radiations. Thus, the valid sampled data number is 9103.

Figure 9.1 shows the calculated density profiles at four different distance ranges of $20 < |X_{\mathrm{GSM}'}| < 50R_E$, $50 < |X_{\mathrm{GSM}'}| < 100R_E$, $100 < |X_{\mathrm{GSM}'}| < 150R_E$, and $150R_E < |X_{\mathrm{GSM}'}|$

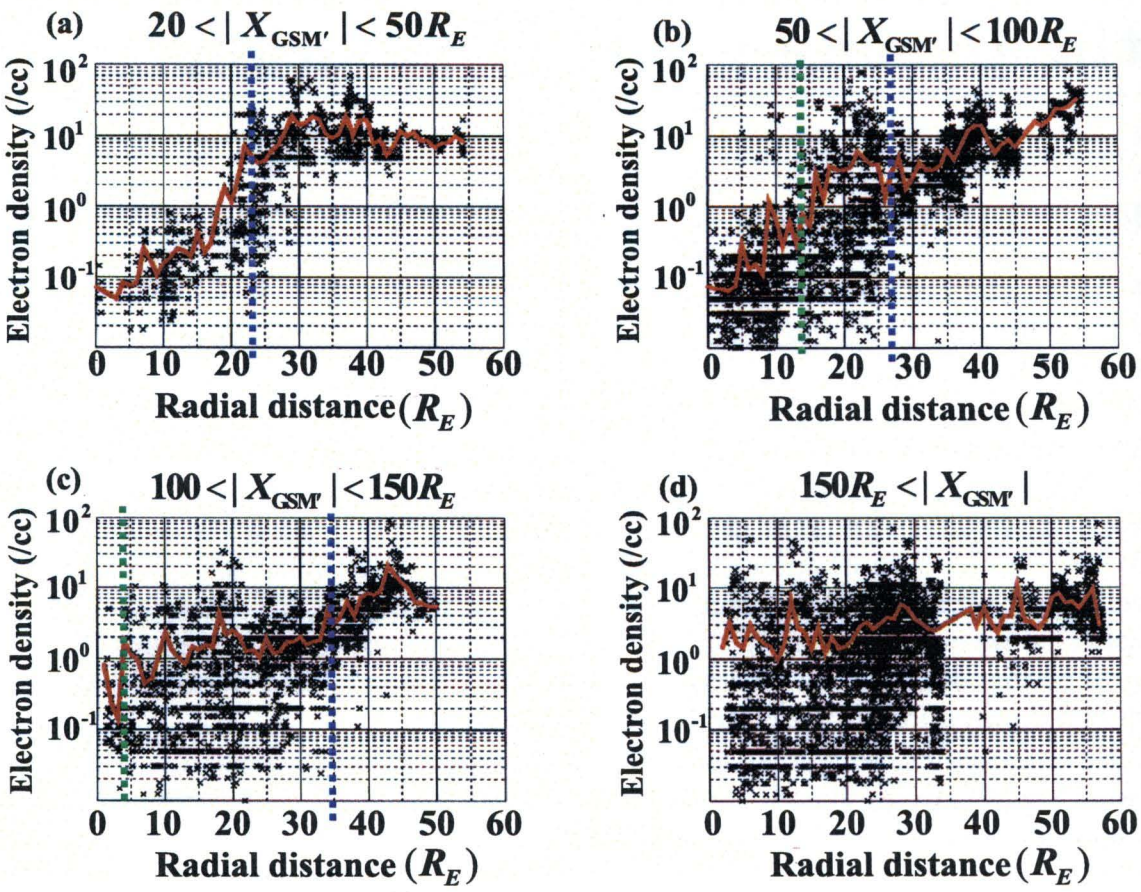

Figure 9.1: Plasma density profiles at four different distance ranges from the earth. The horizontal axis in each panel means radial distance of observation points from the modified $X_{GSM'}$ axis.

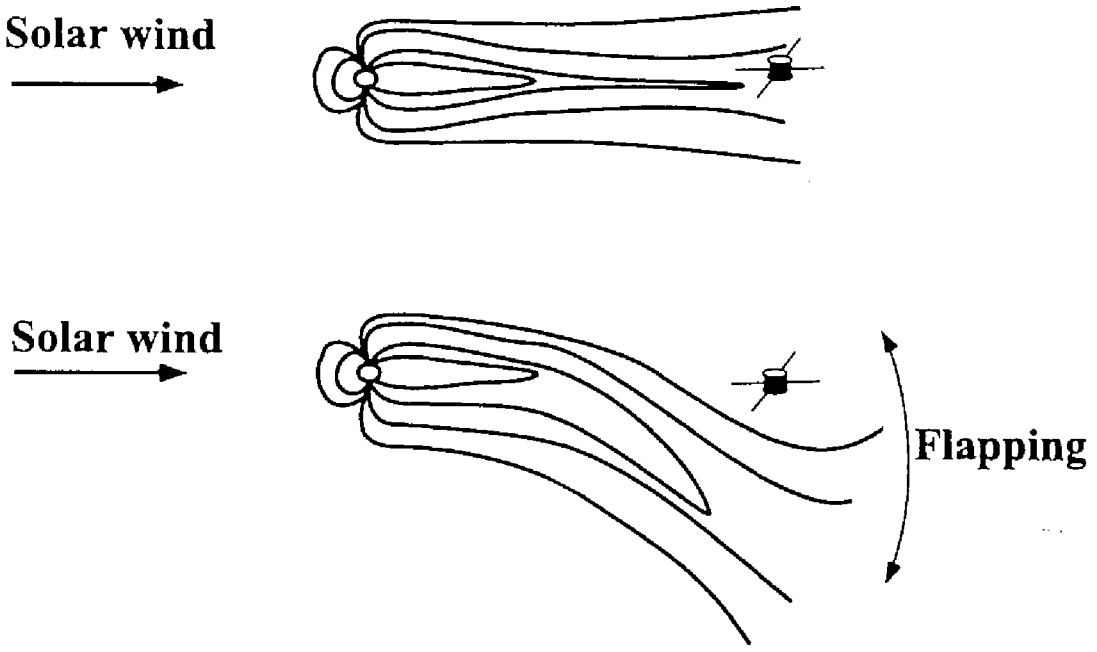

Figure 9.2: Schematical drawing on the tail flapping effect.

from te earth. The horizontal axis in each panel means the radial distance of the observation point from $X_{GSM'}$ axis, where $X_{GSM'}$ mean X axis of the modified GSM coordinate system (see Appendix A). The red lines in each panel indicate the radial distance dependence of averaged densities.

In each panel, the areas of large radial distance show high densities about 10/cc. These areas correspond to observations of the magnetosheath plasmas. On the other hand, the very low densities less than 1.0/cc correspond to the observations of lobe or plasma sheet plasmas. In the panel (a), we see a sharp change of observed densities around 25 R_E. This sharp change suggests the existence of the magnetopause at 25 R_E as shown by a blue dotted line. We can conclude that averaged tail radius in $20 < |X_{GSM'}| < 50 R_E$ is about 25 R_E. On the other hand, profiles shown in panels (b), (c), and (d) are more complicated. In the ranges of radial distances more than 28 R_E in panel (b), and more than 35 R_E in panel (c), we can see only high density magnetosheath plasmas, while in the ranges between 15 R_E and 28 R_E in panel (b) and less than 35 R_E in panel (c), we can see that observed densities are scattered from low densities to high densities. The scattered data from low densities to high densities mean that both magnetosheath and lobe (or plasma sheet) plasmas can be observed in these ranges of the radial distance. Therefore, we can estimate the maximum tail radius in these $X_{GSM'}$ ranges are 28 R_E and 35 R_E in panels (b) and (c), respectively (shown by blue dotted lines). This difference in the location of the magnetopause seems to be affected by the flaring of the magnetotail. Using these differences of the magnetopause locations, we can roughly estimate the flaring angle as 8°. This value is consistent with the results by *Meng and Anderson* [1974] and *Yamamoto et al.* [1994].

On the other hand, the observations of high density and low density plasmas in the same radial distance range are possibly caused by the flapping of the magnetotail. The magnetotail is believed to flap under the control of the solar wind dynamic pressure. By

effects of the tail flapping, the spacecraft observes the magnetosheath plasmas even when it is locates almost in the center of the magnetotail. Figure 9.2 schematically shows the flapping effect in the geomagnetic tail region. When the spacecraft is located in the center of the geomagnetic tail, it observes plasma sheets or lobe plasmas (upper panel). On the other hand, when the geomagnetic tail flaps, the spacecraft observes the magnetosheath plasmas due to the distortion of the geomagnetic tail axis (lower panel). This result is the same when the spacecraft is located at large distance from the tail axis in the sense that both low and high density plasmas are observed in the same position. Therefore, we can estimate the flapping distance relative to the tail axis by examining the radial distance where both high and low density plasmas are observed in Fig. 9.1.

In Fig. 9.1 (a), we see only a narrow layer around 25 R_E where both high and low density plasmas can be observed. This means that the flapping effect in the range of $20 < |X_{GSM'}| < 50R_E$ is very small, and that the magnetotail structure is stable in this range. Such a layer shown in Fig. 9.1 (b) is wider than that in Fig. 9.1 (a). The lower limit of this layer is displayed by a green dotted line in this figure. The width of this layer in this panel is approximately equal to 16 R_E. In panel (c) for $100 < |X_{GSM'}| < 150R_E$ further wider layer can be confirmed. The width of the layer affected by the flapping is about 32 R_E in this X range. We can see that the deep tail region $150R_E < |X_{GSM'}|$ flaps beyond the tail radius in this region, because in all of radial distances below 40 R_E both high and low density plasmas can be observed.

From the density profiles obtained from the plasma wave measurements, we can estimate the radius of the geomagnetic tail region depending on the distance from the earth, and we also find that the flapping motion is more effective in the distant tail region.

9.3 Distributions of the magnetic noise burst

As shown in Section 3.4, the intense Magnetic Noise Burst (MNB) is the typical wave signature of the magnetosheath region. Originally, the name of Magnetic Noise Burst was used for bursty electromagnetic waves near the neutral sheet [*Gurnett et al.*, 1976]. We also confirm weak and low frequency MNB observed in the plasma sheet. Therefore, by processing the MNB statistically, we can see locations of the magnetosheath and plasma sheet. Figure 9.3 shows the spatial distributions of the MNB on the tail cross-section at four different distance ranges from the earth. We have surveyed the averaged intensity of the MNB using the GEOTAIL PWI data from September 18, 1992 to October 10, 1994. The datasets of the 10 minute average of the MNB intensity were generated from the magnetic field components of the lowest three channels of the MCA (5.62 Hz, 10.0 Hz, and 17.8 Hz). The obtained MNB intensities are mapped as follows. First we divide the $Y - Z$ plane into 120×80 cells with a grid spacing of 1 R_E. The MNB intensities measured by GEOTAIL on a specific location of GEOTAIL are distributed to the adjacent nearest 4×4 grid points in the $Y_{GSM'} - Z_{GSM'}$ plane. The dotted circle represents the region with 30 R_E radius from the tail axis.

In all of four panels, we can clearly see the inner edge of area where the intense MNB can be observed. Since the intense MNB is observed in the magnetosheath region, the inner edge corresponds to the location of the magnetopause. The appearing inner edges agree well with the magnetopause location which we estimated in Fig. 9.1. Concerning the

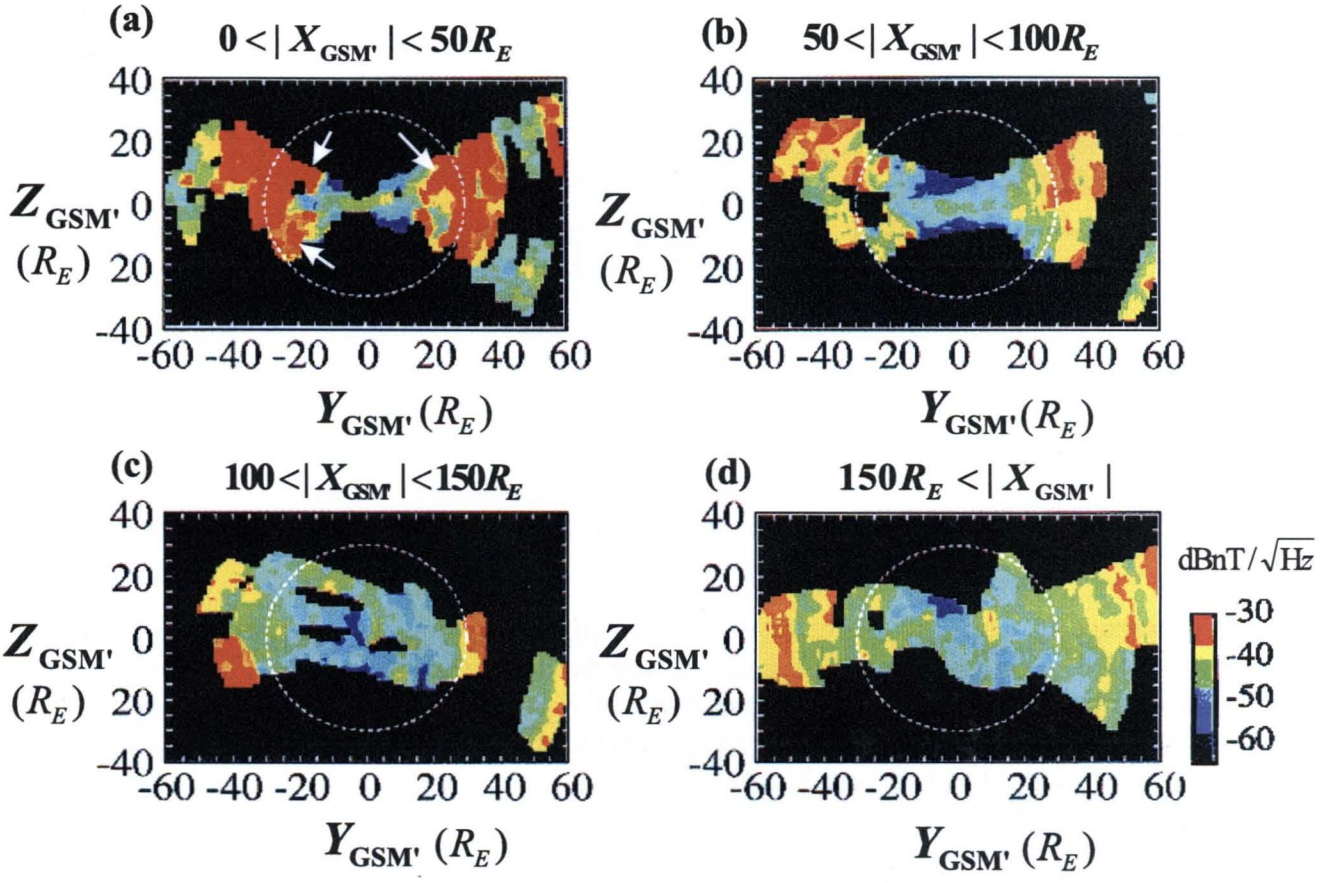

Figure 9.3: Spatial distributions of the MNB on the tail cross-section at four different distance ranges from the earth.

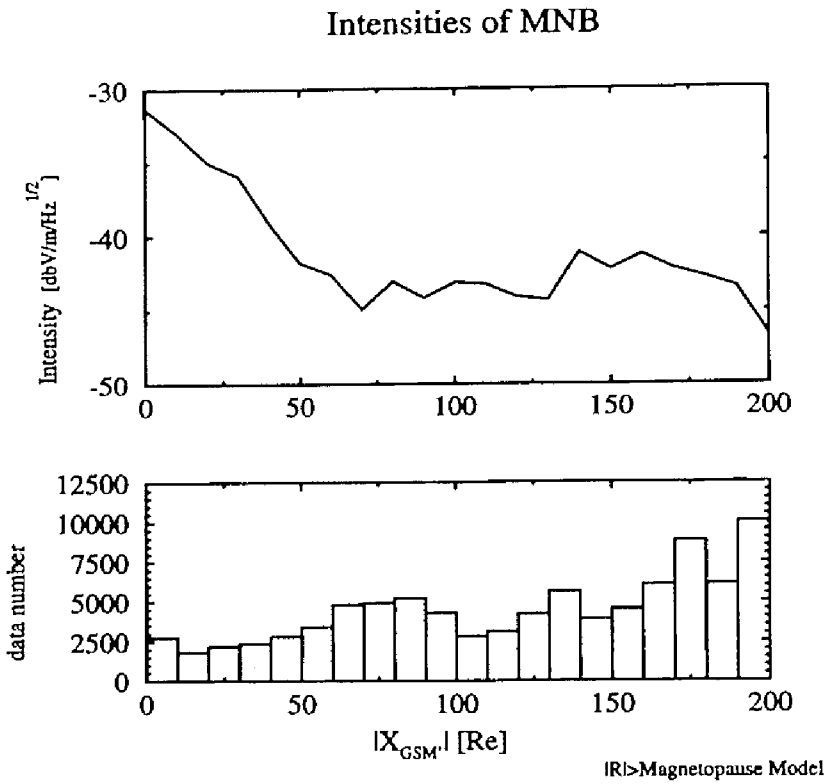

Figure 9.4: Distance dependence of the MNB intensities (upper) and data counts of the MNB observations (lower).

difference of the MNB intensities mapped in each panel, we note that the intensities of the MNB decrease with the increase of the distance from the earth. This tendency can be clearly seen in Fig. 9.4. The upper panel of Figure 9.4 shows the distance dependence of the MNB intensities. The averaged intensities of the MNB are exponentially decreased up to 75 R_E down the tail, and beyond 75 R_E they are almost constant. This tendency is very interesting. We believe it is closely related to the generation of the MNB, but this problem is beyond the present thesis. We will perform detailed analyses about this tendency in the future.

In panel (a) of Fig. 9.3, the intense MNB can be also detected within the circle area with 25 R_E radius (shown by arrows), which is estimated as the tail radius in this distance range using density profiles in the previous section. We believe that this permeation of the MNB suggests the location of the Low Latitude Boundary Layer (LLBL). We show that the MNB can be also observed in the LLBL in Fig. 3.8 (We note that the intense MNB is not observed in the plasma mantle of the magnetopause boundary). Therefore, the permeation of the MNB suggests that the spacecraft observes the LLBL plasmas. This permeation is not clearly seen in panels (b), (c), and (d). This means that the LLBL exists only in the neartail region.

The structure of the plasma sheet is hard to identify in Fig. 9.3. Only in panel (b), weak MNB can be observed around the center of the tail. This weak MNB seems to correspond

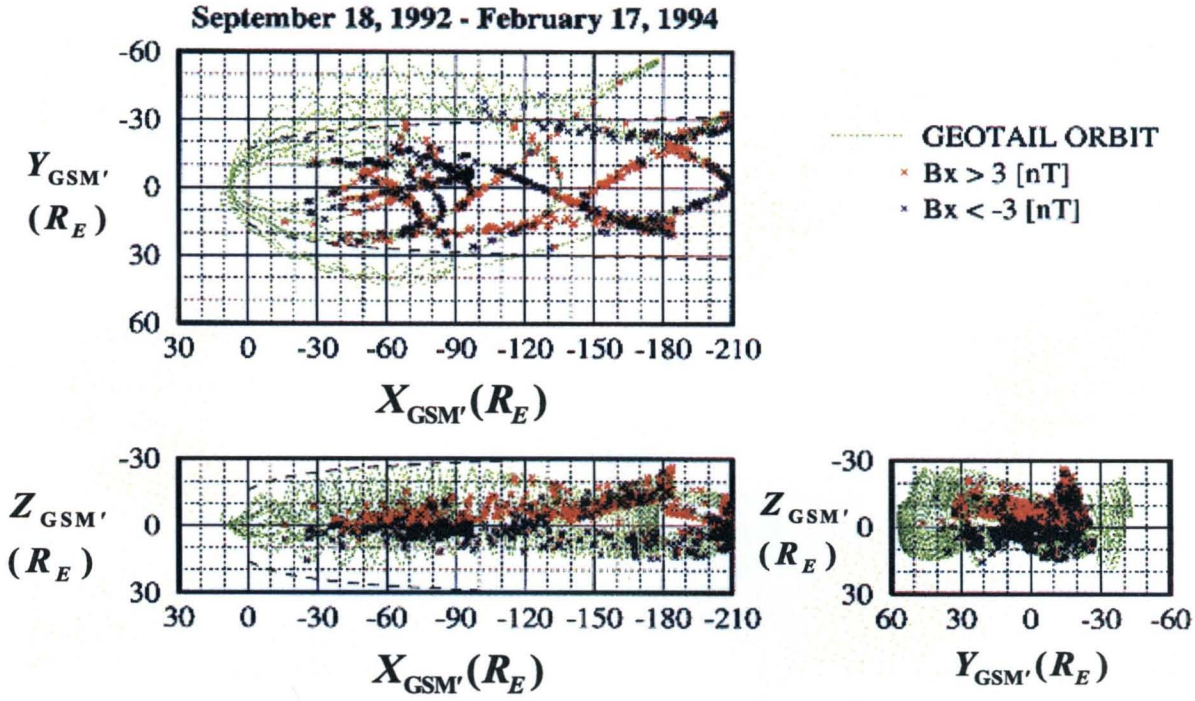

Figure 9.5: Observation points of the electron plasma waves along the Geotail orbits.

to the plasma sheet. The structure of the plasma sheet can be more clearly identified by electron plasma waves discussed in the following section.

9.4 Distributions of the electron plasma waves

9.4.1 Plasma sheet structure

We introduced that electron plasma waves are observed in the lobe region close to the plasma sheet boundary in Chapters 3 and 7. Therefore, electron plasma waves are good indicators for identifying the edge of the plasma sheet. In this section, we show that the statistical analyses of electron plasma waves provide the structure of the plasma sheet in the geomagnetic tail region.

We plot observation points of the electron plasma waves along the Geotail orbits in Fig. 9.5. The red and blue cross signs denote the observation point of the electron plasma waves in the north lobe and south lobe, respectively. This division of the north and south lobes is judged by referring to azimuthal angles of the ambient magnetic field. Three panels are for $X_{GSM'} - Y_{GSM'}$, $X_{GSM'} - Z_{GSM'}$ and $Y_{GSM'} - Z_{GSM'}$ in the modified GSM coordinate system. Green lines denote the Geotail orbits.

We see the clear structure of the plasma sheet in the neartail region less than 100 R_E down the tail on $X_{GSM'} - Z_{GSM'}$ plane. The red and blue cross signs are almost confined in the northern and southern hemisphere in this distance range, respectively. The estimated thickness of the plasma sheet is about less than 20 R_E. The above structure can be more

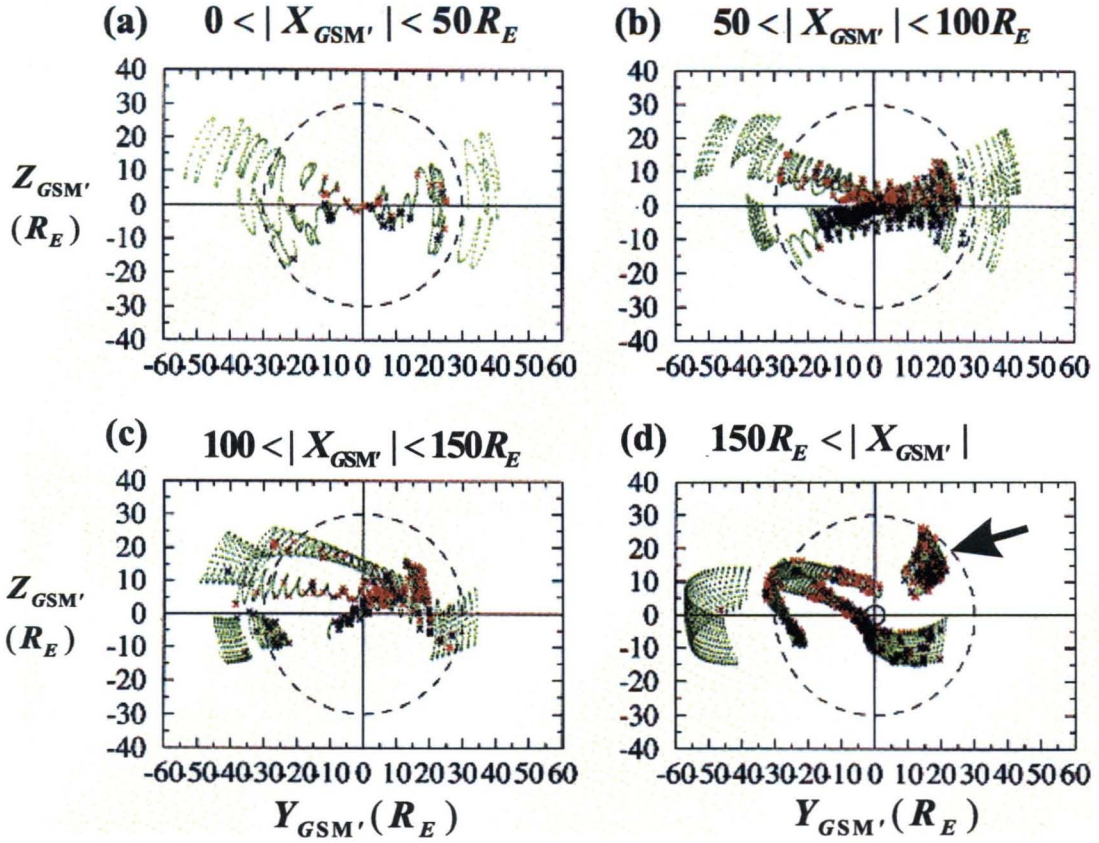

Figure 9.6: Distribution of the electron plasma wave observation points on $Y_{\mathrm{GSM}'} - Z_{\mathrm{GSM}'}$ plane at four different distances from Earth.

clearly seen in the tail cross section plots of Fig. 9.6.

Figure 9.6 shows the distribution of the electron plasma wave observation points on $Y_{\mathrm{GSM}'} - Z_{\mathrm{GSM}'}$ plane at four different distances from the earth. The panel (b) for $50 < |X_{\mathrm{GSM}'}| < 100 R_E$ shows that electron plasma waves are confined in the low latitude region. Since the Geotail orbits are restricted in low latitude regions in this distance range, we cannot determine the thickness of the plasma sheet from this panel. However, when we convert these plots to those in observation probabilities, we can show the plasma sheet thickness very clearly as introduced later in Fig. 9.7.

Electron plasma waves in the high latitude region can be also seen in panels (c) and (d). Especially, in the panel (d), both plasma sheets in the northern and southern hemispheres are observed in the high latitude region of the northern hemisphere shown by arrow. This high latitude plasma sheet seems to be caused by flapping effect, which we showed in Section 9.2 or by some deformations of tail structures.

In Figs. 9.5 and 9.6, we cannot conclude the thickness of the plasma sheet, but in Fig. 9.7, we can estimate the thickness in average is almost equal to 10 R_E in the neartail region. The color code shown in Fig. 9.7 denotes the observation probabilities of the electron plasma waves. They are calculated considering the spacecraft stay period in each observation point. The probabilities shown in panels (b) and (c) are evidently high in the low latitude region

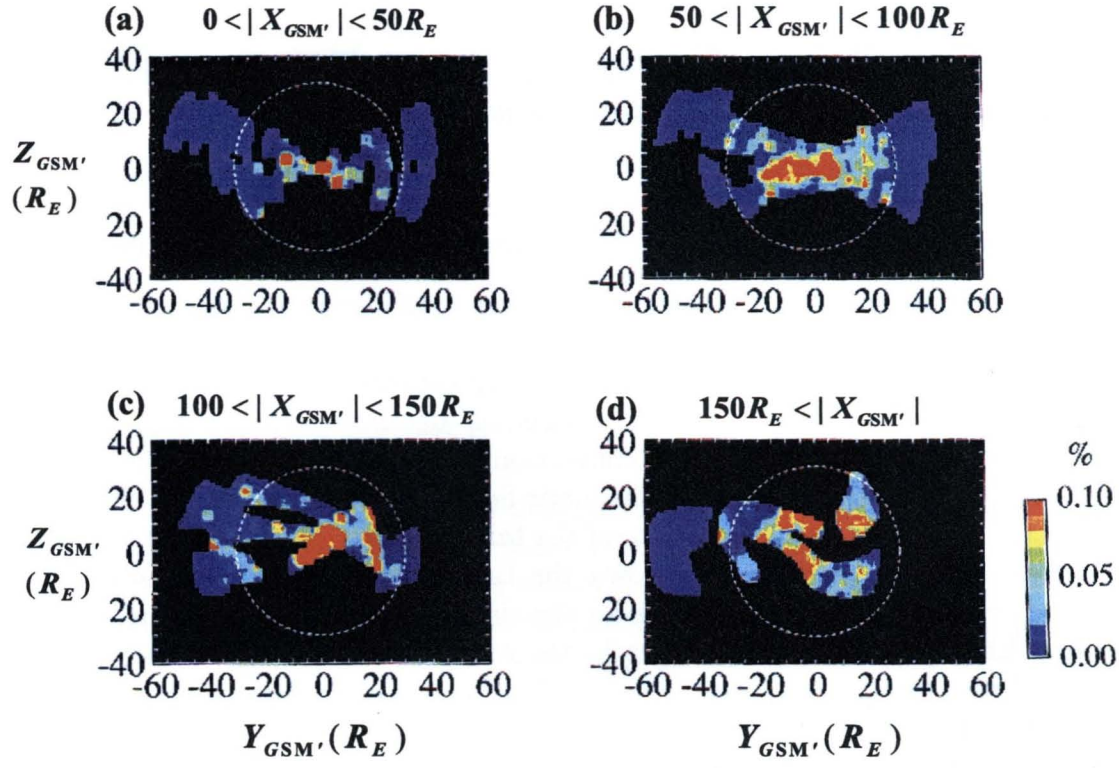

Figure 9.7: Observation probabilities of the electron plasma waves.

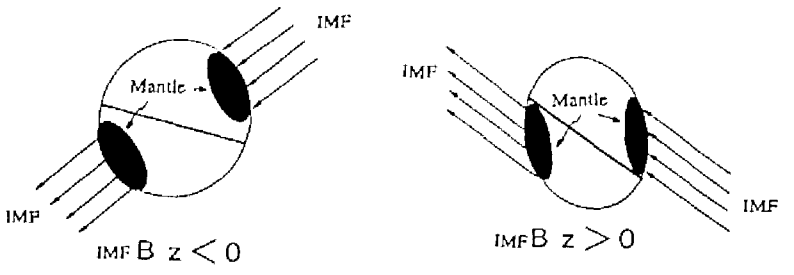

Figure 9.8: B_z dependence of the current sheet tilt angle during positive B_y of the IMF in the view from the tail toward the earth. For a negative B_y, a mirror image about the z axis applies. [*after Maezawa et al.*, 1997].

and they are confined within 10 R_E. Therefore, we can conclude that the thickness of the plasma sheet in average is about 10 R_E in the distance range from 50 R_E to 100 R_E down the tail.

9.4.2 IMF dependence of the plasma sheet structure

Sibeck et al. [1985] reported that during the interval of strong B_y component of the IMF, lobe field lines are strongly bent in the direction of the IMF. Further, *Sibeck et al.* [1986] showed that the current sheet structure strongly depends on B_y component of the IMF and that the current sheet in the magnetotail tilt because of the torque which is caused by reconnected field lines' pulling the convection direction in the tail region [*Cowley*, 1979, 1981]. Using the Geotail plasma and magnetic field data, *Maczawa et al.* [1997] extensively examine the IMF direction dependence of the tail structure. They showed that the distant tail current sheet beyond 150 R_E down the tail is tilted by 20° on the average either clockwise or anti-clockwise depending on the sign of B_y component of the IMF. Further, they found that the tile angle is larger for the northward IMF than for the southward one (see Fig. 9.8).

The above-mentioned tilt of the current sheet should appear as the tilt of the plasma sheet. Therefore, the plasma sheet structure detected by electron plasma waves is expected to reflect the tilt of the current sheet. In order to examine this expectation, we divide the observed electron plasma waves into four groups referring to the IMF direction as shown in Fig. 9.9. The IMF direction is obtained by the fluxgate magnetometer data onboard IMP 8 satellite. Since IMP 8 does not always stay in the solar wind, we only use the data obtained in the solar wind. The time delay on the solar wind traveling from IMP 8 to Geotail is calculated from solar wind velocities detected by the plasma measurement onboard IMP 8 and the relative distance between IMP 8 and Geotail. The data are plotted according to four different quadrants, i.e., (a) $B_z > 0$ and $B_y < 0$, (b) $B_z > 0$ and $B_y > 0$, (c) $B_z < 0$ and $B_y < 0$, and (d) $B_z < 0$ and $B_y > 0$. The data plotted in each panel are collected in all ranges of distance from the earth, but since we only use the data observed when the IMP 8 observed the solar wind plasmas, fewer datasets are available for the statistics in this case. Red and blue triangles represent observation points of electron plasma waves in the north and south lobes, respectively. Red and blue solid lines are the least squares straight-line

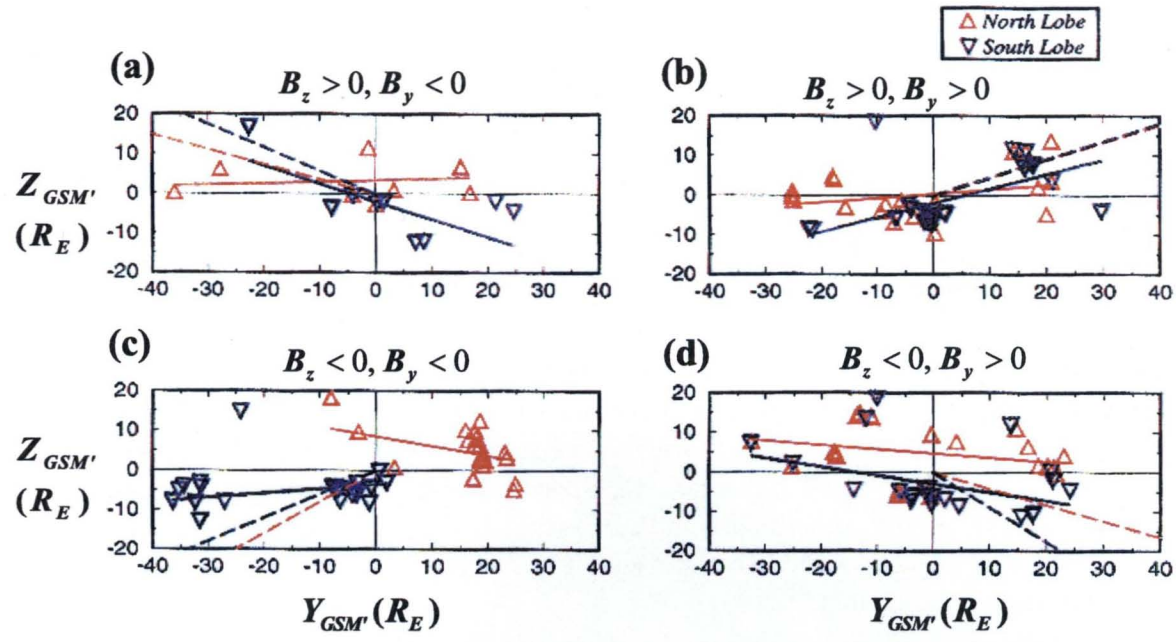

Figure 9.9: IMF dependence of the plasma sheet structure.

fits on observation points in the north and south lobes, respectively, while red and blue dotted lines are the same but for the averaged direction of the IMF during the intervals of plotted data. We note that this plot is a view from the earth to the tail, which is inverse to the view direction of Fig. 9.8.

The clear tendency on the tilt of the plasma sheet can be clearly seen only upper two panels. The tilt of the south hemisphere plasma sheet displayed by blue lines is very evident in panels (a) and (b). Further, respective tilts of the clockwise and anti-clockwise directions for $B_y < 0$ and $B_y > 0$ are consistent with results by *Sibeck et al.* [1986], and *Maezawa et al.* [1997]. The estimated tilt angles in panels (a) and (b) are 20.5° and 20.6°. This angle almost agrees with the angle of 20° obtained by *Maezawa et al.* [1997]. However, in both (a) and (b) panels, we cannot see the same tendency about the electron plasma waves observed in the north lobe. We do not have clear explanations about this. Possibly, we need more data to identify the reason about this, but we need to wait for another spacecraft to investigate the distant tail region, because the Geotail has already moved on the near tail orbit phase. *Maezawa et al.* [1997] showed that the tilt angle in $B_z < 0$ is much smaller than that in $B_z > 0$. This seems to be one of the reasons why the clear tilt cannot be seen in lower two panels which correspond to the case for $B_z < 0$.

9.5 Summary and discussion

In the present chapter, we attempted to apply the plasma wave measurements to the study of the macroscopic magnetotail structures. We succeeded to identify the magnetopause location using plasma density distribution calculated from the lower cutoff frequencies of the CR, and the intensities of the MNB emissions. The estimated location of the magnetopause

and its flaring effect agree well with the classical stationary magnetotail model and other observations. We also showed that flapping effects are more evident in the distant tail region. Further, we found that the permeated MNB emissions into the magnetosphere also suggest the existence of the LLBL only in the near tail region.

The electron plasma waves are very useful for identifying the structure of the plasma sheet. We showed that the thickness of the plasma sheet is about 10 R_E in the neartail region. The electron plasma wave observations showed that in the distant tail region, the northern and southern hemisphere plasma sheets are observed in the very high latitude region. This result seems to be the effect of the tail flapping or of some tail deformations. We also succeeded to show the tilt of the plasma sheet due to the torque of the IMF B_y component. The observed tilt angle of 20° agrees with other observations.

Our attempt to apply the plasma wave data to the study of the magnetotail structure showed that the magnetotail structure in average agrees well with the stationary magnetotail model introduced in Chapter 1. Because of the lack of data in the distant tail, we cannot perform enough discussion for the flaring and flapping effects in the distant tail region. However, we succeeded to show that the plasma waves are very useful for studying the macroscopic structures.

The advantage of plasma waves in the study of the macroscopic structure is that plasma waves are much more sensitive than other observed phenomena. For example, the existence of electron beams is sometimes hard to be identified in electron velocity distributions observed by plasma measurements, because the detected velocity distributions frequently reflect results of diffusion processes due to excited plasma waves. However, we can easily identify enhancements of electron plasma waves using their monochromatic spectra in local electron plasma frequencies. We stress that a plasma wave observation is one of the important tools for studying macroscopic phenomena.

Before concluding the present chapter, we demonstrate that plasma wave observations are useful for analyzing time variation of the macroscopic structure. Fig. 9.10 shows the frequency-time spectrogram generated from the SFA data. The event shown in this figure is the encounter of the interplanetary shocks which wave signatures are introduced in Chapter 3. During the period shown in this figure, the spacecraft was located in the distant magnetotail region at (GSM X', GSM Y', GSM Z')= (-209, -3, 0 R_E). We see a lot of the type III solar radio bursts in the frequency range between 20 kHz to 800 kHz. These active type III solar radio bursts mean that the activities in the solar surface are very high and solar flares frequently take place during this period.

As shown in the location in the GSM coordinates, Geotail was located in the center of the magnetotail region. However, we find the very interesting changes of observed characteristic regions in the magnetotail in this event. As shown in the bottom of this figure, the spacecraft observed magnetopause crossings (MP crossings) several times during 00:00 to 05:00 (UT) on June 23, 1993. After this interval, the intense MNB and high frequency lower cut off frequency of the CR (or UHR noise) mean that the spacecraft stay in the magnetosheath region during the interval from 04:00 on June 23, 1993 to 05:00 (UT) on June 24, 1993. The plasma densities are intensified around the interval from 10:30 to 20:00 (UT) on June 23, 1993. The maximum density reaches about 30/cc. This density intensification suggests the encounter with the interplanetary shock (IP shock). After the IP shock encounter, the spacecraft continues to stay in the magnetosheath, however, it starts

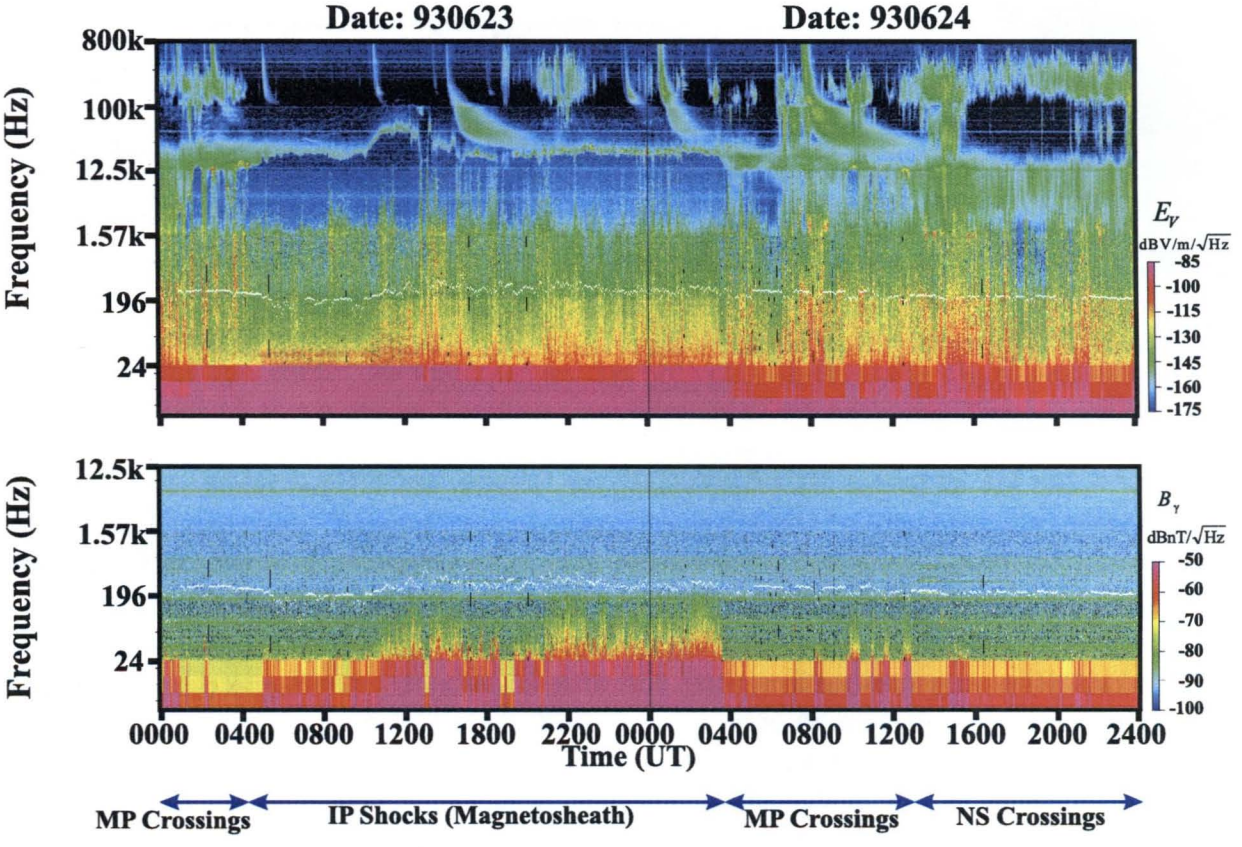

Figure 9.10: Multiple crossings of the magnetopause and neutral sheets.

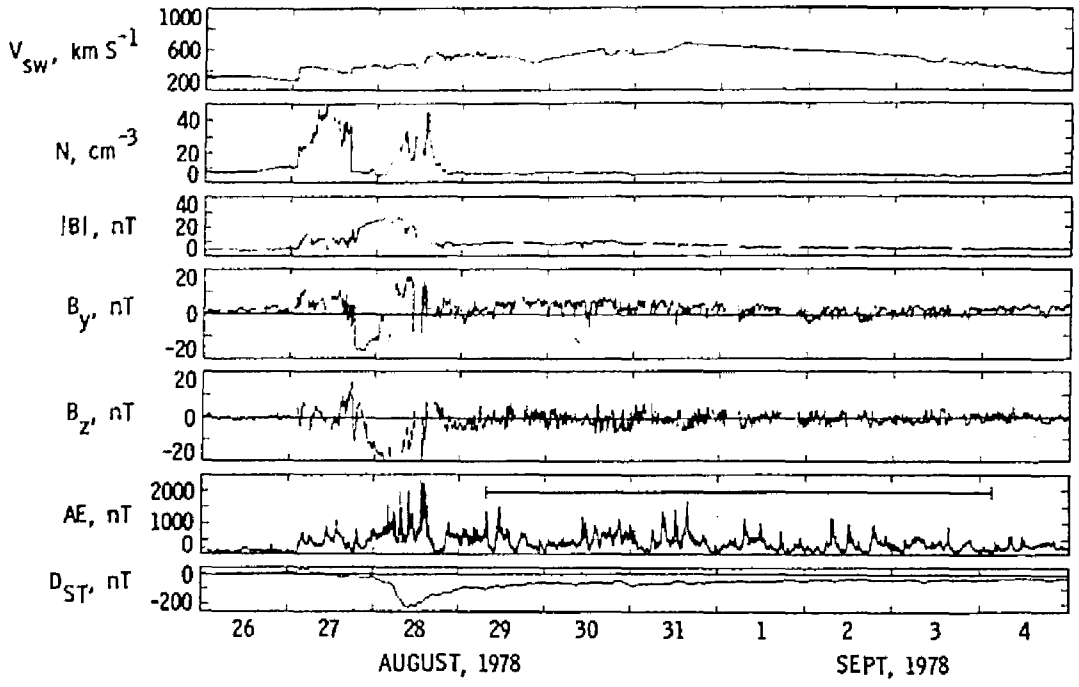

Figure 9.11: An example of a solar-flare-related high-speed interplanetary stream and its geomagnetic effects [*after Tsurutani and Gonzalez*, 1993].

to repeat the MP crossings after 04:00 (UT) on June 24, 1993. The sudden density changes and sudden enhancement of the MNB well indicate the above MP crossings. Further, after this MP crossings, the MGF fluxgate data (not shown) showed the spacecraft experiences the multiple neutral sheet crossings (NS crossings) after 13:00 (UT) on June 24, 1993.

In an early interval in Fig. 9.10, the spacecraft was inside the magnetosphere, but it moved into the magnetosheath region, and after the stay in the magnetosheath, it moved back to the magnetosphere. A series of the above trajectory suggests the dynamic motion of the magnetotail region, because the speed of the spacecraft is very slow relative to the dynamic motion of the magnetotail. Further, it is highly possible that such a dynamic motion is closely related to the IP shock observed in the magnetosheath. We occasionally observe similar MP crossings just before or after the passage of plasmoids.

These sudden observations of the magnetopause in the center of the magnetotail suggest the strong deformation of the magnetotail structure. In the case of Fig. 9.10, the spacecraft experience both multiple MP and NS crossings in short periods. This implies that the radius of the magnetotail becomes smaller than usual. This fact is consistent with the observations of the IP shocks. Since the dynamic pressure of the solar wind in IP shocks is much higher than that in the normal solar wind, the radius of the magnetotail should be smaller. This compression of the magnetotail structure possibly leads to the trigger of substorms. The relation of interplanetary shocks and geomagnetic activities are not clearly explained. Statistically, their relation is evident, but physical linkage of them is still unclear [*Tsurutani and Gonzalez, references therein*, 1993]. Figure 9.11 shows an example of an interplanetary shock and its geomagnetic effects. From top to bottom, the panels

give the solar wind velocity, plasma density, magnetic field magnitude, two components of the magnetic field in GSE coordinates, the auroral electrojet index (AE) and D_{ST}. The sudden increase of solar wind densities take place on August 27 and 28, 1978. These density enhancements and increse of solar wind velocities and magnetic field magnitudes correspond to the encounter with the interplanetary shocks. It is evident that the D_{ST} and AE indices increase synchronizing with the encounter with the interplanetary shocks. The increase of D_{ST} and AE indices mean the increase of the ring current and auroral electrojet currents, respectively. The main substorm which occurred on August 28 and the increase of AE index are due to negative B_z component of the IMF, but even in the positive B_z component, AE index increases on August 27. Further, the ring current activity displayed as D_{ST} is extended even after the passage of the interplanetary shocks. A similar feature can be seen in Fig. 9.10. The AKR emissions are intensified at 21:00 (UT) on June 23, 09:00 (UT) and 12:00 (UT) on June 24. As we introduced in Chapter 1, the AKR emissions are excited by high energy electrons injected from the magnetotail region to the polar region. Therefore, they reflect well occurrence of substorms [*e.g., Murata et al.,* 1995b]. The intensified AKR emissions shown in Fig. 9.10 are possibly related to the interplanetary shocks, but the detailed physical linkage between them is not clear.

Another interesting point in the event shown in Fig. 9.10 is the repetition of the magnetopause or neutral sheet crossings. Figure 9.12 is the expanded plot of the frequency-time spectrogram for the interval from 10:00 to 12:00 (UT) on July 24, 1993. The distinct regions of the spacecraft are indicated in the bottom. As shown in this figure, the spacecraft repeated to move across the magnetopause in short periods. The abrupt decrease of the CR lower cutoff frequency at 10:20 (UT) is the first magnetopause crossing in this figure. We confirm this by the abrupt disappearance of the MNB in the lower magnetic field component. This magnetopause crossing corresponds to the type 2 which we introduced in Chapter 3. The spacecraft moves back to the magnetosheath at 10:52 (UT), but it again moves into the magnetosphere at 11:00 (UT). These magnetopause crossings also correspond to the type 2 with very sharp boundaries. After the magnetopause crossing at 11:00 (UT), the spacecraft gradually moves back to the magnetosheath through the boundary layer from 11:18 (UT) to 11:28 (UT) and moves into the magnetosphere from 11:45 (UT). These two magnetopause boundaries belong to the type 1.

These repetitions of the magnetopause crossings are very interesting, because their time periods are very short. For example, the time duration between the second and third magnetopause crossings is only 8 minutes. Further, during the interval from 11:18 (UT) to 11:30 (UT), the lower cutoff frequency of the CR repeats to change periodically. This means that plasma densities change in short time periods. It is difficult to explain such short period variations with a few minutes by the dynamic motion of the magnetotail, because the solar wind dynamic pressure does not change in such a short period. It seems to be reasonable to explain these variations by the wavelike structures of the magnetopause. Such wavelike structures are frequently observed when the geomagnetic activities are high. Similar repetitions can be seen in the neutral sheet crossings (not shown). This result suggests that the plasma sheet also has the wavelike structure in this event. The wavelike structure of the boundary is frequently discussed in the relation to the Kelvin-Helmholtz (K-H) instability. However, the relation among interplanetary shocks, wavelike structures and the KH instability is not clear.

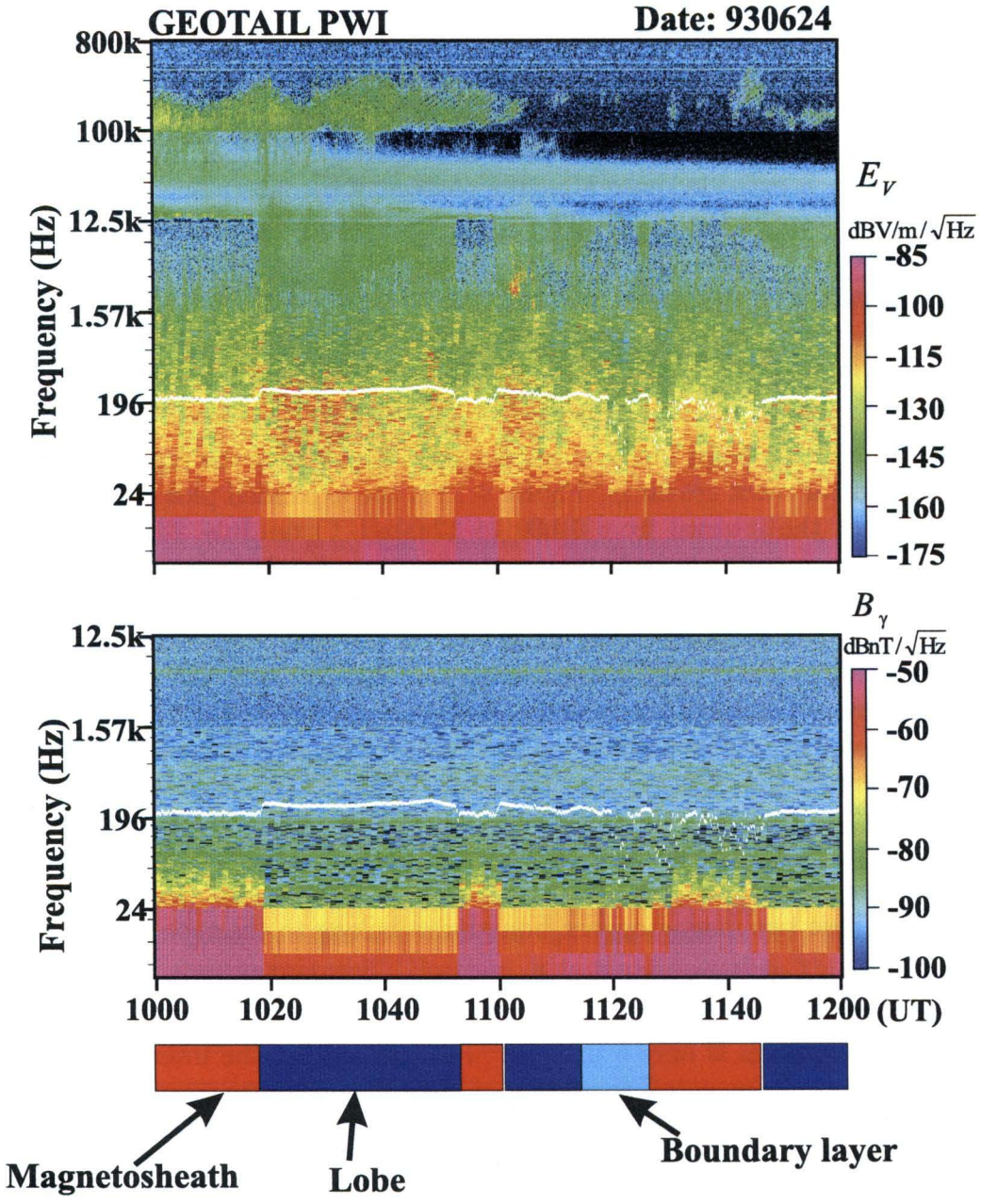

Figure 9.12: Multiple magnetopause crossings just after the encounter with the interplanetary shocks.

As shown in the latter part of this section, we can discuss the dynamic motion of the magnetotail and structures of boundaries using plasma wave data. In the previous plasma wave observations, microscopic phenomena have been mainly discussed. However, since macroscopic phenomena consist of microscopic phenomena, they should not be discussed separately. We believe that plasma wave observations provide a link between microscopic and macroscopic phenomena. The application of plasma wave observations to the study of macroscopic magnetotail structure discussed in the present chapter is the first step to link microscopic phenomena to macroscopic phenomena.

Chapter 10

Summary and concluding remarks

10.1 Summary

We discussed plasma wave phenomena observed by Geotail spacecraft in the magnetotail region. In the present thesis, after the description of the plasma wave instrument (PWI) onboard Geotail spacecraft, we mainly focused on the waveform observations of the Broadband Electrostatic Noise (BEN), Narrowband Electrostatic Noise (NEN), and electron plasma waves. The Wave-Form Capture (WFC) receiver succeeded in observing these waveforms for the first time. Until the Geotail success, no one has seen the waveforms of the BEN and NEN before or no one has recognized that the electron plasma waves consist of parallel and perpendicular polarized components relative to the ambient magnetic field. The Geotail plasma wave observations showed the importance and usefulness of waveform observations. Spectrum data are very convenient, but sometimes they are misleading. Our waveform observations also succeeded in the sense that many scientists have recognized the importance of waveforms. This is evident in the fact that several spacecraft after the Geotail extensively started to perform waveform observations. They have been observing various waveforms in various regions. Some of the observed waveforms are quite similar to those observed by Geotail.

We also discussed the magnetotail structures using the plasma wave signatures in each distinct region as a new attempt to apply plasma wave observation data to the macroscopic magnetotail physics. Followings are summaries of each chapter in the present thesis.

In Chapter 1, we introduced the stationary and the quasi-stationary model of the magnetotail region, which are essentially connected to plasma wave phenomena observed in the magnetotail. Especially, three kinds of x type neutral lines are very important on plasma wave generations, because plasma particles are believed to be accelerated around the x type neutral lines. Further, continuous reconnections at near-earth neutral line result in emissions of the plasmoids. We see the drastic change of wave activities at the encounter of plasmoids. Further, we claimed the importance and objectives of plasma wave observations in space by spacecraft, referring to the history of plasma wave measurements. We also provided a brief introduction of representative plasma waves, which are indirectly related to other chapters.

Chapter 2 described the Plasma Wave Instrument (PWI) onboard Geotail spacecraft as well as the spacecraft itself. The PWI is the first plasma wave subsystem to be designed

to meet the objectives for investigating the distant magnetotail region. Further, it has a newly designed WFC receiver as well as sophisticated classical spectrum receivers. After the description of the PWI receivers and sensors, we explained the detailed calibration method including the effect of antenna impedance in space plasmas. The PWI has the function to measure antenna impedance in plasmas. Obtaining antenna impedance precisely is important especially for waveform measurements by the WFC, because errors of antenna impedance cause some distortions of waveforms leading to errors of calculations of the Poynting flux or wavenormal vector.

We also showed the results of the ElectroMagnetic Compatibility (EMC) tests in Geotail spacecraft in Chapter 2. Electromagnetic pollution caused by other instruments is always a problem in plasma wave measurements. Geotail is the first Japanese scientific spacecraft in which the EMC tests were systematically conducted. After introducing the Geotail EMC specifications and measurement system, we showed representative noises which we found during the EMC tests on the ground and proposed the EMC strategies to the future mission.

In Chapter 3, we summarized the plasma wave signatures observed in the distinct regions in the magnetosphere. Since plasma waves reflect results of wave-particle interactions, knowledge of plasma wave signatures in each region is very helpful for studying microscopic phenomena taking place in each region. Further, the plasma wave signatures are very useful for the region identification. By statistically processing the plasma wave signatures introduced in Chapter 3, we discuss the macroscopic structures in Chapter 9.

Chapters 4 and 5 provided detailed waveform analyses and discussions of the Electrostatic Solitary Waves. We revealed the waveforms of the Broadband Electrostatic Noise (BEN) which is commonly observed in the plasma sheet boundary layer (PSBL). The WFC receiver detected a series of isolated bipolar pulses during the observations of BEN. The observed pulses are purely electrostatic and we addressed them Plasma Sheet Boundary Layer Electrostatic Solitary Waves (PSBL ESW). Based on our detailed analyses such as spin dependence and polarization analyses, we proposed the PSBL ESW potential, which has an isolated structure propagating along the ambient magnetic field. The proposed potential structure is one-dimensional and uniform in the perpendicular direction relative to the ambient magnetic field, because observed ESW do not have perpendicular electric field components. One-dimensional potential model agrees well with the PSBL ESW observed in the distant tail region. However, after Geotail was put on the near-tail orbits, we frequently observe the PSBL ESW with perpendicular electric field components. The observed electric field vectors on $E_{\parallel} - E_{\perp}$ plane rotate in a half of a circle for one ESW waveform. Further, the PSBL ESW with perpendicular electric field components are not always observed and we also observed the PSBL ESW without perpendicular components, simultaneously. These observation results suggest isolated potentials with two-dimensional structures. Difference from the one-dimensional structures is the scale of the perpendicular uniform structure. In the two-dimensional potential structures, observing their edges is more likely. When spacecraft encounters the edge of potentials, we observe the ESW with perpendicular electric field components, while when spacecraft moves across other parts of the potential structure, we observe the ESW without perpendicular components.

We succeeded in reproducing the above one or two-dimensional potential structures under collaborations of computer experiments. Our one-dimensional computer experiments

showed that Langmuir waves are destabilized by the bump-on-tail instability and that their nonlinear evolution results in the formation of isolated one-dimensional potential structure, which is a kind of the BGK mode. The reproduced potential structure is quite similar to the PSBL ESW potential reported by waveform observations. We also showed by two-dimensional computer experiments that two-dimensional isolated potential structures can be formed in the middle stage of the nonlinear evolution and that as time elapses, these perpendicular structures become uniform by diffusion effects due to cyclotron motions. Based on these one-dimensional and two-dimensional computer experiments, we proposed a scenario on the formation of one-dimensional or two-dimensional PSBL ESW as follow. In the initial stage, the Langmuir waves are excited by the bump-on-tail instability. When the excited Langmuir waves reach a nonlinear stage, they start to coalesce each other. Since the perpendicular diffusion process takes place more slowly than the coalescence process in the parallel direction, at this stage, the formed potentials are isolated in both parallel and perpendicular directions. When spacecraft observe the PSBL ESW at this stage, it is likely to observe two-dimensional ESW. When further perpendicular diffusion process proceeds, one-dimensional potential structure can be formed. The potential at this final stage corresponds to one-dimensional PSBL ESW.

The solitary structures have already been observed in the polar magnetosphere and bow shocks by other spacecraft. Therefore, we discussed the possibility that the above scenario is applicable to other solitary structures by comparing their pulse widths with local electron or ion plasma oscillation periods. If the formation of solitary structures is the result of the nonlinear evolution of the Langmuir waves, their pulse widths are related to local electron plasma oscillation periods. The comparison results showed that the solitary structures observed by FAST and Polar spacecraft belong to the same category of the PSBL ESW. However, those observed by Viking spacecraft are different from the PSBL ESW. This result is very consistent with their potential polarities, because the potential polarity of the FAST and Polar solitary waves is positive and that of the Viking spacecraft is negative. Since the PSBL ESW potentials are expected to be positively charged from computer experiment results, the above result is consistent.

While Chapter 4 was dedicated to study the generation mechanism of the PSBL ESW, in Chapter 5, we attempted to identify source regions of the PSBL ESW. By using the Geotail antenna polarities and waveforms of the PSBL ESW, we succeeded in identifying propagation direction of the PSBL ESW. In the BGK potential mode, isolated potentials propagate in the same direction of electron beams. Therefore, we can estimate source location relative to the spacecraft position by identifying the propagation direction. The preliminary statistical analyses of the PSBL ESW propagation directions show that observation possibility of the earthward ESW is highest in the near-earth region. Further, we introduced an event in which both earthward and tailward ESW are observed simultaneously. At this event, the spacecraft was located just in front of the plasmoid and it is also close to the expected position of the distant neutral line. We expect that this situation leads to the observation of both earthward and tailward propagating ESW.

In Chapter 6, we performed waveform observations of the Narrowband Electrostatic Noise (NEN), which is another common plasma wave in the tail lobe. The WFC receiver revealed that waveforms of the NEN are not noise. The observed waveforms of the NEN are continuous quasi-sinusoidal waves. Some waveform deformations and quick change of

their frequencies result in the NEN spectra. We address these NEN waveforms lobe Electrostatic Quasi-Mnochromatic Waves (lobe EQMW). The lobe EQMW is quasi-sinusoidal, but their frequencies quickly change in a very short time scale. This means that the lobe EQMW is closely related to electron dynamics. Previous observations report that the NEN is the Doppler-shifted ion acoustic wave, but our estimation of the Doppler shift velocity showed that it is unlikely to shift ion acoustic waves to the NEN frequency range by the Doppler-shift. We examined another plausible NEN excitation mechanism called Electron velocity space hole mode. We surveyed correlations between the NEN emissions and electron velocity distributions, and found the coincidence of the existence of structures in electron velocity distributions and the NEN emissions. Further, the relation of the NEN frequency and the local electron plasma frequencies agree well with the electron velocity space hole theory. Thus, we concluded that the NEN (lobe EQMW) is generated by the electron velocity hole instability.

In Chapter 7, we showed the waveform observations of the electron plasma waves observed in the lobe close to the PSBL. The observed waveforms are strongly modulated in their amplitudes. Our detailed polarization analyses revealed that such modulated electron plasma waves include parallelly propagating Langmuir waves, and perpendicularly propagating Electron Cyclotron Harmonic waves (ECH). Since electron plasma frequencies are much higher than electron cyclotron frequencies, the upper hybrid resonance frequency, where ECH waves are likely to be most unstable, is almost equal to the Langmuir wave frequencies. Therefore, it is very difficult to distinguish the Langmuir waves from ECH waves without polarization analyses. The amplitude modulations of the ECH waves are very evident because of their spectral structures. We do not need any nonlinear theories to explain their amplitude modulations. In the previous observations by other spacecraft in various regions, most of the papers judged that observed modulated waveforms are the Langmuir waves and they attempted to explain their modulations by using the nonlinear parametric theory but their attempts have not completely succeeded because of poor correlations between the Langmuir waves and low frequency ion acoustic waves, which should be excited due to the nonlinear parametric processes. Therefore, we applied our results to other observations and pointed out the possibility that their observations of modulated waveforms include the ECH waves. Nonetheless, we also found that a part of modulated electron plasma waves corresponds to the parallelly propagating Langmuir waves. We discuss their modulation mechanisms referring to the results of computer experiments on the nonlinear spatial trapping effects. The excited Langmuir waves trap beam electrons spatially. The subsequent phase shift due to the phase mixing of electrons leads to spatial localization of excited wave amplitudes. Thus, the nonlinear spatial trapping effects cause the spatial amplitude modulations of the excited Langmuir waves. When we observed such spatial amplitude modulations, the observed temporal waveforms appear to be the modulated Langmuir waves. In this theory, we do not need any nonlinear parametric effects. We concluded that the most plausible excitation mechanism is the nonlinear spatial trapping effect.

Chapter 8 showed the waveform observations of the BEN and NEN in the magnetosheath region as the counter part of the magnetotail. The observed waveforms of these two waves are quite similar to the PSBL ESW and lobe EQMW, respectively. We address them Magnetosheath ESW (MS ESW) and Magnetosheath EQMW (MS EQMW). Since occurrence

of the MS ESW is very rare and they appear very abruptly, we have not performed enough data analyses for the MS ESW. However we confirmed that their electric field is polarized along the ambient magnetic field. On the other hand, the MS EQMW are commonly observed in the magnetosheath region. Since their frequency ratios to local electron plasma frequencies are almost the same as those for the lobe EQMW, it is highly possible that these waves are the same plasma wave mode. However, in the previous observation and theoretical studies, they are believed to be the Doppler-shifted ion acoustic waves. We also confirmed that the solar wind bulk velocity reasonably can shift ion acoustic waves to the MS NEN frequency in the magnetosheath. However, we showed that the MS NEN frequencies are independent of the magnetic field directions. Since the MS NEN (MS EQMW) propagates along the ambient magnetic field, if they are Doppler-shifted, some frequency changes should be seen during changing of the ambient magnetic field direction. Therefore, from this independence of the MS NEN (MS EQMW) frequencies, we concluded that the MS NEN is not the Doppler-shifted ion acoustic waves. We also claimed the generation of the MS ESW is due to the electron velocity hole mode, but we did not find clear evidence in observed electron velocity distributions for this mechanism.

In Chapter 9, we attempted to apply the plasma wave measurement data to the study of the macroscopic magnetotail structures. Generally, the plasma wave data are made use of for the study of the microscopic phenomena such as wave-particle interactions. However, as we introduced in Chapter 4, each distinct region is characterized by specific plasma waves. Therefore, by processing the plasma wave signatures statistically, we can study the macroscopic structure. In the present thesis, we succeeded in showing the structures of the magnetopause, Low Latitude Boundary Layer (LLBL) and plasma sheet.

10.2 Energy flows from the solar wind

The solar wind continuously injects its energy to the magnetosphere. Excitation of plasma waves is one of the styles in energy consumption of injected solar wind energies. Of course, the total amount of energy consumption by plasma waves is much smaller than other macroscopic energy consumption such as emissions of plasmoids. However, it is true that the real energy source of plasma waves excited in the magnetosphere is originated from the solar wind.

Plasma waves are classified into two groups: They are electromagnetic waves and electrostatic waves. In the present thesis, we mainly focus on the electrostatic waves. Generally, electromagnetic waves propagate far from source regions, while electrostatic waves thermalize particles and they are damped very quickly. Therefore, electrostatic waves do not propagate to remote points far away far points from source regions.

Figure 10.1 schematically shows the energy flows from the solar wind through plasma waves to the background plasmas. The black, red and blue arrows represent energy transfer due to plasma bulk, electron dynamics and ion dynamics, respectively. All of shown waves were not discussed in the present thesis, however, in order to present a comprehensive energy flow, we include most of plasma waves observed by Geotail in this figure.

The left sequence beginning from the dayside reconnection is the main channel of energy transfer from the solar wind to the magnetosphere. We briefly explained this reconnection process in Chapter 1. Injected energies are released through the magnetic reconnection

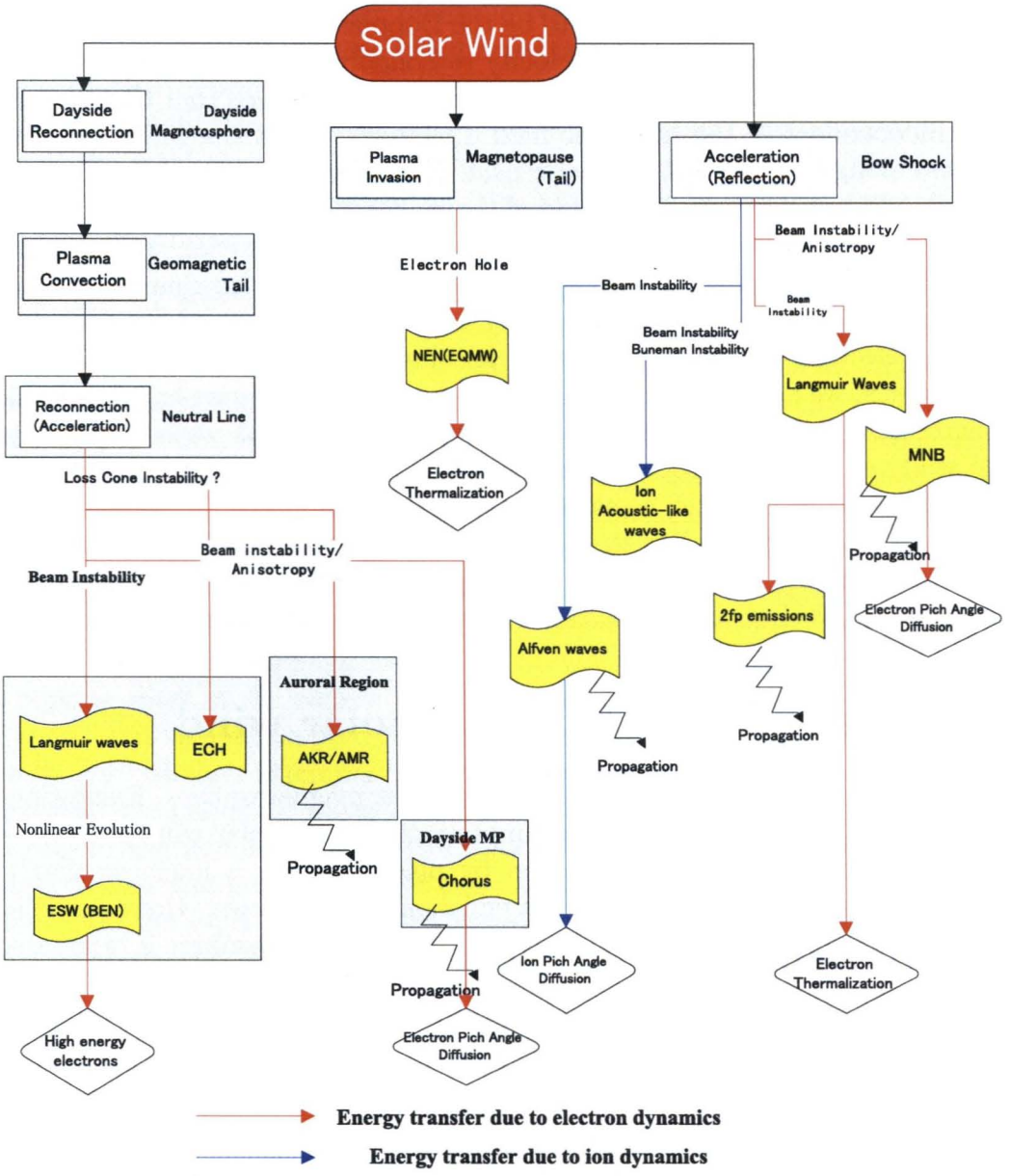

Figure 10.1: Energy flow chart from the solar wind through plasma waves to background plasmas

process at x type neutral line. At this x type neutral line, particles are believed to be accelerated and electron beams are ejected from this point. Ejected electron beams excite Langmuir waves propagating along the magnetic field lines, which are connected to the regions around the plasma sheet boundary layer. Some parts of Langmuir waves suffer strong amplitude modulations, and other parts of Langmuir waves evolve to the nonlinear stage leading to formations of the BGK mode. The formed BGK potentials can be observed as the PSBL ESW. As we showed in Chapters 4 and 5, ESW potentials trap electrons and produce trapped high energy electrons.

What controls the evolution of the Langmuir waves ? Why does a part of the Langmuir waves lead to the modulated Langmuir waves and other parts lead to the ESW ? Computer experiments by *Omura et al.* [1996] provide an important clue to the answer to these questions. *Omura et al.* [1996] showed that the bump-on-tail instability leads to the formation of the BGK potentials, while they also showed the weak beam instability ends with the quasi-linear diffusion after excitation of the Langmuir waves, where the definition of the weak beam is the density ratio of electron beams is less than 0.3 and beam velocity is much larger than thermal velocity of another electron component. The above results of computer experiments show that the scenario of the nonlinear evolution in the beam excited Langmuir waves strongly depends on the types of electron velocity distributions.

On the other hand, as shown in the second sequence of Fig. 10.1, the solar wind invades through the magnetopause, and some mixtures between solar wind plasmas and magnetospheric plasmas take place. These mixtures cause structures in electron velocity distribution leading to destabilization of the electron velocity space hole mode observed as lobe EQMW (lobe NEN).

The third sequence beginning at the bow shock is the energy flow around the bow shock and its upstream region, which we did not focus on in the present thesis. In the bow shock region, reflected ions excite low frequency Alfvén mode waves with large amplitudes due to an ion beam instability. The similar ion beam instability also takes place in the cometary ion pick up process [*e.g., Kojima et al.*, 1989]. Through excitations of the Alfvén waves, they cause the pitch angle scattering and ions are thermalized.

The accelerated electrons at the bow shocks excite the Langmuir waves and $2f_p$ emissions. The $2f_p$ emissions are believed to be generated by nonlinear wave-wave interactions triggered by beam excited Langmuir waves. They are electromagnetic waves emitted from the tangential IMF lines connecting to the bow shock [*Lacombe et al.*, 1988; *Kasaba et al.*, 1997]. The intense MNB around the bow shock can be destabilized due to the beam and/or anistropy of electrons, which are formed due to accelerations and the mirror force at the bow shock [*Zhang et al.*, 1998b].

Figure 10.2 compliments Fig. 10.1 by showing the spatial distribution of each wave generation source region. We can see more clearly the process from energy injection to wave excitations through magnetic reconnections at the neutral point.

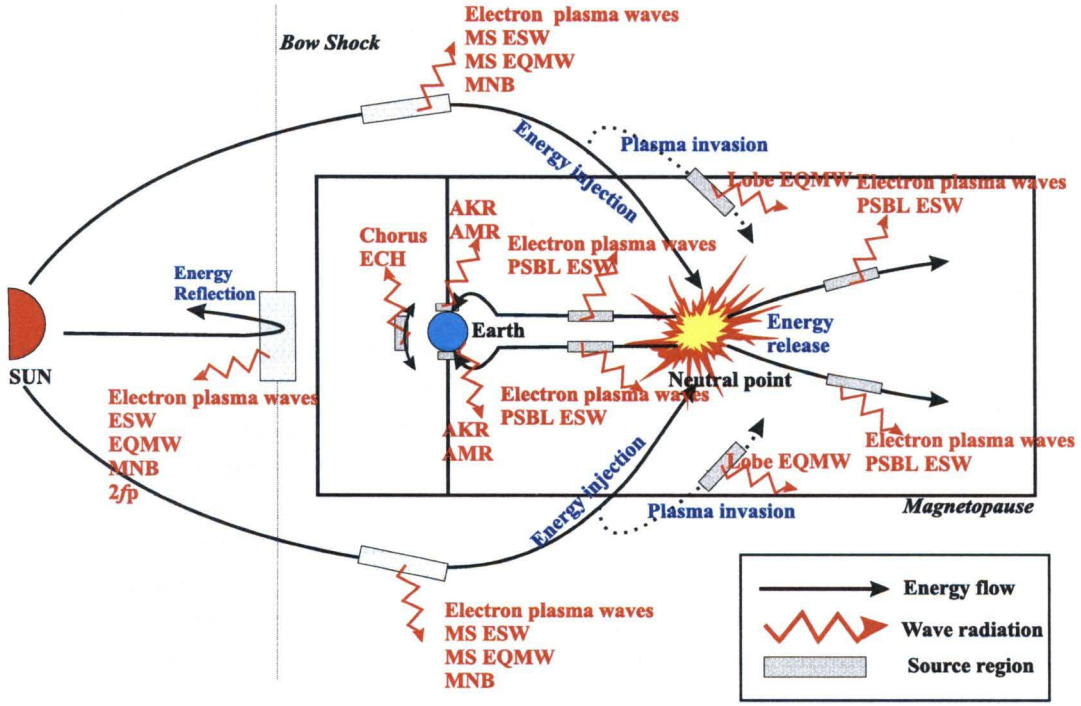

Figure 10.2: Spatial distribution of plasma wave excitations as consumption of solar wind energies.

10.3 Remained problems to be resolved in the future

10.3.1 Source of electron beams

The generation mechanisms of the PSBL ESW and the modulated electron plasma waves are related to electron beams. In the present thesis, we assume that the electron beams are originated around the neutral lines. The near-earth neutral line (NENL) and the distant neutral line are the most plausible source region of energetic electron beams, because energy conversion of the magnetic field to particles can be expected to take place. The detailed plasma features around the NENL have been showned by *Nagai et al.* [1998]. However, the detailed acceleration mechanism at the neutral point is still unclear theoretically. As we showed in Chapters 5 and 7, the electron beam components can be found in the PSBL or lobe region close to the PSBL with good correlations with the ESW and modulated electron plasma waves. Since magnetic field lines in these regions are expected to connect with the NENL or distant neutral points, the electron accelerations at the neutral points seem to be consistent with the observation results. On the other hand, the above model has a difficulty to explain the fact that the ESW and modulated electron plasma waves can be observed in the wide range of the distance from Earth. As we introduced in the present thesis, the near-earth and distant neutral points are expected to be located around 20 R_E to 30 R_E and around 100 R_E, respectively. If we assume that the observed electron beam components are originated at these neutral points, we need to explain why such electron beams can propagate far from the source region, because the electron beam components with the ESW

and modulated electron plasma waves can be observed in the wide range of the distance from Earth. In general, electron beams are quickly thermalized and cannot reach the far point from the source region through the excitation of plasma waves. Therefore, we need to explain why electron beams are not thermalized due to wave-particle interactions while their traveling from the source region. The same problem is also remained in the type III solar radio bursts, which we introduced in Chapter 7. The type III solar radio bursts can be generated by electron beams emitted from the Sun flare. However, the Langmuir waves, which are the parent waves of the type III solar radio bursts, can be observed in the solar wind at 1 AU from Sun, as shown in Fig. 7.3. This means that electron beams emitted from Sun can reach the Earth without suffering diffusion processes due to wave-particle interactions. *Gurnett et al.* [1993] attempted to explain the electron beams surviving in the long distance using the observation results of the modulated Langmuir waves. Since the modulated Langmuir waves are the results of the nonlinear parametric interactions (wave-wave interactions), they claimed that the wave-particle interaction end in an earlier stage before causing the enough electron diffusions and that the nonlinear wave-wave interactions dominate appearing as the modulated Langmuir waves. They pointed out that the observation of modulated Langmuir waves is the proof that the wave-wave interaction dominates in the evolution of the Langmuir waves excited by solar electrons.

This model can be applied to electron beams in the lobe or PSBL regions, because we also find the modulated Langmuir waves around the interface between the Lobe and PSBL. However, as we discussed in Chapter 7, we did not find any proofs showing that the modulated Langmuir waves are generated due to the nonlinear parametric instabilities, because there exists no correlation between the modulated Langmuir waves and ion acoustic waves. Further, computer experiments show that the modulated Langmuir waves can be observed even without any nonlinear parametric instabilities. Therefore, applying the model for surviving electron beams in the generation of the type III radio bursts to the case of electron beams in the geomagnetic tail region is questionable.

In order to explain existence of electron beams in the lobe, or PSBL, we propose another model using the electron velocity filter effect. Figure 10.3 is the schematical drawing for this model. Since the plasma sheet consists of hot electrons and plasmas in the lobe are very cold, the high energy components of electrons in the plasma sheet can escape from the plasma sheet along the ambient magnetic field. The higher energy components can escape faster from the plasma sheet. Thus, only high energy components remain far from the plasma sheet along the ambient magnetic field. This is the effect of so-called velocity filter. The final velocity distribution shown in Fig. 10.3 consists of the cold lobe electrons and beam electrons caused by the velocity filter effect. This model can explain the reason why the electron beam excited Langmuir waves and ESW are observed in the wide area. However, electrons need to travel in the long distance in order to be affected by velocity filters. Therefore, it is unlikely to expect this effect just at the interface region of the plasma sheet and lobe regions where the beam excited electron plasma waves can be observed.

This formation mechanism of electron beams is the most important unresolved problem on the plasma wave generation in the geomagnetic tail region, because electron beams are the free energy source of the electron plasma waves and ESW.

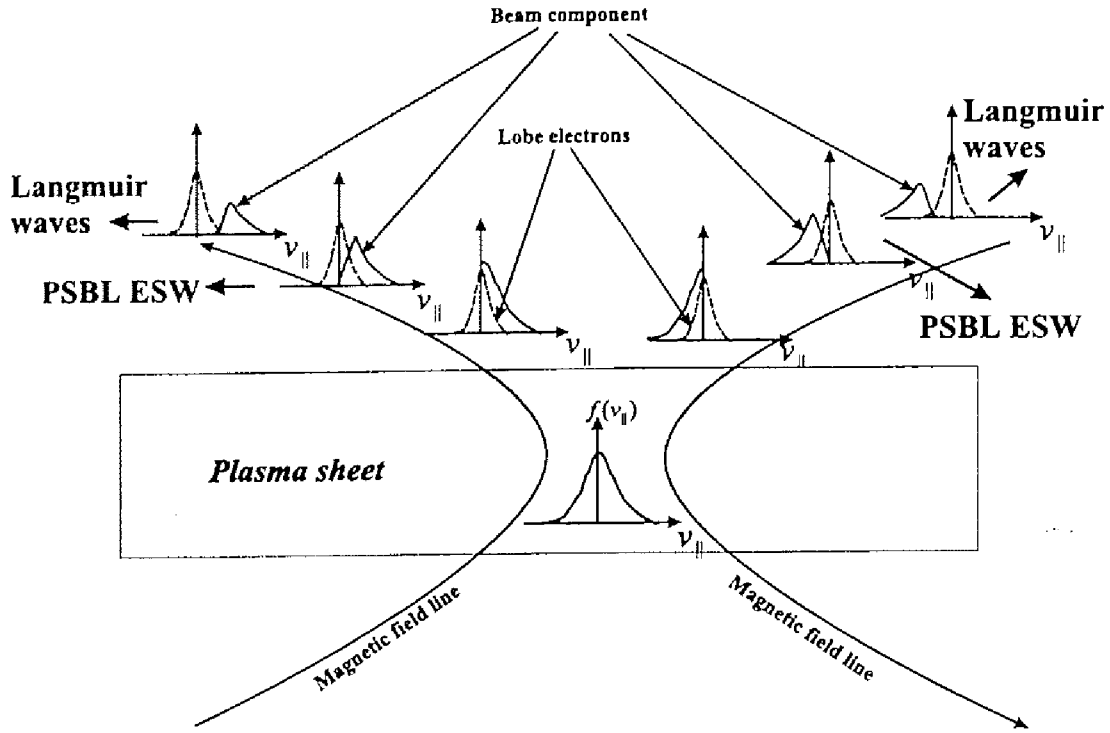

Figure 10.3: Schematical drawing for the formation of electron beams due to the velocity filter effect

10.3.2 Low frequency component of the BEN

In the present thesis, we showed that the high frequency portion of the BEN consists of a series of pulse waveforms called ESW. The waveforms of the ESW are very interesting results of strong nonlinear phenomena in space plasmas. However, as we discussed in Section 4.7, we cannot explain all of the natures of the BEN only by the ESW. Especially, low frequency components with quasi-upper cutoff at f_{ce} and lower cutoff at the LHR frequency lead us an idea that low frequency components of the BEN are whistler mode waves. However, the low frequency components of the BEN are not accompanied by magnetic components. The Geotail waveform observations succeeded in discovering the ESW in the BEN, but until explaining the generation mechanism of its low frequency component, we cannot conclude the BEN emissions. Practically, spectrum energies of low frequency components are much larger than those of high frequency components including the ESW. Further, we need to provide a model on the simultaneous excitation of the ESW and low frequency components of the BEN.

The remained problems on the BEN are listed as follows.

1. What is the generation mechanism of the BEN low frequency components ?

2. Why do the BEN low frequency components have the lower cutoff at the LHR frequency ?

3. Why can the low frequency component be observed with the ESW simultaneously ?

Table 10.1: List of planetary missions with plasma wave observations

Mercury	Venus	Earth	Mars	Jupiter	Saturn	Uranus	Neptune	Pluto
None	Pioneer Venus	Many Galileo*	Phobos2 Nozomi**	Voyager1*, 2* Galileo**	Voyager 1*, 2* Cassini**	Voyager 2*	Voyager 2*	None

*: Only flyby
**: Ongoing mission

4. Is the generation of low frequency components related to high energy ion flows in the PSBL ?

10.4 Missions to other planets

As summarized in the previous section, a portion of the solar wind energies is converted into plasma waves in the magnetosphere. This situation is the same in other planets of the solar system. Several spacecraft have already observed plasma wave emissions around the planets, but their observations are very coarse because of the limitation of the onboard receivers.

A Japanese mission to Mars called "Planet-B," which was renamed as "Nozomi" after the launch, was successfully launched on June 4, 1998. It has the most sophisticated wave receivers among those in other previous planetary missions. We expect to find detailed plasma wave features in the Mars planetosphere.

This Nozomi is the first Japanese planetary mission. We have just started missions to other planets. In this section, we provide a brief introduction of plasma wave observations around other planets, and propose several targets in planetary missions in the view point of plasma wave observations. Table 10.1 summarizes the previously conducted planetary missions including the ongoing missions. Since the Nozomi, and Cassini have not arrived at Mars and Saturn, most of plasma wave observations have been done by Voyager spaceprobes. However, the observations by Voyager spaceprobes are restricted into one time encounter with planets, because they only observe planets during their flyby. The Pioneer Venus spacecraft observed Venus planetosphere for more than 14 years. However, frequency resolutions are very limited and it did not have magnetic sensors. The Phobos 2 was the Russian Mars mission. It was injected into an elliptical orbit around Mars, but the mission was ended only in 3 months.

From the above results, we find that the data obtained in the previous mission are very limited. We expect further high quality plasma wave data in the future mission as well as Nozomi and Cassini missions.

Planets in the solar system are mainly divided into two groups. They are magnetized planets and unmagnetized planets. Jupiter, Saturn, Uranus, Neptune and Earth are the magnetized planets, while Venus and Mars are the unmagnetized planets. Mercury is very special. It has intrinsic weak magnetic fields. Its magnetosphere was discovered by Mariner 10 spacecraft [*Ness et al.*, 1974; *Ness et al.*, 1975]. Further, since it is very close to the Sun, and the dynamic pressure of the solar wind is very high, the dayside magnetosphere might be extremely compressed and it is possible that its planetary surface

directly interacts with the solar wind plasmas. Therefore, Mercury belongs to both groups.

As for the magnetized outer planets, plasma waves in Jupiter, Saturn, Uranus, and Neptune were surveyed by the Voyager 1 and 2 spaceprobes. Figure 10.4 shows a series of frequency-time spectrograms observed by Voyager spaceprobes in each planet (the spectrogram for Earth was only generated by the ISEE-1 spacecraft).

The commonly observed emissions are the whistler mode emissions including chorus and hiss type emissions. These emissions are characterized by the magnetized planets. Such intense whistler emissions in inner magnetospheres (planetospheres) are not observed in the unmagnetized planets. The whistler waves are hard to propagate because of weak or no ambient magnetic fields in the unmagnetized planets.

The electromagnetic radiation similar to the terrestrial continuum radiation can be commonly observed in the magnetized planets. As we introduced in Chapter 1, the generation of the continuum radiation needs the large density gradient and intrinsic magnetic field. Therefore, the magnetized planets with plasmasphere (ionosphere) and intrinsic magnetic field can generate the continuum radiation. Recently, Galileo spacecraft discovered the magnetosphere of Ganymede, a Jovian moon [*Gurnett et al.*, 1996; *Kivelson et al.*, 1996] and it showed that the Ganymede is the source of the continuum-type radiation generated due to the mode coupling [*Kurth et al.*, 1997].

Very high frequency waves mainly radiated in the polar region in each planet such as AKR in Earth also characterize the magnetized planets. Voyager spaceprobes have already observed as Decametric wavelength emissions (DAM), Hectometer wavelength emission (HOM) in Jupiter, Saturnian Kilometric Radiation (SKR) in Saturn, Uranian Kilometric Radiation (UKR) in Uranus [*Kaiser*, 1989]. The AKR in the Earth is closely related to the geomagnetic activities. It is very interesting to focus on these high frequency waves and to survey their relations to the activities of each planet magnetosphere. Especially, the SKR emissions have the following interesting characteristics. First, the Saturn's tilt angle is very small, but the SKR emissions tend to recur synchronizing with the Saturn rotation period. Secondly, the SKR emissions strongly depend on the solar wind pressure [*Desch and Rucker*, 1983]. Thirdly, the SKR emissions are also affected by the magnetic tail of Jupiter [*Scarf*, 1979]. These mysterious points of the SKR emissions will be resolved by the Cassini spacecraft.

As for the electrostatic waves, the broadband electrostatic noise was observed in Venus, Saturn, and Jupiter.

Figure 10.5 shows the comparison of the BEN spectra observed in Earth and Venus [*Intrigator and Scarf*, 1984]. We can see that the BEN in Venus is ten times more intense than that in the Earth. The main interest of ours is the existence of the ESW waveforms in the Venus BEN emissions. We need to wait for missions to Venus with waveform receivers. However, since the planetary plasmas in Venus directly interact with the solar wind plasmas, plasmas in the upper plasmaspheres are picked up by the solar wind. Therefore, we can expect dense ion beams in the Venus plasma tail region. From this point, we can infer the BGK mode excited by ion beam instabilities. The potential amplitudes of the BGK mode excited by ion beams should be much larger than those by electrons in order to trap ions in their potentials. Thus, the intense BEN emissions in Venus might be explained by the BGK mode related to ion dynamics. This situation is the same in Mars. Since Nozomi spacecraft has the waveform receiver, it has the possibility to detect ESW with

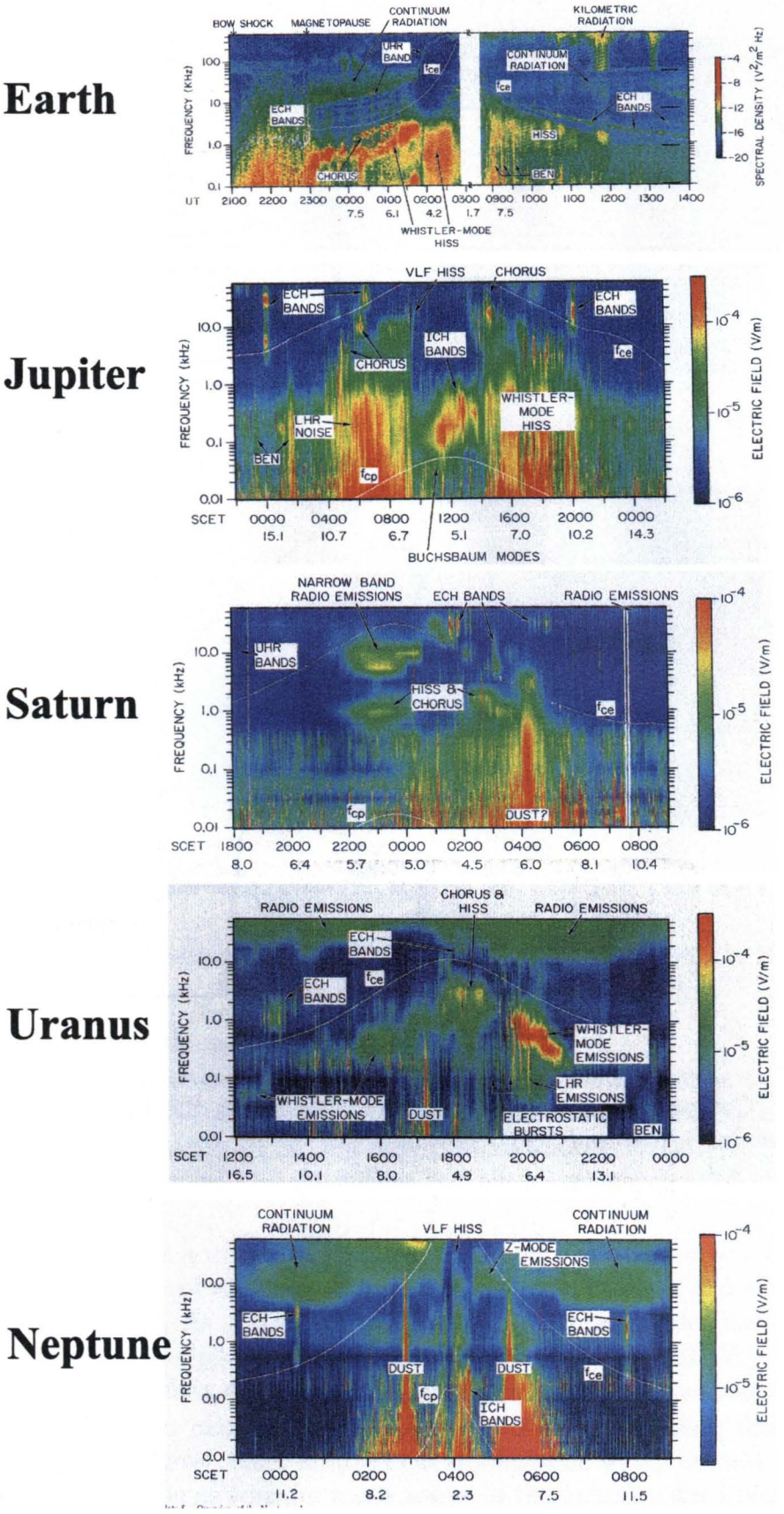

Figure 10.4: A series of frequency-time spectrograms observed by Voyager spaceprobes in each planet's magnetosphere [*after Kurth and Gurnett*, 1991].

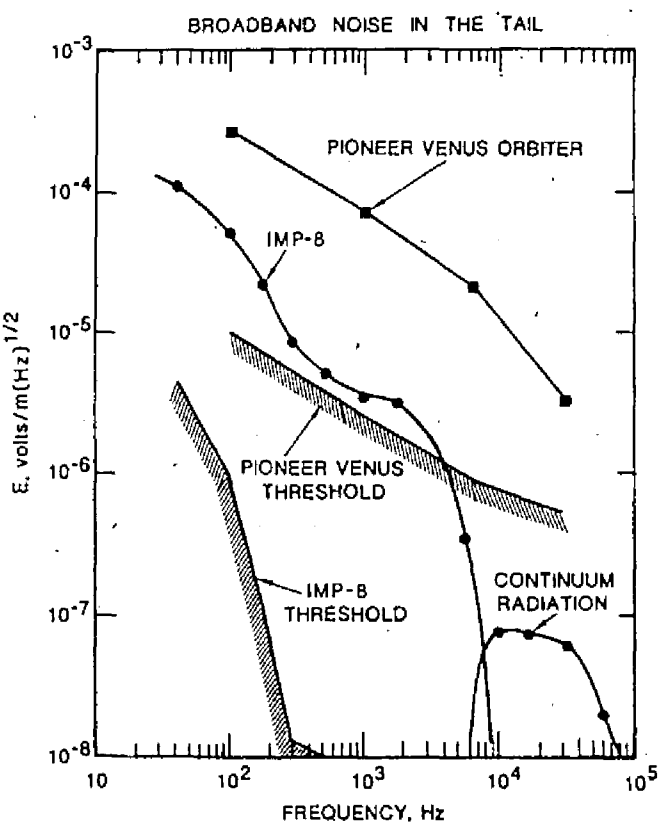

Figure 10.5: Comparison of the BEN spectra observed in the Earth and Venus magnetospheres [*after Intrigator and Scarf*, 1984].

Table 10.2: Representative waves observed by the previous planetary missions

Mechanism	Venus	Mars	Mercury	Earth	Saturn	Jupiter	Uranus	Neptune
High Energy Electrons (Polar region)	×	×	MKR	AKR, THR, AMR	SKR	DAM, HOM	UKR	NKR (?)
Mode Conversion (Magnetic equator)	×	×	Continuum radiation	Continuum radiation	Continuum radiation (Narrowband radio emissions)	Continuum radiation	Continuum radiation	Continuum radiation
Anisotropy+Beam	?	Whistler mode	Chorus/Hiss	Chorus/Hiss	Chorus/Hiss	Chorus/Hiss	Chorus/Hiss	Hiss
Lightning	Whistler burst	?	×	Whistler	?	Whistler	?	Whistler
Electron beam	Langmuir waves/ BEN	?	Langmuir waves/ BEN/NEN	Langmuir waves/ BEN	Langmuir waves/ BEN	Langmuir waves/ BEN	?	?
Ion beam (Pickup ion)	Ion acoustic waves	Ion acoustic waves	Ion acoustic waves	×	×	×	×	×

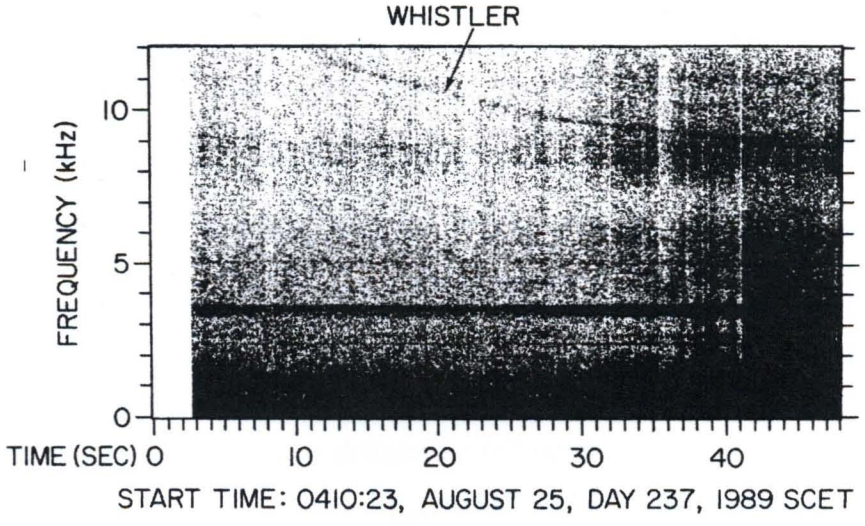

Figure 10.6: Whistler observed in Neptune [*after Gurnett et al.*, 1992].

large amplitudes excited by ion beams.

The representative waves observed by previous planetary missions except for Mercury are summarized in Table 10.2. No one has seen plasma waves in the Mercury magnetosphere, because the Mariner 10 spacecraft did not have plasma wave receivers. We list the possible plasma waves in the Mercury magnetosphere by refering to observation results in other planets.

One of the roles in plasma wave observations in planetary missions is to identify lightning discharges by observations of whistlers. Figure 10.6 shows an example of a whistler observed in Neptune by Voyager 2. As introduced in Chapter 1, such a whistler has been known to be a good signature of the lightning discharge in Earth (see Fig. 1.8). Voyager discovered whistlers excited by lightning discharge in Jupiter and Neptune atmospheres.

It is not so difficult to observe the whistlers emitted by lightning discharges in the magnetized planets. However, since emitted electromagnetic waves are not trapped in the intrinsic magnetic field line as whistler mode waves in the unmagnetized planets, we might

not see clear dispersion of whistler waves even if the lightning discharge takes place. This difficulty caused the controversy whether bursty whistler noise observed by Pioneer Venus spacecraft are connected with lightning discharges or not [*e.g., Scarf and Russell*, 1983; *Singh and Russell*, 1986; *Russell et al.*, 1989; *Taylor et al.*, 1987; *Gurnett et al.*, 1991]. We can expect the same situation in Mars.

Our planetary missions have just begun. The present thesis focused on plasma waves in the terrestrial magnetosphere, but the results can be extended to plasma waves in other planets. The important point is that observations of wave spectra alone are no longer enough in the study of plasma wave phenomena, even in planetary missions in which specifications of receivers are extremely restricted from weight and capacity of telemetry. In the present thesis, we showed that waveform observations provide us a plenty of information of plasma waves. We hope that this thesis contributes to future planetary missions.

Appendix A

Definitions of coordinate systems

The orbit and the attitude of the GEOTAIL spacecraft are defined in either the Geocentric Solar Ecliptic (GSE) or the Geocentric Solar Magnetospheric (GSM) coordinate systems. Further, in the present thesis, when we discuss our data and compare them with other instrument data in the fixed frame, we make use of the spacecraft coordinate system. In this Appendix A, we describe each coordinate system which we make use of in the present thesis.

A.1 Spacecraft coordinate system

The spacecraft coordinate system is utilized when we discuss our data and compare them with other instrument data in the fixed frame. For the case of the Geotail, since the spin axis is almost perpendicular to the ecliptic plane, data shown in the spacecraft coordinate system almost corresponds to those in the following GSE coordinate system.

The spacecraft coordinate system is defined as follows:

$$\begin{aligned} z &= \xi_{\text{spin}} \\ y &= \frac{\xi_{\text{spin}} \times \xi_{\text{sun}}}{|\xi_{\text{spin}} \times \xi_{\text{sun}}|} \\ x &= y \times z \end{aligned} \tag{A.1}$$

where ξ_{spin} and ξ_{rmsun} denote the unit vectors along the spacecraft spin axis and the direction to the Sun, respectively (see Fig. A.1 (a)).

A.2 Geocentric solar ecliptic coordinate system (GSE)

Geocentric Solar Ecliptic (GSE) coordinate system is utilized for analyzing the data obtained in the bow shock and the solar wind. The GSE is described as follows:

$$\begin{aligned} x &= \xi_{\text{sun}} \\ z &= \xi_{\text{ecliptic}} \\ y &= z \times x \end{aligned} \tag{A.2}$$

where ξ_{ecliptic} denotes the northward unit vector of along the axis perpendicular to the ecliptic plane (see Fig. A.1 (b)).

A.3 Geocentric solar magnetospheric coordinate system (GSM)

The Geocentric Solar Magnetospheric (GSM) coordinate system is mainly dedicated to discussing the phenomena observed in the magnetotail region. In the present thesis, we mainly make use of the modified GSM coordinate system, which will be introduced later. The GSM coordinate system is described as follows:

$$\begin{aligned} x &= \xi_{\text{sun}} \\ y &= \frac{\xi_{\text{dipole}} \times \xi_{\text{sun}}}{|\xi_{\text{dipole}} \times \xi_{\text{sun}}|} \\ z &= x \times y \end{aligned} \tag{A.3}$$

where ξ_{dipole} denotes the unit vector along the magnetic dipole axis of the Earth (see Fig. A.1 (c)).

A.4 Solar magnetic coordinate system (SM)

We do not make use of the Solar Magnetic (SM) coordinate system, but we describe its definition for the reference. The SM coordinate system is used for the discussions on phenomena in the inner magnetosphere. Especially, it is frequently used for analyzing the data obtained around the dayside magnetopause. The SM coordinate system is described as follows:

$$\begin{aligned} z &= \xi_{\text{dipole}} \\ y &= \frac{\xi_{\text{dipole}} \times \xi_{\text{sun}}}{|\xi_{\text{dipole}} \times \xi_{\text{sun}}|} \\ x &= y \times z. \end{aligned} \tag{A.4}$$

A.5 HVD coordinate system

We introduce the HVD coordinate system for the reference. The HVD coordinate system is used for the satellite observations in the inner magnetosphere such as the ionosphere. The HVD coordinate system is defined as follows:

$$\begin{aligned} H &= \xi_{\text{dipole}} \\ D &= \frac{\xi_{\text{dipole}} \times \xi_{\text{R}}}{|\xi_{\text{dipole}} \times \xi_{\text{R}}|} \\ V &= D \times H \end{aligned} \tag{A.5}$$

where xi_{R} denotes the unit vector from the center of the Earth toward a satellite.

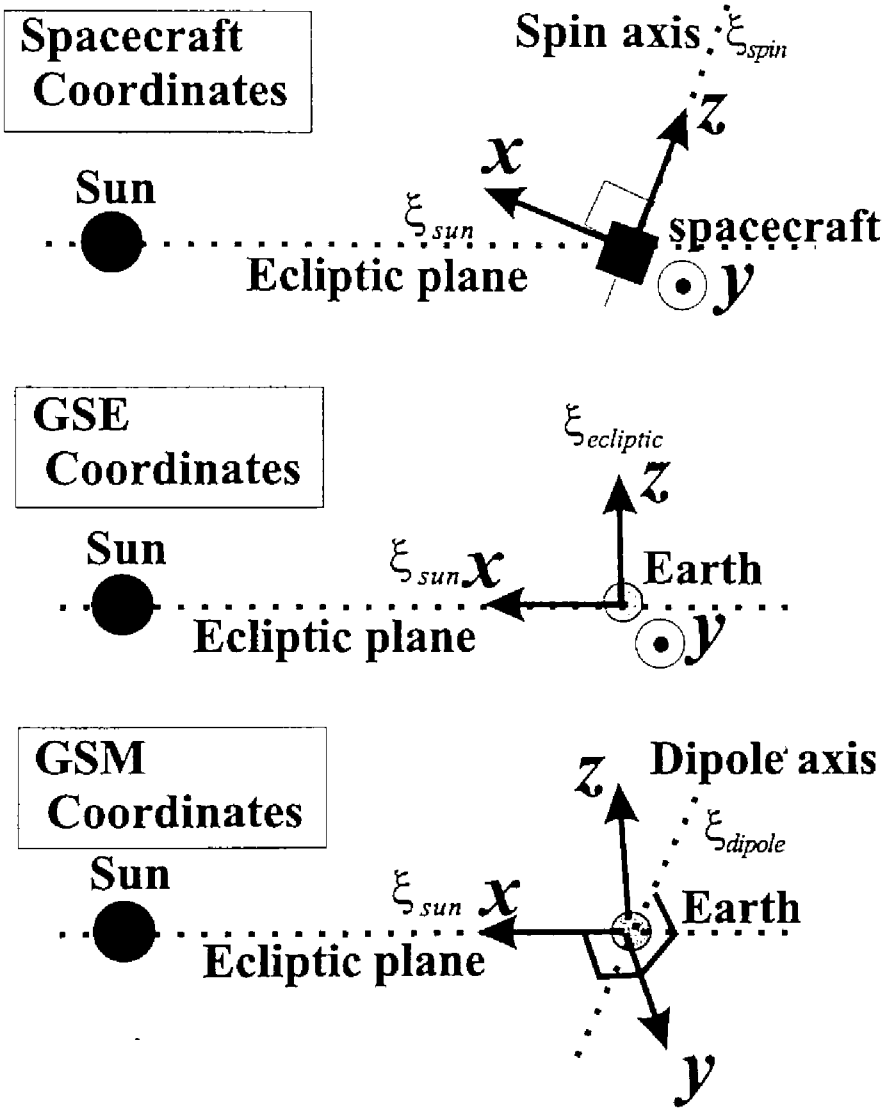

Figure A.1: Coordinate systems which we make use of in the present thesis. (a) Spacecraft coordinates, (b) GSE coordinates, and (c) GSM coordinates

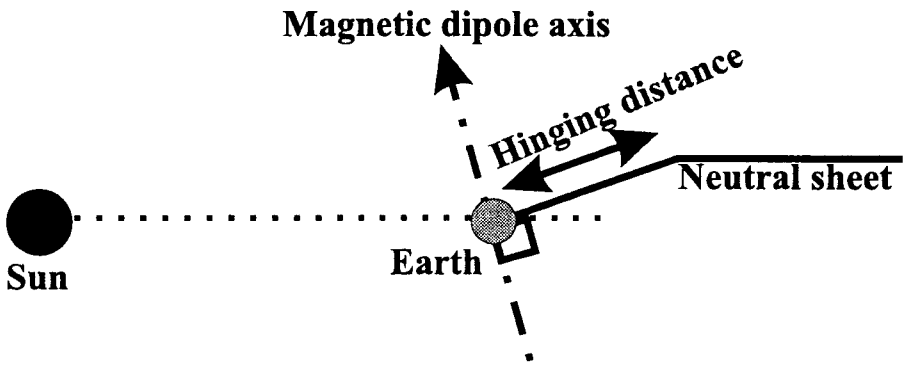

Figure A.2: Modification of the neutral sheet. We assume that the hinging distance is 10 R_E.

A.6 Modified GSM coordinate system

When we discuss the data observed in the magnetotail, we need to consider the modification of the tail axis including the aberration angle due to the effect of the revolved speed (30 km/s) of the Earth and the solar wind flow. Further, as shown in Fig. A.2, we need to consider the modification of the neutral sheet structure. The hinging distance shown in Fig. A.2 is the distance from the Earth (at midnight) at which the X-independent surface in the tail is attached to the geomagnetic equator.

We mainly use this modified GSM coordinate system in Chapter 9, because we discuss the magnetotail structure using plasma wave signatures. In the present thesis, we assume that the average solar wind aberration angle is 4° and that the hinging distance is 10 R_E [Fairfield, 1980; Yamamoto et al., 1994].

Appendix B

Acronyms

AE: Auroral Electronjet index

AKR: Auroral Kilometric Radiation

AMPTE IRM: Active Magnetospheric Particle Tracer Explorer Ion Release Module

BEN: Broadband Electrostatic Noise

BGK mode: Bernstein-Greene-Kruskal mode

CAL mode: CALibration mode

CE: Conducted Emission EMC

CIR: Corotating Interaction Regions

CME: Coronal Mass Ejection

CPI: Comprehensive Plasma Instrument

CPS: Central Plasma Sheet

CR: Continuum Radiation

CS: Conducted Susceptibility EMC

DHU: Data Handling Unit

DSN: Deep Space Network

ECH: Electron Cyclotron Harmonics

EFD: Electric FielD Experiment

EMC: ElectroMagnetic Compatibility

ESA: European Space Angency

ESW: Electrostatic Solitary Waves

EQMW: Electrostatic Quasi-Monochromatic Waves

FAST: The Fast Auroral SnapshoT (FAST) small-class explorer

FEM: Finite Element analysis Method

FFT: Fast Fourier Transform

FXI: Inboard FluXgate magnetometer

FXO: Outboard FluXgate magnetometer

GEOS: Goddard Earth Observing System

GPIB: General Purpose Interface Bus

GSE: Geocentric Solar Ecliptic coordinates

GSE: Ground Support Equipment

GSM: Geocentric Solar Magnetospheric coordinates

GTL: Geomagnetic Tail Laboratory

IMF: Interplanetary Magnetic Field

IMP: Interplanetary Monitoring Platform

IMP mode: IMPedance measurement mode

IP shock: InterPlanetary shock

ISAS: Institute of Space and Astronautical Science

ISEE: International Sun-Earth Explorer

ISTP: International Solar Terrestrial Physics

K-H instability: Kelvin-Helmholtz instability

LEP: Low Energy Particle experiment

LFA: Low Frequency Analyzer

LHR: Lower Hybrid Resonance

LLBL: Low Latitude Boundary Layer

MS: MagnetoSheath

MP: MagnetoPause

MST-F: MaST for Fluxgate magnetometers

MST-S: MaST for Search coils

MCA: Multi-Channel Analyzer

MGF: MaGnetic Field measurement

MLT: Magnetic Local Time

MNB: Magnetic Noise Bursts

NASA: National Aeronautics and Space Administration

NEN: Narrowband Electrostatic Noise

NENL: Near Earth Neutral Line

NS: Neutral Sheet

OGO: Orbiting Geophysical Observatories

PANT: Probe ANTenna

PCD: Power Converter and Distributor

PIM: Peripheral Interface Module

PSBL: Plasma Sheet Boundary Layer

PWI: Plasma Wave Instrument

RASC: Radio Atmospheric Science Center

RE: Radiated Emission EMC

RS: Radiated Susceptibility EMC

SAS: Sun Aspect Sensor

SC: Search Coils

SCATHA: Spacecraft Charging at High Altitude

SFA: Sweep Frequency Analyzer

SM: Solar Magnetic coordinates

SOHO: SOlar and Heliospheric Observatory

SW: Solitary Waves

TKR: Terrestrial Kilometric Radiation

TP emission: Totem Pole emission

UDSC: Usuda Deep Space Center

UHR: Upper Hybrid Resonance

WANT: Wire ANTenna

WDL: Weak Double Layer

WFC: Wave-Form Capture

References

[1] Akimoto, K. and N. Omidi, The generation of broadband electrostatic noise by an ion beam in the magnetotail, *Geophys. Res. Lett.*, *13*, 97-100, 1986.

[2] Anderson, R. R., C. C. Harvey, M. M. Hoppe, B. T. Tsurutani, T. E. Eastman, and J. Etcheto, Plasma waves near the magnetopause, *J. Geophys. Res.*, *87*, 2087-2107, 1982.

[3] Ashour-Abdalla, M., C. F. Kennel, and W. Liversey, A parametric study of electron multiharmonic instabilities in the magnetosphere, *J. Geophys. Res.*, *84*, 6540-6546, 1979.

[4] Ashour-Abdalla, M., and H. Okuda, Electron acoustic instabilities in the geomagnetic tail, *Geophys. Res. Lett.*, *13*, 366-369, 1986a.

[5] Ashour-Abdalla, M. and H. Okuda, Theory and simulations of broadband electrostatic noise in the geomagnetic tail, *J. Geophys. Res.*, *91*, 6833-6844, 1986b.

[6] Ashour-Abdalla, M., R. L. Richard, and F. V. Coroniti, A simulation study of electron hole distributions, *Geophys. Res. Lett.*, *16*, 1137-1140, 1989.

[7] Aso, T., Radio frequency impedance probe and its application to ionospheric probing, PhD thesis, Dept. of Electr. Eng., Kyoto University, 1974.

[8] Baker, D. N., S. J. Bame, J. Birn, W. C. Feldman, J. T. Gosling, E. W. Hones, Jr., R. D. Zwickl, J. A. Slavin, E. J. Smith, B. T. Tsurutani, and D. G. Sibeck, *Geophys. Res. Lett.*, *10*, 1042-1045, 1984.

[9] Balmain, M., The impedance of a short dipole antenna, *IEEE. Trans. Antennas Propag.*, *AP-12*, 605-619, 1964.

[10] Bame, S. J., J. R. Asbridge, H. E. Felthauser, E. W. Jr. Hones, and I. B. Strong, Characteristics of the plasma sheet in the Earth's magnetotail, *J. Geophys. Res.*, *72*, 113-129, 1967.

[11] Barrington, R. E., and J. S. Belrose, Preliminary results from the VLF receiver aboard Canada's Alouette satellite, *Goddard Space Flight Center Publ. X-615-63-36*, 1963.

[12] Belmont, G., D. Fontaine, and P. Canu, Are equatorial electron cyclotron waves responsible for diffuse auroral precipitation ?, *J. Geophys. Res.*, *88*, 9163-9170, 1983.

[13] Berchem, J. P., D. Schriver, and M. Ashour-Abdalla, Simultaneous excitation of broadband electrostatic noise and electron cyclotron waves in the plasma sheet, *Geophys. Res. Lett.*, *18*, 729-732, 1991.

[14] Bernstein, I. B., J. M. Greene, and M. D. Kruskal, *Phys. Rev.*, *108*, 546-550, 1957.

[15] Boström, R., G. Gustafsson, B. Holback, G. Holmgren, and H. Koskinen, and P. Kintner, Characteristics of solitary waves and weak double layers inthe magnetospheric plasma, *Phys. Rev. Lett.*, *61*, 82-85, 1988.

[16] Brown. L. W, The galactic radio spectrum between 130kHz and 2600kHz, *Astrophys. J.*, *180*, 359, 1973.

[17] Burinskaya, T. M. and C. -V. Meister, Contribution of the ion-beam acoustic instability to the generation of broadband electrostatic noise in the earth's magnetotail, *Planet. Space Sci.*, *37*, 145-150, 1989.

[18] Burinskaya, T. M. and C. -V. Meister, Contribution of the ion-beam acoustic instability to the generation of broadband electrostatic noise -Three dimensional quasilinear approach-, *Planet. Space Sci.*, *38*, 695-700, 1990

[19] Cain, J. C., I. R. Shapiro, J. D. Stolarik, and J. P. Heppner, A note on whistlers observed above the ionosphere, *J. Geophys. Res.*, *66*, 2677-2680, 1961.

[20] Calvert, W., The auroral plasma cavity, *Geophys. Res. Lett.*, *8*, 919-922, 1981.

[21] Chapman, S. and V. C. A. Ferraro, A new theory of magnetic storms, *Terr. Magn. Atmos. Electr.*, *36*, 77-97, 1931.

[22] Coroniti, F. V., and M. Ashour-Abdalla, Electron velocity space hole modes, and narrowband electrostatic noise in the distant tail, *Geophys. Res. Lett.*, *16*, 747-750, 1989.

[23] Coroniti, F. V., E. W. Greenstadt, B. T. Tsurutani, E. J. Smith, R. D. Zwickl, and J. T. Gosling, Plasma waves in the distant geomagnetic tail: ISEE 3, *J. Geophys. Res.*, *95*, 20977-20995, 1990.

[24] Coroniti, F. V., M. Ashour-Abdalla, and R. L. Richard, Electron velocity space hole modes, *J. Geophys. Res.*, *98*, 11349-11358, 1993.

[25] Coroniti, F. V., E. W. Greenstadt, S. L. Moses, B. T. Tsurutani, and E. J. Smith, On the absence of plasma wave emissions and the magnetic field orientation in the distant magnetosheath, *Geophys. Res. Lett.*, *21*, 2761-2764, 1994.

[26] Cowley, S. W. H., On the distribution of B_y in the geomagnetic tail, *Planet. Space Sci.*, *27*, 769-793 1979.

[27] Cowley, S. W. H., Magnetospheric asymmetries associated with the Y-component of the IMF, *Planet. Space Sci.*, *29*, 79-96 1981.

[28] Cowley, S. W. H., R. J. Hynds, I. G. R. Richardson, P. W. Daly, T. R. Sanderson, K.-P. Wenzel, J. A. Slavin, and B. T. Tsurutani, Energetic ion regions in the deep geomagnetic tail: ISEE-3, *Geophys. Res. Lett.*, *11*, 275-278, 1984.

[29] Desch, M. D., and H. O. Rucker, The relationship between Saturnian kilometric radiation and the solar wind, *J. Geophys. Res.*, *88*, 8999-9006, 1983.

[30] Dovner, P. O., A. I. Eriksson, R. Boström, and B. Holback, Freja multiprobe observations of electrostatic solitary structures, *Geophys. Res. Lett.*, *21*, 1827-1830, 1994.

[31] Dubouloz, N., R. Pottelette, M. Malingre, and R. A. Treumann, Generation of broadband electrostatic noise by electron acoustic solitons, *Geophys. Res. Lett.*, *18*, 155-158, 1991a.

[32] Dubouloz, N., R. Pottelette, M. Malingre, G. Holmgren, and P. A. Lindqvist, Detailed analysis of broadband electrostatic noise in the dayside auroral zone, *J. Geophys. Res.*, *96*, 3565-3579, 1991b.

[33] Dunckel, N., B. Ficklin, L. Rorden, and R. A. Helliwell, Low-frequency noise observed in the distant magnetosphere with Ogo 1, *J. Geophys. Res.*, *75*, 1854-1862, 1970.

[34] Dungey, J. W., Interplanetary magnetic field and the auroral zones, *Phys. Res. Lett.*, *6*, 47-48, 1961.

[35] Dupree, T. H., Theory of phase-space density holes, *Phys Fluids*, *25*, 277-289, 1982.

[36] Dusenbery, P. B. and L. R. Lyons, The generation of electrostatic noise in the plasma sheet boundary layer, *J. Geophys. Res.*, *90*, 10935-10943, 1985.

[37] Dusenbery, P. B., Generation of broadband noise in the magnetotail by the beam acoustic instability, *J. Geophys. Res.*, *91*, 12005-12016, 1986.

[38] Ejiri, M., H. Oya, and T. Obayashi, A modified plasma resonance observed with a rocket-borne gyro-plasma probe, *Rep. Ions. Space Res. Jpn.*, *22*, 201-203, 1968.

[39] Ergun, R. E., C. W. Carlson, J. P. McFadden, F. S. Mozer, G. T. Delory, W. Peria, C. C. Chaston, M. Temerin, I. Roth, L. Muschietti, R. Elphic, R. Strangeway, R. Pfaff, C. A. Cattell, D. Klumpar, E. Shelley, W. Peterson, E. Moebius, and L. Kistler, FAST satellite observations of large-amplitude solitary structures, *Geophys. Res. Lett.*, *25*, 2041-2044, 1998.

[40] Fairfield, D. H., A statistical determination of the shaper and position of the geomagnetic neutral sheet, *J. Geophys. Res.*, *85*, 775-780, 1980.

[41] Frandsen, A. M. A., R. E. Holzer, and E. J. Smith, OGO search coil magnetometer experiment, *IEEE Trans. Geosci. Electr.*, *GE-6*, 61, 1969.

[42] Frank, L. A., K. L. Ackerson, W. R. Paterson, J. A. Lee, M. R. English, and G. L. Pickett, The comprehensive plasma instrumentation (CPI) for the Geotail spacecraft, *J. Geomag Geoelectr*, *46*, 23-37, 1994.

[43] Franz, J. R., P. M. Kintner, J. S. Pickett, POLAR observations of coherent electric field structures, *Geophys. Res. Lett.*, *25*, 1277-1280, 1998.

[44] Fredricks, R. W., and F. L. Scarf, Recent studies of magnetospheric electric field emissions above the electron gyrofrequency, *J. Geophys. Res.*, *78*, 310-314, 1973.

[45] Fujimoto, M., T. Mukai, H. Kawano, M. Nakamura, A. Nishida, Y. Saito, T. Yamamoto, and S. Kokubun, A Geotail observation of low-latitude boundary layer, *Adv. Space Res.*, *20*, 813-822, 1997.

[46] Fujimoto, M., T. Terasawa, T. Mukai, Y. Saito, T. Yamamoto, and S. Kokubun, Plasma entry from the flanks of the near-Earth magnetotail: Geotail observations, *J. Geophys. Res.*, *103*, 4391-4408, 1998.

[47] Gallagher, D. L. and D. A. Gurnett, Auroral kilometric radiation: Time-averaged source location, *J. Geophys. Res.*, *84*, 6501-6509, 1979.

[48] Gosling, J. T., E. Hilder, R. M. MacQueen, R. H. Munro, A. I. Poland, and C. L. Ross, Mass ejections from the Sun, A view from Skylab, *J. Geophys. Res.*, *79*, 4581-4587, 1974.

[49] Gosling, J., T., A. J. Hundhausen, and S. J. Bame, Solar wind stream evolution at large heliospheric distances: Experimental demonstration and the test of a model, *J. Geophys. Res.*, *81*, 2111-2122, 1976.

[50] Gosling, J. T., Coronal mass ejections and magnetic flux ropes in interplanetary space, in *Physics of Magnetic Flux Ropes, Geophys. Monogr. 58*, edited by C. T. Russell, E. R. Priest, and L. C. Lee, AGU, Washington D.C., 343, 1990.

[51] Grabbe, C. L., and T. E. Eastman, Generation of broadband electrostatic noise by ion beam instabilities in the magnetotail, *J. Geophys. Res.*, *89*, 3865-3872, 1984.

[52] Grabbe, C. L., New results on the generation of broadband electrostatic waves in the magnetotail, *Geophys. Res. Lett.*, *12*, 483-486, 1985.

[53] Grabbe, C. L., Numerical study of the spectrum of broadband electrostatic noise in the magnetotail, *J. Geophys. Res.*, *92*, 1185-1192, 1987.

[54] Grabbe, C. L., Wave propagation effects of broadband electrostatic noise in the magnetotail, *J. Geophys. Res.*, *94*, 17299-17304, 1989.

[55] Green, J. L., D. A. Gurnett and S. D. Shawhan, The angular distribution of auroral kilometric radiation, *J. Geophys. Res.*, *82*, 1825-1838, 1977.

[56] Gurnett, D. A., and B. J. O'Brien, High-latitude geophysical studies with satellite Injun 3, *J. Geophys. Res.*, *69*, 65-89, 1964.

[57] Gurnett, D. A., and R. R. Shaw, Electromagnetic radiation trapped in the magnetosphere above the plasma frequency, *J. Geophys. Res.*, *78*, 8136-8149, 1973.

[58] Gurnett, D. A., The Earth as a radio source: Terrestrial kilometric radiation, *J. Geophys. Res.*, *79*, 4227-4238, 1974.

[59] Gurnett, D. A., The earth as a radio source: The nonthermal continuum, *J. Geophys. Res.*, *80*, 2751-2763, 1975.

[60] Gurnett, D. A. and L. A. Frank, Electron plasma oscillations associated with type III radio emissions and solar electrons, *Solar Physics*, *45*, 477-493, 1975.

[61] Gurnett, D. A., L. A. Frank, and R. P. Lepping, Plasma waves in the distant magnetotail, *J. Geophys. Res.*, *81*, 6059-6071, 1976.

[62] Gurnett, D. A., and L. A. Frank, Plasma waves in the polar cusp: Observations from Hawkeye 1, *J. Geophys. Res.*, *82*, 1447-1462, 1978.

[63] Gurnett, D. A., F. M. Neubauer, and R. Schwenn, Plasma wave turblence associated with an interplanetary shock, *J. Geophys. Res.*, *84*, 541-552, 1979.

[64] Gurnett, D. A., J. E. Maggs, D. L. Gallagher, W. S. Kurth, and F. L. Scarf, Parametric interaction and spatial collapse of beam-driven Langmuir waves in the solar wind, *J. Geophys. Res.*, *86*, 8833-8841, 1981.

[65] Gurnett, D. A., Plasma waves and instabilities, in *Collisionless shocks, Geophysical Monograph 35,* ed. by B. T. Tsurutani and R. G. Stone, 207-224, 1985.

[66] Gurnett, D. A., W. S. Kurth, A. Roux, E. Gendrin, C. F. Kennel, and S. J. Bolton, Lightning and plasma wave observations from the Galileo flyby of Venus, *Science*, *253*, 1522-1525, 1991.

[67] Gurnett, D. A., W. S. Kurth, L. J. Granroth, I. H. Cairns, W. M. Macek, R. L. Poynter, S. L. Moses, F. V. Coroniti, C. F. Kennel, adn D. D. Barbosa, Plasma wave observations at Neptune, *Adv. Space Res.*, *12*, 47-54, 1992.

[68] Gurnett, D. A., G. B. Hospodarsky, W. S. Kurth, D. J. Williams, and S. J. Bolton, Fine structure of Langmuir waves produced by a solar electron event, *J. Geophys. Res.*, *98*, 5631-5637, 1993.

[69] Gurnett, D. A., W. S. Kurth, A. Roux, S. J. Bolton, and C. F. Kennel, Evidence for a magnetosphere at Ganymede from plasma wave observations by the Galileo spacecraft, *Nature*, *384*, 535-537, 1996.

[70] Hammond, C. M., G. K. Crawford, J. T. Gosling, **H. Kojima**, J. L. Phillips, H. Matsumoto, A. Balogh, L. A. Frank, S. Kokubun and T. Yamamoto, Latitudinal structure of a coronal mass ejection iferred from Ulysses and Geotail observations, *Geophys. Res. Lett.*, *22*, 1169-1172, 1995.

[71] Hashimoto, K., H. Matsumoto, **H. Kojima**, T. Murata, I. Nagano, T. Okada, K. Tsuruda, and T. Iyemori, Auroral myriametric radiation observed by Geotail, *Geophys. Res. Lett.*, *21*, 2927-2930, 1994.

[72] Hashimoto, K., S. Kudo, and H. Matsumoto, Source of auroral myriametric radiation observed with Geotail, *J. Geophys. Res., in print*, 1998.

[73] Hones, E. W. Jr., Substorm processes in the magnetotail: Comments on 'On hot tenuous plasmas, fireballs, and boundary layers in the Earth's magnetotail' by L. A. Frank, K. L. Ackerson, and R. P. Lepping, *J. Geophys. Res.*, *35*, 5633-5640, 1977.

[74] Hospodarsky, G. B., D. A. Gurnett, W. S. Kurth, M. G. Kivelson, R. J. Strangeway, and S. J. Bolton, Fine structure of Langmuir waves observed upstream of the bow shock at Venus, *J. Geophys. Res.*, *99*, 13363-13371, 1994.

[75] Hubbard, R. F. and T. J. Birmingham, Electrostatic emissions between electron gyroharmonics in the outer magnetosphere, *J. Geophys. Res.*, *83*, 4837-4850, 1978.

[76] Hudson, M. K., W. Lotko, I. Roth, and E. Witt, Solitary waves and double layers on auroral field lines, *J. Geophys. Res.*, *88*, 916-926, 1983.

[77] Hwang, K. S., N. H. Stone, K. H. Wright, Jr., and U. Samir, The emissions of broadband electrostatic noise in the near vicinity of the shuttle orbiter, *Planet. Space Sci.*, *35*, 1373-1379, 1987.

[78] Intrigator, D. S., and F. L. Scarf, Wave-particle interactions in the Venus wake and tail, *J. Geophys. Res.*, *89*, 47-55, 1984.

[79] Jones, D., Beaming of terrestrial myriametric radiation, *Adv. Space. Res.*, *1*, 373, 1981a.

[80] Jones, D., First remote sensing of the plasmapause by terrestrial myriametric radiation, *Nature*, *294*, 728, 1981b.

[81] Jones, D., Terrestrial myriametric radiation from the earth's plasmapause, *Planet. Space. Sci.*, *30*, 399-410, 1982.

[82] Jones, D., Latitudinal beaming of planetary radio emissions, *Nature*, *288*, 225-229, 1990.

[83] Kaiser, M. L., Observations of non-termal radiation from planets, *Plasma waves and instabilities at comets and in magnetosphere, edited by B. Tsurutaniand H. Oya, Geophysical Monograph, AGU, Washignton*, 221-237, 1989.

[84] Kasaba, Y., **H. Kojima**, H. Matsumoto, and T. Murata, Search for Hectometric and Kilometric radiation from Jupiter by GEOTAIL spacecraft during the impact of Comet Shoemaker-Levy 9, *J. Geomag Geoelectr*, *48*, 361-370, 1996.

[85] Kasaba, Y., H. Matsumoto, and R. R. Anderson, Geotail observation of $2f_p$ emission around the terrestrial electron foreshock, *Adv. Space Res.*, *20*, 699-702, 1997.

[86] Kellog, P. J., S. J. Monson, K. Goetz, R. L. Howard, J.-L. Bougeret, and M. L. Kaiser, *Geophys. Res. Lett.*, *23*, 1243-1246, 1996.

[87] Kennel, C. F., F. V. Scarf, R. W. Fredricks, J. H. Mcgehee, and F. V. Coroniti, VLF electric field observations in the magnetosphere, *J. Geophys. Res.*, *75*, 6136-6152, 1970.

[88] Kennel, C. F., F. L. Scarf, F. V. Coroniti, E. J. Smith, and D. A. Gurnett, Nonlocal plasma turbulence associated with interplanetary shocks, *J. Geophys. Res.*, *87*, 17-34, 1982.

[89] Kennel, C. F., and M. Ashour-Abdalla, Electrostatic waves and the strong diffusion of magnetospheric electrons, in *Magnetospheric Plasma Physics, edited by A. Nishida, pp.245, Center for Academic Publications*, Tokyo, Japan, 1982.

[90] King, J. H., Additional spacecraft data sources contributing to the ISTP program, *Adv. Space Res.*, *20*, 595-608, 1997.

[91] Kivelson, M. G., K. K. Khurana, C. T. Russell, R. J. Walker, J. Warnecke, F. V. Coroniti, C. Polanskey, D. J. Southwood, and G. Schulbert, Discovery of Ganymede's magnetic field by the Galileo spacecraft, *Science*, *384*, 537-541, 1996.

[92] Kokubun, S., T. Yamamoto, M. H. Acuña, K. Hayashi, K. Shiokawa, and H. Kawano, The Geotail magnetic field experiment, *J. Geomag Geoelectr*, *46*, 7-21, 1994.

[93] **Kojima, H.**, H. Matsumoto, Y. Omura, and B. T. Tsurutani, Nonlinear evolution of high frequency R-mode waves excited by water group ions near comets: computer experiments, *Geophys. Res. Lett.*, *16*, 9-12, 1989.

[94] **Kojima, H.**, H. Matsumoto, T. Miyatake, I. Nagano, A. Fujita, L. A. Frank, T. Mukai, W. R. Paterson, Y. Saito, S. Machida, and R. R. Anderson, Relation between electrostatic solitary waves and hot plasma flow in the plasma sheet boundary layer: GEOTAIL Observations, *Geophys. Res. Lett.*, *21*, 2919-2922, 1994.

[95] **Kojima, H.**, H. Matsumoto, S. Chikuba, S. Horiyama, M. Ashour-Abdalla and R. R. Anderson, GEOTAIL waveform observations of broadband/narrowband electrostatic noise in the distant tail, *J. Geophys. Res.*, *102*, 14439-14455, 1997a.

[96] **Kojima, H.**, H. Furuya, H. Usui, and H. Matsumoto, Modulated electron plasma waves observed in the tail lobe: GEOTAIL waveform observations, *Geophys. Res. Lett.*, *24*, 3049-3052, 1997b.

[97] Koons, H. C., and J. F. Fennell, Fine structure in electrostatic emission bands between electron gyrofrequency harmonics, *J. Geophys. Res.*, *89*, 3015-3018, 1984.

[98] Koskinen, H. E. J., R. Boström, and B. Holback, Viking observations of solitary waves and weak double layers on auroral field lines, *Phys. of Space Plasmas, SPI conference proceedings and reprints series*, *7*, 147-156, 1987.

[99] Kosikinen H. E. J., R. Lundin, and B. Holback, On the plasma environment of solitary waves and weak double layers, *J. Geophys. Res.*, *95*, 5921-5929, 1990.

[100] Kurth, W. S., and D. A. Gurnett, Plasma waves in planetary magnetospheres, *J. Geophys. Res.*, *96*, 18977-18991, 1991.

[101] Kurth, W. S., D. A. Gurnett, A. Roux, and J. Bolton, Ganymede: A new radio source, *Geophys. Res. Lett.*, *24*, 2167-2170, 1997.

[102] Lacombe, C., C. C. Harvey, S. Hoang, A. Mangeney, J.-L. Steinberg, and D. Burgess, ISEE observations of emission at twice the solar wind plasma frequency, *Ann Geophys.*, *6*, 113, 1988.

[103] Leiphart, J. P., Penetration of the ionosphere by very-low-frequency radio signals-interim results of the Lofti 1 experiment, *Proc. IRE, 50*, 6, 1962.

[104] Lotko, W., and C. F. Kennel, Spiky ion acousitc waves in collisionless auroral plasma, *J. Geophys. Res.*, *88*, 381-394, 1983.

[105] Lui, T. Y., Road map to magnetotail domains, *Magnetotail physics, edited by A. T. Lui, The Johns Hopkins University Press, Baltimore and London*, 1987.

[106] Lyons, L. R., Electron diffusion driven by magnetospheric electrostati waves, *J. Geophys. Res.*, *79*, 575-580, 1974.

[107] Machida, S., T. Mukai, Y. Saito, T. Obara, T. Yamamoto, A. Nishida, M. Hirahara, T. Terasawa, and S. Kokubun, GEOTAIL low energy particle and magnetic field observations of a plasmoid at X_{GSM}=$-142R_E$, *Geophys. Res. Lett.*, *21*, 2995-2998, 1994.

[108] Maczawa, K., T. Hori, T. Mukai, Y. Saito, T. Yamamoto, S. Kokubun, and A. Nishida, Structure of the distant magnetotail and its dependence on the IMF B_y component: Geotail observations, *Adv. Space Res.*, *20*, 949-959, 1997.

[109] Mälkki, H. Koskinen, R. Boström, and B. Holback, On theories attempting to explain observations of solitary waves and weak double layers in the auroral magnetosphere, *Physica Scripta*, *39*, 787-793, 1989.

[110] Mälkki, A., A. I. Eriksson, P.-O. Dovner, R. Boström, B. Holback, G. Holmgren, and H. E. J. Koskinen, A statistical survey of auroral solitary waves and weak double layers 1. Occurence and net volatage, *J. Geophys. Res.*, *98*, 15521-15530, 1993.

[111] Mälkki, A., and R. Lundin, Altitude distributions of upward flowing ion beams and solitary structures in the Viking data, *Geophys. Res. Lett.*, *21*, 2243-2246, 1994.

[112] Marchenko, V. A., and M. K. Hudson, Beam-driven acoustic solitary waves in the airoral acceleration region, *J. Geophys. Res.*, *100*, 19791-19803, 1995.

[113] Matsumoto H., and Y. Omura, Particle simulations of electromagnetic waves and their applications to space plasmas, *Computer Simulations of Space Plasmas, ed. by H. Matsumoto and T. Sato, Terra Sci. Pub. and Reidel Co.*, 43-102, 1985.

[114] Matsumoto, H., I. Nagano, R. R. Anderson, **H. Kojima**, K. Hashimoto, M. Tsutsui, T. Okada, I. Kimura, Y. Omura and M. Okada, Plasma wave observations with Geotail spacecraft, *J. Geomag Geoelectr*, *46*, 59-95, 1994a.

[115] Matsumoto, H., **H. Kojima**, T. Miyatake, Y. Omura, M. Okada, I. Nagano, and M. Tsutsui, Electrostatic Solitary Waves (ESW) in the Magnetotail: BEN Wave forms observed by GEOTAIL, *Geophys. Res. Lett.*, *21*, 2915-2918, 1994b.

[116] Matsumoto, H. and H. Usui, Intense bursts of electron cyclotron harmonic waves observed at the dayside magnetopause with GEOTAIL spacecraft, *Geophys. Res. Lett.*, *24*, 49-52, 1997a.

[117] Matsumoto, H., **H. Kojima**, Y. Kasaba, T. Miyake, R. R. Anderson and T. Mukai, Plasma waves in the upstream and bow shock regions observed by GEOTAIL, *Advanced Space Research*, *20*, 683-693, 1997b.

[118] Matsumoto H., **H. Kojima**, Y. Omura, and I. Nagano, Plasma waves in geospace: Geotail observations, *New perspectives on the Earth's magnetotail , edited by A. Nishida, D. N. Baker, and S. W. H. Cowley, Agu Monograph, in print*, 1998.

[119] Matsumoto, H., L. A. Frank, Y. Omura, **H. Kojima**, W. R. Paterson, M. Tsutsui, R. R. Anderson, S. Horiyama, S. Kokubun, and T. Yamamoto, Generation Mechanism of ESW based on GEOTAIL Plasma Wave Observation, Plasma Observation and Particle Simulation, *Submitted to Geophys. Res. Lett.*, 1998.

[120] McPherron, R. L., Physical processes producting magnetospheric substorms and magnetic storms, *Geomagnetism Volume 4, edited by J. A. Jacobs, Academic Press, New York*, 1991.

[121] Meng, C.-I., and K. A. Anderson, Magnetic field configuration in the magnetotail near 60 R_E, *J. Geophys. Res.*, *79*, 5143-5153, 1974.

[122] Miyake, T., Y. Omura, H. Matsumoto, and **H. Kojima**, Two-dimensional computer simulations of electrostatic solitary waves observed by Geotail spacecraft, *J. Geophys. Res.*, *103*, 11841-11850, 1998.

[123] Mottez, F., S. Perraut, A. Roux, and P. Louarn, Coherent structures in the magnetotail triggered by counterstreaming electron beams, *J. Geophys. Res.*, *102*, 11399-11408, 1997.

[124] Mozer, F. S., The need for high time resolution measurements in the magnetosphere, *Magnetospheric physics, edited by B. Hultqvist, and C.-G. Falthammer, Plenum Press, New York*, 1990.

[125] Mozer, F. S., R. Ergun, M. Temerin, C. Cattell, J. Dombeck, and J. Wygant, New features of time domain electric-field structures in the auroral acceleration region, *Phys. Rev. Lett.*, *79*, 1281-1284, 1997.

[126] Mukai, T., S. Machida, Y. Saito, M. Hirahara, T. Terasawa, N. Kaya, T. Obara, M. Ejiri, and A. Nishida, The low energy particle (LEP) experiment onboard the Geotail satellite, *J. Geomag Geoelectr*, *46*, 669-692, 1994.

[127] Mukai, T., M. Fujimoto, M. Hoashino, S. Kokubun, S. Machida, K. Maezawa, A. Nishida, Y. Saito, T. Terasawa, and T. Yamamoto, *J. Geomag Geoelectr*, *48*, 541-560, 1996.

[128] Murata, T., H. Matsumoto, **H. Kojima**, A. Fujita, T. Nagai, T. Yamamoto, and R. R. Anderson, Estimation of tail reconnection lines by AKR onsets and plasmoid entries observed with Geotail spacecraft, *Geophys. Res. Lett.*, *22*, 1849-1852, 1995a.

[129] Murata, T., Study of Magnetotail dynamics via Computer Experiments and Spacecraft Observations, Ph. D. Thesis (supervised by H. Matsumoto), Kyoto University, 1995b.

[130] Murata, T., H. Matsumoto, **H. Kojima** and T. Iyemori, Correlations of AKR index with Kp and Dst indices, *Proceedings of the NIPR Symposium on Upper Atomosphere Physics*, *10*, 64-68, 1997.

[131] Nagai, T., R. Nakamura, T. Mukai, T. Yamamoto, A. Nishida, and S. Kokubun, Substorms, tail flows and plasmoids, *Adv. Space Res.*, *20*, 961-971, 1997.

[132] Nagai, T., M. Fujimoto, Y. Saito, S. Machida, T. Terasawa, R. Nakamura, T. Yamamoto, T. Mukai, A. Nishida, and S. Kokubun, Structure and dynamics of magnetic reconnection for substorm onsets with Geotail observations, *J. Geophys. Res.*, *103*, 4419-4440, 1998.

[133] Nagano, I., S. Yagitani, **H. Kojima**, Y. Kakehi, T. Shiozaki, H. Matsumoto, K. Hashimoto, T. Okada, S. Kokubun, and T. Yamamoto, Wave form analysis of the continuum radiation observed by GEOTAIL, *Geophys. Res. Lett.*, *21*, 2911-2914, 1994.

[134] Nagano, I., S. Yagitani, **H. Kojima**, and H. Matsumoto, Analysis of wave normal and poynting vector of the chorus emissions observed by Geotail, *J. Geomag Geoelectr*, *48*, 299-307, 1996.

[135] Nagano, I., X.-Y. Wu, S. Yagitani, K. Miyamura, and H. Matsumoto, Unusual whistler with very large dispersion near the magnetopause: Geotail observation and ray-tracing modeling, *J. Geophys. Res.*, *103*, 11827-11840, 1998.

[136] Nakamura, M., M. Fujimoto, H. Kawano, T. Mukai, Y. Saito, T. Yamamoto, K. Tsuruda, T. Terasawa, and S. Kokubun, Geotail observation at the dayside magnetopause –Confirmation of reconnection events, *Adv. Space Res.*, *20*, 779-788, 1997.

[137] Ness, N. F., The Earth's magnetic tail, *J. Geophys. Res.*, *70*, 2989-3005, 1965.

[138] Ness N. F., K. W. Behannon, R. P. Lepping, Y. C. Ehang, and K. H. Schatten, Magnetic field observations near Mercury: Preliminary results from Mariner 10, *Science*, *185*, 151-159, 1974.

[139] Ness, N. F., K. W. Behannon, and R. P. Lepping, The magnetic field of Mercury, 1, *J. Geophys. Res.*, *80*, 2708-2716, 1975.

[140] Nishida, A., T. Hada, K. A. Anderson, R. R. Anderson, S. J. Bame, and E. W. Hones, Jr., Broadband electrostatic noise in the magnetotail: Its relation to plasma sheet dynamics, *J. Geophys. Res.*, *90*, 4453-4460, 1985.

[141] Nishida, A., T. Mukai, T. Yamamoto, Y. Saito, and S. Kokubun, Magnetotail convection in geomagnetically active times, 1. Distance to the neutral lines, *J. Geomag Geoelectr*, *48*, 489-501, 1996.

[142] Omidi, N., Broadband electrostatic noise produced by ion beams in the Earth's magnetotail, *J. Geophys. Res.*, *90*, 12330-12334, 1985.

[143] Omura Y., and H. Matsumoto, KEMPO1; Technical guide to one-dimensional electromagnetic particle code, *Computer Space Plasma Physics, ed. by H. Matsumoto and Y. Omura, terra Sci. Pub. Co.*, 21-65, 1993.

[144] Omura, Y., **H. Kojima**, and H. Matsumoto, Computer simulation of Electrostatic Solitary Waves: A nonlinear model of broadband electrostatic noise, *Geophys. Res. Lett.*, *21*, 2923-2926, 1994.

[145] Omura, Y., H. Matsumoto, T. Miyake, and **H. Kojima**, Electron beam instabilities as generation mechanism of electrostatic solitary waves in the magnetotail, *J. Geophys. Res.*, *101*, 2685-2697, 1996.

[146] Omura, Y., **H. Kojima**, N. Miki, T. Mukai, H. Matsumoto Electrostatic solitary waves carried by diffused electron beams observed by GEOTAIL spacecraft, *to be submitted to Advances in Space Research*, 1998.

[147] Onsager, T. G., R. H. Holzworth, H. C. Koons, O. H. Bauer, D. A. Gurnett, R. R. Anderson, H. Lühr, and C. W. Carlson, *J. Geophys. Res.*, *94*, 13397-13408, 1989.

[148] Onsager, T. G., M. F. Thomsen, R. C. Elphic, J. T. Gosling, R. R. Anderson, and G. Kettmann, Electron generation of electrostatic waves in the plasma sheet boundary layer, *J. Geophys. Res.*, *15*, 15509-15519, 1993.

[149] Oya, H., and T. Obayashi, Measurement of ionospheric electron density by a gyroplasma probe: A rocket experiment by a new impedance probe, *Rep. Ionos. Space Res. Jpn.*, *20*, 199-213, 1966.

[150] Parker, E. N., Dynamics of interplanetary gas and magnetic fields, *Astrpphys. J.*, *128*, 664-675, 1958.

[151] Parks, G. K., M. McCarthy, R. J. Fitzenreiter, J. Etcheto, K. A. Anderson, R. R. Anderson, T. E. Eastman, L. A. Frank, D. A. Gurnett, C. Huang, R. P. Lin, A. T. Y. lui, K. W. Oglivie, A. Pedersen, H. Reme, and D. J. Williams, Particle and field characteristics of the high-latitude plasma sheet boundary layer, *J. Geophys. Res.*, *89*, 8885-8906, 1984.

[152] Pottelette R., M. Malingre, N. Dubouloz, B. Aparicio, R. Lundin, G. Holmgren, and G. Marklund, High-frequency waves in the cusp/cleft regions, *J. Geophys. Res.*, *95*, 5957-5971, 1990.

[153] Richter, A. K., K. C. Hsieh, A. H. Luttrell, E. Marsch, and R. Schwenn, Review of interplanetary shock phenomena near and within 1 AU, *AGU Monograph, Collisionless shocks in the heliosphere: Reviews of current research edited by B. T. Tsurutani, and R. G. Stone*, 33-50, 1985.

[154] Rodriguez, P., Magnetosheath electrostatic turblence, *J. Geophys. Res.*, *84*, 917-930, 1979.

[155] Roeder, J. L., and H. C. Koons, A survey of electron cyclotron waves in the magnetosphere and the diffuse aurora electron precipitation, *J. Geophys. Res.*, *94*, 2529-254, 1989.

[156] Russell, C. T., The configuration of the magnetosphere, *Critical Problems of Magnetospheric Physics, National Academy of Science*, 1-16, 1972.

[157] Russell, C. T., and R. L. McPherron, The magnetotail and substorms, *Space Sci. Rev.*, *15*, 205-266, 1973.

[158] Russell, C. T., M. von Dornum, and F. L. Scarf, Source locations for impulsive electric signals seen in the night ionosphere of Venus, *ICARUS*, *80*, 390-415, 1989.

[159] Saito, Y., T. Mukai, M. Hirahara, S. Machida, A. Nishida, T. Terasawa, S. Kokubun, and T. Yamamoto, *Geophys. Res. Lett.*, *21*, 2999-3002, 1994.

[160] Saito, Y., T. Mukai, T. Terasawa, A. Nishida, S. Machida, M. Hirahara, K. Maezawa, S. Kokubun, and T. Yamamoto, Slow-mode shocks in the magnetotail, *J. Geophys. Res.*, *100*, 23567-23581, 1995.

[161] Scarf, F. L., L. A. Frank, K. L. Ackerson, and R. P. Lepping, Plasma wave turbulence at distant crossings of the plasma sheet boundaries and the neutral sheet, *Geophys. Res. Lett.*, *1*, 189-192, 1974.

[162] Scarf, F. L., R. W. Fredericks, D. A. Gurnett, and E. J. Smith, The ISEE-C plasma wave investigation, *IEEE Trans. Geosci. Electr.*, *GE-16*, 191-195, 1978.

[163] Scarf, F. L., Possible traversals of Jupiter's distant magnetic tail by Voyager and by Saturn, *J. Geophys. Res.*, *84*, 4422-4424, 1979.

[164] Scarf, F. L., J. K. Alexander, R. A. Helliwell, M. Kelly, P. Kellog, P. M. Kintner, W. S. Kurth, H. Matsumoto, P. Rodriguez, S. D. Shawhan, *TRW Proposal*, No. 36749, 1980.

[165] Scarf, F., F. V. Coroniti, C. F. Kennek, R. W. Fredricks, D. A. Gurnett, and E. J. Smith, ISEE-3 wave measurements in the distant geomagnetic tail and boundary layer, *Geophys. Res. Lett.*, *11*, 335-338, 1984.

[166] Scarf, F. L., F. V. Coroniti, C. F. Kennel, E. J. Smith, J. A. Slavin, B. T. Tsurutani, S. J. Bame, and W. C. Feldman, Plasma wave spectra near slow mode shocks in the distant magnetotail, *Geophys. Res. Lett.*, *11*, 1050-1053, 1984b.

[167] Scarf, F. L., and C. T. Russell, Lightning measurements from Pioneer Venus Orbiter, *Geophys. Res. Lett.*, *10*, 1192-1195, 1983.

[168] Schriver, D., and M. Ashour-Abdalla, Generation of high-frequency broadband electrostatic noise: The role of cold electrons, *J. Geophys. Res.*, *92*, 5807-5819, 1987.

[169] Schriver, D., and M. Ashour-Abdalla, Cold plasma heating in the plasma sheet boundary layer: Theory and simulations, *J. Geophys. Res.*, *95*, 3987-4005, 1990.

[170] Schriver, D., M. Ashour-Abdalla, R. Treumann, M. Nakamura, and L. M. Kistler, The lobe to plasma sheet boundary layer transition: theory and observations, *Geophys. Res. Lett.*, *17*, 2027-2030, 1990.

[171] Shawhan, S. D., G. B. Murphy, and J. S. Picket, Plasma diagnostics package assessments of the STS-3 Orbiter plasma environment, *J. Spacecraft Rockets*, *21*, 387, 1984.

[172] Sibeck, D. G., G. L. Siscoe, J. A. Slavin, E. J. Smith, B. T. Tsurutani, and R. P. Lepping, The distant magnetotail's response to a strong interplanetary magnetic field B_y: Twisting, flattening, and field line bending, *J. Geophys. Res.*, *90*, 4011-4019, 1985.

[173] Sibeck, D. G., J. A. Slavin, E. J. Smith, and B. T. Tsurutani, Twisting of geomagnetic tail, *solar wind-magnetosphere coupling, edited by Y. Kamide and J. A. Slavin, Terra Publishing Company, Tokyo*, 731-738, 1986.

[174] Singh, R. N., and C. T. Russell, Further evidence for lightning on Venus, *Geophys. Res. Lett.*, *13*, 1051-1054, 1986.

[175] Slavin J. A., and Y. Kamide, Solar wind-magnetosphere coupling: Introduction, *Solar wind-magnetosphere coupling ed. Y. Kamide, and J. Slavin, Terra Scientific, Tokyo*, 9-12, 1986.

[176] Speise, T. W., Geomagnetic tail, *Geomagnetism Volume 4, edited by J. A. Jacobs, Academic Press, New York*, 1991.

[177] Stasiewicz, K., B. Holback, V. Krasnoselskikh, M. Boehm, R. Bostrom, and P. M. Kintner, Pparametric instabilities of Langmuir waves observed by Freja, *J. Geophys. Res.*, *101*, 21515-21525, 1996.

[178] Storey, L. R. O., An investigation of whistling atmospherics, *Phil. Trans. Roy. Soc. London, A, 246*, 113, 1953.

[179] Taylor, H. A., Jr., P. A. Cloutier, and Z. Zheng, Venus "Lightning" signals reinterpreted as in situ plamsa noise, *J. Geophys. Res.*, *92*, 9907-9919, 1987.

[180] Temerin, M., K. Cerny, W. Lotko, and F. S. Mozer, Observations of double layers and solitary waves in the auroral plasma, *Phys. Rev. Lett.*, *48*, 1175-1179, 1982.

[181] Tsurutani, B. T., and T. T. von Rosenvinge, ISEE-3 distant geotail results, *Geophys. Res. Lett., 10*, 1027-1029, 1984.

[182] Tsurutani, B. T. and W. D. Gonzalez, On the solar and interplanetary causes of geomagnetic storms, *Phys. Fluids B, 5*, 2623-2630, 1993.

[183] Tsutsui, M., R. J. Strangeway, B. T. Tsurutani, H. Matsumoto, J. L. Phillips, and M. Ashour-Abdalla, Wave mode identification of electrostatic noise observed with ISEE 3 in the deep tail boundary layer, *J. Geophys. Res., 96*, 14065-14073, 1991.

[184] Tsutsui, M., **H. Kojima**, I. Nagano, H. Sato, T. Okada, H. Matsumoto, T. Mukai, and M. Kawaguchi, Magnetic radiations from harness wires of spacecraft, *IEICE Trans. Commun, E75-B*, 174-182, 1992.

[185] Tsutsui, M., I. Nagano, **H. Kojima**, K. Hashimoto, H. Matsumoto, S. Yagitani, and T. Okada, Meaurements and Analysis of Antenna Impedance aboard the GEOTAIL Spacecraft, *Radio Science, 32*, 1101-1126, 1997.

[186] Usui, H., J. Koizumi, and H. Matsumoto, Statistical study on electron cyclotron harmonic waves observed at the dayside magnetosphere, *Advances in Space Research, 20*, 857-860, 1997.

[187] Usui, H., W. R. Paterson, H. Matsumoto, L. A. Frank, M. Nakamura, H. Matsui,T. Yamamoto, O. Nishimura, and J. Koizumi, GEOTAIL electron observations in association with intense bursts of ECH waves in the dayside magnetosphere, *submitted to J. Geophys. Res.*, 1998.

[188] Vago, J. L., P. M. Kintner, S. W. Chesney, R. L. Arnoldy, K. A. Lynch, T. E. Moore, and C. J. Pollock, Transverse ion acceleration by localized lower hybrid waves in the topside auroral ionosphere, *J. Geophys. Res., 97*, 16935-16957, 1992.

[189] White, D. R. J., Electromagnetic interference and compatibility, Vol. 1, *Interference Control Technologies, Inc.*, 1981.

[190] Wu, C. S. and L. C. Lee, A theory of the terrestrial kilometric radiation, *Astrophys. J., 230*, 621, 1979.

[191] Wygant, J. R., M. Bensadoun, and F. S. Mozer, Electric field measurements at subcritical, oblique bow shock crossings, *J. Geophys. Res., 92*, 11109-11121, 1987.

[192] Yamamoto, T., K. Shiokawa, and S. Kokubun, magnetic field structures of the magnetotail as observed by Geotail, *Geophys. Res. Lett., 21*, 2875-2878, 1994.

[193] Yamashita, F., Computer experiments on space plasma measurements by radio waves, Master Thesis, Dept. of Electr. Eng., Kyoto University, 1998.

[194] Zhang, Y., H. Matsumoto, and **H. Kojima**, Lion roars in the magnetosheath, *J. Geophys. Res., 103*, 4615-4626, 1998a.

[195] Zhang, Y., H. Matsumoto, **H. Kojima**, and Y. Omura, Extreamely intense whistler mode waves near the bow shock: Geotail observations, *accepted for the publication in J. Geophys. Res.*, 1998b.

[196] Zhang, Y., and H. Matsumoto, Magnetic noise bursts associated with the CME event on Feb. 21, 1994: The Geotail observations, *accepted for the publication in J. Geophys. Res.*, 1998c.

Publications

1. Matsumoto, H., Y. Omura, **H. Kojima** and B. T. Tsurutani, Linear analysis and computer simulation of wave instabilities driven by cometary Ions, Proceedings of Chapman conference on plasma waves and instabilities in magnetospheres and at comets, 26-29, 1987.

2. **Kojima, H.**, H. Matsumoto, Y. Omura, and B. T. Tsurutani, Nonlinear evolution of high frequency R-mode waves excited by water group ions near comets: computer experiments, *Geophys. Res. Lett., 16*, 9-12, 1989.

3. Tsutsui, M., **H. Kojima**, I. Nagano, H. Sato, T. Okada, H. Matsumoto, T. Mukai, and M. Kawaguchi, Magnetic radiations from harness wires of spacecraft, *IEICE Trans. Commun, E75-B*, 174-182, 1992.

4. Takahashi, K., S. Kokubun, H. Matsuoka, K. Shiokawa, K. Yumoto, M. Nakamura, H. Kawano, T. Yamamoto, A. Matsuoka, K. Tsuruda, H. Hayakawa, **H. Kojima**, and H. Matsumoto, GEOTAIL observation of magnetosonic Pc3 waves in the dayside magnetosphere, *Geophys. Res. Lett., 21*, 2899-2902, 1994.

5. Nagano, I., S. Yagitani, **H. Kojima**, Y. Kakehi, T. Shiozaki, H. Matsumoto, K. Hashimoto, T. Okada, S. Kokubun, and T. Yamamoto, Wave form analysis of the continuum radiation observed by GEOTAIL, *Geophys. Res. Lett., 21*, 2911-2914, 1994.

6. Matsumoto, H., **H. Kojima**, T. Miyatake, Y. Omura, M. Okada, I. Nagano, and M. Tsutsui, Electrostatic Solitary Waves (ESW) in the Magnetotail : BEN Wave forms observed by GEOTAIL, *Geophys. Res. Lett., 21*, 2915-2918, 1994.

7. **Kojima, H.**, H. Matsumoto, T. Miyatake, I. Nagano, A. Fujita, L. A. Frank, T. Mukai, W. R. Paterson, Y. Saito, S. Machida, and R. R. Anderson, Relation between electrostatic solitary waves and hot plasma flow in the plasma sheet boundary layer: GEOTAIL Observations, *Geophys. Res. Lett., 21*, 2919-2922, 1994.

8. Omura, Y., **H. Kojima**, and H. Matsumoto, Computer simulation of Electrostatic Solitary Waves: A nonlinear model of broadband electrostatic noise, *Geophys. Res. Lett., 21*, 2923-2926, 1994.

9. Hashimoto, K., H. Matsumoto, **H. Kojima**, T. Murata, I. Nagano, T.Okada, K. Tsuruda, and T. Iyemori, Auroral myriametric radiation observed by GEOTAIL, *Geophys. Res. Lett., 21*, 2927-2930, 1994.

10. Matsumoto, H., I. Nagano, R. R. Anderson, **H. Kojima**, K. Hashimoto, M. Tsutsui, T. Okada, I. Kimura, Y. Omura, and M. Okada, Plasma Wave Observations with GEOTAIL Spacecraft, *J. Geomag. Geoelectr., 46*, 59-95, 1994.

11. Hammond, C. M., G. K. Crawford, J. T. Gosling, **H. Kojima,** J. L. Phillips, H. Matsumoto, A. Balogh, L. A. Frank, S. Kokubun, and T. Yamamoto, Latitudinal structure of a Coronal Mass Ejection inferred from Ulysses and Geotail observations, *Geophys. Res. Lett., 22*, 1169-1172, 1995.

12. Murata, T., H. Matsumoto, **H. Kojima**, A. Fujita, T. Nagai, T. Yamamoto, and R. R. Anderson, Estimation of tail reconnection lines by AKR onsets and plasmoid entries observed with GEOTAIL spacecraft, *Geophys. Res. Lett., 22*, 1849-1852, 1995.

13. Nagano, I., S. Yagitani, **H. Kojima**, and H. Matsumoto, Analysis of Wave Normal and Poynting Vector of the Chorus Emissions Observed by GEOTAIL, *J. Geomag. Geoelectr., 48*, 299-307, 1996.

14. Kasaba, Y., **H. Kojima**, H. Matsumoto, and T. Murata, Search for Jovian Hectometric and Kilometric radiation by GEOTAIL spacecraft during the impact of Comet Shoemaker-Levy 9, *J. Geomag. Geoelectr., 48*, 361-370, 1996.

15. Omura, Y., H. Matsumoto, T. Miyake, and **H. Kojima**, Electron beam instabilities as generation mechanism of electrostatic solitary waves in the magnetotail, *J. Geophys. Res., 101*, 2685-2697, 1996.

16. Matsumoto, H., **H. Kojima**, Y. Kasaba, T. Miyake, R. R. Anderson, and T. Mukai, Plasma Waves in the Upstream and Bow Shock Regions Observed by GEOTAIL, *Advances in Space Research, 20*, 683-693, 1997.

17. **Kojima, H.**, H. Furuya, H. Usui and H. Matsumoto, Modulated electron plasma waves observed in the tail lobe: GEOTAIL waveform observations., *Geophys. Res. Lett., 24*, 3049-3052, 1997.

18. **Kojima, H.**, H. Matsumoto, S. Chikuba, S. Horiyama, M. Ashour-Abdalla, and R. R. Anderson, GEOTAIL Waveform Observations of Broadband/Narrowband Electrostatic Noise in the Distant Tail, *J. Geophys. Res., 102*, 14439-14455, 1997.

19. Murata, T., H. Matsumoto, **H. Kojima** and T. Iyemori, Correlations of AKR index with Kp and Dst indices, *Proceedings of the NIPR Symposium on Upper Atomosphere Physics, 10*, 64-68, 1997.

20. Tsutsui, M., I. Nagano, **H. Kojima**, K. Hashimoto, H. Matsumoto, S. Yagitani, and T. Okada, Measurements and analysis of antenna impedance aboard the GEOTAIL spacecraft, *Radio Science, 32*, 1101-1126, 1997.

21. Zhang, Y., H. Matsumoto, **H. Kojima**, and Y. Omura, Extremely intense whistler mode waves near the bow shock: GEOTAIL observations, Submitted to J. Geophys. Res., 1997.

22. Zhang, Y., H. Matsumoto, and **H. Kojima**, Lion roars in the magnetosheath: The GEOTAIL observations, *J. Geophys. Res., 103*, 4615-4626, 1998.

23. Miyake, T., Y. Omura, H. Matsumoto and **H. Kojima**, Two-Dimensional Computer Simulations of Electrostatic Solitary Waves Observed by GEOTAIL Spacecraft., *J. Geophys. Res., 103*, 11841-11850, 1998.

24. Matsumoto, H., **H. Kojima**, Y. Omura, and I. Nagano, Plasma waves in Geospace: GEOTAIL Observation, *AGU Monograph, in press*, 1998.

25. Anderson, R. R., D. A. Gurnett, H. Matsumoto, K. Hashimoto, **H. Kojima**, G. Rostoker,I. Nagano, Y. Kasaba, S. Kokubun, and T. Yamamoto, GEOTAIL, POLAR and CANOPUS observations of plasma waves and geomagnetic activity related to the April 7, 1997, solar flare and coronal mass ejection, *Submitted to Geophys. Res. Lett.*, 1998.

26. Matsumoto, H., L. A. Frank, Y. Omura, **H. Kojima**, W. R. Paterson, M. Tsutsui, R. R. Anderson, S. Horiyama, S. Kokubun, and T. Yamamoto, Generation Mechanism of ESW based on GEOTAIL Plasma Wave Observation, Plasma Observation and Particle Simulation, *Submitted to Geophys. Res. Lett.*, 1998.

Oral presentations (International conference only)

1. **Kojima, H.**, H. Matsumoto, Y. Omura, and B. T. Tsurutani, Electromagnetic Waves Instabilities driven by Cometary Heavy Ions: 2-Dimensional Computer Experiments, AGU Fall Meeting, San Francisco, USA, 1989.

2. **Kojima, H.**, H. Matsumoto, Y. Omura, and B. T. Tsurutani, Properties of Nonlinear Steepened Waves and Whistler Wave Packets: 1-D Computer Experiments, Western Pacific Geophysics Meeting, Kanazawa, Japan, 1990.

3. **Kojima, H.**, H. Matsumoto, I. Nagano, and M. Tsutsui, Waveform Observations with GEOTAIL Plasma Wave Instrument, AGU Fall Meeting, San Francisco, USA, 1992.

4. **Kojima, H.**, I. Nagano, A. Fujita, H. Matsumoto, S. Kokubun, T. Yamamoto, L. A. Frank, and W. R. Paterson, Plasma Wave Features of the Boundary Layers in the Magnetosphere, AGU Fall Meeting, San Francisco, USA, 1993.

5. **Kojima, H.**, H. Matsumoto, I. Nagano, M. Tsutsui, Y. Omura, and T. Miyatake, GEOTAIL Wave Form Observation of Broadband Electrostatic Noise in the Geomagnetic Tail, AGU Spring Meeting, Baltimore, USA, 1993.

6. **Kojima, H.**, H. Matsumoto, I. Nagano, R. R. Anderson, K. Hashimoto, M. Tsutsui, T. Okada, I. Kimura, Y. Omura, and M. Okada, GEOTAIL Wave Form Observation of Broadband Electrostatic Noise in the Geomagnetic Tail, IAGA, 1993 (Invited).

7. **Kojima, H.**, H. Matsumoto, S. Horiyama, S. Chikuba, R. R. Anderson, Y. Omura, T. Mukai, L. A. Frank, S. Machida, Y. Saito, M Hirahara, W. R. Paterson, T. Yamamoto, and S. Kokubun, Broadband/Narrowband Electrostatic Emissions Observed by GEOTAIL Spacecraft in the Geomagnetic Tail Region, AGU Fall Meeting, San Francisco, USA, 1994 (Invited).

8. **Kojima, H.**, C. M. Hammond, G. K. Crawford, J. T. Gosling, H. Matsumoto, L. A. Frank, S. Kokubun, T. Yamamoto, and A. Balogh, Evolution of CIR's and Stream Interface:GEOTAIL ULYSSES Observations, AGU Spring Meeting, Baltimore, USA, 1994.

9. **Kojima, H.**, A. Hamada, A. Fujita, H. Matsumoto, I. Nagano, L. A. Frank, T. Mukai, T. Yamamoto, S. Kokubun, W. R. Paterson, S. Machida, and Y. Saito, Plasma wave features in the geomagnetic tail regions: GEOTAIL observations, Eighth International Symposium on Solar Terrestrial Physics, Sendai, Japan, 1994.

10. **Kojima, H.**, H. Matsumoto, S. Horiyama, T. Miyatake, Y. Omura, I. Nagano, M. Tsutsui, L. A. Frank, T. Mukai, T. Yamamoto, S. Kokubun, W. R. Paterson, S. Machida, and Y. Saito, GEOTAIL Waveform Observations of the Broadband Electrostatic Waves in the Magnetotail Region, International Workshop on Nonlinear Waves and Chaos in Space Plasmas, Kyoto, Japan, 1994.

11. **Kojima, H.**, H. Matsumoto, S. Horiyama, R. R. Anderson, T. Yamamoto, S. Kokubun, T. Mukai, S. Machida, and Y. Saito, Propagation Analyses of the Electrostatic Solitary Waves Observed with the GEOTAIL Spacecraft, AGU Fall Meeting, San Francisco, USA, 1995.

12. **Kojima, H.**, S. Horiyama, H. Matsumoto, Y. Omura, R. R. Anderson, S. Kokubun, T. Mukai, and Y. Saito, Electrostatic waves observed in the magnetosheath, 31st Scientific Assembly of COSPAR, The University of Birmingham, England, 1996.

13. **Kojima, H.**, H. Hamada, D. Morikawa, H. Matsumoto, T. Murata, R. R. Anderson, T. Yamamoto, and S. Kokubun, Statistical Analyses of Plasma Waves Observed in the Tail Region: Application of Plasma Waves to the Study of the Geomagnetic Tail Structure, Chapman Conference, Kanazawa, 1996 (Invited).

14. **Kojima, H.**, H. Matsumoto and I. Nagano, Geotail plasma wave observation in the geomagnetic tail and in the dayside magnetopause, COSPAR Colloquium: Magnetospheric research with advanced techniques, Beijing, China, 1996.

15. **Kojima, H.**, Micro- and Macro-Physics of Magnetotail Plasma via GEOTAIL Plasma Wave Observation -Nonlinear waves and its significance to magnetospheric physics, Gordon Research Conference, New England College, 1996 (Invited).

16. **Kojima, H.**, H. Matsumoto, Y. Omura and R. R. Anderson, Broadband Electrostatic Noise in the Plasma Sheet, AGU Fall Meeting, San Francisco, 1997.

17. **Kojima, H.**, H. Matsumoto, and Y. Omura, electrostatic solitary waves observed in the geomagnetic tail and polar regions, 32nd COSPAR Scientific Assembly, Nagoya, 1998 (Invited).

18. **Kojima, H.**, K. Ohtsuka, H. Matsumoto, Y. Saito, T. Mukai, S. Kokubun, and T. Yamamoto, Plasma waves in the slow mode shocks observed by GEOTAIL spacecraft, 32nd COSPAR Scientific Assembly, Nagoya, 1998.